University of Pennsylvania
ScholarlyCommons

Publicly Accessible Penn Dissertations

2019

Seeing The Light (higgs): Searches And Measurements Of Higgs Boson Decays To Photons

Khilesh Pradip Mistry
University of Pennsylvania, khilesh.mistry@gmail.com

Follow this and additional works at: https://repository.upenn.edu/edissertations

 Part of the Elementary Particles and Fields and String Theory Commons

Recommended Citation
Mistry, Khilesh Pradip, "Seeing The Light (higgs): Searches And Measurements Of Higgs Boson Decays To Photons" (2019). *Publicly Accessible Penn Dissertations*. 3234.
https://repository.upenn.edu/edissertations/3234

This paper is posted at ScholarlyCommons. https://repository.upenn.edu/edissertations/3234
For more information, please contact repository@pobox.upenn.edu.

Seeing The Light (higgs): Searches And Measurements Of Higgs Boson Decays To Photons

Abstract
This dissertation presents two results involving Standard Model Higgs bosons decaying to at least one photon. These analyses are performed using 79.8/fb of proton-proton collisions collected at $\sqrt{s}$=13 TeV with the ATLAS detector at the Large Hadron Collider.

Differential and fiducial cross section measurements of the Higgs boson decaying to two photons are presented.The inclusive diphoton cross section was measured to be 55 ± 9 (stat.) ± 4 (syst.) ± 0.1 (theo.) fb compared with the Standard model prediction of 64 ± 2 fb. In addition to inclusive cross section measurement, fiducial cross section results are shown for regions targeting the vector boson fusion, VH, and ttH production modes of the Higgs boson as well as a region targeting beyond the Standard Model contributions. Differential results are given for multiple measured spectra involving kinematics of the diphoton system or variables with jets produced in association with the Higgs boson. No significant deviations from the Standard Model are observed and in their absence, limits are set on alternative hypotheses involving higher order couplings between Standard Model particles and the Higgs boson.

Additionally, a search for a Standard Model Higgs bosons decaying into at least one photon and missing transverse momentum was performed.The photon can arise from a Higgs boson decaying into one or two neutralinos, which in turn decay into a gravitino and photon.Higgs bosons produced in association with a Z boson are considered in order to reduce the number of background events. No excess with respect to the Standard Model prediction is observed. Assuming a Standard Model ZH production cross section, the branching fraction of a Higgs boson to neutralinos or neutralino/gravitino is constrained to be less than 5-11% at the 95% confidence level for nearly massless gravitinos.

Degree Type
Dissertation

Degree Name
Doctor of Philosophy (PhD)

Graduate Group
Physics & Astronomy

First Advisor
Hugh H. Williams

Keywords
Gravitino, Higgs, Neutralino, Photon, SUSY, TRT

Subject Categories
Elementary Particles and Fields and String Theory | Physics

This dissertation is available at ScholarlyCommons: https://repository.upenn.edu/edissertations/3234

SEEING THE LIGHT (HIGGS): SEARCHES AND MEASUREMENTS OF HIGGS BOSON DECAYS TO PHOTONS

Khilesh Pradip Mistry

A DISSERTATION

in

Physics and Astronomy

Presented to the Faculties of The University of Pennsylvania
in Partial Fulfillment of the Requirements for the Degree of Doctor of Philosophy
2019

Hugh H. Williams, Mary Amanda Wood Professor of Physics
Supervisor of Dissertation

Joshua Klein, Edmund J. and Louise W. Kahn Professor, Physics
Graduate Group Chairperson

Dissertation Committee

I. Joseph Kroll, Professor, Physics
Justin Khoury, Professor, Physics
Elliot Lipeles, Associate Professor, Physics
Burt Ovrut, Professor, Physics
Hugh H. Williams, Mary Amanda Wood Professor of Physics

SEEING THE LIGHT (HIGGS): SEARCHES AND MEASUREMENTS OF HIGGS BOSON DECAYS TO PHOTONS

COPYRIGHT
2019
Khilesh Pradip Mistry

This work is licensed under a Creative Commons
Attribution-NonCommercial-ShareAlike 3.0 Unported License.

To view a copy of this license, visit
http://creativecommons.org/licenses/by-nc-sa/3.0

or send a letter to:

Creative Commons
444 Castro Street, Suite 900
Mountain View, CA 94140
USA

Acknowledgements

First and foremost, I would like to thank all the mentors and advisers I had, who encouraged me and allowed me to be part of this incredible journey through the physics world. This includes Bruce Schumm, my advisor at UCSC, who taught me so much about electronics, readout systems, and debugging. I can't express my extreme gratitude to my adviser for the past six years, Brig Williams, who took me on as a grad student and continued to help me grow. Your careful leadership of the group has allowed not only myself, but all graduate students in our group to thrive and stand out in the ATLAS collaboration. The insights, guidance of my research, and big picture view – of not only my analyses but TRT issues – has been invaluable and reminded me that I have so much more to learn about being a successful problem solver and physicist. Joe Kroll, I appreciate your fierce advocation for all of the Penn students, helping us navigate and not get lost in such a big collaboration. To Elliot Lipeles and Evelyn Thomson, you and your students make the group so much more than just a group, and it is this environment of caring and brilliance that made this grad school experience amazing.

Working in the TRT group was far and away my favorite part of graduate school. I wouldn't have been successful without Anatoli, Dominik, Andrea, and Andrey - the amazing coordinators. I have learned an incredible amount about teamwork and the successful Run 2 operations would not have been possible without the DCS, GAS, Offline, etc teams. The DAQ team of past and present members: Mike, Dominick, Ben, Jamie, Jon, Sarah, Ximo, Zoltan, Chris, Bijan, Elodie, Vincent, Daniil, Joe, Keisuke, Ian, Shion, Colin, Mike, Paul, Brig, and Mitch, I am deeply indebted to you all. The TRT was already in great shape due to the diligence of the commissioning and Run 1 teams. For the Run 2 DAQ team, the prep and operations of the last 4 years would not have been so smooth without all your hard teamwork. Sarah and Chris, thank you for your leadership and friendship during my years as a young grad student.

Next I'd like to thank the ATLAS collaboration. Working first hand on TRT DAQ made me really appreciate the scale and complexities of this experiment. This was one of many teams on the TRT, which was but one of the 10+ sub-systems of the detector. The operations teams, shifters, data pipeline and quality experts, and combined performance groups do a remarkable amount of thankless work, but without them the nice physics analyses would cease to exist. As I ventured out into the collaboration, first I joined the photon ID group and the $H \to \gamma\gamma$ group. There, I worked with Giovanni Marchiori and Nicolas Berger. As my first conveners, I'm grateful for them sharing their knowledge about all things photons, statistics, and ATLAS software. Chris and Florian, you taught me an exceptional amount about cross sections, background modeling, and how to think about different problems. I could not have done this without as great of a postdoc as I had in Chris. With your leadership on the TRT as well as guidance and patience through my thesis work, I learned so much from you about being a good physicist and person.

During grad school I had to take a detour back home for medical reasons. I am immensely thankful to all those who helped me during this trying time and could never properly acknowledge everyone. First I need to express my extreme gratitude to my doctors, Emmanuel Raad in Geneva and Gina Farinholt in San Diego. Without them and the excellent teams of specialists and nurses, I would not be here today. Allie Longworth, thank for you helping me relax and for teaching me to find an outlet, through music, for all the negative thoughts. I also had amazing support from the entire Penn group. I felt tremendous warmth and kindness from everyone, especially Brig, who was very patient, caring, and understanding through the whole situation. Thank you Bijan, for taking time each week to visit me in Hôpital de La Tour while I was in Geneva. Thank you Joe, for spending time with me in Scripps Memorial, helping me keep a feeling of connection to the physics world and a sense of normality. Thanks Christian and Jack, for visiting me in San Diego and chatting all the time. Tatyana, thanks for the kind emails and encouragements to get back and get started again. And thanks to all my friends and family from back home: Dennis, Brian, Bergren, Kenny, Henry, Zac, Zach, Aaron, Paul, ..., Dom, Daniel, Jared, ..., etc. There are too many names to list here, but know that you all made a difference during these times. And of course my parents, Pradip and Prabha - I know it was a struggle, but I couldn't have done it without you.

The Penn ATLAS group (past and present) has been nothing but fun and collaborative learning. This includes Alex, Kurt, Jamie, John, Jon, Chris L., Liz, Brett, Ryan, Sarah, Chris M., Keisuke, Shion, Jeff, Joana, Rob, Billy, Will, Leigh, Bijan, Joey, Christian, Elodie, Rachael, Tony, Ian, Lucas, Ben, Joe, and James. I'm indebted to Jamie, for taking me under his wing my first year, and giving me the foundations to become a DAQ and photon expert. I'm grateful for Alex and Kurt as they

would answer all the random questions and allowed me to stay at Vermont and Candyland during the first years. Joey, I couldn't ask for a better officemate. You are an all time great of the Kool Coffee Klub. Bijan, thanks for everything in grad school. We roomed together in Geneva and Philly. We worked together on DAQ and almost on the same analysis. Talking with you is always fascinating and your attitude and knowledge has changed me for the better. Leigh, I enjoyed and will miss all the cathartic conversations and the of building structures in the office. Christian, I wish I could thank you but you need to pay me my coffee money first. To Penn ATLAS, thanks for all the crazy lunch conversations, 3 hour long afternoon breaks, mattermost and git shenanigans, and the Kool Coffee Klub. It's been a wild ride.

I didn't really like Philadelphia as a first year student, but now I hate to leave it. I will miss the beautiful historic buildings, its warm friendliness, and tasty soft pretzels. I have come to love it not only for those things, but for the people I have met. Part of coming to love Philly was the Sansom house and their honorary members. Christian, know that I will dunk on you one day. I will miss the beers, bike building, basketball, office conversations, and all the trash talking that goes along with it. Ashley, thanks for always making me laugh and helping me push myself in all things athletic. Tatyana, thanks for the card, the caring, and dinner fun. As for others in my cohort, Eric M., you were a great captain of the Higgs Bowlsons and I really enjoyed your ideas that you would share with the office. Thanks Asja, for help in various times, insightful conversations during the years, and for the butterfly wings and biking books. Eric W., the chill sessions were real.

Once again, I need to recognize Ashley and Tatyana, for my second home on Chadwick Street. So many good meals, conversations, movies, work, and general silliness. I'm going to miss the comfort of that home, the biking adventures we had together, and the crazy amount cooking/baking. Some of my favorite meals have been there, cooking for our other friends. Thanks to Eric H., Lia, and Charlotte for always bringing good wine and even better conversation.

There are so many more friends, neighbors, and family I have neglected to mention or don't have the space, but thank you. Tatyana, I really could not have done any of this without you. Your support, help during stressful times, understanding, and love is unlike anything I have or could have wished to experience. The trips to France, Geneva, and Tunisia, bike adventures, restaurant experiences, and all the delicious baked treats, are just a handful of the things I will always cherish. Everyday life with you is always an excitement. Last but definitely not least, none of this would be possible without my loving family: my parents - Pradip and Prabha, my sister - Meera, and of course, Peach. You were always supportive, patient, and have sacrificed so much for me. Thank you and I love you all.

ABSTRACT

SEEING THE LIGHT (HIGGS): SEARCHES AND MEASUREMENTS OF HIGGS BOSON DECAYS TO PHOTONS

Khilesh Pradip Mistry

H. H. Williams

This dissertation presents two results involving Standard Model Higgs bosons decaying to at least one photon. These analyses are performed using $79.8\,\text{fb}^{-1}$ of proton–proton collisions collected at $\sqrt{s} = 13\,\text{TeV}$ with the ATLAS detector at the Large Hadron Collider.

Differential and fiducial cross section measurements of the Higgs boson decaying to two photons are presented. The inclusive diphoton cross section was measured to be $55 \pm 9\,(\text{stat.}) \pm 4\,(\text{syst.}) \pm 0.1\,(\text{theo.})\,\text{fb}$ compared with the Standard model prediction of $64 \pm 2\,\text{fb}$. In addition to inclusive cross section measurement, fiducial cross section results are shown for regions targeting the vector boson fusion, VH, and $t\bar{t}H$ production modes of the Higgs boson as well as a region targeting beyond the Standard Model contributions. Differential results are given for multiple measured spectra involving kinematics of the diphoton system or variables with jets produced in association with the Higgs boson. No significant deviations from the Standard Model are observed and in their absence, limits are set on alternative hypotheses involving higher order couplings between Standard Model particles and the Higgs boson.

Additionally, a search for a Standard Model Higgs bosons decaying into at least one photon and missing transverse momentum was performed. The photon can arise from a Higgs boson decaying into one or two neutralinos, which in turn decay into a gravitino and photon. Higgs bosons produced in association with a Z boson are considered in order to reduce the number of background events. No excess with respect to the Standard Model prediction is observed. Assuming a Standard Model ZH production cross section, the branching fraction of a Higgs boson to neutralinos or neutralino/gravitino is constrained to be less than 5-11% at the 95% confidence level for nearly massless gravitinos.

Contents

List of Tables

List of Figures

List of Common Abbreviations

VBF Vector boson fusion Higgs production. xiv, 8, 9, 11, 69–71, 73, 74, 79, 80, 95, 100, 103, 104, 106, 109–111, 115, 183–185, 187, 222

ggF Gluon gluon Fusion Higgs production. xiv, 8, 9, 11, 70–72, 74, 99, 100, 103, 104, 109–111, 115

ADC Analog to Digital Converter. 54

AFII ATLAS Fast Simulation II. 74, 81, 167

ASDBLR amplification, shaping, discrimination, and base-line restoration. xv, 35–37, 43, 44

ASIC Application-Specific-Integrated-Circuit. 35

BF Branching Fraction. xiii, xvii, 12, 113–115, 118, 172, 177–182

BNL Brookhaven National Lab. 36, 38

BSM Beyond the Standard Model. xv, 2, 17, 23, 67–69, 71, 103, 104, 107, 110, 111, 113, 116, 171, 172, 175, 176, 185, 186

CERN Organisation Europiéenne pour la Recherche Nucléaire. xiv, 1, 20, 21, 32, 34, 37, 85

CL Confidence Level. xii, xiii, xv, xvii, 103, 104, 110, 111, 115, 171, 172, 176–180, 182, 186

CP Charge conjugation-Parity. 14, 70, 108, 109

CSC Cathode Strip Chamber. 30, 31

DAC Digital to Analog Conversion. 37–44

DAQ Data Acquisition. xiv, 2, 33–35, 43, 45, 185, 186

DTMROC Drift Time Measurement ReadOut Chip. 35–37, 39–42, 45

EFT Effective Field Theory. 67, 71, 109

EM electromagnetic. 1, 31, 53, 55, 56, 93

EWK Electroweak. 4, 5, 11, 16, 74

FF Fudge Factor. 52, 58, 60, 61, 200–207, 209–215, 217

GMSB Gauge Mediated Supersymmetry Breaking. xvi, 16–19, 113, 114

GOL Gigabit Optical Link. 36, 45–49, 188, 189, 191, 199

GR General Relativity. 13

HLT High Level Trigger. 32

IBL Insertable B-Layer. 25

ID Inner Detector. 24, 31, 64, 65

ID Identification. xiii, xvi, 51, 57, 59, 76–78, 119, 153–157, 181

IDS Iteratively Dynamically Stabilized. 98

Iso Isolation. 51, 154, 169

JVT Jet Vertex Fraction. 101

KDE Kernel Density Estimation. xv, 59, 60

L1 Level 1 Trigger. 32

LAr Liquid Argon calorimeter. 28–30, 54, 92

LEP Large Electron-Positron Collider. 17, 55, 109

LHC Large Hadron Collider. xvii, 2, 5, 8, 9, 11, 13, 16, 17, 20–25, 32, 35, 45, 46, 63, 64, 67, 72, 114, 120, 188, 191–198

LINAC2 Linear Accelerator 2. 20

LO leading order. 73, 74, 116

LSP Lightest Supersymmetric Particle. xii, xiii, xvii, 16, 113–118, 120–126, 129, 175, 177–182

LVDS Low Voltage Differential Signals. 36

MC Monte Carlo. 58, 61, 78, 81, 99, 101, 103, 104, 116, 131–133, 145, 146, 159–164, 167, 169, 173, 174, 217

MDT Monitored Drift Tube. 30, 31

MLE Maximum Likelihood Estimator. 88

MOND Modified Newtonian Dynamics. 14

MS Muon Spectrometer. 24, 30, 64

MSSM Minimal Supersymmetric Standard Model. xii, 15, 17, 18, 116

N^{3}LL next-to-next-to-next-to-leading logarithmic. 11, 105

N^{3}LO next-to-next-to-next-to-leading order. 9, 73, 74, 103, 105

NLL next-to-leading logarithmic. 73, 74, 105

NLO next-to-leading order. 9, 11, 73, 74, 103, 105

NLSP next-to-lightest supersymmetric particle. xii, xiii, xvii, 16, 17, 113–118, 120–126, 129, 175, 177–182

NMSSM Next-to-Minimal Supersymmetric Standard Model. xvi, 18, 113, 114

NNLL next-to-next-to-leading logarithmic. 104, 105

NNLO next-to-next-to-leading order. 11, 72–74, 104, 105

NP Nuisance Parameter. 88–91, 170

OFC Optimal Filtering Coefficient. 54

PDF Parton Distribution Function. xii, 11, 20, 72–74, 116, 117

PDF Probability Distribution Function. 60, 61, 64, 76, 89, 97, 99, 103, 104, 136

PER Photon Energy Resolution. xv, 92–95, 97

PES Photon Energy Scale. xv, 92–95, 97

PS Proton Synchrotron. 20

PSB Proton Synchrotron Booster. 20

QCD Quantum Chromodynamics. 5, 8, 9, 11, 13, 52, 70–74, 103–105, 117, 120, 145

QED Quantum Electrodynamics. 7

QFT Quantum Field Theory. 1, 3

QPLL Quartz Phase Locked Loop. 45–47, 50

ROD ReadOut Driver. xii, xv, xvii, 36, 45–50, 188–191, 193–199

ROS ReadOut System. 36

RPC Resistive Place Chamber. 30, 31

SCT SemiConductor Tracker. 26

SILH Strongly Interacting Light Higgs. 108, 109

SM Standard Model of particle physics. xiii, xvii, 1, 3, 13–18, 72, 103, 107–116, 119, 131–133, 160, 170–183, 186

SPS Super Proton Synchrotron. 20

SUSY Supersymmetry. 2, 14–18, 66, 113, 116, 170

SVD Single Value Decomposition. 98

TGC Thin Gap Chamber. 30, 31

TRT Transition Radiation Tracker. xiv, 2, 27, 30, 34–38, 40, 43, 45, 46, 63, 185, 186, 188

TTC Timing and Trigger Control. 36, 45

vev vacuum expectation value. 6–8, 18

VME Versa Module Eurocard. 36, 189

Preface

After finishing my undergraduate studies and R&D work on silicon readout electronics for the International Linear Collider (ILC) at the University of California, Santa Cruz, I joined the ATLAS group at University of Pennsylvania in 2013. In July before classes began, my adviser – Brig Williams – allowed me to spend time at CERN in Geneva, Switzerland in order to learn about the Transition Radiation Tracker (TRT) and its Data Acquisition (DAQ) system. During that time, it was CERN's Long Shutdown I and I spent the majority of my time in the TRT test-bench setup in Bâtiment 104. There, I learned about the TRT DAQ readout system, timings of the clocks and data, and how to repair the different broken boards. This would be my area of expertise for the remainder of grad school, and I think I spent the most time in this room of all TRT DAQ people over the last 6 years. Additionally, during that first summer, I had the pleasure of going into the ATLAS detector many times, helping replace boards and generally explore. Hearing and reading about the detector is one thing, but seeing is another. No matter how many times boards needed to be replaced during subsequent on-call shifts over the next years, I was always excited to go into the detector. Especially when the magnet field was present, when no lights were on and the field was pulling the patch panels in every direction.

Back in Philadelphia, I started classes and jumped right into doing radiation studies on the front-end TRT boards. These radiation studies were vital at the time as we had seen adverse and unexpected shifting of voltage values on the front-end boards. It was vital to figure out the cause and potential future issues in order to be prepared for Run 2 and beyond. This was a natural fit considering I had just finished working on the T-506 Experiment at SLAC which irradiated silicon diode sensors and tested their radiation tolerance. Classes, along with trips to CERN for Milestone detector weeks and radiation tests were the larger parts of my life from 2013 through 2015. During this time, I also joined the diphoton+$E_{\mathrm{T}}^{\mathrm{miss}}$ SUSY group, where I worked on a SUSY search along

with Bruce. It was a very overwhelming time, getting ramped up on my first analysis work, all the while taking classes and doing the radiation studies. Sometime in 2014 I was also was referred to some papers by Brig about uncovered searches involving Higgs decays to neutralinos and gravitinos. This signature would eventually become my dissertation topic. In April 2015 I finished the radiation studies, showing the damage was indeed caused by radiation, and predicted the effect was almost saturated and should not pose a problem for the remainder of the TRT lifetime. This task qualified me as an author on the ATLAS collaboration, and I started packing up things in Philadelphia in order to move to CERN for the remainder of my Ph.D. Around this time I started getting involved in the photon identification group, implementing photon isolation in the trigger, performing initial studies for the optimization of the identification, and deriving correction factors ("fudge factors") for the input variables of the identification.

Unfortunately, sometimes life has other plans. A month after moving to Saint-Genis-Pouilly, France in May, I was hospitalized for a reoccurring medical condition. I had to move back home to San Diego, CA for the remainder of 2015 and did not engage in much research. I ended up making a poster on the TRT DAQ upgrades for Run 2, which was presented at the Topical Workshop on Electronics for Particle Physics in Lisbon, Portugal in September of 2015. Even though I have mentioned them in the acknowledgements, I must pause briefly and thank everyone again, this time without specifics. Everyone never gave up on me and helped in many unimaginable ways. All of these encouragements helped me get back on track, helped me learn from those days, and helped me feel like I should go back and continue my studies, even though there was a brief time I considered dropping out completely. In the end, I did not, and instead returned not to Geneva but Philadelphia in January of 2016. It was here I eventually found a home and really hit my stride in grad school.

After getting back into the swing of things and continuing with deriving the fudge factors in the photon ID group, I was taken under the wing of our outstanding postdoc, Chris Meyer, and collaborated with him closely during the buzz of the 750 GeV diphoton excess. This was an excess seen in the diphoton invariant mass spectrum in 2015. I worked on cross checks of the 2016 data samples in order to confirm the validity of the excess. Caught up in the excitement, I made multiple bets with Bijan, Christian, and Joey about the existence of a new scalar or spin-2 particle decaying into two photons. The optimist in me wanted to believe there was beyond the Standard Model physics just around the corner. Alas I did not win the bets, as evidenced by www.bijanwasright.com and my fashion choices for the next month in the form of wearing "Tae-shirts". My work contributed to a *tiny* part of this analysis, making a conference note for the 2016 International Conference on High Energy Physics (ICHEP) in Chicago, IL, and ended up being published in Physical Letters

B [1]. Shortly after the ICHEP conference, the photon ID group released a public note containing some of my photon ID contributions [2].

Nonetheless, after the excitement was quashed by 2016 data, I continued to collaborate closely with Chris, joining the Higgs to diphoton fiducial and differential cross section team. I first started to understand the signal parameterization and extract photon energy scale and resolution uncertainties of the signal model. After that, I joined the teams studying the background parameterization. I performed F-test studies, testing data sidebands to make sure our model accurately described the data. This lead me into building full templates of the backgrounds and performing "spurious signal" estimates as well as understanding the different biases of the functional fitting. I remember both fondly and unfavorably of the final weeks leading up to the ICHEP as it marked the first cups of coffee (to this point in life I had resisted temptations and could always make time for sleep), 2 a.m. meetings and excitement. We released a conference note [3] for the conference, using $13.3\,\text{fb}^{-1}$of 2015–2016 data and it was my first public result in which I played a major role in the analysis team.

During the remainder of 2016, I went to CERN for multiple weeks of on-call shifts and TRT troubleshooting. Over the latter parts of 2016, I started generating Monte Carlo and re-reading literature about Higgs decays to neutralinos and gravitinos in a detector final state of photons and missing transverse momentum. This resulted in my candidacy exam presentation during December of 2016, where I described my plans to search for Higgs decays to neutralinos and gravitinos with an associated Z boson.

In 2017, I once again was involved with many aspects of the Higgs to diphoton fiducial and differential cross sections signal and background parameterization and photon ID fudge factors. I was an editor on 3 ATLAS internal notes during this year, one for my photon ID work, one for TRT upgrades during Run 2, and one for the Higgs to diphoton group. I frequently went to CERN for TRT on-call shifts and work, contributing to the HOLA card assembling, testing and upgrade campaign that upgraded the back-end data throughput rate of the TRT by 20%. During this time, I converted the entire TRT codebase from the outdated CMT compilation scheme to CMake. After another conference note was released for the Higgs to diphoton fiducial and differential cross sections for the 2017 European Physical Society Conference on High Energy Physics in Venice, Italy [4], I transitioned full time into the SUSY electroweak group to focus of the Higgs to neutralinos and gravitinos search.

From mid 2017 through June 2018, I spent almost all of my time on this, intermixed with my continuing responsibilities of TRT and Higgs to diphoton cross section research. This was a very challenging and rewarding experience for me, as the group I interacted with consisted of myself,

and Brig and Chris for advice/direction. This was in direct contrast to my experience in the Higgs to diphoton group as I worked with at least 10 active analyzers and the greater group consisted of more than 25 people. This means I personally did nearly everything in the analysis from the first signal generation to the final unblinding and limit setting. I produced all the "ntuples" for analysis, wrote all the C++/python analysis code, and produced every plot. With help writing from Brig and Chris, the result was released as a conference note in 2018 [5] at the Conference on Large Hadron Collider Physics in Bologna, Italy.

During 2018, the paper on the differential and fiducial cross sections from the 2015–2016 was finally accepted by Physical Review D [6]. Additionally, the group released a small conference note update at the 2018 International Conference on High Energy Physics in Seoul, Korea [7]. The photon ID group also had their paper accepted by the European Physical Journal C on the measurement of the photon identification efficiencies, in which my contributions of corrections to input variables were vital [8].

In the later parts of 2018 and early 2019, I took on more TRT responsibilities, preparing the TRT system for Run 3 and getting to the root of a timing issue that had been affecting the TRT throughout Run 2. This involved creating a framework to combine information from two data sources, finding and teasing out puzzling patterns, and then proposing a solution to the issue. The issue is still being sorted out as now that is it the Long Shutdown II, some infrastructure needed to perform rigorous testing has been out of commission. Furthermore, I received the opportunity to present my Higgs to neutralinos and gravitinos search at the Les Rencontres de Physique de la Vallée d'Aoste conference in La Thuile, Italy in March of 2019.

During 2018 and 2019, I started writing this document, trying to do justice to all the various projects I've contributed to in the last 6 years. I think my research in grad school tells a nice story in both the overall experience and physics interests. My work started in July 2013, repairing TRT readout boards in Bâtiment 104 and my last trip to CERN in March 2019 ended doing the same. I have had perhaps one of the more well rounded experiences of an ATLAS graduate student, making significant contributions to detector operations, combined performance groups, and physics analysis teams (both in a measurement and search). My physics interests started with classifying and optimizing photon signatures in the detector, which lead to measuring Higgs properties in the diphoton decay channel very precisely. With no deviations from the Standard Model observed, I then sought a new signature of the Higgs boson decaying with photons in the final state. I had the opportunity to do the analysis by myself, which is very rare in such a big experiment, and I'm extremely proud of that. The dissertation presents my research about the various aspects described

above, with more emphasis on the Higgs to diphoton cross section measurement and the Higgs to neutralinos search.

Overall, being in the Penn group and part of the ATLAS experiment has been an unbelievable experience. I had the opportunity to be involved on cutting edge physics projects with a diverse and motivated teams from around the world. Because ATLAS is a 3,000+ person collaboration from 40 different countries, the work presented in this dissertation is just a small piece in the ATLAS physics program and is built upon their contributions as well as mine. I am awed by the teamwork and behind-the-scenes, thankless effort of many people who keep ATLAS the detector operating, maintain the computing systems and data pipelines, organize the collaboration, and contribute to combined performance. The glory is all in the analysis results, but without the endeavors of these other people there would be no ATLAS experiment.

The Penn ATLAS group and physics department has also been a second family to me, during the hard times and good. The camaraderie, technical help, silly lunchtime conversations, and hours long coffee breaks in the afternoons have truly made the grad school experience entertaining. I'm afraid that at my next adventure, I won't find a group as interesting, self-motivated, and enjoyable to be around as I was definitely spoilt here. I will never regret devoting my mid-20's to this project and grad school as the experiences I shared was truly worthwhile and fulfilling. This includes both in my physics career and with friends and family in both Geneva and Philadelphia.

Khilesh Pradip Mistry
Philadelphia, May 2019

Chapter 1

Introduction

After centuries of studying the world around us, physicists in the early 1900's started probing the fundamental structure of atoms and the subatomic world. Throughout the 20th century, with the help of giant technological leaps as well as visionary theorists, nuclear/particle physicists brought us from studying scattering light to the nuclear era and particle collider experiments. In 50's, 60's and 70's theorists, guided by a stream of experimental discoveries and results, formulated what is known as the Standard Model of particle physics (SM), a theory of symmetries in nature. This model combines three of the four fundamental forces of nature – the electromagnetic (EM) force, the strong nuclear force, and the weak nuclear force – into a Quantum Field Theory (QFT) containing force carriers (bosons) and matter particles (fermions). While the Standard Model has been enormously successful, accurately predicting a large assortment of phenomena and encasing all previous experimental results in a beautiful yet complex framework, there were still problems. One well known problem was mass: the Standard Model had no way to generate masses for particles such as the predicted, discovered, and indeed massive electrons, muons, and W, Z bosons (force carriers of a unified description of electromagnetic and weak forces). In 1964, a mechanism to generate these masses was proposed by Robert Brout, François Englert, Peter Higgs, and others. This predicted a yet-to-be-seen particle, the Higgs boson.

In 2012, after almost 50 years since the first paper describing the Higgs mechanism, the discovery of the Higgs boson was announced by the ATLAS and CMS experiments at the Organisation Europiéenne pour la Recherche Nucléaire (CERN). The confirmation of the Higgs boson in the Standard Model brought other inconsistencies and omissions of the theory to the forefront. A difference in the scale between gravity and the weak force causes the theory to become "fine tuned" as the Planck mass scale (or some Grand Unification Energy) plays a role in calculable corrections to the

Higgs mass. Other problems included the lack of unification of the fundamental forces at higher energies and from the astronomical observations, nothing to explain the dark matter in the universe. In the 70's and 80's, before the Higgs discovery, theorists postulated the existence of Supersymmetry (SUSY), which would be an extension to the Standard Model. SUSY provides a solution to many of the aforementioned problems and predicts a vast new landscape of particles, none of which have been discovered. The Large Hadron Collider (LHC) and its experiments ATLAS and CMS were designed to find both the Higgs and SUSY, if it were to be accessible.

This dissertation touches on various aspects of the previously mentioned research areas, looking to probe and understand the Standard Model and the Higgs boson. The analyses performed utilized data collected from the ATLAS detector at the LHC during 2015–2017. The main discussion focuses on the Higgs boson and its properties. A precision measurement of the Higgs boson decaying to two photons is presented. Measurements of cross sections, the probability to produce the Higgs boson decaying to two photons from the incoming proton–proton collisions, are performed differentially – measuring this probability as a function of kinematic and event variables. Next, a Higgs decaying to a photon and beyond the Standard Model particles is searched for, inspired by SUSY models which can help overcome some of the deficiencies of the Standard Model.

This thesis begins with an introduction to the Standard Model and possible physics beyond it in Chapter 2. The experimental apparautus, the LHC and the ATLAS detector, are briefly described in Chapter 3. Next, Chapter 4 dives deeper into a sub-detector on ATLAS called the Transition Radiation Tracker (TRT). A large chunk of my graduate career was spent working on the Data Acquisition (DAQ) team for the TRT and this chapter consists of an overview of the system and details of a couple projects. Chapter 5 explains how measured detector signatures are transformed into meaningful physics objects in a process called reconstruction. The measurements of Higgs boson properties in decays to two photons are detailed in Chapter 6, where the differential and fiducial cross sections are presented. Chapter 7 presents the search for the Higgs boson decaying into new Beyond the Standard Model (BSM) particles and at least one photon. Finally, Chapter 8 summarizes the results presented in the dissertation and looks toward the future.

Chapter 2

Theoretical Framework

"The most cherished goal in physics, as in bad romance novels, is unification."

— Leo Smolin

2.1 The Standard Model

The Standard Model of particle physics (SM) is a Quantum Field Theory (QFT) that describes the fundamental forces, particles, and their interactions [9, 10]. It is a quantized Yang-Mills theory [11] that includes three of the four fundamental forces; electromagnetic, strong and weak. The Standard Model is a non-Abelian gauge theory, invariant under the $SU(3)_C \otimes SU(2)_L \otimes U(1)_Y$ where C refers to quark "color" charge, L refers to the "left" helicity handedness of the particles, and Y refers to the hypercharge.

The SM particles, shown in Figure 2.1, can be grouped into three distinct categories:

1. **Fermions**: The matter fields of the theory describing elementary particles. These are spin 1/2 particles, split into 3 generations of increasing mass, and subdivided into leptons and quarks depending on their interactions under $SU(3)_C$. The quarks carry color charge and the up and down type quarks can be written in their left-handed doublet and right-handed singlet as:

$$\begin{pmatrix} \mathrm{u} \\ \mathrm{d} \end{pmatrix}_L, u_R, d_R \ . \tag{2.1}$$

   The leptons are colorless and grouped the same way:

$$\begin{pmatrix} \nu \\ e^- \end{pmatrix}_L, \nu_R, e_R^- \ . \tag{2.2}$$

   In the absence of the Higgs field, the fermions are massless.

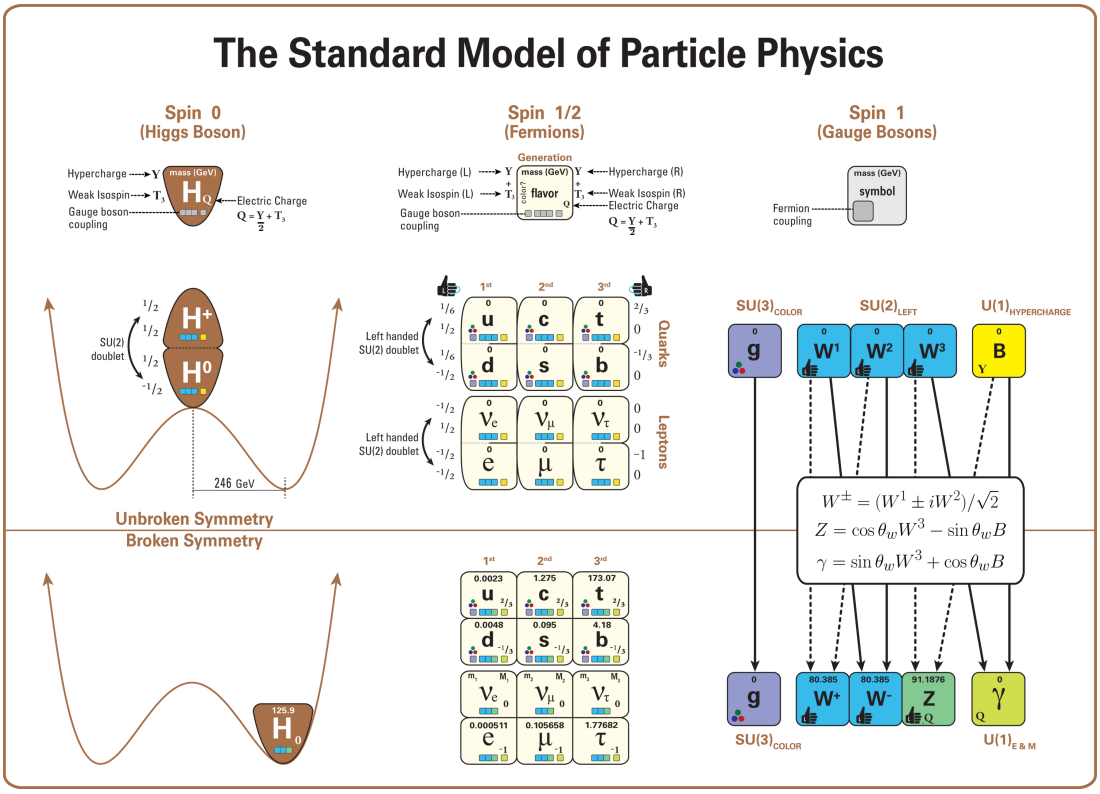

Figure 2.1: The Standard Model of particle physics which is based on Quantum Fields Theories of the strong, electromagnetic and weak forces. This cartoon shows the 12 fermions, (6 quarks, 6 leptons) and their interactions with the three forces. It also shows the gauge bosons, which mediate the fundamental forces of the theory. The effects of the Higgs field on the model are evident by the couplings and mixings shown in the diagram. Figure from [12].

2. **Gauge Bosons**: The spin 1 force carriers of the theory, which mediate the interactions. Before symmetry breaking, the Electroweak (EWK) force is mediated by the $W^1_\mu, W^2_\mu, W^3_\mu$, and B_μ gauge bosons while the gluons, G^i_μ, oversee the interactions of the strong force. In the absence of the Higgs field, these gauge bosons are massless.

3. **Higgs Boson**: The Higgs boson is a spin 0 particle arising from the Higgs mechanism (described in the next section) and spontaneously breaks the EWK symmetry. This symmetry breaking allows for the mixing of the EWK gauge bosons, and allows gauge bosons and fermions to acquire mass while still respecting gauge invariance.

The $SU(2)_L \otimes U(1)_Y$ is a unification of the electromagnetic and weak forces known as the electroweak force and devised by Glashow, Weinberg and Salam [13–15]. $SU(2)_L$ is based on an

isospin (I) symmetry only for left handed particles; therefore the fermions are divided into left and right handed helicity eigenstates where the left transform as doublets, and the right as singlets. $U(1)_Y$ is a symmetry that relates the electric charge (Q) of particles to the third component of the isospin through:

$$Y = 2(Q - I_3) \ . \tag{2.3}$$

Through the Higgs mechanism, the generators of $SU(2)_L$ $(W^1_\mu, W^2_\mu, W^3_\mu)$ mix with the generator of $U(1)_Y$ (B_μ) to form the observed $W^\pm$ bosons, Z^0 boson, and γ (photon, A_μ). The resulting symmetry is only of $U(1)_Q$. This will be explained in the next section.

The $SU(3)_C$ symmetry is a non-Abelian theory of the strong force, or Quantum Chromodynamics (QCD) [16]. This symmetry is generated by gluons (G^i_μ), and its non-Abelian nature allows for a very different nature than the EWK force. Gluons can self-interact and are also "confined" by their color(red, green, or blue). This means any particle that interacts with the strong force cannot exist alone in nature and therefore are found in bound states called hadrons [17,18]. They must be part of color neutral triplets (red+green+blue – baryons), or doublets (color-anticolor – mesons). Another important property of the strong force is "asymptotic freedom" [19–21]. The strong coupling constant is not small and is non-perturbative at low energies, but decreases at higher energies such as those at the LHC. In this region the coupling is much smaller ($\alpha_s \sim 0.1$) and QCD calculations can be done in a perturbative region.

2.2 The Higgs Mechanism

"This summer I have discovered something totally useless."

— Peter Higgs, 1964

As mentioned previously, in the electroweak theory all particles are predicted to be massless. The terms which would give mass to gauge bosons violates the local symmetry of the underlying theory. The Higgs mechanism was theorized by Higgs, Englert and Brout in 1964 and was incorporated into the electroweak theory by Weinberg to give masses to gauge bosons and fermions while preserving the gauge symmetry [22–24].

The Higgs mechanism spontaneously breaks the symmetry of the electroweak theory. This means the underlying theory does not contain an explicit breaking term, but these terms arise from the ground state of new, ad hoc field called the Higgs field. This field is a complex scalar field that is a

doublet of the $SU(2)_L$ isospin symmetry:

$$\phi = \frac{1}{\sqrt{2}} \begin{pmatrix} \phi^+ \\ \phi^0 \end{pmatrix}_L . \tag{2.4}$$

Before symmetry breaking the electroweak Lagrangian of the Standard Model is of the form:

$$\boldsymbol{\mathcal{L}} = \mathcal{L}_{\text{gauge}} + \mathcal{L}_{\text{lepton}} , \tag{2.5}$$

and a new term is added:

$$\begin{aligned} \mathcal{L}_{\text{Higgs}} &= T_{\text{Higgs}} - V_{\text{Higgs}} \\ T_{\text{Higgs}} &= (D_\mu \phi)^\dagger (D^\mu \phi) = |(\partial_\mu - \frac{ig}{2} W_\mu^a \sigma^a - \frac{ig'}{2} B_\mu Y)\phi|^2 \\ V_{\text{Higgs}} &= \mu^2 (\phi^\dagger \phi) + \lambda (\phi^\dagger \phi)^2 . \end{aligned} \tag{2.6}$$

T_{Higgs} is the kinetic term, expressed in terms of a gauge covariant derivative which allows for transformations to preserve the gauge invariance and physical properties. The derivative contains the coupling constants g and g' of the W_μ^a and B_μ fields of $SU(2)_L$ and $U(1)_Y$. The Pauli matrices of $SU(2)_L$ are denoted by σ^a and the hypercharge of $U(1)_Y$ is Y.

The potential of the Higgs field is chosen to be $\mu^2(\phi^\dagger\phi)^2 + \lambda(\phi^\dagger\phi)$ where μ^2 and λ are free parameters of the new field. This is the most general form of a potential that can induce symmetry breaking. The Higgs potential can be seen in Figure 2.2 and is known as the "Mexican hat potential" as it resembles a sombrero. The potential is rotationally symmetric and the μ^2 and λ are restricted such that there is a non-zero minimal potential for the non-negative $\phi^\dagger\phi$ field. For $\mu^2 < 0$ and $\lambda > 0$ the minimum lies in a circle at radius $\nu = \sqrt{-\mu^2/\lambda}$ and is called the vacuum expectation value (vev). When the symmetry of the field is spontaneously broken (μ^2 goes from non-negative to less than 0), the field's minimum changes from 0 to this vev, and one is free to choose the direction of the symmetry breaking. Conventionally this is chosen such that $\phi^+ = 0$ and $\langle \phi^0 \rangle = \nu$. That is to say:

$$\phi = \frac{1}{\sqrt{2}} \begin{pmatrix} \phi_1 + i\phi_2 \\ \phi_3 + i\phi_4 \end{pmatrix} \longrightarrow \phi = \begin{pmatrix} 0 \\ \nu + \frac{H}{\sqrt{2}} \end{pmatrix}, \langle \phi \rangle = \frac{1}{\sqrt{2}} \begin{pmatrix} 0 \\ \nu \end{pmatrix} . \tag{2.7}$$

where H is now the *real* scalar field. Plugging this into the kinetic term and expanding around the minimum, one can rearrange terms to see the manifestations of the newly mixed $W^\pm$, Z^0:

$$T_{\text{Higgs}} \supset \frac{\nu^2}{8} \left\{ g^2 \left((W_\mu^1)^2 + (W_\mu^2)^2 \right) + \left(g W_\mu^3 - g' B_\mu \right)^2 \right\} . \tag{2.8}$$

The W^+ and W^- are formed from the combination (and its complex conjugate) of the W^1 and W^2 terms with a mass of $m_W = \frac{vg}{2}$. The Z^0 is formed through a mixture of the W^3 and B field and

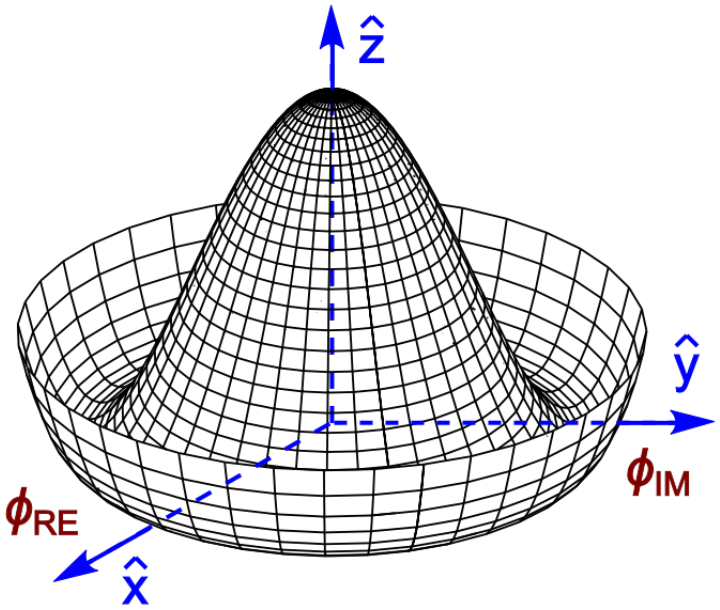

Figure 2.2: Cartoon of the Higgs potential which resembles a "Mexican hat". The z axis is the potential $V(\phi)$. The displacement of the field from the top of the hill to the lower ring, when μ^2 changes from non-negative to negative, is not a single point but a circle. The symmetry is spontaneously broken when the ϕ is chosen.

has a mass of $m_{Z^0} = \frac{\nu}{2}\sqrt{g^2 + g'^2}$. A second field of the W^3 and B remains massless and is known as the photon. In all, the overall $SU(2)_L$ symmetry of the model remains unchanged but it has now been broken near this minimum. The process preserves the photon as massless and retains a $U(1)_Q$ symmetry which can be described with Quantum Electrodynamics (QED) [25].

Similarly, fermions obtain their masses through Yukawa interactions [26]:

$$\mathcal{L}_{\text{Yukawa}} = -\lambda_\psi(\bar{\psi}_L \phi \psi_R + \bar{\psi}_R \phi^\dagger \psi_L) \ , \tag{2.9}$$

where the fermionic fields (ψ, left-handed doublets or right-handed singlets) have 3 point interactions with the Higgs field. After symmetry breaking, the mass terms can be written as $m_\psi \sim \lambda_\psi \nu$ where the fermion mass is now coupled directly to the vev through a Yukawa coupling (λ_ψ). Because Higgs boson and its vev are now intertwined with the Yukawa couplings, the fermion masses are proportional to their Higgs coupling strength.

Another key part of the symmetry breaking leads to a $\mu^2 H^2$ term in the potential. This would be an excitation of the Higgs field manifesting itself as a new particle with mass $m_H = \mu = \sqrt{2\lambda\nu}$. Once again, the free parameters in the model which need to be measured experimentally are μ, λ, and the

Yukawa couplings. We have measured the mass of the Higgs boson as 125.09 ± 0.21 GeV [27], the W boson as 80.379 ± 0.012 GeV [28, 29], and the Z boson as 91.1876 ± 0.0021 GeV [30, 31] implying a vev of $\nu \approx 246$ GeV.

2.3 Higgs Physics at the Large Hadron Collider

Higgs Production

There were roughly 8 million Higgs bosons produced at the LHC during Run 2, which corresponds to a rate of 1 Higgs boson produced every 2 seconds. The production occurs in a few main ways, through direct couplings or higher order loop couplings. These production modes can be used to explore Yukawa couplings, QCD corrections, and other properties of the Higgs boson and Standard Model particles. The cross sections or probabilities of these interactions to occur vary with $\sqrt{s}$, thus descriptions, tables, and figures will assume a $\sqrt{s} = 13\,\text{TeV}$ unless stated otherwise. The cross sections are calculated by the LHC Higgs Cross Section Working Group and published in the Yellow Report 4 [32]. In descending order of frequency they are:

1. **Gluon gluon Fusion Higgs production (ggF)**: Gluon-gluon fusion (Figure 2.3) is the dominant process for which Higgs bosons are produced at the LHC. Even though Higgs bosons are produced through ggF 87% of the time, gluons are massless particles and subsequently have no tree level couplings to the Higgs boson. For this reason, gluons interact with Higgs boson through quark loops where the dominant contribution is from top quarks.

2. **Vector boson fusion Higgs production (VBF)**: Vector boson fusion (Figure 2.5), which occurs 6.9% of the time, leaves a distinct signature of two quark jets with large pseudorapidity and large dijet mass. At tree level, this process occurs when two incoming quarks each radiate a Z boson or W boson (there needs to be one positively charged and one negatively charged) and they "fuse" through a t-channel exchange to produce a Higgs. This production mode can probe the couplings of the Higgs boson to vector bosons.

3. **Associated Higgs production with vector bosons (VH)**: In this production mode, the Higgs is generally radiated by a vector boson via its coupling to the Higgs field (Figure 2.4). This process is referred to as "Higgs-strahlung". Through the $ggZH$ channel, the Higgs and Z can also be radiated from a quark box diagram. Higgs bosons are produced in association with a W boson approximately 2.6% of the time and with a Z boson roughly 1.7% of the time.

4. **Associated Higgs production with top (or bottom) quarks ($t\bar{t}H/b\bar{b}H$)**: Higgs bosons are also produced in association with two top (bottom) quarks (Figure 2.6), which allows for the measurement of the top (bottom) Yukawa coupling. At the LHC, this occurs roughly 0.9% of the time but can be tagged with multiple b-jets and leptons in the event. Theoretically, the Higgs can be produced with any two quarks in association, though the top and bottom quarks have the highest cross sections as their Yukawa couplings are the largest.

Other Higgs production mechanisms, such as Higgs bosons produced in association with a single top quark, or top quark and W are subleading and are not discussed here.

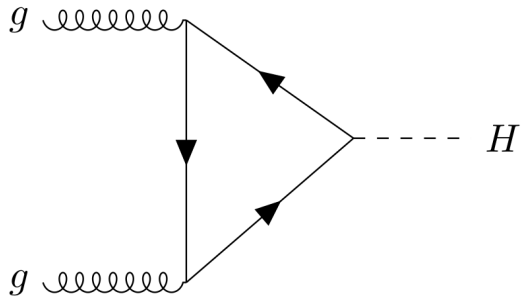

Figure 2.3: Feynman diagram of the ggF Higgs production mode where the Higgs is produced from gluons through a quark loop. 87% of all Higgs bosons created at $\sqrt{s} = 13\,\text{TeV}$ are produced via ggF.

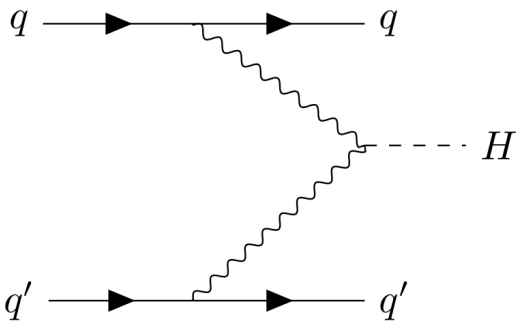

Figure 2.4: Feynman diagram of the VBF Higgs production mode where the Higgs is produced via the fusion of two vector bosons. This production mechanism leaves a distinct signature of two jets separated in pseudorapidity and with large dijet mass. The Higgs is produced by the VBF mode 6.9% of the time.

A table of cross sections for these processes can be seen in Table 2.1 and the calculated cross sections for different center-of-mass energies and Higgs masses can be seen in Figure 2.7. The cross section for ggF was calculated at next-to-next-to-next-to-leading order (N^3LO) in QCD, next-

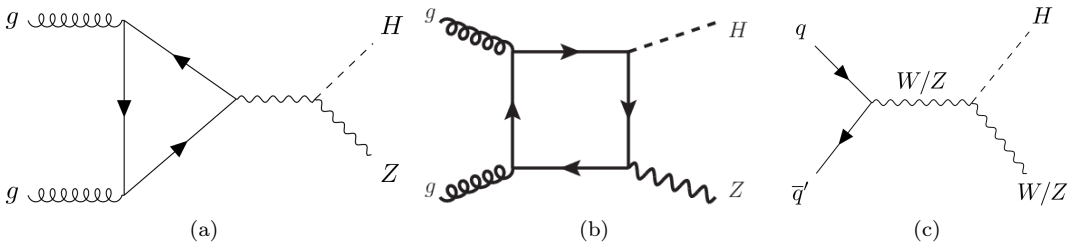

Figure 2.5: Feynman diagrams of the VH Higgs production mechanism. In this scenario the Higgs is radiated from a quark (b), or vector boson itself (a,c). This production is rare for both the W and Z, as only 4.3% of Higgs bosons are created this way.

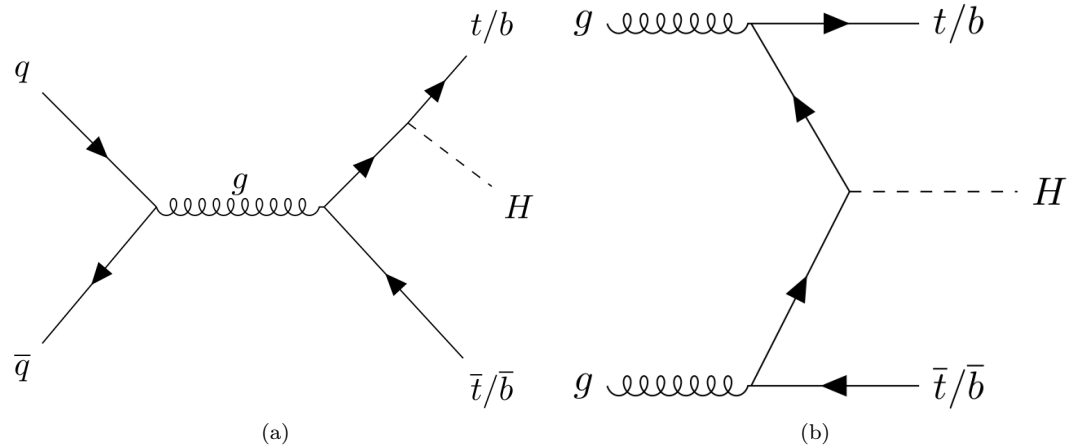

Figure 2.6: Feynman diagrams of the $t\bar{t}H/b\bar{b}H$ Higgs production mechanism. In this scenario the Higgs is radiated from a quark, and thus Yukawa couplings to the top and bottom quarks can be studied. This production is extremely rare as for both $t\bar{t}H$ and $b\bar{b}H$, only 1.8% of Higgs bosons are created this way. In theory, all quarks may contribute to this diagram, but since the Yukawa couplings to the top and bottom are much larger than the others these two are the relevant production modes.

to-leading order (NLO) in EWK, and contains next-to-next-to-next-to-leading logarithmic (N^3LL) corrections of the soft, virtual and collinear gluon effects. The VH and VBF processes were calculated in next-to-next-to-leading order (NNLO) in QCD, NLO in EWK corrections, while the $t\bar{t}H$ values were calculated in NLO for both EWK and QCD corrections.

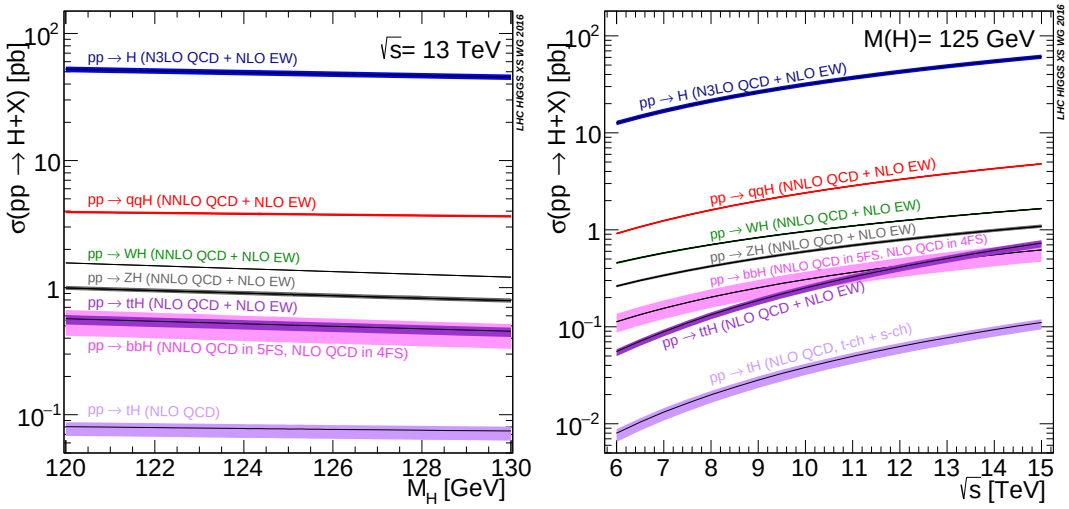

(a) Production σ vs. Higgs mass

(b) Production σ vs. $\sqrt{s}$

Figure 2.7: Calculated production mechanism cross sections for a Standard Model Higgs boson. (a) shows the changes in cross section for different masses near the expected Higgs boson mass of 125.09 ± 0.21 GeV. (b) shows the calculated cross sections as a function of center-of-mass energy of the proton-proton collisions. The uncertainty bands are from QCD scale and Parton Distribution Function (PDF) uncertainties.

Table 2.1: Table of cross sections for the six most common Higgs production methods at the LHC at $\sqrt{s} = 13\,\text{TeV}$. The uncertainty associated with the calculations are theoretical uncertainties only.

Production Mode	σ[pb]
ggF	48.5 ± 3.4
VBF	3.8 ± 0.1
WH	1.37 ± 0.06
ZH	0.86 ± 0.03
$t\bar{t}H$	0.51 ± 0.05
$b\bar{b}H$	0.5 ± 0.1

Higgs Decays

The Higgs boson, with a mass of 125.09 ± 0.21 GeV, is not a stable particle and has a predicted lifetime of 1.56×10^{-22} seconds. Its decay mode rates are directly tied to its couplings to Standard Model particles and their masses. For the case of fermions, as discussed in Section 2.2, the coupling is the Yukawa coupling and therefore is linear in mass. Since the top quark is the heaviest fermion currently observed, the Higgs fermionic decays should happen most frequently in the $t\bar{t}$ channel but this is not the case as it is kinematically forbidden. There exists a decay mode of the Higgs into two very off-shell tops, but the predicted rate of this is much smaller than what is experimentally measurable. Gauge bosons couplings are proportional to the square of their mass, but the Higgs boson is not greater than twice the W or Z mass so decays to pairs of vector bosons occur with one being off-shell.

Because of its mass, the heaviest on-shell particle the Higgs can decay to is the b-quark. This decay is predicted to occur with a branching fraction of 58.4%. Decays to other light quarks occur, but the next most common decay mode is into a pair of charm quarks, occurring only 2.9% of the time. The Higgs can also couple to gluons in the same way it is produced (through quark loops) and decays to a final state of two gluons 8.2% of the time. Decays into two W or Z bosons are allowed only when one of the bosons produced is off-shell. The Higgs decays to a pair of Ws 21.4% of the time, and a pair of Zs with a Branching Fraction (BF) of 2.6%. Interestingly, like the massless gluons, the Higgs can decay into a final state of two photons through a quark or W loop with a BF of 0.227%. Other decay modes of the Higgs boson are allowed, and are noted in the Figure 2.8 and Table 2.2.

Table 2.2: Higgs branching fractions for Standard model decay final states. All of the calculated branching fractions have about a 3-6% theoretical uncertainty.

Decay mode	Branching Fraction [%]
$b\bar{b}$	58.4
WW	21.4
gg	8.2
$\tau\tau$	6.3
$c\bar{c}$	2.9
ZZ	2.6
$\gamma\gamma$	0.227
$Z\gamma$	0.154
$\mu\mu$	0.022

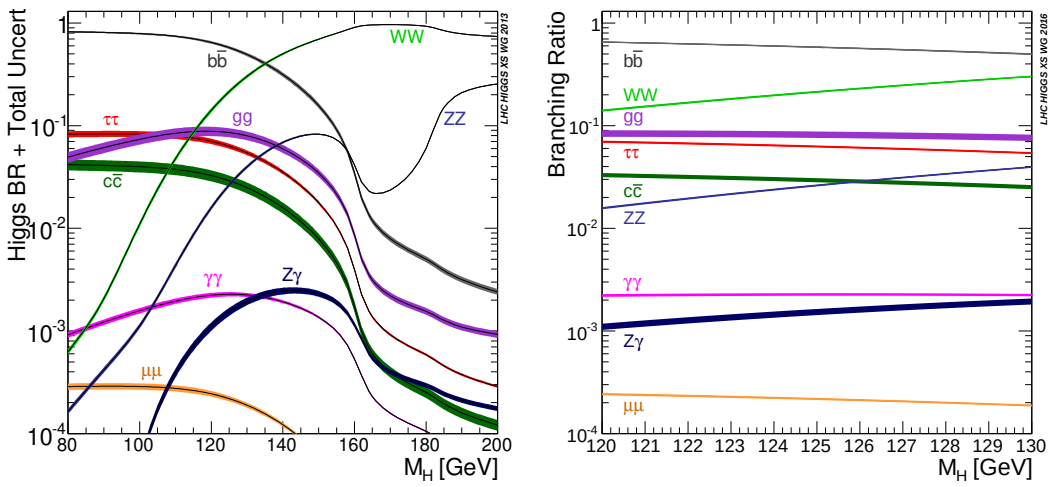

(a) (b)

Figure 2.8: Branching fractions of the Standard Model Higgs boson decays as a function of Higgs mass. (a) shows how the different decay modes can be enhanced or diminished due to different turn on thresholds depending on the Higgs mass range and (b) narrows into the range near the measured Higgs mass of ~ 125 GeV.

Each decay mode of the Higgs has its pros and cons experimentally. The decays to b-quarks happen often, but at the LHC there are lots of energetic QCD events which can mimic the signature. The decay of two Zs into a final state of 4 leptons is very clean but once the Z's branching fraction to leptons is considered, this is a very rare decay with a branching fraction of 0.0125%. The Higgs decay to two photons is very clean with well understood backgrounds of SM diphoton process and mis-identifications of quarks and gluons as photons. This signature will be explored in Chapter 6 and used to perform precision Higgs measurements. The experimental signatures used to discover the Higgs in 2012 combined the ZZ, $\gamma\gamma$, and WW channels.

2.4 Beyond the Standard Model

While the discovery of the Higgs boson has "capped" the Standard Model in its long string of successes describing physical phenomena, it still is an incomplete theory. First and foremost, the SM does not account for the gravitational interaction. Thus far the framework of General Relativity (GR) is separated from the SM and has not been incorporated into the SM successfully. Cosmological observations lead to the conclusion that most of the ordinary matter and energy we see in the universe is a small part of a much bigger picture, in the form of dark energy and dark matter. Dark

energy is an unknown form of energy driving the universe to expand and its predicted to make up $\sim 68\%$ of the known energy-matter composition of the universe. It was discovered through the measurement of Type 1A supernovae light, which was seen to be weaker than expected due to an expansion of the accelerating universe [33, 34]. Other astrophysical evidence, such at the Bullet cluster [35] and galaxy rotation curves [36], shows indirect proof of dark matter as some extra matter not visible to us is required in order to correctly describe our measurements. Conversely, this could be due to the current model of gravity not being entirely correct, and other frameworks such as Modified Newtonian Dynamics (MOND) aim to address this issue without requiring the existence of dark matter.

Additionally, the question of why the universe and atoms are composed of quarks and not antiquarks is unanswered. The fundamental theory predicts a symmetry of matter and antimatter but we observe a preference toward matter in the universe (the universe is composed of matter and not antimatter). We also observe some asymmetry of decays in the weak sector known as Charge conjugation-Parity (CP) [37–43]. This is allowed in all sectors of the Standard Model and while CP violation contributes, it cannot fully explain the dominance of matter over antimatter in the universe. Furthermore, we can ask why there is no observed CP violation in the strong sector or what gives rise to this CP violation?

And finally, there are questions about the Higgs. Is there only one Higgs boson or others lurking at higher or lower masses? There is an inherent problem of "naturalness", where radiative corrections to the Higgs boson mass can be orders of magnitude larger than the mass we observe. A cancelation of different terms or some "fine tuning" of parameters would need to occur in order to observe the 125 GeV Higgs. All these problems and unanswered questions are indicative of some deeper theory or some underlying greater symmetry. This section presents some frameworks and models which aim to address some of these questions.

2.4.1 Supersymmetry

While no particular model can address every problem of the SM, the class of models involving Supersymmetry (SUSY) [44–49] is introduced as am extension to the Standard Model that can address many of the aforementioned problems. In its most basic form, SUSY is a new space-time symmetry which relates bosons and fermions. A new operator is added to the theory that transforms a boson to a fermion, and vice versa. SUSY predicts the existence of additional particles that differ from their SM partners by half a unit of spin only, preserving all other quantum numbers. The

varieties of Supersymmetry models are extensive and plentiful, and to fully explore and understand the richness of SUSY the following references may help [50–53]. I will briefly describe the foundations of the Minimal Supersymmetric Standard Model (MSSM) as a basis for other more complex SUSY variants.

In the Minimal Supersymmetric Standard Model, the SM particles and their transformed SUSY partners are placed in supersymmetric-multiplets. The fermions transform differently depending on the handedness of the SM fermion, and are grouped in chiral supermultiplets. The supersymmetric fermions, now with spin 0, are known as "sfermions" (add an s to the beginning of the particle – sbottom, selectron, ... etc). The transformed bosons (named by adding an -ino, Wino, Bino, ... etc) are grouped into gauge supermultiplets called gauginos and have spin 1/2. These states can mix into neutralinos (4 neutral mixes of the gauginos) and charginos (2 charged mixes of the gauginos). The Higgs boson transforms as a chiral supermultiplet with a Higgsino, but a second chiral Higgs multiplet is need to complete the symmetric model without quantum anomalies, which manifest themselves from the additional symmetry breaking. These can also mix with the gauginos, forming neutralinos and charginos with Higgsino components. A table of the chiral and gauge supermultiplets of the MSSM can be seen in Table 2.3.

Chiral supermultiplets			
Names		Spin 1/2	Spin 0
Quarks, squarks	Q	(u_L, d_L)	$(\tilde{u}_L, \tilde{d}_L)$
3 generations	$\bar{u}$	$\bar{u}_{\mathrm{L}} = (u_{\mathrm{R}})^{\mathrm{c}}$	$\tilde{\bar{u}}_{\mathrm{L}} = \tilde{u}^{\dagger}_{\mathrm{R}}$
	$\bar{d}$	$\bar{d}_{\mathrm{L}} = (d_{\mathrm{R}})^{\mathrm{c}}$	$\tilde{\bar{d}}_{\mathrm{L}} = \tilde{d}^{\dagger}_{\mathrm{R}}$
Leptons, sleptons	L	$(\nu_{\mathrm{L}}, e_{\mathrm{L}})$	$(\tilde{\nu}_{\mathrm{L}}, \tilde{e}_{\mathrm{L}})$
3 generations	$\bar{e}$	$\bar{e}_{\mathrm{L}} = (e_{\mathrm{R}})^{\mathrm{c}}$	$\tilde{\bar{e}}_{\mathrm{L}} = \tilde{e}^{\dagger}_{\mathrm{R}}$
Higgs, Higgsinos	H_{u}	$\left(\tilde{H}^{+}_{\mathrm{u}}, \tilde{H}^{0}_{\mathrm{u}}\right)$	$\left(H^{+}_{\mathrm{u}}, H^{0}_{\mathrm{u}}\right)$
	H_{d}	$\left(\tilde{H}^{0}_{\mathrm{d}}, \tilde{H}^{-}_{\mathrm{d}}\right)$	$\left(H^{0}_{\mathrm{d}}, H^{-}_{\mathrm{d}}\right)$
Gauge supermultiplets			
Names		Spin 1	Spin 1/2
Gluinos, gluinos		g	$\tilde{g}$
W boson, Wino		$W^{\pm}$,W^{0}	$\tilde{W}^{\pm}$,$\tilde{W}^{0}$
B boson, Bino		B	$\tilde{B}$

Table 2.3: Chiral and gauge supermultiplets in the MSSM.

This dissertation will explore just two classes of models using the newly discovered Higgs boson as a probe [54]. Key aspects of the SUSY models are (1) how the supersymmetry is broken, (2) how the SUSY particles interact with Standard Model particles, and (3) from an experimentalist point of view, what are the lightest undiscovered SUSY particles?

2.4.2 Gauge Mediated Supersymmetry Breaking

In one class of models explored, Gauge Mediated Supersymmetry Breaking (GMSB) [55–62] models, the supersymmetry is broken in a secluded sector not directly accessible to Standard Model particles (the visible sector) and at the collider. The breaking is communicated to the Standard Model via messenger particles or mediators, generally through loops. This introduces two key scales to the theory M, the messenger scale, and $\sqrt{F}$,the SUSY breaking scale. There are some GMSB mechanisms that produce a 125 GeV Higgs boson consistent with current measurements [63–67].

In model-independent SUSY frameworks, the spontaneous breaking of global supersymmetry will provide a Goldstone fermion, in this case the goldstino. This is analogous to how spontaneous EWK symmetry breaking provides a Goldstone bosons. When SUSY is promoted to a local symmetry, the goldstino is "eaten" by the spin 3/2 gravitino and becomes its longitudinal component; giving the gravitino mass [68, 69]. This is referred to as the "super-Higgs" mechanism. In GMSB models, the lightest supersymmetric particle is generally this gravitino, with a mass proportional to the SUSY breaking scale over the Planck mass:

$$m_{\tilde{G}} = \frac{F}{\sqrt{3}M_P} \ . \tag{2.10}$$

The gravitino is stable in R-parity conserving models[1] and does not couple to SM particles. Therefore the next-to-lightest supersymmetric particle (NLSP) will decay to a gravitino (Lightest Supersymmetric Particle (LSP)) and another SM particle. Moreover, the phenomenology of GMSB models is mainly driven by the next-to-lightest supersymmetric particle properties. For instance, if the NLSP is a Bino-like neutralino there can be a significant branching fractions of NLSPs to a photon and gravitino.

In these models the gravitino is generally very light as the SUSY breaking scale and messenger scale is on the order of hundreds of TeV. The gravitino can also be heavier in more generalized models, but this leads to non-prompt signatures at the LHC. The signature which is sought after in this dissertation is under the assumption of a mostly Bino NLSP neutralino with a Higgsino component allowing couplings to the SM Higgs. Since gravity is weak, only the longitudinal components

[1] This will be assumed in this dissertation.

(goldstino) of the spin 3/2 gravitino will interact, allowing for effective couplings of the SM Higgs to neutralinos and gravitinos.

NLSP compositions and masses are mostly constrained by searches for direct production of charginos or neutralinos at the Large Electron-Positron Collider (LEP), Tevatron, and the LHC. In order for the lightest neutralino to be an allowed Higgs decay product, it must be mostly Bino. This is in part due to bounds for significantly Wino or Higgsino NLSPs being more constrained by LEP's bounds on couplings to gauge bosons, which exclude charginos lighter than 103.5 GeV [70,71]. Some of the strongest constraints on light neutralinos decaying to photons come from direct searches at LEP for photons and missing transverse momentum, which limits $\sigma(e^+e^- \to \gamma\gamma + E_{\mathrm{T}}^{\mathrm{miss}})$ to less than $\sim 10^{-2}$pb [72,73]. In the Standard Model without the Higgs, this signature would arise from t-channel W exchanges with radiated photons (from the electrons or W) or a Z decaying to $\nu\bar{\nu}$ with photons radiated from the incoming electrons. Any enhancement can arise from intermediate particles (like neutralinos or Higgs) decaying to invisible particles and photons. One vital part of this model is the neutralino mixing matrix contains only one Higgsino mixing factor, which allows for couplings to the SM Higgs. Two Higgsino or Wino mixing factors are required for the Bino-like neutralino to couple to the Z boson and thus this allows the model to escape LEP constraints [74,75]. For this reason, the mostly Bino NLSP would have little to couple to in e^+e^- and pp colliders and direct production would be greatly suppressed.

In minimal MSSM GMSB models the lightest neutralino is constrained to be heavier than half of the Higgs mass, but this is not the case for general GMSB models. With these assumptions in the mind, there can be significant branching fractions of Higgs boson decays to neutralinos and gravitinos in decays paths such as $h \to \tilde{\chi}_1^0\tilde{\chi}_1^0 \to \gamma\tilde{G}\gamma\tilde{G}$ or $h \to \tilde{\chi}_1^0\tilde{G} \to \gamma\tilde{G}\tilde{G}$. For example, in one simplified model for the $h \to \tilde{\chi}_1^0\tilde{G} \to \gamma\tilde{G}\tilde{G}$ decay path, the BSM terms in the Lagrangian can contain:

$$\mathcal{L}_{BSM} \supset \frac{m^2}{\sqrt{2}F}\left\{g_{\tilde{\chi}_1^0\tilde{G}}h\tilde{\chi}_1^0\tilde{G} + \frac{g_{\tilde{\chi}_1^0\gamma}}{m}\tilde{G}\sigma^{\mu\nu}F_{\mu\nu}\tilde{\chi}_1^0\right\} + h.c.\ ; \tag{2.11}$$

where h is the Higgs boson, $\tilde{G}$ is the gravitino, $\tilde{\chi}_1^0$ is the Bino-like neutralino, $\sigma^{\mu\nu}$ are the Pauli matrices, $F_{\mu\nu}$ is the photon field strengths, g are the coupling parameters, and m is a scale related to soft SUSY soft parameters. This can lead to the decay width of the Higgs to a single gravitino and neutralino as:

$$\Gamma(h \to \tilde{\chi}_1^0\tilde{G}) = \frac{m_h}{16\pi}\frac{g_{\tilde{\chi}_1^0\tilde{G}}^2 m^4}{F^2}\left(1 - \frac{m_{\tilde{\chi}_1^0}^2}{m_h^2}\right)^2 . \tag{2.12}$$

and subsequent decays of the neutralino to photon + gravitino with partial widths of:

$$\Gamma(\tilde{\chi}_1^0 \to \gamma\tilde{G}) = \frac{m_{\tilde{\chi}_1^0}^2}{16\pi} \frac{g_{\tilde{\chi}_1^0\gamma}^2 m^2}{F^2} \ . \tag{2.13}$$

Note the neutralino mass scale is one of the controlling parameter for the neutralino to photon decay width. In order for this process to be physically meaningful, the SUSY breaking scale cannot be too far away from m. From the literature, the Higgs branching fraction of this process can range from sub percent levels up to 15% depending on model assumptions [76, 77]. Similar models can be constructed with the decay paths of Higgs bosons to two neutralinos in the case when $m_{\tilde{\chi}_1^0} < m_h/2$ in generalized MSSM GMSB models. In this case the event may have the decay chain of $h \to \tilde{\chi}_1^0\tilde{\chi}_1^0 \to \gamma\tilde{G}\gamma\tilde{G}$ where in the final state there will be two photons and two gravitinos [78]. These models are the inspirations of the search performed in Chapter 7.

2.4.3 The Next-to-Minimal Supersymmetric Standard Model

The content of the Next-to-Minimal Supersymmetric Standard Model (NMSSM) is extremely similar to that of the MSSM, but differs only by an additional superfield singlet utilized to address the "μ problem" of the MSSM [79]. This problem is not described here but can be read about in the previous reference. The addition of this field promotes the μ parameter in the Higgs superpotential to a singlet which then acquires a non-zero vev and an effective μ parameter is then given by the $\lambda\langle S\rangle$ where $\langle S\rangle$ is the vev of the singlet.

In the Peccei-Quinn symmetry limit of the NMSSM (Discussed in the Ref. [79–81]), a small value of λ produces singlino mixing in the neutralino sector and produces a SM Higgs phenomenology with slight modifications. This can then allow the SM-like Higgs boson to decay to a pair of neutralinos [80, 82, 83]. These decay couplings are proportional to:

$$c_{h\tilde{\chi}_1^0\tilde{\chi}_2^0} \approx \frac{\nu}{\langle S\rangle},\ c_{h\tilde{\chi}_1^0\tilde{\chi}_1^0} \approx \frac{\lambda\nu}{\langle S\rangle \tan\beta} \ ; \tag{2.14}$$

where ν is the vev of the SM Higgs and $\tan\beta = \frac{\nu_u}{\nu_d}$ is the ratio of the vevs of the neutral Higgs fields that couple to up and down type fermions. The heavier neutralino can then decay as $\tilde{\chi}_2^0 \to \tilde{\chi}_1^0 + x$.

In this dissertation, the x will be restricted to being a photon. Therefore the total decay signatures of Higgs can look like $h \to \tilde{\chi}_2^0\tilde{\chi}_1^0 \to \gamma\tilde{\chi}_1^0\tilde{\chi}_1^0$ or $h \to \tilde{\chi}_2^0\tilde{\chi}_2^0 \to \gamma\tilde{\chi}_1^0\gamma\tilde{\chi}_1^0$. These decays occur when the second neutralino is Bino-like and the lightest neutralino is mostly singlino-like. The branching fraction of Higgs bosons to this final state is dependent on the mass of the neutralinos but can be of

order 10%. In contrast to the GMSB scenarios, the mass of the lightest neutralino is not preferred to be nearly massless.

Chapter 3

Experimental Setup

3.1 The Large Hadron Collider

The Large Hadron Collider (LHC) [84] is a circular 27 kilometer particle accelerator located just outside of Geneva, on the border between France and Switzerland. The LHC, which sits 100 m underground, consists of supercooled, superconducting magnets and radiofrequency cavities that accelerate beams of protons (or lead ions) to greater than 99.9% the speed of light. The beams are composed of bunches of protons and accelerated up to an energy of 6.5 TeV each. Beams are then collided every 25 nanoseconds (40 MHz) in the heart of experiments, reaching a center of mass energy of 13 TeV. Although the proton bunches have order TeV energies, the proton is a composite object made of quarks and gluons (partons). The energy distribution of these partons is not known, and governed by PDFs.

The protons collided are extracted from a tank of ionized hydrogen gas. The first stage in the acceleration process begins in the Linear Accelerator 2 (LINAC2), where the protons are accelerated to 50 MeV. After that, the protons are injected into their first circular accelerator, the Proton Synchrotron Booster (PSB), and attain an energy of 1.4 GeV. Next, they enter two more circular accelerators, the Proton Synchrotron (PS) and then the Super Proton Synchrotron (SPS), which increase them in energy to 25 and 450 GeV, respectively. Finally, protons are injected into the LHC in two separate beams, traveling in opposite directions. The energy is ramped up to 6.5 TeV and the protons are ready to collide. Figure 3.1 shows a schematic of the CERN accelerator complex.

These protons collide in experiments such as ATLAS [86], recreating the environment just after the Big Bang. At a time when energy and mass are fluid and fundamental forces are bound by symmetries yet unbroken, this environment is ripe for learning about electroweak processes, the

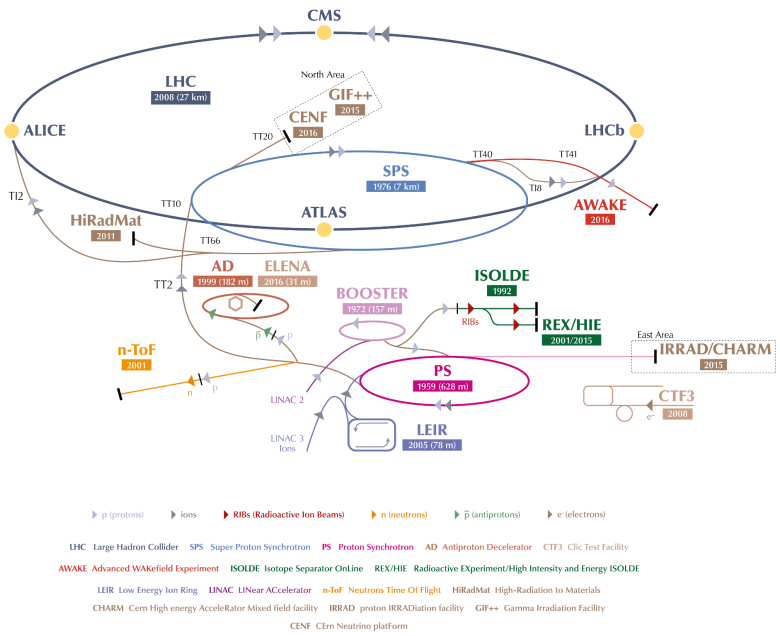

Figure 3.1: A schematic of the CERN accelerator complex [85].

Higgs boson, and looking for supersymmetric particles. There are four main interaction points on the LHC ring: ATLAS, CMS [87], LHCb [88], and ALICE [89]. ATLAS and CMS are multipurpose detectors designed to study the topics mentioned above. LHCb is an asymmetric detector built to study the decay of b-hadrons and study the matter-antimatter composition of the universe. ALICE was constructed to study the primordial soup of quark-gluon plasma in the early universe, primarily through the lead-lead beam mode of the LHC.

3.1.1 Luminosity

Depending on the number of protons in each bunch, the "compactness" of each bunch, and how the beams collide, interactions in the detectors can be very different. A quantity known as luminosity is designed to measure this. The luminosity is defined as:

$$\mathcal{L} = \frac{N_1 N_2 f_{rev} k \gamma}{4\pi \epsilon_n \beta^*} F \ ; \tag{3.1}$$

where N_1 and N_2 are the number of protons for each colliding bunch, f_{rev} is the frequency of the beams which is 11.245 kHz, k is the bunches per beam, γ is the Lorentz factor, ϵ_n is the emittance of the beams or brightness of the beams which is determined by the injectors, β^* is the beta function or amount of "squeeze" of the beam, and F is a geometric factor due to the crossing angle of the beams [90]. The nominal values are N_1,$N_2 = 10^{11}$ protons per bunch and $k = 2,808$ bunches. The instantaneous luminosity was designed to reach a value of $1 \times 10^{34}\text{cm}^{-2}\text{s}^{-1}$ or 10 $\text{nb}^{-1}\text{s}^{-1}$, though because of the wonderful LHC experts, luminosities of up to $2 \times 10^{34}\text{cm}^{-2}\text{s}^{-1}$ were achieved. This instantaneous luminosity falls off as the fill continues due to the growing emittance of the beams. The total amount of luminosity delivered is just the integral of the luminosity with respect to time:

$$\mathcal{L}_{int} = \int \mathcal{L} dt \ . \tag{3.2}$$

The total amount of luminosity collected by ATLAS in Run 2 was 140 fb^{-1}. This corresponds to 3.2 fb^{-1} in 2015, 32.9 fb^{-1} in 2016, 43.7 fb^{-1} in 2017, and 60.1 fb^{-1} in 2018. The physics analyses in this thesis are performed only with the 2015-2017 datasets, though detector work sections cover the whole Run 2 period. The luminosity collected and the data taking efficiency of ATLAS for both Run 1 and Run 2 data taking campaigns can be seen in Figure 3.2.

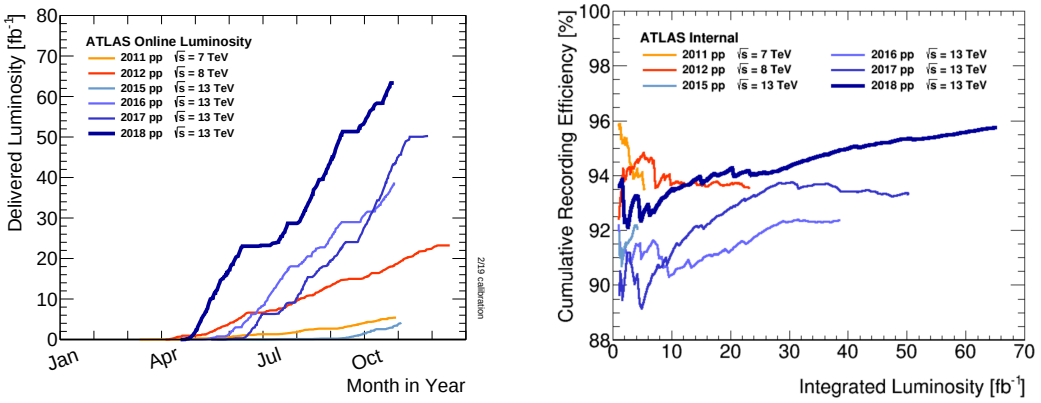

(a) Time vs. luminosity collected

(b) Luminosity collected vs. data taking efficiency

Figure 3.2: (a) Month vs. Cumulative luminosity delivered to ATLAS during stable beams and for high energy pp collisions. (b) Cumulative luminosity versus data taking efficiency. Both plots show the different years of Run 1 and Run 2 operations.

3.1.2 Pileup

The colliding bunches contain many protons, therefore many hard pp interactions can occur. The actual number of interactions (μ) depends on each interaction's beam parameters, but in ATLAS we define a quantity known as $\langle\mu\rangle$. This average interactions per bunch crossing is known as pileup of which there are two kinds, in-time and out-of-time. In-time pileup are other interactions in the same bunch crossing while out-of-time pileup refers to interactions from other bunch crossings. The pileup in the event can cause degradation of object resolution, ambiguity in primary vertex location, and track mis-reconstructions. Algorithms used in ATLAS are designed to be robust against pileup dependence. The pileup profile in Run 2 can be seen in Figure 3.3, and ranges from 10 to 70. The plot contains 146 fb^{-1} of online data which differs from the 140 $\text{fb}^{-1}$of physics data. This is because the collected data are further scrutinized to ensure all parts of the detector were operational.

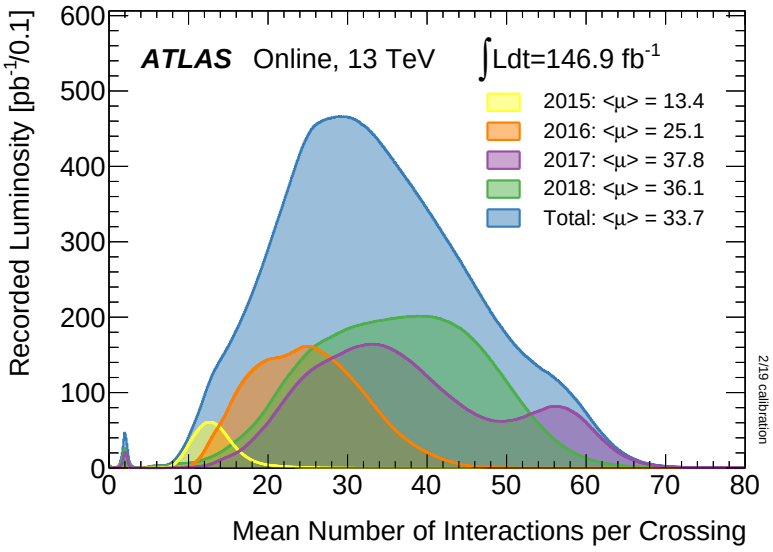

Figure 3.3: Average interactions per bunch crossing in recorded Run 2 ATLAS data.

3.2 The ATLAS Detector

The ATLAS detector is a multi-purpose cylindrical particle detector located at Point 1 in the LHC ring. Its primary design purpose was to discover the Higgs boson and search for new BSM physics. It has almost full 4π coverage, a length of 44 meters, and is 25 meters tall. If the reader of this thesis is located an University of Pennsylvania, this corresponds to roughly the dimensions of of Huntsman

Hall (located at 38th and Walnut) tipped on its side. The detector was designed to reconstruct and identify photons, electrons, muons, and collimated jets of hadrons. This is done with the conjunction of three separate systems. The innermost section, the Inner Detector (ID), tracks all charged particles. In the next sub-system, the calorimeters aim to stop the electromagnetic and hadronic particles and measure their energy. The outermost layer is the Muon Spectrometer (MS), used to track and identify muons. The whole detector is immersed in a magnetic field, provided by a solenoid magnet after the Inner Detector and a toroidal magnet after the calorimeters. Each sub-system is composed of a barrel system, centered around the interaction point, and an endcap system, placed further along the z-axis.

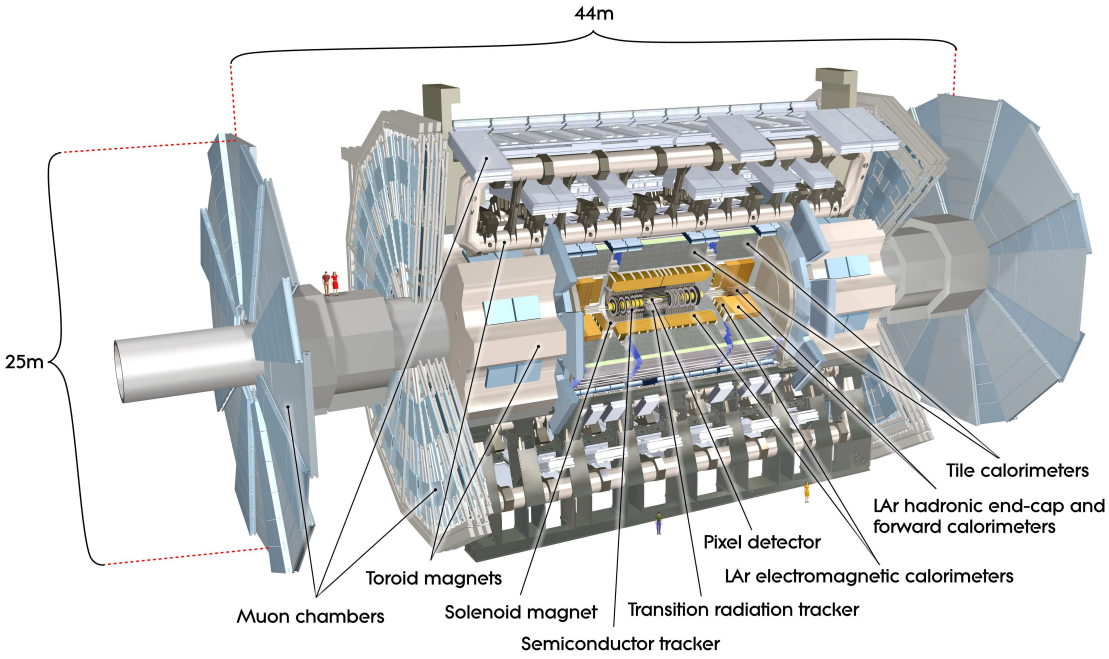

Figure 3.4: General cut-away view of the ATLAS detector [91].

ATLAS uses a right-handed coordinate system with its origin at the nominal interaction point and the z-axis along the beam pipe. The x-axis points from the interaction point to the center of the LHC ring, and the y-axis points upwards. Because partons are the colliding fundamental objects, the initial momentum in the z direction is not known for individual events, but it is known that the initial momentum in the x-y plane is zero. Therefore, vector quantities such as momenta are projected into the transverse (x-y) plane. The cylindrical coordinate ϕ is used in the transverse

plane, where ϕ is the azimuthal angle around the z-axis. $\phi = 0$ corresponds to pointing inwards towards the center of the ring.

The final coordinate ATLAS uses is called the rapidity (y) or pseudorapidity (η). Rapidity is defined as $y = \frac{1}{2}\frac{E+p_z}{E-p_z}$, where E is the energy of the particle and p_z is the momentum in the z direction. This is equivalent to pseudorapidity, defined in terms of the polar angle θ as $\eta = -\ln\tan(\theta/2)$, when particles are massless. At the LHC where particle masses are orders of magnitudes less than the average energy, this assumption holds true. The pseudorapidity is used instead of θ as it is Lorentz invariant under boosts. When discussing distances between two particles, angular distance is measured in units of $\Delta R \equiv \sqrt{(\Delta\eta)^2 + (\Delta\phi)^2}$.

3.2.1 Inner Detector

The Inner Detector [92–94] is immersed in a 2 T axial magnetic field and tracks charged particles to $|\eta| < 2.5$. The magnetic field allows for extraction of charge, momentum, and decay vertex information. The primary interaction vertex is characterized by a d_0 or impact parameter, and z_0 which is the longitudinal impact parameter. The d_0 corresponds to the distance between the z-axis and the point of closest approach of the vertex. z_0 is defined as the z-coordinate of the point of closest approach. The Inner Tracker provides excellent resolution of these parameters which helps distinguish longer lived particles, such as b-hadrons, from other particles. The system itself is composed of the high granularity pixel detector, followed by a silicon microstrip tracker, and then a straw tube transition radiation tracker which has electron identification capabilities. A schematic of the Inner Detector barrel region can be seen in Figure 3.5.

3.2.1.1 Pixel Detector

The innermost layer of the pixel detector, inserted into ATLAS during 2014, is called the Insertable B-Layer (IBL) [95] and is positioned at R = 33.25 mm away from the z-axis. This provided better resolution of the vertex and d_0 information with Run 2's higher pileup environment. The IBL has 8 million readout channels. Each pixel on the IBL is 50 μm $\times$ 250 μm wide and provides tracking resolution of 8 μm in the x-y plane and 40 μm in the z direction. After the IBL, the pixel detector [96, 97] is arranged in three concentric, cylindrical barrels and three disk endcap layers, providing coverage to $|\eta| < 2.5$. The barrel regions are at distances of R = 50.5, 88.5, 122.5 mm and the endcap disks are at z = 495, 580, 650 mm. Each pixel is a 50 μm $\times$ 400 μm wide and gives

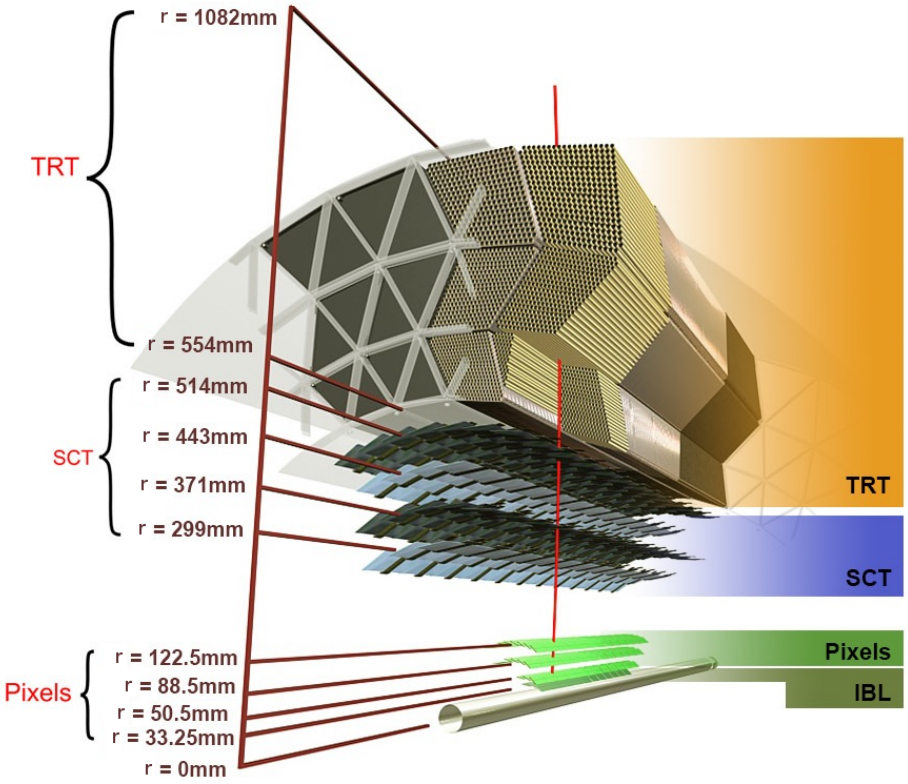

Figure 3.5: A schematic of the ATLAS Inner Detector.

10 μm spatial resolution in the x-y plane and 115 μm in the z direction. In total there are over 1,740 sensors and 80 million readout channels.

3.2.1.2 Semiconductor Tracker

Outside of the pixel detector is the SemiConductor Tracker (SCT) [98–100] which provides tracking to $|\eta| < 2.0$. The SCT layers in the barrel are located at R = 299, 371, 443, 514 mm. In the endcap, there are 9 disks, ranging from $z = 854$ to 2720 mm. Each sensor is similar in design to the pixels, though the sensors are 2D strips. Each strip is 12cm long, has a pitch of 80 μm, and supplies hit resolutions of 17 μm in the x-y plane and 580 μm in the z direction. 768 strips are contained in one of $15,912$ sensors, corresponding to 6.4 million readout channels.

3.2.1.3 Transition Radiation Tracker

The Transition Radiation Tracker (TRT) [101–105] is a proportional drift tube tracker providing tracking coverage and electron identification information up to $\eta < 2.0$. Unlike the silicon based trackers before it, the TRT is composed of 352,256 gas-filled polyimide straws, each 4 mm in diameter. They are nominally filled with a 70%-27%-3% gas mixture of xenon-carbon dioxide-oxygen gas. Each straw has a 32 μm diameter gold-plated tungsten wire running down the center and a 1,500 volt potential is applied between the straw outer casing and the wire. When a charged particle passes through the straw, it ionizes the gas and the electrons drift toward the wires while the ions will drift toward the outer wall. As the electrons approach the wire, an avalanche of electrons is induced, amplifying the signal by a factor of $\sim 20,000$. Timing information can be extracted from this avalanche, leading to 130 μm resolution of the straw hits. The barrel TRT region encompasses the region of $563 < \mathrm{R} < 1066$ mm with $|z| < 712$ mm and the endcap region is $644 < \mathrm{R} < 1004$ mm and $848 < |z| < 2710$ mm.

Additionally, between each straw there is a polypropylene-polyethylene fiber mat about 3 mm thick. Charged particles traversing the mats will have a probability of emitting transition radiation photons with energies proportional to their Lorentz factor. This radiation is caused by the charge particle moving between media with different index of refraction. The transition radiation photons will also move into the straws and an ionize the gas along with the charged particles, creating a larger signal than just the particle. The size of the pulse on the wire is exploited in electron identification as due to their lighter mass, electrons will have higher Lorentz factors than pions, muons, and other charged particles.

More information on the TRT and the data acquisition system can be explored in Chapter 4.

3.2.2 Calorimeters

The ATLAS calorimeter system consists of two main types of calorimeters, one for electromagnetic energy measurements and one for hadronic energy measurements. The system provides coverage to $|\eta| < 4.9$ and measures energy for all particles except for muons, neutrinos, or perhaps unseen stable sparticles. Both of the calorimeters are sampling calorimeters, with layers of absorbers to induce showers and active layers to measure the energy of said showers. Figure 3.6 shows a cutaway view of the calorimeters in ATLAS.

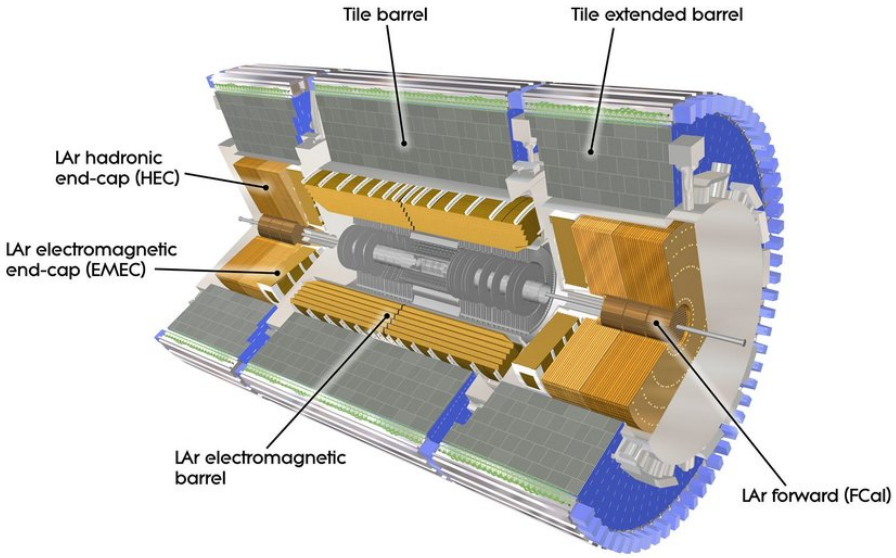

Figure 3.6: Cutaway view of the ATLAS Calorimeters.

3.2.2.1 Electromagnetic Calorimeter

The Liquid Argon calorimeter (LAr) [106] is used to detect shower and measure the energy of electrons and photons in the $|\eta| < 3.2$ region. Lead is used as an absorber due to its heavy nucleus, and electrons will interact with the lead and emit bremsstrahlung photons. Photons then convert to e^+e^- pairs, creating a narrow energy deposit as this process, called showering, continues. The active material used to measure the energy of the shower is liquid argon and was selected due to its radiation hardness and linear response in energy.

The LAr calorimeter is unique in its accordion geometry (Figure 3.7) which makes it fully hermetic, and allows for pointing information of photons. By definition the distance in a given material that a photon or electron loses $1/e$ of its energy is called the radiation length (X_0). The calorimeter is more than $22X_0$s deep with the hope of capturing all the energy of the incoming electromagnetic objects. Three layers are defined with up to different X_0s, varying depths, and granularities in η and ϕ. The "zeroth" layer is the presampler, installed to estimate the upstream energy losses due to material and is positioned before some detector infrastructure, separate from the calorimeter. The first layer has a thickness of about 4.4 radiation lengths at $\eta = 0.5$. In the ranges $|\eta| < 1.4$ and $1.5 < |\eta| < 2.4$, the first layer is segmented into high granularity strips in the η direction, with a cell

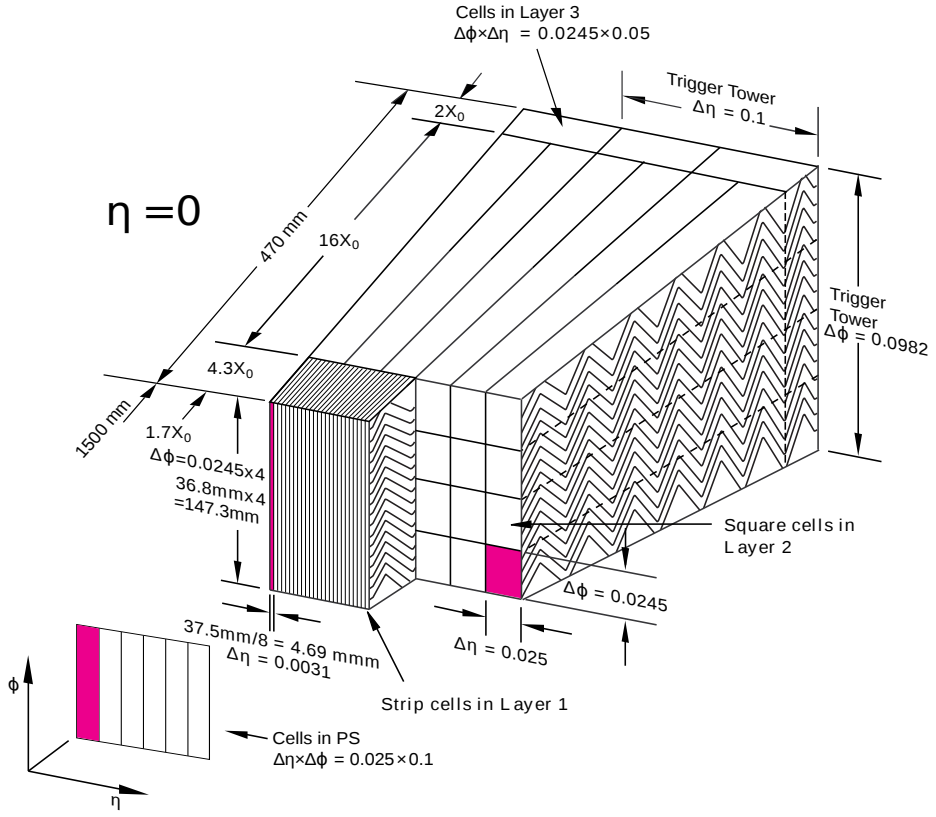

Figure 3.7: Sketch of the ATLAS electromagnetic calorimeter near $\eta = 0$.

size of 0.003×0.0982 in $\Delta\eta \times \Delta\phi$. For $1.4 < |\eta| < 1.5$ and $2.4 < |\eta| < 2.5$ the segmentation of the first layer is coarser, and the cell size is $\Delta\eta \times \Delta\phi = 0.025 \times 0.0982$. This granularity was designed to provide discrimination between single photon showers and showers from two collimated photons decaying from from neutral hadrons. The second layer has a thickness of roughly 16 radiation lengths with a granularity of $\Delta\eta \times \Delta\phi = 0.025 \times 0.0245$ and collects most of the energy of the shower. The third layer is 0.05×0.0245 in $\Delta\eta \times \Delta\phi$, with a depth of $2X_0$s. This last layer is used to correct for leakage of high energy electromagnetic showers into the beyond the electromagnetic calorimeter.

3.2.2.2 Hadronic Calorimeter

The Tile calorimeter [107], made of three layers in the barrel and two wheels in the endcap, provides coverage and measures energies from hadrons in the region of $|\eta| < 4.9$. The calorimeter is composed of steel plate absorbers and plastic scintillating tiles as the active material in the barrel region ($\eta < 1.5$), copper absorber with LAr active material in the endcap region ($1.5 < |\eta| < 3.2$), and

copper/tungsten absorbers with LAr active material in the forward region ($3.2 < |\eta| < 4.9$). The active material is readout through fibers and into photomultiplier tubes. Hadronic showers differ from their electromagnetic counterparts as they decay through the strong interaction, producing showers of mostly pions. About a third of these pions decay electromagnetically. These showers are generally much wider than electromagnetic showers. The active material in the first two layers of the barrel have a granularity of 0.1×0.1 in $\Delta\eta \times \Delta\phi$ while the last layer has a cell size of $\Delta\eta \times \Delta\phi = 0.2 \times 0.1$. In the endcap region the first wheel has a granularity of $\Delta\eta \times \Delta\phi = 0.1 \times 0.1$ while the second has a resolution of $\Delta\eta \times \Delta\phi = 0.2 \times 0.2$. Similar to the radiation length, an interaction length (λ) is defined by the distance for which the number of boosted charged particles diminishes by a factor of $1/e$. The depth of the hadronic calorimeter is 9.7λ in the barrel and 10λ in the endcap and forward region.

3.2.3 Muon Spectrometer

The Muon Spectrometer (MS) [108] is the outermost layer of ATLAS, consisting of two different tracking and triggering systems. The system is interspersed between the toroidal magnet and is the largest sub-system by volume. The MS provides muon tracking and triggering to $|\eta| < 2.7$, split between a barrel region extending to $|\eta| < 1.05$ and the endcap beyond. The system is subject to the toroid's 0.5 T magnetic field which bends the muons, allowing sagita measurements of the tracks in order to calculate muon p_{T} to 3% precision. Figure 3.8 shows the MS system.

The barrel region of the MS contains three cylindrical layers of Monitored Drift Tubes (MDTs) [109] for tracking, of which the last two layers are surrounded by Resistive Place Chambers (RPCs) [110] for triggering. The RPCs are sheet capacitors with 2 mm gaps filled with $C_2H_2F_4$ gas and have an electric field of 4,500 V/mm. Ionized electrons from tracks are read out through both sides of the detector. This provides trigger timing resolutions of better than 2 nanoseconds. MDTs are essentially bigger version of TRT straws. They are 3 cm diameter drift tubes filled with argon gas with a central an tungsten wire. The potential difference between the tube and the wire is held at 3,000 Volts. Muons traversing the tube ionize the gas, and charge is collected on the central wire. Using the drift time, the spatial precision can be attained to 80 μm.

The endcap region of the MS contains four wheels composed of MDTs, as well as Cathode Strip Chambers (CSCs) [111] and Thin Gap Chambers (TGCs) [112]. In the first layer, at higher $|\eta|$ of 2.5-2.7, the high flux of particles necessitates the use of a different technology as the occupancy of the MDTs becomes too high. The CSCs are used in this region and are composed of proportional

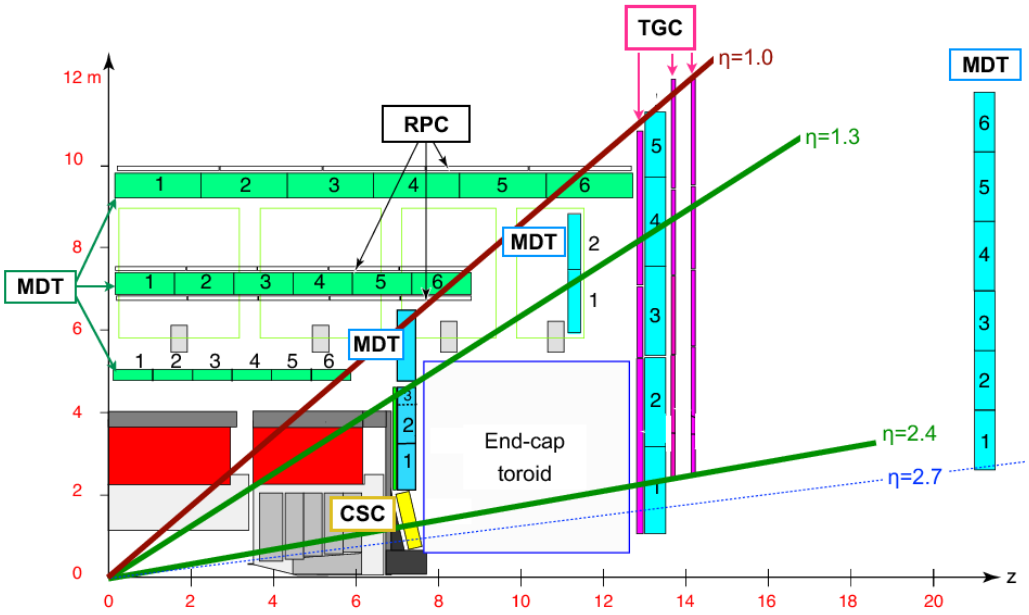

Figure 3.8: Schematic showing a quarter of the muon system in a plane containing the beam axis.

chambers with tungsten wires at 2i,600 volts, which are perpendicular to readout strips in an argon-carbon dioxide-tetrafluoromethane gas mixture. This is very much like a strip version of the MDT, with finer granularity and precision of 60 μm. The TGCs surround the third wheel of the endcap in three layers. TGCs are very similar to CSCs, but instead have gold plated tungsten wires held at 3,100 Volts in a mix of carbon dioxide and n-pentane. This provides a timing resolution of ~ 4 nanoseconds. Both the TGCs and RPCs are 99% efficient to trigger on muons in a single bunch crossing of 25 nanoseconds.

3.2.4 Magnet System

The ATLAS magnet system is composed of two parts; the central solenoid [113] and the toroidal magnet system [114, 115] that gives ATLAS its name. The central solenoid is a 2.3 meter diameter, 5.3 meter long superconducting magnet located between the ID and the EM calorimeter. It is cooled to a temperature of 4.5 K and provides a magnetic field of 2 T to the ID, along the z-axis. In order to minimize energy losses in the calorimeter, it has a thickness of only 5 cm, corresponding to 0.66 radiation lengths. The toroidal magnet system is an air-core system composed of a barrel toroid magnet and two endcap toroids, each containing eight coils. They provide a 0.5 T magnetic field in

the barrel region and 1 T field in the endcap, bending the path of muons. The barrel toroid ranges from R = 9.4 m - 20.1 m and is 25.3 meters long. The endcap toroids are 5 meters deep, with a 10.7 meter diameter. A drawing of the magnet system can be seen in Figure 3.9.

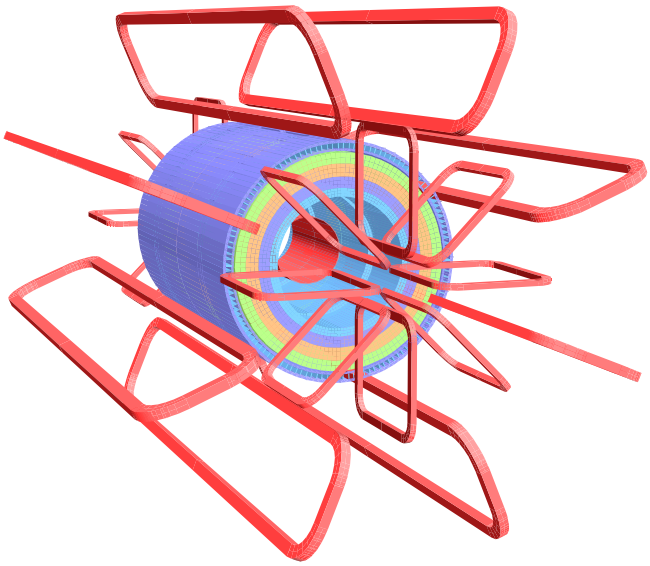

Figure 3.9: A drawing of the toroid magnet system in ATLAS.

3.2.5 Trigger and Data Acquisition System

Throughout Run 2, the LHC collided bunches of protons every 25 ns (40 MHz). If ATLAS were to record every bunch crossing at a raw event size of 1.5 MB, this would correspond to over 60 TBs of data per second written to disk. Obviously this is not feasible or needed as most LHC collisions are parton scattering where interesting electroweak scale physics is absent. A two level trigger is instituted [116], where real-time decision making occurs to filter interesting events. The first level, the Level 1 Trigger (L1), is implemented in hardware and reduces the total rate by a factor of 200 using coarse calorimeter and tracking algorithms. The decision is reached within 2.5 μs of the bunch crossing and triggers the information from the front-end boards to be sent from the detector. The second level, called the High Level Trigger (HLT) [117] is a software trigger that does finer tracking in regions of interest to reconstruct physics quantities. If the event is desirable, the HLT accepts the event and it is written to disk. The HLT reduces the rate from 100 kHz to roughly 1.5 kHz. These events are then sent to CERN's Tier 0 computing infrastructure to be fully reconstructed.

An overview of the trigger and DAQ system is shown in Figure 3.10.

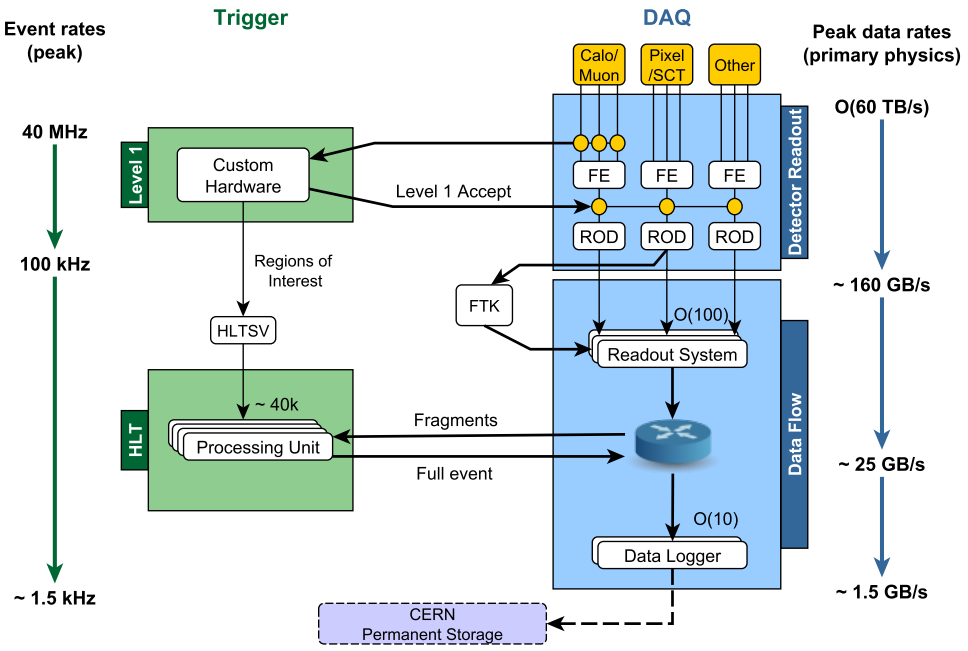

Figure 3.10: Overview of the ATLAS Trigger and DAQ system in Run 2.

Chapter 4

Transition Radiation Tracker Data Acquisition and Studies

This section aims to expand upon the TRT description in Section 3.2.1.3. Keeping the TRT Data Acquisition (DAQ) functioning as well as helping with operations, calibrations, testing, and on-call shifts were some of my favorite work experiences of my time here at Penn. I will outline the TRT DAQ system (Section 4.2) and outline my contributions to radiation testing and detector synchronization issues. With over 3,000 on-call hours logged and countless integrated months spent at CERN, I can barely touch on my experiences here.

4.1 Straw Tube Basics

When a charged particle traverses through a TRT straw, it ionizes the gas and will result in some amount of electrons being liberated from their atoms. As described in Section 3.2.1.3, the straws have a diameter of 4 mm and the potential between the cathode casing and anode wire is 1,500 volts. Those free electrons move toward the wire with a drift velocity of 25 ns/mm[2] and as they get closer, they cause more ionization of other gas atoms inducing an "avalanche" of electrons on the wire. This increase in gain is on the order of $\sim 20,000$. As electrons are ionized, they leave positive ions which drift toward the outer straw casing. The ion drift occurs at a slower rate, order μs/mm and induces a mirror current on the wire.

Depending on where in the straw the charged particle traverses, the first electrons will arrive at the anode wire at various times. This is characterized by the radius of closest approach to the wire and the electrons have a drift time that depends on the gas used in the straw. If a particle traverses

[2]With the nominal gas configuration of xenon-carbon dioxide-oxygen.

just the outer edge of the straw, the maximum drift time would then be ~ 50 ns, which would be in the next LHC bunch crossing. The front-end boards of the TRT were designed to account for the drift time, reading out 3 bunch crossings when triggered.

4.2 Data Acquisition and Electronics

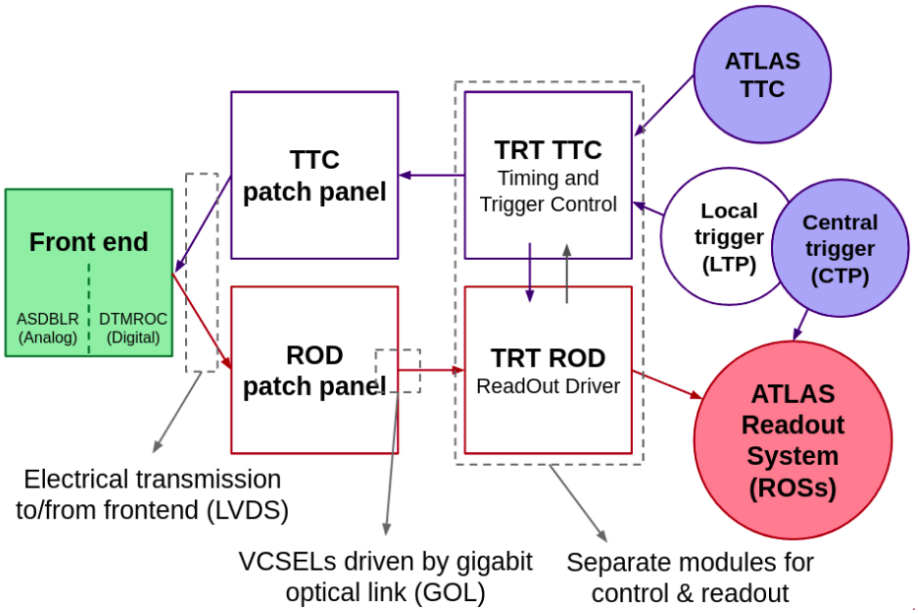

Figure 4.1: Overview of the TRT DAQ System.

An overview of the TRT DAQ system can be seen in Figure 4.1.

Straws are connected to analog Application-Specific-Integrated-Circuits (ASICs) are called the ASDBLR which provides amplification, shaping, discrimination, and base-line restoration. It is a custom ASIC which first amplifies the signal from the central wire with a gain of 1.5 mV/fC and a peaking time of 1.5ns. The signals are then shaped to pick out the electron avalanche from the ion tail. The ion tail is removed, and the baseline is restored. The signal is then passed to two discriminators. The first provides a "low" threshold which is triggered if the pulse amplitude is over $\sim$ 300 eV, corresponding to a tracking hit. In the second, a "high" threshold is applied as a transition radiation discriminator with an effective threshold of $\sim$ 6 keV. The output of the amplification, shaping, discrimination, and base-line restoration (ASDBLR) chip is a ternary output: no hit, low, or high and is fed into the Drift Time Measurement ReadOut Chip (DTMROC).

Each DTMROC has two input ASDBLRs and digitizes the low threshold output of a bunch crossing of 25 ns into eight binary 3.125 ns bins. The high threshold information is set as a single leading bit signifying a high threshold value over the entire 25 ns window. This information is stored with the bunch crossing identifier for 6 μs and if a trigger is sent, starts the process of sending up the identified bunch crossing and neighboring crossings(75ns window, 3 bunch crossings). The data are sent up as Low Voltage Differential Signals (LVDS).

The back-end electronics consist of two custom Versa Module Eurocard (VME) modules, called the Timing and Trigger Control (TTC) board and the ReadOut Driver (ROD). The TTC receives clock and command signals from ATLAS and relays them to the front-end boards through its own patch panel. The RODs receive the data from front-ends, through their own patch panels. These panels serialize the data from the front-ends using Gigabit Optical Link (GOL) chips and transmit them to the RODs via 1.2 Gb/s optical links. The patch panels are located in the Muon Spectrometer.

There are 64 RODs in the barrel containing inputs from 104 DTMROCs (204 ASDBLRs = 1,632 straws). In the endcap, 128 RODs are required, each accepting inputs from 120 DTMROCs (240 ASDBLRs = 1,920 straws). These RODs compress and packages the data to be sent to the ATLAS ReadOut System (ROS).

4.3 Radiation Damage Studies

During the Run 1 operation of the ATLAS detector, effects were observed indicating change of the threshold levels on the front-ends. Figure 4.2 shows the high and low threshold changes in subsequent calibrations, with respect to the first calibration. There is clear evidence of a negative threshold shift, growing and potentially saturating, from the first 30 fb^{-1}. Throughout Run 1 a small efficiency loss in reconstructing $Z \to ee$ decays was observed, indicating some shifting of the high threshold levels. An investigation was launched by radiating the front-end ASDBLR boards trying to reproduce the on-detector shifts. The boards were then irradiated further to study and predict effects of the radiation damage in Run 2 and beyond.

The radiation dose of the inner most TRT layer was estimated to be $\sim$ 30 krads in Run 1. A plan was developed as follows. Irradiate sets of endcap boards (triplet with 12 DTMROCs, 24 ASDBLRs, 192 ASDBLR channels) while powered at Brookhaven National Lab (BNL). The radiation would be given by a cobalt-60 source that produces photons at 1.17 and 1.33 MeV. This was to be done in several increments, first reproducing the Run 1 dosage of radiation, and then further irradiations

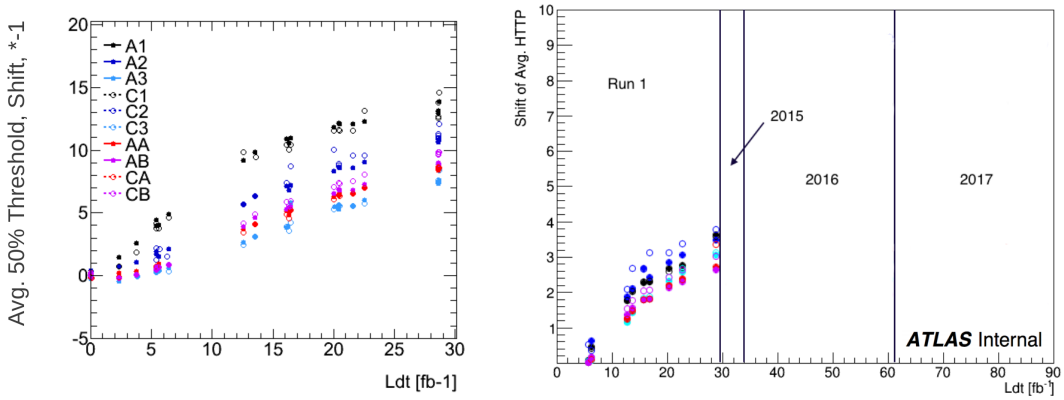

(a) Low thresholds

(b) High thresholds

Figure 4.2: TRT threshold calibration scans for (a) low threshold and (b) high threshold as a function of integrated luminosity. The average 50% occupancy threshold has drifted over time while the injected test pulse has remained constant. Both (a) and (b) show the Run 1 data only. The markers in both plots refer to different layers of the TRT, in the barrel layer 1 (A1,C1) is the closest to interaction point 3 (A3,C3) is the furthest. In the endcap, wheels are split between low z (AA,CA) and high z (AB,CB). The A and C barrel and endcap refers to the two cylindrical halves of the detector, symmetric along the z = 0 interaction point. The markers in plots (b) correspond to the same values shown by the legend in plot (a).

to predict behavior into Run 2 and Run 3. The metric of interest was the threshold at which the ASDBLR outputs would produce a 50% occupancy, for various injected charges. By measuring this 50% threshold, one could deduce shifts and by measuring the value at various injected charge, the gain of the amplifier could also be measured. In the following sections, noise refers to the 50% threshold measured when no pulse is injected. The "TP" refers to the test pulse of a given size in Digital to Analog Conversion (DAC) counts. This pulse originates from the DTMROC as it has the ability to generate a signal shaped like the integral of the expected ionization signal in a TRT straw. Thus when the signal arrives at the ASDBLR preamplifier, the input is a differentiated signal that mimics a typical pulse from a xenon filled straw.

Pictures of the setup at Brookhaven National Lab can be seen in Figure 4.3. Subfigure (a) shows the cobalt-60 source, shielded in an enclosure. When in use the source moves out of the shield where it is surrounded by lead in all directions except for a 25×25 cm opening. The right picture (b) are first TRT endcap triplet boards to be radiated, located 3 meters from the source. At this distance the dose rate was ~ 100 rads/hour, requiring 2 weeks to produce the Run 1 dosage of 30 krads.

Before and after the irradiation, these triplets and a control set were tested at CERN to determine the 50% thresholds. The test program measured the occupancy of each ASDBLR channel

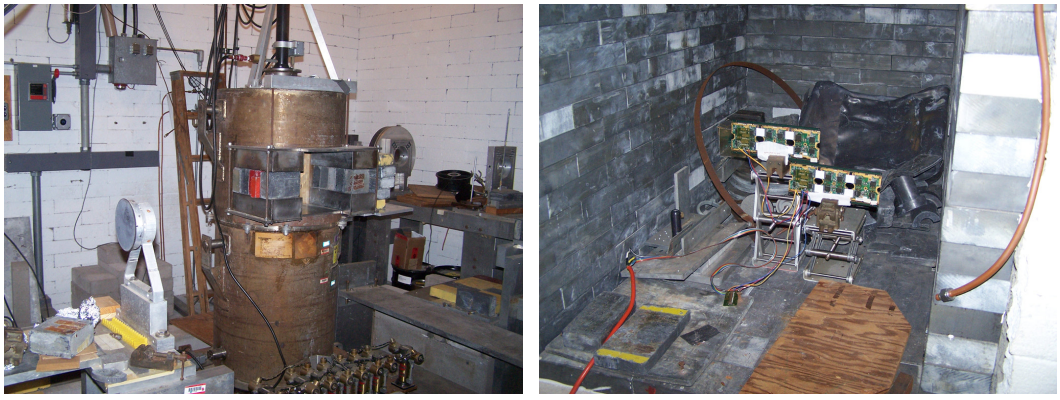

(a) (b)

Figure 4.3: (a) The cobalt-60 source and (b) TRT endcap triplet boards, about 3 meters away from the source.

by scanning thresholds between 0-200 DAC counts and for each value recording 200 events. The fraction of events above threshold over the total number of events determined the occupancy for that particular threshold value. A typical output plot for a channel looks like Figure 4.4. At low values of the threshold, noise will allow the output to be registered as a hit, while at high threshold values, the noise can never pass the threshold. An "S-curve" is drawn out by this scan, with the width is determined by the noise of the system. The 50% point is determined by fitting an error function to the data.

4.3.1 Results

Irradiation to 30 krads

Figure 4.5 shows the change in DAC counts for the first set irradiated to 30 krads, approximately the level of radiation received by the inner most boards of the TRT barrel in Run 1. Both the test pulse and the noise threshold levels shows a decreases in measured threshold levels by ∼12 DAC counts. This is very similar to the 12–15 DAC count shift seen in Figure 4.2.

Irradiation to 60 krads

Next, the same board irradiated to 30 krads was sent back to BNL to receive another 30 krads of radiation. Additionally, a second board was sent with it to be irradiated in order to reproduce results from the first board. Figure 4.6 displays the initial board, irradiated now to a total integrated

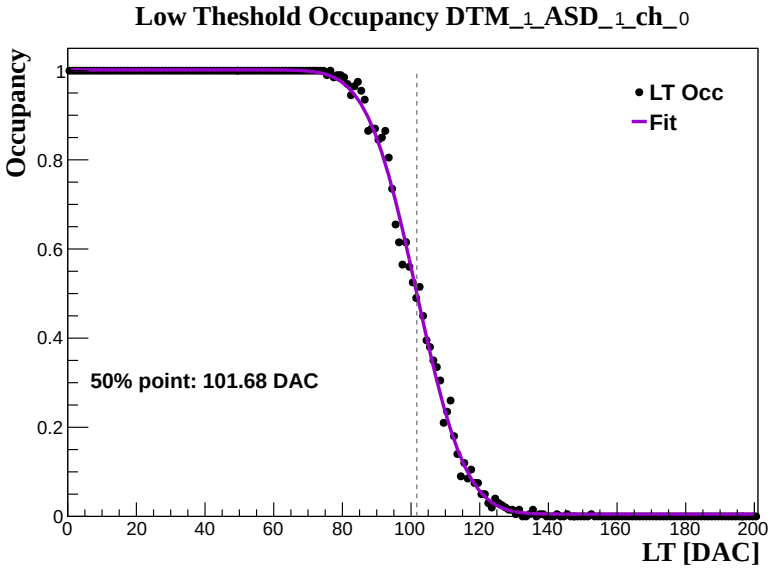

Figure 4.4: Threshold occupancy scan for one channel out of 192 on a single endcap triplet. The black points are the percentage of events (in 200 events) that the threshold value was reached by noise. The 50% point is determined by a fit to the data with an error function.

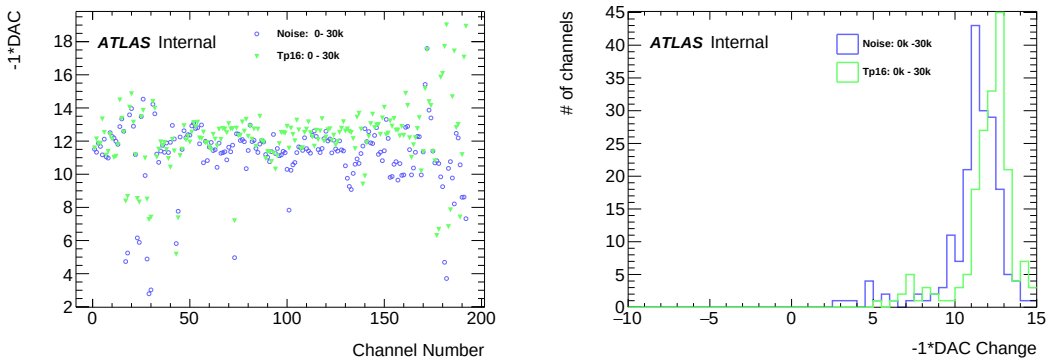

(a) DTMROC channel

(b) Histogram

Figure 4.5: Difference, in DAC counts of the 50% occupancy level, between a board irradiated to 30 krads and the same board not irradiated (0 krads) as (a) a function of channel number. (b) The same difference shown as a histogram.

dose of 60 krads. The original results from the 30 krad irradiation is also shown. The first dose of 30 krads produces a shift of 12–15 DAC counts, but subsequent doses do not induce an additional shift of 12 DAC. Instead it appears the next shift is maybe on the order of 1 or 2 DAC counts. A definite slope change toward 0 was seen at the end of Run 1 so if the radiation damage was truly saturating then one would expect no more shifting will occur. Nonetheless, the exercise to reproduce and predict the dosage is still fruitful since radiation damage was one of many hypotheses.

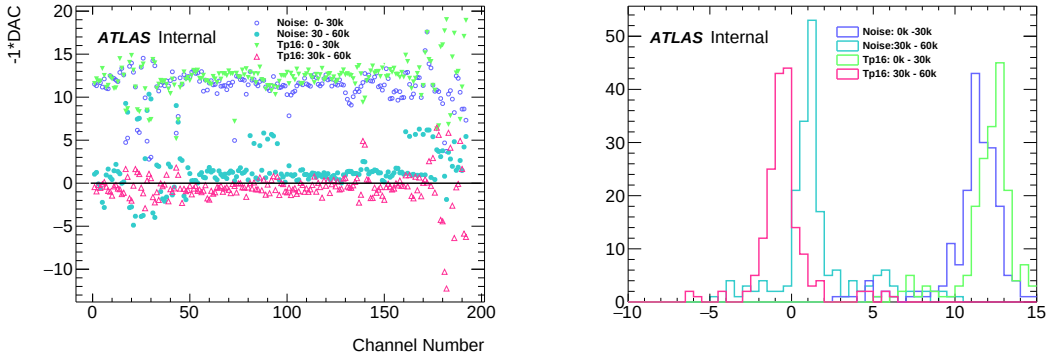

(a) DTMROC channel

(b) Histogram

Figure 4.6: Difference, in DAC counts of the 50% occupancy level, between a board irradiated to 60 krads, the same board irradiated to 30 krads, and not irradiated (0 krads), as (a) a function of channel number. (b) The same difference shown as a histogram.

The second set which was irradiated at the same time as the first set, now had a given dose of 30 krads. The effect seen showed a shift in threshold of $\sim$ 12 DAC, and was consistent with the TRT in Run 1 and with the first board set. The results of this board can be seen in Figure 4.7. This plot also has a test pulse values of 8 and 16 DAC counts, denoted TP8 value and TP16, as well as noise values. This was added to further investigate the slight difference in mean shift of the threshold values. As one can see clearly by the histograms in Figure 4.6, the mean shifts of the varying injected charge for the same dosage differ slightly. In reality this was probably caused by the test pulse injection mechanism from the DTMROC, and the uncertainty in the amount of charge of the injected pulse. There is also some error due to the setup, which will be discussed shortly.

Figure 4.8 shows the control board's measurements between the 0-30 krad radiation and the 30–60 krads irradiation of other triplet boards. The setup changed very little with some lines recording some deviations, but the overall shift is consistent with 0 DAC. It is important to note the radiation process takes multiple weeks so the values measured on the control board and irradiated boards is over multiple months.

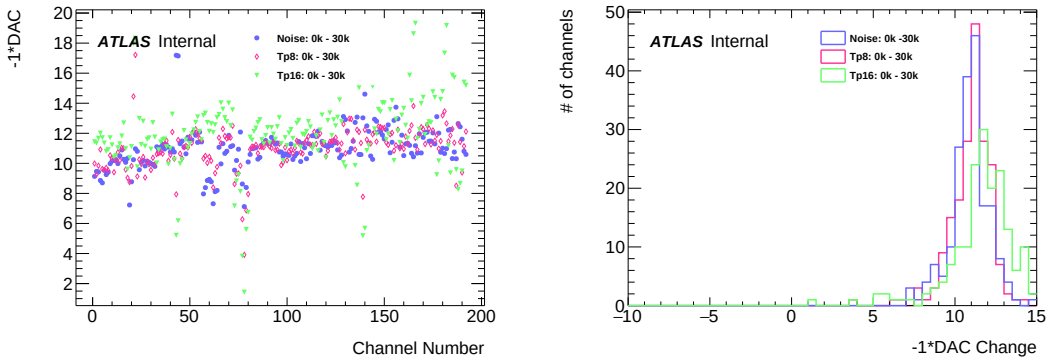

(a) DTMROC channel (b) Histogram

Figure 4.7: Difference, in DAC counts of the 50% occupancy level, between a second board irradiated to 30 krads and the same board not irradiated (0 krads) as (a) a function of channel number. (b) The same difference shown as a histogram.

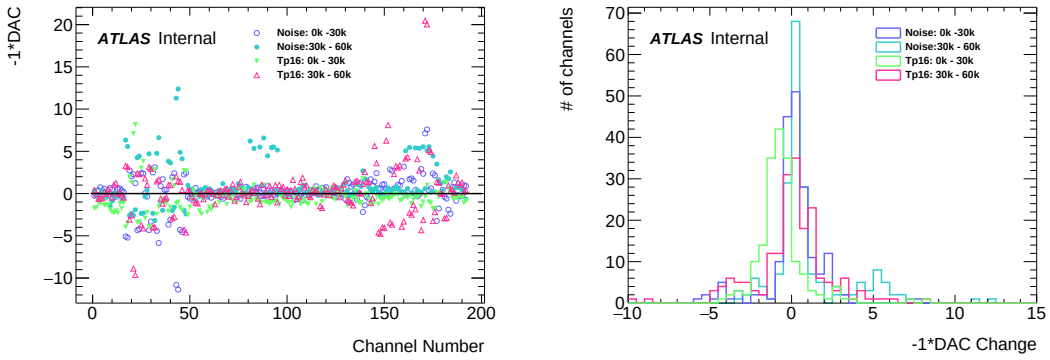

(a) DTMROC channel (b) Histogram

Figure 4.8: (a) Difference between DAC counts of the 50% occupancy level for a control board which was not irradiated as a function of channel number. The radiation levels noted are for the first triplet board. (b) The same difference shown as a histogram.

Irradiation to >200 krads

From the results at 60 krads, the radiation damage of shifting threshold values saturated near the Run 1 dosage of 30 krads. In order to be sure no other features could manifest themselves during late Run 2 or Run 3, boards were sent to be irradiated to 200 and 500 krads. Figure 4.9 shows an endcap triplet irradiated to 30 krads, then 500 krads. Once again the 12–15 DAC count shift is observed for the 30 krad irradiation. There is a minor 1–2 DAC count additional shift, indicating at much higher doses there might be an addition small shift. There also could be residual shifts from

the first 10 krads, and then the effect completely saturates. Figure 4.10 shows an endcap triplet irradiated to 200 krads. The same 12–15 shift in DAC counts is seen for noise, but there seems to be less of an effect fore test pulse. This could be due to damage of the test pulse injector or shaper, but is less understood. These higher irradiation tests were performed with a dosage rate of 5 krads/hour as they would have taken too long at 100 rad/hour. The initial test of 30 krads confirms the results are the same for the faster rate.

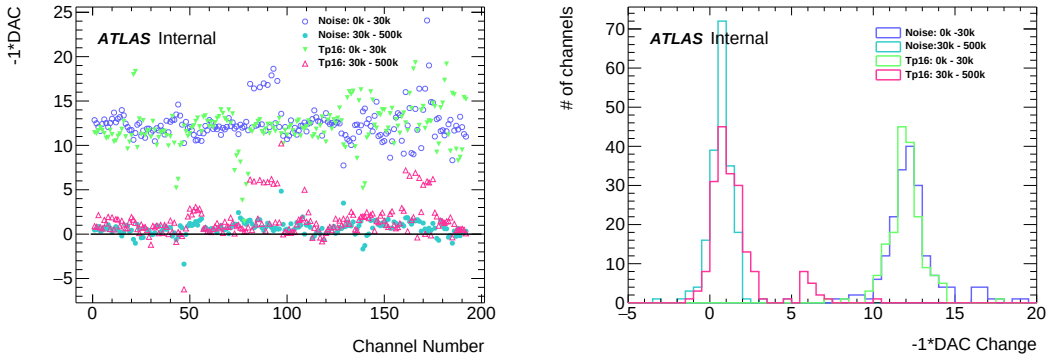

(a) DTMROC channel (b) Histogram

Figure 4.9: Difference, in DAC counts of the 50% occupancy level, between a third board irradiated to 500 krads, 30krads, and the same board not irradiated (0 krads) as (a) a function of channel number. (b) The same difference shown as a histogram.

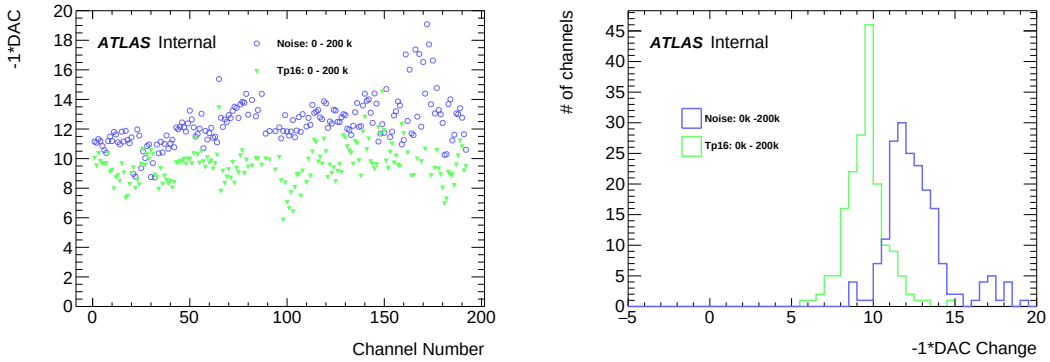

(a) DTMROC channel (b) Histogram

Figure 4.10: Difference, in DAC counts of the 50% occupancy level, between a fourth board irradiated to 200 krads and the same board not irradiated (0 krads) as (a) a function of channel number. (b) The same difference shown as a histogram.

The radiation damage that shifts the thresholds saturates around 30–40 krads, the dose seen in

Run 1. Going forward, it was predicted that the TRT DAQ team would see very little changes in thresholds as the effect should have saturated. Figure 4.11 shows that this prediction was correct. Large jumps in 2016 and 2017 are caused by change of gas configuration.

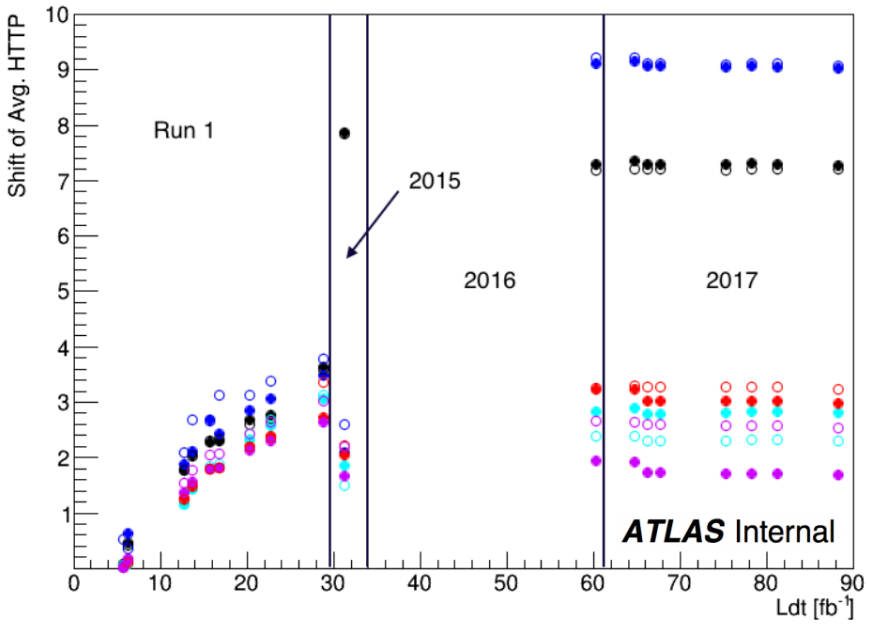

Figure 4.11: TRT threshold calibration scans for high threshold as a function of integrated luminosity. The average 50% occupancy threshold has drifted over time while the injected test pulse has remained constant. The markers refer to different layers of the TRT, in the barrel layer 1 is the closest to interaction point 3 is the furthest. In the endcap, wheels are split between low z (A) and high z (B). The A and C barrel and endcap refers to the two cylindrical halves of the detector, symmetric along the z = 0 interaction point. The markers in plots (b) correspond to the same values shown by the legend in Figure 4.2. Large jumps in 2016 and 2017 are caused by change of gas configuration.

Studies on the Gain of the ASDBLR

"There are no gains, without pains."

— Benjamin Franklin, 1758

Additionally, the gain of the ASDBLR preamplifier was studied for degradation due to radiation. The gain was measured by measuring the 50% threshold, using different injected test pulse values. The injected test pulse amplitudes of above 10 DAC were used in order to ensure a linear response of preamplifier. Figure 4.12 shows an example channel ASDBLR output for an endcap triplet, before and after irradiation to 30 krads. It is obvious that the post irradiation 50% thresholds are lower

(as seen in the previously), but the gain itself did not degrade noticeably. The points above 10 DAC are fit with a linear function and the slope is extracted. Figure 4.13 shows the percentage difference in gain, measuring before and after irradiation, for different sets of endcap triplets. Overall the gain may increase a bit (5%–10%), but the fitting error for the gain is also on the order of 5%. This is not of concern as a slight change in the response of the preamplifier is tolerable in Run 2 and Run 3 data-taking.

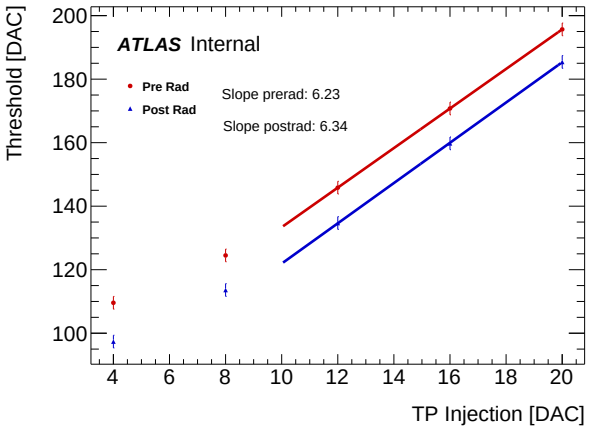

Figure 4.12: Gain measurement example for one channel on an ASDBLR, before and after irradiation (30 krads). The shift in thresholds due to the radiation damage is evident, though the response of the preamplifier did not change significantly.

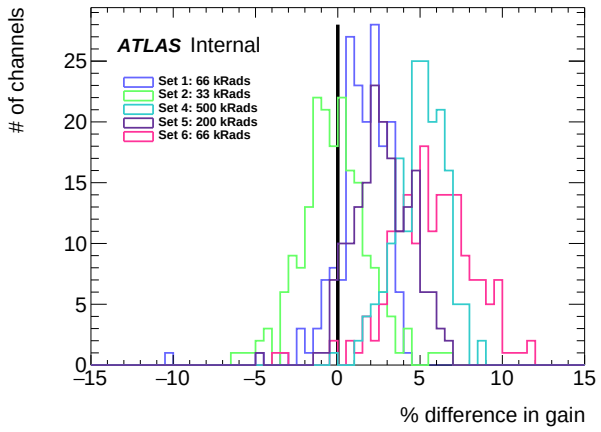

Figure 4.13: Percentage change of gain in all channels of different radiated boards. There is a slight shift in the response of the preamplifier.

4.4 TRT Synchronization

This section details a small part of timing issues encountered in the Run 2 operations. The section is intended more for a TRT DAQ expert, though I will try to give a brief overview of key parameters and parts of interest. All additional plots about the synchronization errors can be seen in Appendix A.

4.4.1 Overview of TRT DAQ Timings and Errors

As discussed previously the TRT TTC's receive their 40 MHz beam clock from the ATLAS TTC, which originates from the LHC. For each set of chips on the front-end boards, the ability to delay the incoming clock is needed in order to account for the different cable delays and provide stable writing of the data into the front-end chips. Both the clock and data delays are adjusted via Delay25 chips [118], which can delay the signals from 0 to 24.5 ns in steps of 0.5 ns. In order to fully determine the timings of different front-end boards, first clock delay scans ("bx") are performed to determine when the clock signal is latched by the DTMROC. After fixing the clock delay, a fine delay scan is performed ("dx"), in order to determine regions of bx-dx phase space where all chips in a GOL group (30 chips, 2.5 front-end boards in the endcap) read back the correct data. There will be regions of instability in both scans, near the rising edge of the clock. A more detailed discussion of the TRT timing constraints and parameters can be reviewed in Ref. [119].

Once these timings are determined, during stable beam data taking in the ATLAS detector, there are a few known situations when timing errors can occur. They generally occur when the Quartz Phase Locked Loop (QPLL) chip [120] has problems and cannot stabilize the incoming clock sufficiently. These errors arise the chip itself or the Quartz crystal associated with it, or large jitters of the LHC clock (this is known to occur from time-to-time). These QPLL chips and quartz crystals are located on the ROD back-end electronics and ROD patch panels. There is one QPLL+crystal per ROD and four QPLL+crystals on a single ROD patch panel, each stabilizing the clock when it is split into four copies, servicing the 4 GOLs on the patch panel.

The errors manifest themselves into two different types of errors, "lock resync errors" and "buffer resync errors" errors. Both are problematic as they require an entire resynchronization of the TRT sub-system which takes about 30 seconds - this is a long time when there are 40 million bunch crossings in a single second. The buffer errors are commonly associated with LHC clock jitter and are usually seen across the detector in random patterns while the lock errors are typically indicative of a bad QPLL (normally on the patch panel) and are consistent in their error pattern. The focus of this section is "anomalous" lock errors seen throughout Run 2 and therefore more details on buffer

errors is beyond the scope of this dissertation.

4.4.2 Investigation into Run 2 Lock Errors

Throughout Run 2, the TRT ran with a low rate of these seemingly random errors, but during the later parts of 2017 and early 2018 data taking, an increase in lock errors was observed. There was no indication that the LHC clock was unstable or of hardware issues which would degrade the propagation of the signals. A framework and simple sqlite3 database was developed, combining error logs from the TRT and beam information from the central ATLAS runquery database. With the framework, resync patterns due of specific error types during different beam conditions could be studied.

The first surprising thing found was that during Run 2 only there was a distinct pattern in the ROD lock errors. Once again, these errors are normally associated with some generic clock jitter and are expected to be random and independently distributed. Instead, it was observed that $\sim 8\%$ of all 192 RODs had more than 10 lock errors, and the patterns were consistent on them. This is to say that when a specific ROD had a lock resync error, it would almost always manifest itself as the same error type, not that all $\sim 8\%$ of RODs showed the same pattern.

This is shown in Figure 4.14, where the RODs with 10 or more lock errors during 2015–2018 stable beam data taking are shown. The lock error shown is a binary string, where the four GOLs on the patch panels are represented as 1's (no error) or 0's (error). The left-most digit refers to the GOL 3, and then counts downward as the right-most digit refers to GOL 0. For instance the binary string `0110` translates into GOL 3 and GOL 0 having errors while GOL 1 and GOL 2 are returning data as expected. For ease of viewing, errors with only one GOL asserting an error is denoted as "GOL X" (where X is the GOL number returning the error) in subsequent figures. In the following figures, the ROD's are indexed by a string of numbers (i.e `0x341401`), this is just an identifier for individual RODs. This should be treated as just an index with no deeper meaning, but further explanations of what specific ROD this refers to can be seen in Ref. [121][3].

This pattern was surprising and initially lead to the conclusion that the problem was somewhere on the ROD patch panel boards. The logic being, the pattern is almost always on a specific GOL and the patch panel is the only board which has this granularity as the ROD itself only has one QPLL+crystal for the incoming serialized data stream. These errors were also very hard to reproduce in test environments as the error occurred[4] once every $\sim 10^{12}$ clock ticks! This is not to say these

[3]This is an internal ATLAS note and may be access restricted.
[4]For the ROD with the highest number of errors.

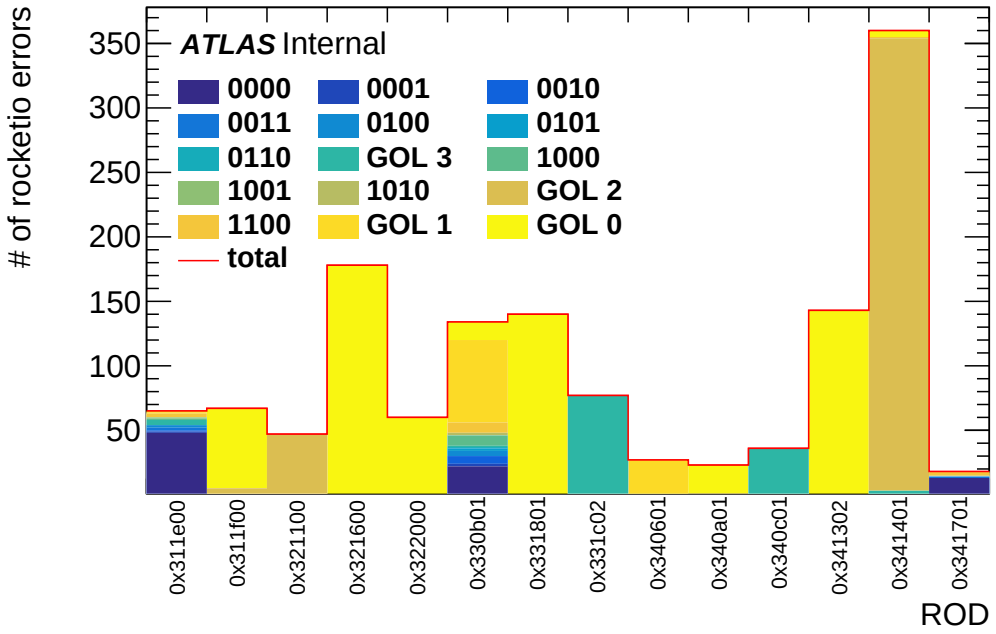

Figure 4.14: RODs with more than 10 lock errors during stable beams and their frequencies. The error type is typically constant, as seen by the solid colors. The lock error shown is a binary string, where the four GOLs on the patch panels are represented as 1's (no error) or 0's (error). The left-most digit refers to the GOL 3, and then counts downward as the right-most digit refers to GOL 0. For ease of viewing, errors with only one GOL asserting an error is denoted as "GOL X" (where X is the GOL number returning the error).

errors were rare as with 14 RODs having errors and thousands of hours of stable beams, there are an enormous amount of clock ticks.

In order to fully confirm this hypothesis, the following tests were done. First, the ROD with the highest number of lock errors was swapped with a neighboring ROD which did not have issues. The ROD with the second highest number of lock resync errors had the patch panel replaced. Then 3 more ROD's with errors had their ROD replaced, the GOL cables swapped, or just unplugged and plugged back into the VME crate. A table of the tests and results can be seen in Table 4.1.

As one can see, there are very mixed results coming from the tests! It appears the problem, which is sensitive to only one GOL on the patch panel can be remedied by replacing the back-end electronic ROD board where there is one QPLL, or can be fixed by replacing the in-detector patch panel (with four QPLLs). The test also indicate the changing of a ROD can alleviate, but not completely resolve the issue. This can also be seen visually in Figure 4.15 for ROD `0x341401`, Figure 4.16 for ROD

Table 4.1: Lock error tests performed on RODs and the results. In order to help track down the root of the error and which side the error was on (back-end or in-detector), patch panels were replaced, RODs were swapped, or cables were swapped.

ROD	Action	Result
0x341401	ROD swap	errors persisted, **decrease in error rate**
0x341302	ROD patch panel swap	**no more errors**
0x331c02	ROD swap	**no more errors**
0x321600	GOL cable swap	error persisted, error rate constant
0x331801	re-seat ROD	error persisted, error rate constant

0x341302, and Figure 4.17 for ROD 0x331c02.

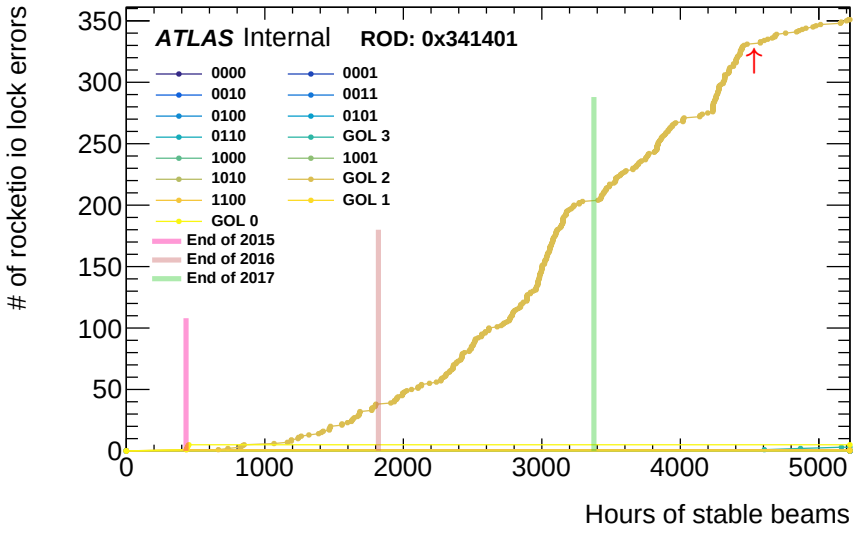

Figure 4.15: Integrated stable beam lock resync errors vs. hours of stable beam time for ROD 0x341401. GOL 2 consistently shows the same error pattern throughout Run 2, with ends of years shown in the colored lines. The red arrow denotes when the ROD swap occurred, and the subsequent change in error rate is obvious.

The result is somewhat puzzling but can be intuited as follows[5]. The timing problem is inherently on the ROD patch panel and occurs infrequently due to some issue there. This is why replacing the patch panel solves the problem. But since the problem has to do with a timing issue, if one can "clean up" the clock jitter in other ways, then one can completely solve or alleviate the problem. Consequently, this is why swapping or replacing the ROD in the back-end electronics can halt or

[5]This is purely a hypothesis at the time of the thesis writing but will be confirmed or refuted soon.

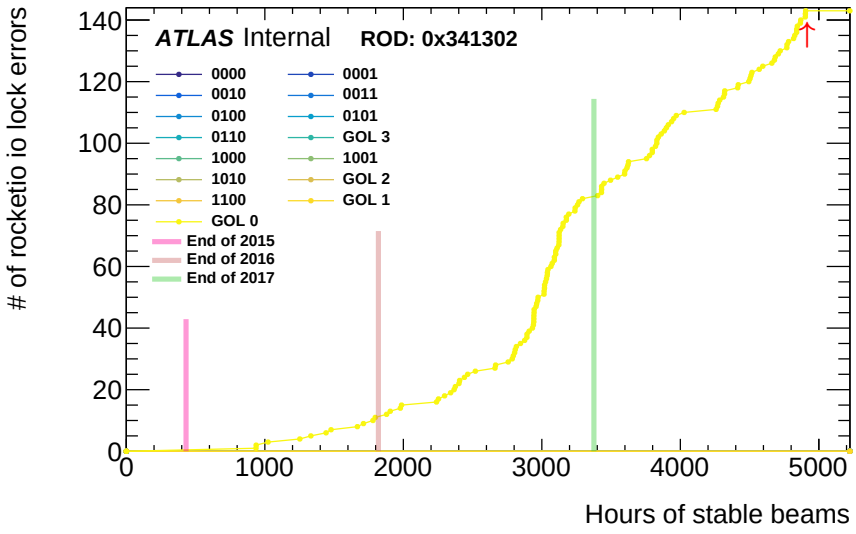

Figure 4.16: Integrated stable beam lock resync errors vs. hours of stable beam time for ROD `0x341302`. GOL 0 consistently shows the same error pattern throughout Run 2, with ends of years shown in the colored lines. The red arrow denotes when the ROD patch panel replacement occurred, and the errors ceased after that action.

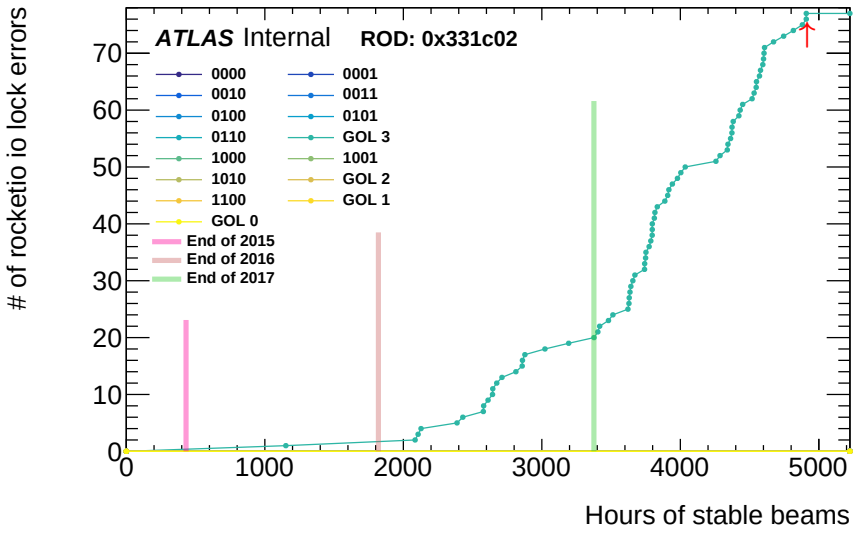

Figure 4.17: Integrated stable beam lock resync errors vs. hours of stable beam time for ROD `0x331c02`. GOL 3 consistently shows the same error pattern throughout Run 2, with ends of years shown in the colored lines. The red arrow denotes when the ROD swap occurred, and the errors ceased after that action.

reduce the error rate. The underlying issue is that the QPLL chip or crystal is just on the edge of its stability, hence the error rate is order 10^{12} clock ticks. This problem is exacerbated by higher occupancy in high pileup environments as the resync error rates increase during 2017 and 2018. Therefore, the stability can be restored by 1. replacing the patch panel, removing the problematic QPLL from the system, or 2. stabilizing the incoming clock on the patch panel. It is done by swapping the ROD/QPLL in the back-end electronics, which in turn stabilized the 40 MHz clock before it is sent down to the patch panel.

A board was designed with University of Pennsylvania instrumentation engineers in order to measure the clock jitter from the back-end ROD. The measurement would be performed with the boards that reduced, stopped, and caused resyncs on a particular patch panel. If there is a sizeable difference in this jitter than the hypothesis that the problem is truly a clock stabilization issue can be confirmed. This would indicate the problem is inherently on the ROD patch panel. If this is the case, measuring all ROD output jitters could help anticipate these errors and preventative measures could be taken. If no difference is observed more tests can be designed, triggering on the lost lock signal of the QPLL and looking at various signals on the ROD patch panel and ROD boards.

Chapter 5

Object Reconstruction and Identification

After the data has been triggered and collected from the various sub-detectors, the events need to be "built" from the raw detector signals. The process of taking these electronic pulses and consolidating them into "physics objects" is referred to as reconstruction. The ATLAS detector is capable of reconstructing the particle or decay products of almost all fundamental Standard Model particles. Neutrinos, which have a very low interaction cross section, are inferred by imposing a conservation of momentum requirement in the transverse plane. This chapter will give an overview of objects used in the analyses present in this thesis. These objects include photons, electrons, muons, jets (quarks and gluons), and missing transverse momentum. ATLAS can also reconstruct τs and large radius jets, though these will not be discussed. After reconstruction, identification criteria are imposed on objects as reconstructed objects may not be faithful to their true origins. This is to say, a reconstructed photon may not actually arise from a photon, but may have originated from an electron, quark, or gluon. In order to increase the confidence that photon candidates are originate from photons, Identification (ID) and Isolation (Iso) requirements are imposed. These are designed to have high efficiency and low background efficiency (high background rejection) for reconstructed objects which match their true origin. Section 5.1 will dive deeply into the end-to-end procedure used to define a photon as they are most important objects for this dissertation. Other sections will outline basic techniques used to reconstruct and identify other objects. Electrons and muons, which are important for studying electroweak vector bosons, are discussed in Section 5.2 and Section 5.3, respectively. Jets, important for many aspects of photon searches and measurements, are outlined in Section 5.4. And finally, missing transverse momentum is discussed in Section 5.5.

5.1 Photons

> *"All the fifty years of conscious brooding have brought me no closer to answer the question, 'What are light quanta?' Of course today every rascal thinks he knows the answer, but he is deluding himself."*
>
> — Albert Einstein, 1951

Prompt photons play a prominent role in the overall ATLAS physics program. They can be used to study QCD's non-perturbative regions, parton distribution functions, electroweak processes, and the Higgs boson. They are defined as all photons in the final state which did not originate from hadron decays. The identification of prompt photons can be quite challenging at a hadron collider, as there is an overwhelming number of reconstructed photons arising from light hadron decays in jets and a smaller number coming from hadrons which leave a significant amount of their energy in the electromagnetic calorimeter. This section will detail the reconstruction process, as well as the identification, and isolation selection criteria defined by the ATLAS experiment. The work done, particularly on the photon "Fudge Factor (FF)" (Section 5.1.3.2), is outlined in a publication note [2] and paper [8]. Understanding the reconstruction, identfication, and isolation of the photon objects is vital as both analyses described later in the thesis involve Higgs bosons decaying to one or two photons.

5.1.1 Reconstruction

In general, this section describes the reconstruction of photons or electrons in the ATLAS detector, though the electron reconstruction also requires a more complicated track matching algorithm.

From the first iteration of ATLAS's reconstruction software until 2016, a fixed cluster size "sliding window" algorithm was utilized to reconstruct photon objects in the electromagnetic calorimeter. Further reading of this algorithm can be seen in Ref. [122]. The reason for the fixed cluster size in the past was due to the inability to calibrate dynamically sized clusters. Improvements to the calibration scheme due to the advances of multivariate techniques [123] has now allowed for dynamically sized clusters. Advantages of this new technique include the ability to associate low energy bremsstrahlung photons back to original electron or converted photon. Using these dynamic clusters allows for a linear energy response across a vast range of energies. This in turn translates to better energy resolution of the photon objects.

The basis of this new dynamically changing cluster is called the "topo-cluster". More information about the algorithm can be seen in Ref. [124]. Generally, instead of the cluster being defined in some fixed size, it is dynamically changing based on the spatial (hence topology) energy significance with respect to the seed cell and each cell added to the cluster.

First, the reconstruction algorithm selects the topo-clusters in the EM calorimeter which form the basis of the photon candidates and orders them in p_{T} descending order. These initial seeds' energy must exceed 1.5 GeV. Starting with the highest p_{T} candidate, the algorithm then is defined as follows. A re-fit of the all tracks associated to EM calorimeter clusters is performed, and matches them to the selected topo-cluster. This includes converted photon vertices in the re-fitted tracks, and contributions from bremsstrahlung photons. These bremsstrahlung objects are required to be lower in p_{T} than in initial seed cluster. The satellite (associated bremsstrahlungs) clusters are also required to be within a $\Delta\eta \times \Delta\phi = 0.075 \times 0.125$ (3x5 calorimeter cells) window around the barycenter of the seed. For converted photons, a satellite cluster is added to the seed cluster if its track is associated with the seed cluster, or if has the same conversion vertex (without a track). A cartoon of the above description can be seen Figure 5.1. Once the "super-cluster" (seed cluster + satellite clusters) is formed, the algorithm iterates to the next highest p_{T} seed cluster. If the cluster was used as a satellite cluster previously it is skipped or else the process begins again. This procedure is repeated until there are no seed clusters left.

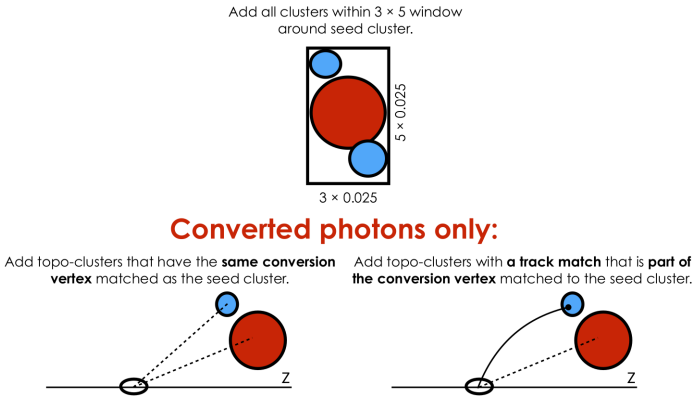

Figure 5.1: Cartoon illustrating photon super cluster reconstruction.

This process is performed in parallel for photons and electrons, and then some ambiguity is resolved between the two particle containers. Some overlap is allowed in order to maintain high reconstruction efficiencies for both objects. This actually plays a important role in the Higgs to

neutralinos analysis described in Chapter 7. The candidate photons are then passed to the calibration stage.

5.1.2 Calibration

The calibration of photon energies in the electromagnetic calorimeter requires multiple steps: the initial energy calculation, multiple steps of residual corrections dependent on location, and scale adjustments.

5.1.2.1 Calorimeter Energy

The deposit of energy in the electromagnetic liquid argon calorimeter induces electrical currents proportional to the deposited energy. The LAr cells are sampled at 40 MHz and if an event is triggered, four samples of the current are read out to provide the basis of the energy measurement. Each measurement is read as a 12 bit sequence digitized by an Analog to Digital Converter (ADC). The counts are then corrected, first by the pedestal of the readout electronics, p. The pedestal corresponds to the measured response of the electronics when there is no signal present [125]. Each measurement is then multiplied by an Optimal Filtering Coefficient (OFC) [126] used to predict the amplitude of the pulse and then summed. OFCs are chosen from predicted pulse shapes and noise correlation functions to minimize the total variance from electronic and pileup noise. Finally the summed currents are then turned into a meaningful physics quantity by two factors $\mathrm{F}_{\mathrm{ADC}\to\mu\mathrm{A}}$ and $\mathrm{F}_{\mu\mathrm{A}\to\ \mathrm{MeV}}$ [127]. The first, $\mathrm{F}_{\mathrm{ADC}\to\mu\mathrm{A}}$, converts the digital counts to the input current, and is derived from special electronics calibrations. Finally, $\mathrm{F}_{\mu\mathrm{A}\to\ \mathrm{MeV}}$ is the conversion factor to translate the current into MeV, and this factor was determined from test beam studies. The formula for the cell energy can be written fully as:

$$\mathrm{E} = \mathrm{F}_{\mu\mathrm{A}\to\ \mathrm{MeV}} \times \mathrm{F}_{\mathrm{ADC}\to\mu\mathrm{A}} \times \sum_{i=1}^{4} a_i(s_i - p) \ . \tag{5.1}$$

5.1.2.2 Calibration Procedure

The calibration procedure is outlined here. For a more detailed paper on this process, for both electrons and photons please refer to Ref. [128].

Once the energies in the cells are calculated, the procedure is as follows:

1. Properties of the shower development in the calorimeter structure are used to minimize the effect of material before the calorimeter. A multivariate algorithm estimates this effect and is

trained on simulated samples. This algorithm is then applied to data, and corrects the energies due to the material effects.

2. Minor adjustments to the energy scales of the different layers is performed. Note this is not the overall scale adjustment, but local adjustments. This is determined from studies of muons and electrons interacting with the calorimeter. These corrections are applied to the data before electron or photon energies are calculated, and is important for the total energy scale adjustment to be valid across the entire energy spectrum.

3. Corrections for known irregularities in the calorimeter response are applied. This can encompass boundary effects of the segmented calorimeter modules, and different voltage settings for different regions during operation.

4. The overall energy scale is adjusted using $Z \to ee$ decays. There is no standard candle for photon decays, so the Z is used as a correction to photons and electrons. The correction is done by observing the reconstructed mass of Z and setting it equal to the known value measured by LEP [129].

5. The last step is a validation of this technique by comparing the energy response in a orthogonal sample. $J/\psi \to e^+e^-$ events are employed for electrons and radiative Z boson decays for photons.

5.1.3 Identification

Since the production of prompt photons is order of magnitudes less than the production of non-prompt photons (fake photons), the ATLAS photon identification was designed to separate these sources. Several discriminating variables were designed based off of the lateral and longitudinal electromagnetic shower development in the calorimeter. These involve ratios of energies in different EM calorimeter locations, or the leakage of energy into the hadronic calorimeter. The definitions of the discriminating variables are listed in Table 5.1, and Figure 5.2 shows a cartoon of the variables. Prompt photons generally produce narrower energy deposits in the calorimeter and have smaller leakage of energy in the hadronic calorimeter. Additionally, the first layer of the calorimeter is segmented very finely which is used to distinguish between a single prompt photon and the double-peaked structure of $\pi^0 \to \gamma\gamma$ decays.

Table 5.1: Discriminating variables used for *Loose* and *Tight* photon identification.

Category	Description	Name	*Loose*	*Tight*
Acceptance	$\|\eta\| < 2.37$, with $1.37 \leq \|\eta\| < 1.52$ excluded	–	✓	✓
Hadronic leakage	Ratio of E_{T} in the first sampling layer of the hadronic calorimeter to E_{T} of the EM cluster (used over the range $\|\eta\| < 0.8$ or $\|\eta\| > 1.52$)	$R_{\mathrm{had_1}}$	✓	✓
	Ratio of E_{T} in the hadronic calorimeter to E_{T} of the EM cluster (used over the range $0.8 < \|\eta\| < 1.37$)	R_{had}	✓	✓
EM middle layer	Ratio of 3×7 $\Delta\eta \times \Delta\phi$ to 7×7 cell energies	R_η	✓	✓
	Lateral shower width measured in the middle layer	w_{η_2}	✓	✓
	Ratio of 3×3 $\Delta\eta \times \Delta\phi$ to 3×7 cell energies	R_ϕ		✓
EM strip layer	Lateral shower width calculated from three strips around the strip with maximum energy deposit	$w_{s\,3}$		✓
	Total lateral shower width measured in the strip layer	$w_{s\,\mathrm{tot}}$		✓
	Energy outside the core of the three central strips but within seven strips divided by energy within the three central strips	F_{side}		✓
	Difference between the energy associated with the second maximum in the strip layer and the energy reconstructed in the strip with the minimum value found between the first and second maxima	ΔE_s		✓
	Ratio of the energy difference associated with the largest and second largest energy deposits to the sum of these energies	E_{ratio}		✓
	Ratio of the energy measured in the first sampling of the electromagnetic calorimeter to the total energy of the EM cluster	f_1		✓

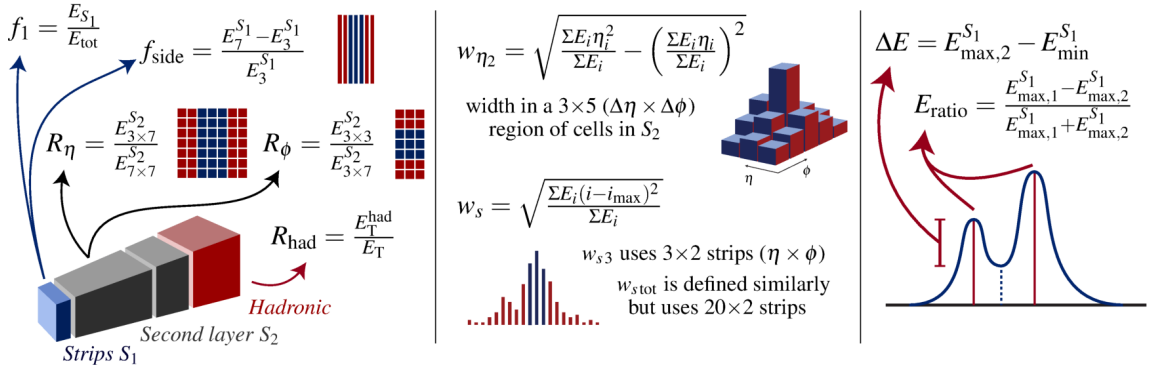

Figure 5.2: Cartoon describing the photon identification discriminating variables. This is taken from Ref. [130]. $E_C^{S_N}$ refers to the energy deposited in the N-th longitudinal layer of the electromagnetic calorimeter for a given cluster C. E_i is the energy in the i-th cell.

With the variables, two sets of rectangular cuts[6] are defined: *Loose* and *Tight* identification criteria. These sets of cuts are tuned to reduce the dependency of the identification criteria on pileup, and were re-tuned from the Run 1 criteria. The *Loose* selection only depends on the shower shapes in the second layer of the calorimeter, while the *Tight* selection adds information from the first, finely segmented strip layer. The ID criteria is optimized for converted and unconverted photons separately and in bins of $|\eta|$ (0.0-0.6, 0.6-0.8,0.8-1.15, 1.15-1.37, 1.52-1.81, 1.81-2.01, 2.01-2.37) in order to account for the calorimeter geometry and varying amount of material before the calorimeter.

5.1.3.1 Pseudo Photons

Loose photons, with some additional requirements on the strip variables, are used to construct control regions of "pseudo photons". These are primarily used to estimate backgrounds from jets that are mis-reconstructed as photons.

These pseudo photons are designed to be "jet-like" photons. Pseudo photons are defined to be *Loose* photons that fail one or more of four *Tight* photon identification strip variables and pass the rest of the *Tight* identification criteria. These four discriminating variables are ΔE_s, F_{side}, $w_{s\,3}$, and E_{ratio}. The strip variables are less correlated with isolation and this procedure allows for a data-driven method to calculate backgrounds from jets mis-identified as photons using a 2D plane of ID and isolation.

[6] A set of linear discriminants such $R_{\text{had}} < x_1$, $\Delta E_s > x_2$, ..., etc where cut values (x_1, x_2, ..., etc) form an optimal phase space, separating "signal" from "background".

5.1.3.2 "Fudge Factors"

The nominal ATLAS Monte Carlo reproduces the shower shapes of the photons reasonably well, but imperfectly. Generally the simulation does well describing the longitudinal shower development, but the transverse showers are not modeled as well. The central values of the actual physical distributions are modeled quite well, but the central values of the variables of interest, which are mostly ratios, are shifted from the corresponding distributions observed in the data. An ad-hoc method of shifting back Monte Carlo to better describe the data is known as "fudging" and so the data/Monte Carlo shower shape adjustments are generally known as "Fudge Factor (FF)". These corrections are applied to simulated photon in the efficiency measurements as well as in general simulated samples containing photons.

In this section the derivation and results of the fudge factors for the shower shape variables are outlined. The corrections were derived from the 2015–2017 dataset. Comparisons to old fudge factors and agreement to Run 2 data is also discussed. The variables ΔE_s, and E_{ratio} are not corrected as there is reasonable agreement between the data and Monte Carlo. Additionally, the variable f_1 was not corrected because the rectangular cut on f_1 is on the order of the FF uncertainty and very non-uniform/physical Monte Carlo (MC) efficiencies are seen if the variable is corrected.

Two samples are defined that are used to calculate the fudge factors. The first is the collection of *Tight* and `FixedCutLoose` isolated photons (see Section 5.1.4 for discussion on isolation). This provides a high purity sample of high p_{T} photons though there is some small bias in the variable

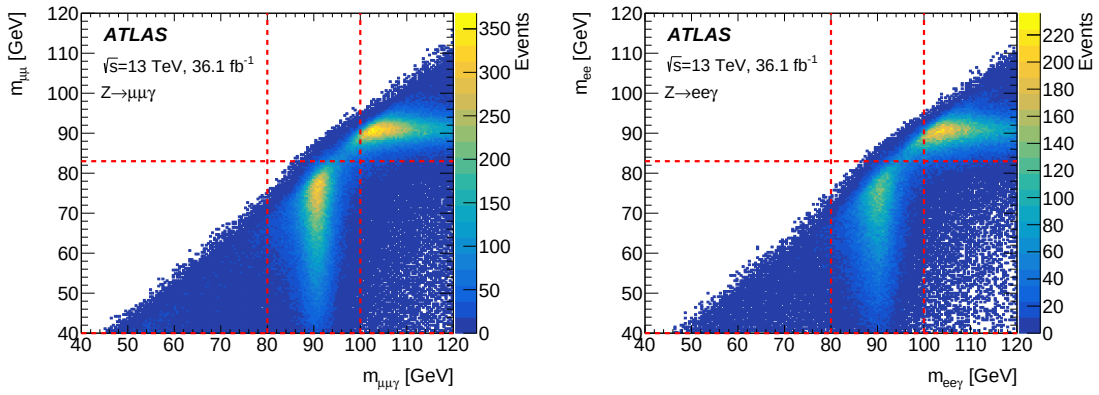

(a) $Z \to \mu\mu\gamma$ (b) $Z \to ee\gamma$

Figure 5.3: 2D mass plane of $m_{\ell\ell\gamma}$ vs. $m_{\ell\ell}$ for (a) muons and (b) electrons with 2015–2016 data. The horizontal and vertical dashed lines show the selections used to isolate radiative decays: $40 < m_{\ell\ell} < 83$ GeV and $80 < m_{\ell\ell\gamma} < 100$ GeV.

distributions as identification requirements are applied to the selected photons. The second sample exploits the radiative Z ($Z \to ll\gamma$) decay to extract a clean, unbiased sample of photons. Photons are selected by applying kinematic requirements on the dilepton pair, the invariant mass of the two leptons−photon final state, and ID requirements on the two leptons. Other than the `FixedCutTight` calorimeter isolation and p_{T}, η requirements no other selection criteria, including ID, are applied to the photon candidate[7]. A two-dimensional distribution of the dilepton invariant mass, m_{ll}, versus the invariant mass or the three particle final-state, $m_{ll\gamma}$, is shown is Figure 5.3. To minimize the background from $Z+$jets, the requirements of 40 GeV $< m_{ll} <$ 83 GeV and 80 GeV $< m_{ll\gamma} <$ 100 GeV are applied. The signal photons are final state radiation photons where $m_{ll\gamma} \approx M_Z$ and $m_{ll} < M_Z$. The fudge factors for photons with $p_{\mathrm{T}} < 50$ GeV are calculated with radiative Z photons while higher p_{T} fudge factors are computed with the isolated photon sample.

After the photon selection, the events are split into 11 p_{T} bins and 8 $|\eta|$ bins for each discriminating variable. The bins are as follows: p_{T} : $[8, 15, 20, 25, 30, 40, 50, 60, 80, 100, 250, 1000]$ GeV, $|\eta| = [0.0, 0.6, 0.8, 1.15, 1.37, 1.52, 1.81, 2.01, 2.37]$. In addition, the photons are separated between converted and unconverted photons. The binning is chosen as the shower shape forms maybe be sensitive to η, p_{T}, and conversion type.

After this stage each binned histogram is then smoothed using an adaptive Kernel Density Esti-

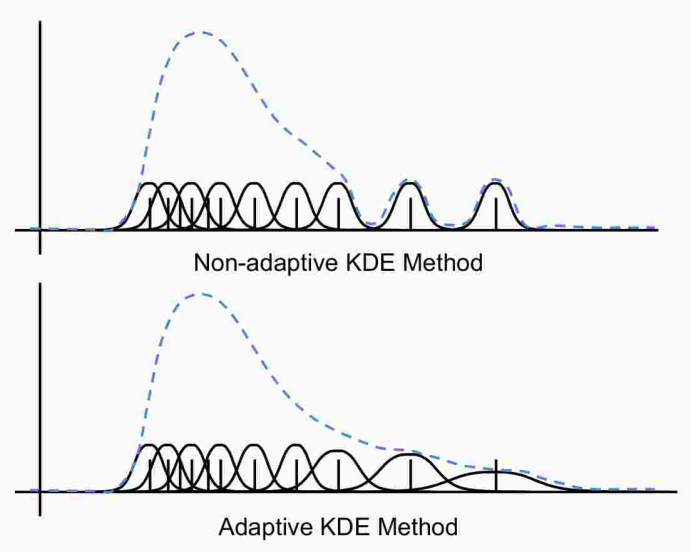

Figure 5.4: Cartoon illustrating adaptive vs. non-adaptive KDE smoothing.

[7]The isolation requirement does not use information from the calorimeter cells in the cluster and therefore does not bias the distributions.

mation (KDE). As a first pass, each histogram may be smooth enough to use for the FF extraction, but because of bin granularity and statistical fluctuations, FF extraction performance is significantly degraded without KDE smoothing. For a histogram, each particular value of the given shower shape is plotted as a Dirac-δ-function. Each Dirac-δ function is then replaced by a kernel function (Gaussian) with some user-determined width depending on the granularity required (fine factors), and the Gaussians are subsequently summed to form a final Probability Distribution Function (PDF). These fine factors were tuned such that the PDFs retained important features, but not statistical jitter and this choice was optimized with a χ^2 calculation of the KDE with data. The adaptive KDE works in the same general way except that in low statistics regions the width of the Gaussians is increased. Figure 5.4 shows the non-adaptive KDE smoothing compared with the adaptive smoothing. Due to size limitations of the histograms, the extreme tails of some distributions were condensed into a single overflow or underflow bin. Figure 5.5 shows an example of high and lower statistics KDE smoothing effects, where the raw histograms are in blue and the KDS smoothed PDF is shown in red.

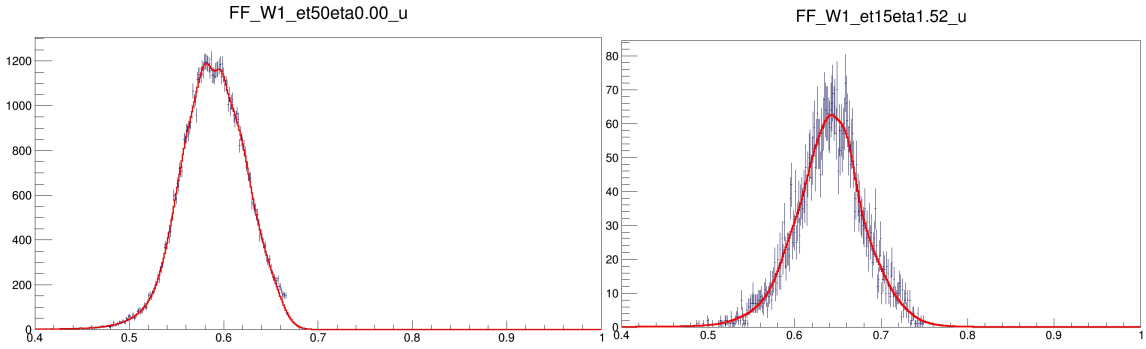

(a) High statistics (b) Low statistics

Figure 5.5: Showing (a) high and (b) low statistics regions with KDE smoothing. The KDE smoothed PDF is in red, with unsmoothed histogram in blue. The adaptive KDE allows the PDF to extract the underlying shape and not be subject to the lower statistics fluctuations.

After the PDFs are created, the data and Monte Carlo PDFs for a given variable (in the p_{T}, $|\eta|$ bin) are plotted together and a χ^2 is calculated between the two PDFs. The overflow and underflow bins are not included in the χ^2 calculation. The Monte Carlo PDFs is shifted positively by one bin (out of 500) and a χ^2 is calculated again. This shift is repeated up to 60 bins in both the positive and negative directions. The χ^2 is then plotted and the minimum bin, corresponding to a shift value of the PDF is found. This shift value is referred to as the fudge factor. A simple study of a aligning the mean of the Monte Carlo with the that of the data is shown to provide similar results to this

method.

An example of the calculated shift and the resulting χ^2 is shown in Figure 5.6. The red line in the χ^2 plot is the 2012 FF value. This is for the variable $w_{s\,\mathrm{tot}}$ for a converted photon with $60 < p_{\mathrm{T}} < 80$ GeV and $0 < |\eta| < 0.6$.

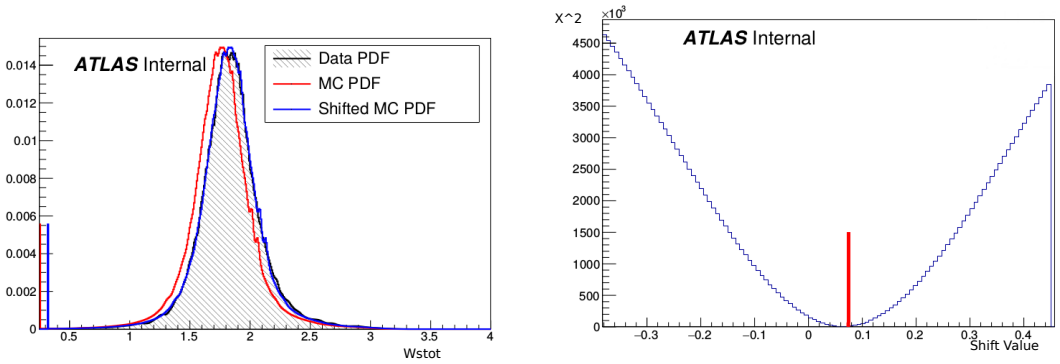

(a) Variable distribution

(b) χ^2 of shift

Figure 5.6: An example of the χ^2 shifting method for the $w_{s\,\mathrm{tot}}$ variable. This bin contains converted photons with $60 < p_{\mathrm{T}} < 80$ GeV and $0 < |\eta| < 0.6$. (a) shows the data, Monte Carlo, and shifted Monte Carlo PDF. (b) displays the χ^2 value as a function of the shift value. The red line in the χ^2 plot is the 2012 FF value.

The typical size of the correction is roughly 10% of the root mean square of the distribution of the variable. These values are then used to correct shower shapes in the measurements for the photon efficiency (in MC) and all ATLAS analyses with photons, including the two described in this dissertation. An example of the fudge factors effect can be seen in Figure 5.7 for converted and unconverted photon candidates originating from radiative Z decays. The R_η and $w_{s\,3}$ variables for inclusive photons (in p_{T} and η) are shown. Other discriminating variables can be viewed in Appendix B. As one can note, the agreement is much better after the correction, though some residual discrepancies are observed in the tails of distributions. This is mainly due to the χ^2 method in producing the fudge factors. More complicated techniques such as Smirnov transforms are being studied to help alleviate these discrepancies.

5.1.4 Isolation

In addition to the identification criteria, the photons are required to be "isolated". This means the amount of energy in the calorimeter or tracks in the Inner Detector around the identified photon must be below a certain threshold. This is used to reduce hadronic background processes. There

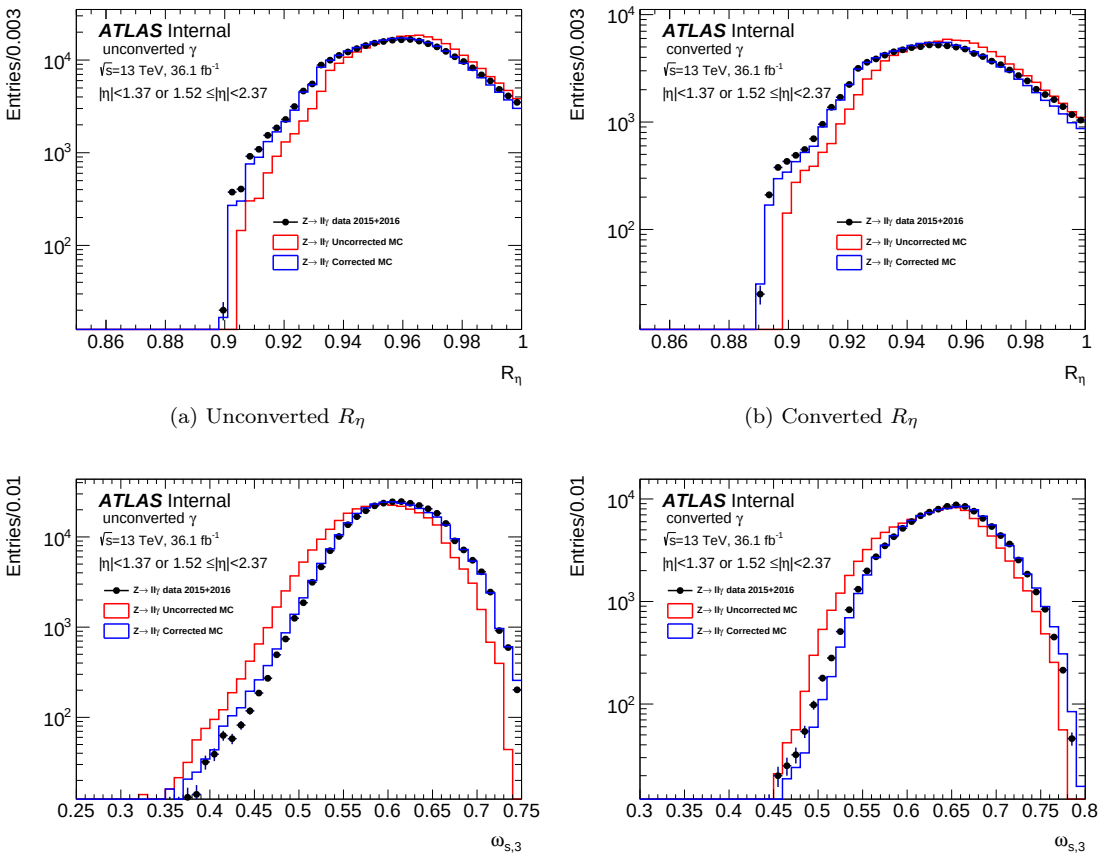

(a) Unconverted R_η

(b) Converted R_η

(c) Unconverted $w_{s\,3}$

(d) Converted $w_{s\,3}$

Figure 5.7: Distributions of (a),(b) R_η and (c),(d) $w_{s\,3}$ for (b)(d) converted and (a),(c) unconverted photon candidates with $p_{\mathrm{T}} \in [10, 50]$ GeV and $|\eta| < 2.37$ (excluding $1.37 \leq |\eta| < 1.52$) selected from $\ell^+\ell^-\gamma$ events. The data are compared with simulated $Z \to \ell\ell\gamma$ events where the red solid histogram corresponds to the uncorrected Monte Carlo, and the solid blue line is the corrected simulation via the fudge factor.

are two types of isolation criteria used in the ATLAS experiment. The calorimeter isolation, $E_{\mathrm{T}}^{\mathrm{iso}}$, is defined on the transverse energy[8] in a cone with angular size ΔR around the photon. The $E_{\mathrm{T}}^{\mathrm{iso}}$ is the sum of energy of the topo-clusters in that cone, after removing the energy from the photon, pileup, and underlying event. A track based isolation variable, $p_{\mathrm{T}}^{\mathrm{iso}}$, is defined as the sum of charged-particle track p_{T} ($p_{\mathrm{T}}>$ 1 GeV) within a given ΔR.

With the two isolation variables, 3 working points are defined by the ATLAS experiment. A loose isolation requirement is defined and generally used by most analyses on ATLAS. It is referred to as `FixedCutLoose`:

$$E_{\mathrm{T}}^{\mathrm{iso}}\big|_{\Delta R<0.2} < 0.065 \cdot E_{\mathrm{T}} \text{ and } p_{\mathrm{T}}^{\mathrm{iso}}\big|_{\Delta R<0.2} < 0.05 \cdot E_{\mathrm{T}}\,; \tag{5.2}$$

a tight isolation requirement, called `FixedCutTight`, is used in the Higgs to neutralinos analysis in Chapter 7 and is defined as:

$$E_{\mathrm{T}}^{\mathrm{iso}}\big|_{\Delta R<0.4} < 0.022 \cdot E_{\mathrm{T}} + 2.45 \text{ GeV and } p_{\mathrm{T}}^{\mathrm{iso}}\big|_{\Delta R<0.2} < 0.05 \cdot E_{\mathrm{T}}. \tag{5.3}$$

Finally an alternative version of the tight isolation requirement, based only on the calorimeter isolation, `FixedCutTightCaloOnly`:

$$E_{\mathrm{T}}^{\mathrm{iso}}\big|_{\Delta R<0.4} < 0.022 \cdot E_{\mathrm{T}} + 2.45 \text{ GeV}. \tag{5.4}$$

5.2 Electrons

Prompt electrons are predominantly produced from decays of $t\bar{t}$ pairs as well as W and Z bosons at the LHC. The reconstruction is very similar to that outlined in the photon section, though with additional track requirements as the electron calorimeter deposit will be accompanied by an Inner Detector track.

In the case of electrons traversing the TRT, the TRT may contain many high threshold hits on track, as the electrons emit higher amounts of transition radiation due to their large γ factor. This TRT information from a reconstructed electron, along with track and calorimeter discriminating variables are fed into a likelihood classifier to determine the likelihood of the reconstructed electron being a true prompt electron or an electron arising from background jets or converted photons. This classifier is formed by constructing probability distribution functions of each input discriminating

[8] With respect to the beam.

variable, for signal and background separately. These PDFs are derived from simulations and data using the tag and probe method [131, 132]. A likelihood ratio of the signal over the signal + background is defined. A single cut on the output discriminant of the likelihood function is used to identify electrons into *Tight*, *Medium*, and *Loose* categories. These working points are tuned such that the electron has a 93% (*Loose*), 88% (*Medium*), 80% (*Tight*) efficiency when the electron has a p_{T} of 40 GeV. Furthermore, in this dissertation the electrons are required to be isolated and pass the `GradientLoose` isolation ATLAS working point. This criterion requires a changing cut on both the calorimeter and track isolation such that the efficiency remains equal to $0.057 * p_{\mathrm{T}}$ [GeV] + 95.57%[9]. This corresponds to an efficiency of 95% at 25 GeV and 99% at 60 GeV.

5.3 Muons

Prompt muons also are predominantly produced from decays of $t\bar{t}$ pairs as well as W and Z bosons at the LHC. Unlike electrons, they will only minimally ionize in the calorimeter and continue moving through to the Muon Spectrometer, leaving tracks but ultimately escaping the detector. Muons are then reconstructed and identified using mainly the tracking and muon system information and using the calorimeter deposit minimally. First, Muon Spectrometer tracks are built by constructing segments from hits in different muon sub-systems. Next, a fit is performed on the segments to get track candidates, and then individual hits on track are compared with the fitted track. If the χ^2 between the hits and fitted track is small enough, the track is accepted as a reasonable MS track. The reconstruction algorithm then defines four types of muons with these MS tracks, in combination with Inner Detector and calorimeter information:

1. **Combined:** There is a track in the ID that is consistent with the trajectory of the MS track. A global refit of the track, starting in the MS and extrapolating back to the ID, is performed.

2. **Calorimeter Tagged:** In this case, no muons hits are recorded in the Muon Spectrometer, but there is a track in the ID associated with an energy deposit consistent with a minimally ionizing particle. This is used only in the $|\eta| < 0.1$ region where there is no muon detector coverage.

3. **Segment Tagged:** An Inner Detector track is consistent with a segment in the muon system, but not a full track. The muon is reconstructed using this segment and ID information, and and the kinematics of the muon are derived from the ID track.

[9] This truncates at 100%.

4. **Standalone:** A track in the Muon Spectrometer is not compatible with any Inner Detector tracks or calorimeter deposits but is consistent with originating from the primary vertex. This is used in the $2.5 < |\eta| < 2.7$ region where the ID coverage is lacking.

When applicable, energy losses from the calorimeter system are taken into account as muons lose about 3 GeV going through the calorimeter. If there are multiple coinciding muons reconstructed by the different procedures, the Combined Muon reconstructed is used first, then Segment Tagged, then Calorimeter Tagged, and then Standalone. Muons are then identified using the χ^2 of the fit, requiring hits in different layers of the detectors, p_{T}, and q/p information of the Inner Detector and Muon Spectrometer [133]. They are then classified into *Loose*, *Medium*, and *Tight* categories, similar to electrons. Track isolation, defined in the same way as for electrons, can be calculated and required.

5.4 Jets

Jets are conical showers of hadrons that come from an initial parton. Jets are composed of neutral and charged particles and deposit most of their energy in the hadronic calorimeter with broad showers. This is in contrast with electrons and photons, where most of the energy will be deposited in a narrow electromagnetic calorimeter shower. Similar to electrons and photons, the calorimeter deposits are grouped into topo-clusters. The jets are then reconstructed using the anti-k_t algorithm [134] and tracks are then associated with the calorimeter jet. In this dissertation, jets are defined with the distance parameter $R = 0.4$ and are required to have $|\eta| < 4.4$ and $p_{\mathrm{T}} > 30$ GeV. Jets are then calibrated, taking into account pileup [135, 136], energy losses in the calorimeter, detector material, and soft deposits of energy below topo-cluster noise levels [137].

In general it is useful to b-tag jets, that is identify jets originating from b-hadrons or b-quarks. They are identified using an multivariate algorithm [138] based on the measurable non-prompt decay, high decay multiplicity, and hard fragmentation of b-hadrons compared to gluons and lighter quarks.

5.5 Missing Transverse Momentum

Missing transverse momentum[10] is defined as the transverse momentum which is not detected in a particle detector. Due to conservation of transverse momentum, if all particles produced in the

[10] Also referred to as missing transverse energy, or $E_{\mathrm{T}}^{\mathrm{miss}}$.

collision are detectable then there should be no $E_{\mathrm{T}}^{\mathrm{miss}}$ in the event. In practice detector resolution, material effects, or particle decays into non-instrumented regions of the detector can cause $E_{\mathrm{T}}^{\mathrm{miss}}$ in an event. Events with undetectable particles such as neutrinos or in the case of SUSY, sparticles, can have missing transverse momentum.

Each cell is associated with a hard physics object (electron, muon, photon, jet) or classified as `Soft Term`. The `Soft Term` $E_{\mathrm{T}}^{\mathrm{miss}}$ is calculated from the tracks associated with the primary vertex that do not match a hard physics object. $E_{\mathrm{T}}^{\mathrm{miss}}$ is then computed as the negative sum of the transverse momentum of the different detected objects and the soft term. Each contribution from these objects is calculated in a separated term and then summed in a total $E_{\mathrm{T}}^{\mathrm{miss}}$ variable as Equations 5.5 and 5.6 show.

$$E_{x(y)}^{miss} = E_{x(y)}^{miss,e} + E_{x(y)}^{miss,\gamma} + E_{x(y)}^{miss,\mu} + E_{x(y)}^{miss,jets} + E_{x(y)}^{miss,SoftTerm} \ . \tag{5.5}$$

$$E_{x(y)}^{miss,i} = -\sum_{j=0}^{N_i} (\vec{p_j})_{x(y)} \qquad N_i = N_{jets}, N_e, ... \tag{5.6}$$

Chapter 6

Higgs Differential and Fiducial Cross Sections in the Diphoton Channel

"Furious activity is no substitute for understanding."

— H. H. Williams

6.1 Introduction

In 2012, the discovery of a particle consistent with the Higgs boson was announced by the ATLAS [139] and CMS [140] collaborations. Since the discovery, measurements of its properties and couplings to Standard Model fermions and gauge bosons have been a cornerstone of the LHC research program. In particular, measurements of the differential and fiducial cross sections have been a useful tool in order to study the properties and kinematics associated with Higgs boson production with minimal model assumptions. This chapter presents the measurements of the fiducial and differential cross sections of the Higgs boson decaying into a final state of two photons. These results expand upon the previous analyses by ATLAS [3, 4, 141] and CMS [142] in Run 1 and Run 2. The measurements presented in this chapter are almost entirely made with $36.1\,\text{fb}^{-1}$ of $\sqrt{s} = 13\,\text{TeV}$ data collected in 2015 and 2016, though some differential variables have been measured with $79.8\,\text{fb}^{-1}$ of 2015–2017 data. In addition to these measurements, differential distributions have then been used to set limits on Wilson coefficients of Effective Field Theory (EFT) interpretations that parameterize BSM effects as six dimensional operators added to the Standard Model Lagrangian [143].

This chapter outlines the work published in Ref. [6] for the 2015–2016 dataset, and includes work done for the conference notes [3,4,7] for Run 2 datasets of $13.3\,\text{fb}^{-1}$, $36.1\,\text{fb}^{-1}$, $79.8\,\text{fb}^{-1}$ respectively.

6.1.1 Definition of Fiducial and Differential Cross Sections

The cross section, σ_{total}, of a process is:

$$\sigma_{\text{total}} = \frac{n_{\text{reco}}}{\epsilon_{\text{total}} \cdot \mathcal{L}_{\text{int}}} \; ; \tag{6.1}$$

where n_{reco} is the number of reconstructed signal events in the particular final state, $\mathcal{L}_{\text{int}}$ is the total integrated luminosity of the data, and ϵ_{total} (defined as $\frac{n_{\text{reco}}}{n_{\text{total}}}$) is a term that accounts for the efficiency of the trigger, reconstruction, identification, and isolation.

The total cross section contains model-dependent assumptions as the efficiency (ϵ_{total}) encompasses terms where the detector is not sensitive. For example, objects in events can be produced at too low p_{T} or too forward in η and are subsequently out of detector acceptance. To reduce this model dependence, the measurement of the cross section can be performed in final states restricted to a specific volume of phase space. This is known as the fiducial cross section. The fiducial volume is defined to be as close as possible to the acceptance of the ATLAS detector and experimental selection criteria in order to minimize the model-dependence of the measurement. The fiducial cross section is then written as:

$$\sigma_{\text{fid}} = \frac{n_{\text{reco}}}{C_{\text{i}}^{\text{fid}} \cdot \mathcal{L}_{\text{int}}} \; ; \tag{6.2}$$

where $C_{\text{i}}^{\text{fid}}$ now denotes the "correction factor" which accounts for the detector resolution and inefficiency in the fiducial volume only. This correction factor method (also known as bin-by-bin) unfolds the detector level measurement back to truth distributions. These factors are determined using simulated samples and is discussed in Section 6.6. The differential cross section ($d\sigma/dx$) in a bin of variable x is then given by:

$$\frac{d\sigma_{\text{fid}}}{dx} = \frac{n_{\text{reco}}}{C_{\text{i}}^{\text{fid}} \cdot \Delta x \cdot \mathcal{L}_{\text{int}}} \; . \tag{6.3}$$

6.1.2 Fiducial Regions and Differential Variables

Cross sections are measured in five fiducial regions designed to target specific Higgs boson production modes or be sensitive to BSM physics. The inclusive fiducial region is characterized at the truth level by at least two photons, not originating from the decay of a hadron, that have pseudorapidity $|\eta| < 2.37$, excluding the region $1.37 < |\eta| < 1.52$, and requiring the leading (subleading) photon's transverse momentum to be greater than 35%(25%) of $m_{\gamma\gamma}$ system. The two photons are required to be isolated from hadronic activity by imposing that the sum p_{T} of tracks ($p_{\text{T}} > 1$ GeV) within $\Delta R = 0.2$ is required to be less than $0.05 \times E_{\text{T}}^{\gamma}$. The object and region definitions can be seen in Table 6.1. Four other regions begin with this baseline requirement and then are outlined as follows:

Table 6.1: Summary of the truth level definitions of the five fiducial integrated regions as described in the text.

Objects	Definition
Photons	$\lvert\eta\rvert < 1.37$ or $1.52 < \lvert\eta\rvert < 2.37$, $p_{\mathrm{T}}^{\mathrm{iso},0.2}/p_{\mathrm{T}}^{\gamma} < 0.05$
Jets	anti-k_t, $R = 0.4$, $p_{\mathrm{T}} > 30\,\mathrm{GeV}$, $\lvert y\rvert < 4.4$
Leptons, ℓ	e or μ, $p_{\mathrm{T}} > 15\,\mathrm{GeV}$, $\lvert\eta\rvert < 2.47$ for e (excluding $1.37 < \lvert\eta\rvert < 1.52$) and $\lvert\eta\rvert < 2.7$ for μ
Fiducial region	**Definition**
Diphoton fiducial	$N_\gamma \geq 2$, $p_{\mathrm{T}}^{\gamma_1} > 0.35\,m_{\gamma\gamma}$, $p_{\mathrm{T}}^{\gamma_2} > 0.25\,m_{\gamma\gamma}$
VBF-enhanced	Diphoton fiducial, $N_j \geq 2$, $m_{jj} > 400$ GeV, $\lvert\Delta y_{jj}\rvert > 2.8$, $\lvert\Delta\phi_{\gamma\gamma,jj}\rvert > 2.6$
$N_{\mathrm{lepton}} \geq 1$	Diphoton fiducial, $N_\ell \geq 1$
High $E_{\mathrm{T}}^{\mathrm{miss}}$	Diphoton fiducial, $E_{\mathrm{T}}^{\mathrm{miss}} > 80$ GeV, $p_{\mathrm{T}}^{\gamma\gamma} > 80$ GeV
$t\bar{t}H$-enhanced	Diphoton fiducial, $(N_j \geq 4, N_{b\text{-jets}} \geq 1)$ `OR` $(N_j \geq 3, N_{b\text{-jets}} \geq 1, N_\ell \geq 1)$

1. VBF-enhanced: This region contains events with two jets with a dijet mass m_{jj} of at least 400 GeV, a large separation in rapidity $|\Delta y_{jj}| > 2.8$, and an azimuthal difference between the Higgs boson and the dijet pair of $|\Delta\phi_{\gamma\gamma,jj}| > 2.6$.

2. $N_{\mathrm{lepton}} \geq 1$: This region selects events that contain at least one electron or one muon with $p_{\mathrm{T}} > 15$ GeV. For electrons, the pseudo-rapidity needs to satisfy $|\eta| < 2.47$ (excluding $1.37 < |\eta| < 1.52$) and for muons, $|\eta| < 2.7$ is required.

3. High $E_{\mathrm{T}}^{\mathrm{miss}}$: This region retains events with missing transverse momentum $E_{\mathrm{T}}^{\mathrm{miss}} > 80$ GeV and $p_{\mathrm{T}}^{\gamma\gamma} > 80$ GeV.

4. $t\bar{t}H$-enhanced: This region consists of events with at least one lepton and three jets `OR` no leptons and four jets to study Higgs boson production in association with top quarks. In addition, one of the jets needs to be identified as originating from a bottom quark.

The $N_{\mathrm{lepton}} \geq 1$ and high $E_{\mathrm{T}}^{\mathrm{miss}}$ regions are designed to be enriched with Higgs bosons produced in association with a W or Z boson, though the high $E_{\mathrm{T}}^{\mathrm{miss}}$ region is also sensitive to contributions of Higgs decaying to or produced in association with BSM particles.

After reconstruction, the definitions of the objects are slightly different though the baseline definitions of the fiducial regions are the same. The two highest E_{T} photons are chosen as the $H \to \gamma\gamma$ candidate and are used to identify the diphoton primary vertex. This vertex is selected using a neural network based on track and nominal primary vertex information, as well as the pointing information from the two photons measured in the calorimeter and Inner Detector [144].

This diphoton vertex information improves the diphoton invariant mass resolution as it is utilized to refine the angle of the photon momentum. While reconstructed photons are required to have the same track isolation requirement as the truth photons, an additional calorimeter isolation requirement is imposed. The photon candidates are required to have a calorimeter isolation less than 6.5% of the photon's transverse energy. Reconstructed jets with b-quarks are tagged using a multivariate technique, described in Section 5.4. These, along with other small differences between truth and reconstructed level objects, lead to minor changes in Higgs production mode composition of the defined fiducial regions. These can be seen in Figure 6.1, where the expected Higgs production mode composition of the fiducial regions at truth level and reconstruction level are shown. Notably, fake missing transverse momentum from mis-measured jets and soft QCD has the largest effect as the ggF/VBF contamination in the High $E_{\mathrm{T}}^{\mathrm{miss}}$ region is the most prominent change from truth to reconstruction level.

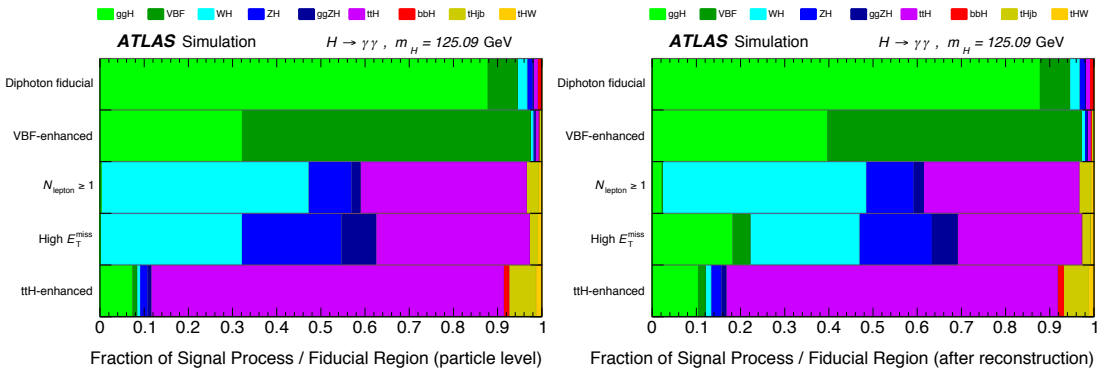

(a) Truth Level (b) Reconstructed Level

Figure 6.1: Expected Higgs boson production mode composition of events in the fiducial regions (a) at truth level and (b) after reconstruction. The signal processes, shown in the various colors, are the different $H \to \gamma\gamma$ production modes.

Differential distributions are then obtained by splitting the fiducial measurement as function of event variables. Table 6.2 shows the different variables and brief definitions. The measured differential variables can be split into four general categories of kinematic variables: Higgs boson kinematics, jet activity, spin-CP sensitive variables, and VBF-topology variables.

Inclusive Higgs boson production is predominantly ggF production where the Higgs momentum is balanced by soft gluons and quarks. The perturbative-QCD modeling of ggF production can be studied by measuring $p_{\mathrm{T}}^{\gamma\gamma}$ and $|y_{\gamma\gamma}|$. The rapidity of the diphoton system ($|y_{\gamma\gamma}|$) is also sensitive to the parton distribution functions of the colliding proton constituents. Jet kinematics and activity

such as the transverse momentum of the leading jet ($p_{\mathrm{T}}^{j_1}$), multiplicity($N_{\mathrm{jets}}^{\geq 30\ \mathrm{GeV}}$), mass ($m_{jj}$), and rapidity of the leading jet ($|y_{j_1}|$) can be sensitive to the Higgs production mechanism. For a Standard Model Higgs, events with zero or one jet is dominated by ggF production and the kinematics of the leading jet can probe the modeling of hard QCD processes. The VBF and VH production modes are more pronounced in two jet events and for events with higher jet multiplicity, the $t\bar{t}H$ production mode is dominant. The cosine of the angle between the beam axis and the photons in the Collins-Soper frame [145] of the Higgs boson, $|\cos\theta^*|$, is used to study the spin of the Higgs boson. For a scalar Higgs boson the $|\cos\theta^*|$ would show an edge around 0.6 due to the fiducial requirements on the diphoton system but for a spin-2 boson, an enhancement would be seen at values greater than 0.6.

Table 6.2: List of measured differential cross section variables. Here, p_{object} denotes the four-momentum of a given object. Subscripts T and z denote the transverse and z components of momentum respectively; y(object) and m(object) denote object's rapidity and mass.

Observable	Definition
$p_{\mathrm{T}}^{\gamma\gamma}$	$(p_{\gamma_1}+p_{\gamma_2})_{\mathrm{T}}$
$\lvert y_{\gamma\gamma}\rvert$	Absolute diphoton rapidity, $\lvert y(p_{\gamma_1}+p_{\gamma_2})\rvert$
$\lvert\cos\theta^*\rvert$	Higgs boson helicity angle in CS frame, $\frac{\lvert(E_{\gamma_1}+p_{z,\gamma_1})(E_{\gamma_2}-p_{z,\gamma_2})-(E_{\gamma_1}-p_{z,\gamma_1})(E_{\gamma_2}+p_{z,\gamma_2})\rvert}{m_{\gamma\gamma}\sqrt{m_{\gamma\gamma}^2+p_{\mathrm{T},\gamma\gamma}^2}}$
$p_{\mathrm{Tt}}^{\gamma\gamma}$	$(p_{x,\gamma_1}*p_{y,\gamma_2}-p_{x,\gamma_2}*p_{y,\gamma_1})/(p_{\gamma_1}-p_{\gamma_2})_{\mathrm{T}}^2$
$\lvert\Delta y_{\gamma\gamma}\rvert$	Rapidity separation of photons, $\lvert y_{\gamma_1}-y_{\gamma_2}\rvert$
$N_{\mathrm{jets}}^{\geq 30\ \mathrm{GeV}}$	Number of anti-k_t jets with $p_{\mathrm{T}} > 30$ GeV and radius parameter $R = 0.4$
$N_{\mathrm{jets}}^{\geq 50\ \mathrm{GeV}}$	Number of anti-k_t jets with $p_{\mathrm{T}} > 50$ GeV and radius parameter $R = 0.4$
$p_{\mathrm{T}}^{j_1}$	Leading jet p_{T}
$p_{\mathrm{T}}^{j_2}$	Sub-leading jet p_{T}
$\lvert y_{j_1}\rvert$	Absolute leading jet rapidity
$\lvert y_{j_2}\rvert$	Absolute subleading jet rapidity
$\mathrm{H_T}$	Scalar p_{T}sum of jets
m_{jj}	Invariant mass of leading and subleading jets system, $m(p_{j_1}+p_{j_2})$
$\lvert\Delta y_{jj}\rvert$	Rapidity separation of leading and subleading jet, $\lvert y_{j_1}-y_{j2}\rvert$
$\lvert\Delta\phi_{jj}\rvert$	Unsigned azimuthal angle difference between leading and subleading jet
$\Delta\phi_{jj,\mathrm{signed}}$	Signed $\lvert\Delta\phi_{jj}\rvert$
$\tau_{C,j1}$	Max value of $\tau_i = \frac{m_{\mathrm{T}}}{2\cosh y^*}, y^* = y_{j_i} - y_{\gamma\gamma}, m_{\mathrm{T}} = \sqrt{p_{\mathrm{T},j_i}^2 + m_{j_i}^2}$
$\sum\tau_{C,j}$	Scalar sum of τ for all jets with $\tau > 8$ GeV
$p_{\mathrm{T},\gamma\gamma jj}$	H + dijet p_{T}, $(p_{\gamma_1}+p_{\gamma_2}+p_{j_1}+p_{j_2})_{\mathrm{T}}$
$\lvert\Delta\phi_{\gamma\gamma,jj}\rvert$	Absolute phi separation of diphoton and dijet systems

In addition to the variables in Table 6.2, double-differential cross section as a function of $p_{\mathrm{T}}^{\gamma\gamma}$ and N_{jets}, and $p_{\mathrm{T}}^{\gamma\gamma}$ and $|\cos\theta^*|$ are measured. These double differential variables are very sensitive to BSM physics and are used primarily to set limits on EFT 6-D operators.

The following discussion of the $H \to \gamma\gamma$ analysis will focus on the fiducial regions and the $p_{\mathrm{T}}^{\gamma\gamma}$, $|y_{\gamma\gamma}|$, and $N_{\mathrm{jets}}^{\geq 30\ \mathrm{GeV}}$ differential variables. All plots for the other variables are available in Appendix C.

6.2 Dataset and Simulation

6.2.1 Dataset

The majority of analysis is performed with the 2015–2016 dataset, though a small conference note was issued with updated differential distributions for $p_{\mathrm{T}}^{\gamma\gamma}$, $N_{\mathrm{jets}}^{\geq 30\ \mathrm{GeV}}$, $|\Delta y_{\gamma\gamma}|$, $p_{\mathrm{T}}^{j_1}$ including the 2017 dataset. Discussion regarding the pileup and luminosity delivered of the dataset can be seen in Section 3.1. The 2015–2016 dataset contains $36.1\,\mathrm{fb}^{-1}$ and the 2015–2017 dataset is about double the luminosity at $79.8\,\mathrm{fb}^{-1}$.

Events are collected with the `HLT_g35_loose_g25_loose` trigger in 2015–2016 and the `HLT_g35_medium_g25_medium_L12EM20VH` trigger in 2017. These triggers select events with two photons, requiring the transverse energy of the highest (second highest) E_{T} photon to be above 35(25) GeV. The deposited electromagnetic calorimeter energy of each object is required to be loosely (or in 2017, slight stronger) consistent with that of the shower originating from a photon.

6.2.2 Simulated Samples

Signal samples were generated for the Higgs boson production mechanisms using various Monte Carlo event generators as described in this section. The mass and width of the Higgs boson were set in the simulation to $m_H = 125\,\mathrm{GeV}$ and $\Gamma_H = 4.07\,\mathrm{MeV}$ [146]. The samples are normalized with the latest available theoretical SM production cross section calculations as summarized in the Yellow Report 4 [32] from the LHC Higgs cross section working group. The $H \to \gamma\gamma$ branching ratio is calculated to be 0.227% with HDECAY [147, 148] and PROPHECY4F [149–151]. The following summarizes the simulation of different production modes:

- Higgs boson production via ggF is simulated at NNLO in QCD using the Powheg NNLOPS program [152], with the PDF4LHC15 PDF set [153]. The simulation achieves NNLO accuracy for inclusive $gg \to H$ observables by reweighting the Higgs boson rapidity spectrum in Hj-MiNLO [154] to that of HNNLO [155]. The parton-level events produced by the Powheg NNLOPS program are sent to Pythia8 [156–158] with the AZNLO parameter set tuned to data [159] in order to provide parton showering, hadronization and underlying event simulation.

The sample is then normalized to the total cross section predicted by a N^{3}LO QCD calculation with NLO electroweak corrections [160–163].

- Higgs boson production via VBF is generated at NLO accuracy in QCD using Powheg-Box [164–167] with the PDF4LHC15 PDF set. The parton-level events are passed to Pythia8 tuned with the AZNLO parameter set to provide parton showering, hadronization and the underlying event simulation. The VBF sample is normalized with an approximate NNLO QCD cross section with NLO electroweak corrections applied [168–170].

- Higgs boson production via VH is generated at NLO accuracy in QCD through qq/qg-initiated production, denoted as $q\bar{q}' \to VH$, and through $gg \to ZH$ production using Powheg-Box [171] with the PDF4LHC15 PDF set and the AZNLO parameter set. Pythia8 is used for parton showering, hadronization and the underlying event. The samples are normalized with calculations at NNLO in QCD and NLO electroweak corrections for $q\bar{q}' \to VH$ and at NLO and next-to-leading logarithmic (NLL) accuracy in QCD for $gg \to ZH$ [172–174].

- Higgs boson production via $t\bar{t}H$ is generated at NLO in QCD using MadGraph5_aMC@NLO [175] with the NNPDF3.0 PDF set [176] and sent to Pythia8 to provide parton showering, hadronization and the underlying event, using the A14 parameter set [177]. The $t\bar{t}H$ sample is normalized with a calculation at NLO in QCD with NLO electroweak corrections [178–181].

- Higgs boson production via $b\bar{b}H$ is simulated using MadGraph5_aMC@NLO interfaced to Pythia8 with the CT10 PDF set [182], and is normalized with the cross section calculation obtained by matching, using the *Santander* scheme, the five-flavor scheme cross section accurate to NNLO in QCD with the four-flavor scheme cross section accurate to NLO in QCD [183–185]. The sample includes the effect of interference with the gluon–gluon fusion production mechanism.

- Associated production of a Higgs boson with a single top-quark and a W-boson (tHW) is generated at NLO accuracy, removing the overlap with the $t\bar{t}H$ sample through a diagram regularization technique, using MadGraph5_aMC@NLO interfaced to Herwig++ [186–188], with the Herwig++ UEEE5 parameter set for the underlying event and the CT10 PDF set using the five-flavor scheme. Simulated Higgs boson events in association with a single top-quark, a b-quark and a light quark (tHq) are produced at leading order (LO) accuracy in QCD using MadGraph5_aMC@NLO interfaced to Pythia8 with the CT10 PDF set

Table 6.3: Summary of the event generators, PDF sets, σ_h, and order of calculation used to model the signal and the diphoton background processes.

Process	Generator	Showering	PDF set	σ [pb]	Order of calculation of σ
ggF	Powheg NNLOPS	Pythia8	PDF4LHC15	48.52	N^{3}LO(QCD)+NLO(EWK)
VBF	Powheg-Box	Pythia8	PDF4LHC15	3.78	NNLO(QCD)+NLO(EWK)
WH	Powheg-Box	Pythia8	PDF4LHC15	1.37	NNLO(QCD)+NLO(EWK)
$q\bar{q}' \to ZH$	Powheg-Box	Pythia8	PDF4LHC15	0.76	NNLO(QCD)+NLO(EWK)
$gg \to ZH$	Powheg-Box	Pythia8	PDF4LHC15	0.12	NLO+NLL(QCD)
$t\bar{t}H$	MadGraph5_aMC@NLO	Pythia8	NNPDF3.0	0.51	NLO(QCD)+NLO(EWK)
$b\bar{b}H$	MadGraph5_aMC@NLO	Pythia8	CT10	0.49	5FS(NNLO)+4FS(NLO)
t-channel tH	MadGraph5_aMC@NLO	Pythia8	CT10	0.07	4FS(LO)
W-associated tH	MadGraph5_aMC@NLO	Herwig++	CT10	0.02	5FS(NLO)
$\gamma\gamma$	Sherpa	Sherpa	CT10		
$V\gamma\gamma$	Sherpa	Sherpa	CT10		

within the four-flavor scheme and using the A14 parameter set. The tHW and tHq samples are normalized with calculations accurate to NLO in QCD [189].

Some descriptions of signal production are taken from [6]. After generation, the events are processed through a Geant4 [190] simulation of the ATLAS detector [191].

The continuum $\gamma\gamma$ and $V\gamma\gamma$ background spectrum are simulated using the Sherpa event generator [192], with the CT10 PDF set and the default parameter set for the underlying-event. The corresponding matrix elements for $\gamma\gamma$ are calculated at leading order in QCD with the real emission of up to three partons. The $V\gamma\gamma$ matrix elements are calculated at LO in QCD as well, though only up to the emission of two partons. The samples are merged with the Sherpa parton shower [193] using the Meps@lo prescription [194]. The $V\gamma\gamma$ simulation, like the signal samples, undergoes the full detector simulation. The $\gamma\gamma$ samples are processed through a fast detector simulation, referred to as ATLAS Fast Simulation II (AFII), based on a parameterization of the performance of the calorimeters [195].

Pileup is included in the simulation for all generated events such that the $\langle\mu\rangle$ reproduces that observed in the data. The inelastic pp collisions were produced using Pythia8 with the MSTW2008lo PDF set [196] and A2 parameter set [197].

6.3 Signal Modeling

The $m_{\gamma\gamma}$ distribution for the $H \to \gamma\gamma$ process is resonant. Assuming no interference with $pp \to \gamma\gamma$ the Standard Model line shape is expected to follow a Breit-Wigner curve which peaks at the Higgs mass and has a width of 4 MeV. Due to the finite resolution of the detector, the measured photon

energy is smeared leading to non-Gaussian contributions to the m_H spectrum. The biggest non-detector inherent contributor of this energy smearing comes from converted photons $\gamma \to e^+e^-$ when one of the electrons loses a large portion of its energy in the Inner Detector. In order to account for finite resolution of the detector, the distribution is modeled by a double-sided Crystal Ball function [198]. This function consists of a Gaussian core with power law tails. The Gaussian is parameterized by a mean $m_H + \Delta\mu_{\mathrm{CB}}$ and the width σ_{CB}. The measured value of $m_H = 125.09 \pm 0.24$ GeV by the Run 1 combination of ATLAS and CMS data is used as mean of the Gaussian and is allowed to shift. The uncertainty of the measured Higgs mass is an additional nuisance parameter used in the signal extraction fit, described in Section 6.5.

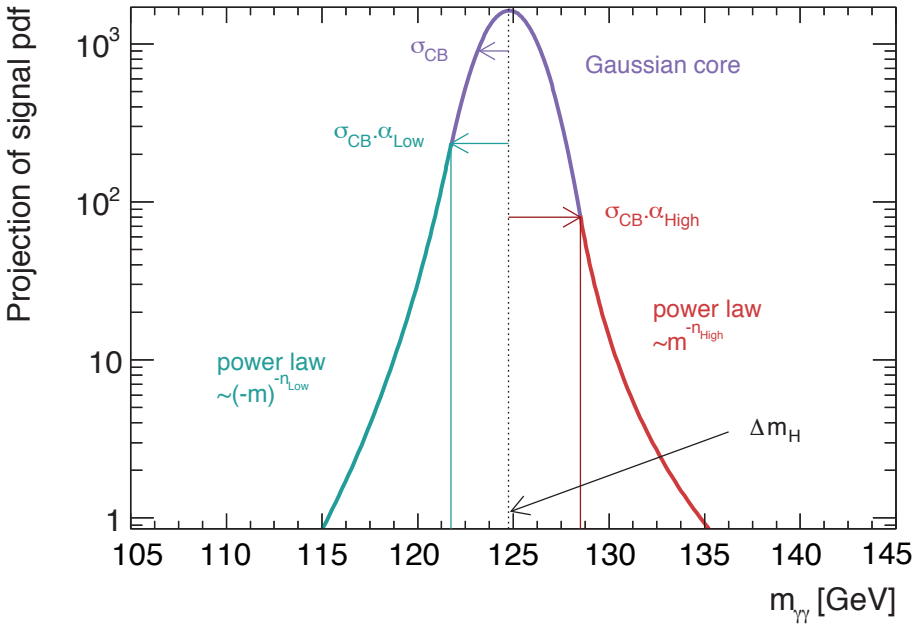

Figure 6.2: A visualization of the double-sided Crystal Ball function.

The power law tails are controlled by the parameters which tune the transition from the Gaussian core to power law tails $\alpha_{\mathrm{CB}}^{(h,l)}$ and the exponents $n_{\mathrm{CB}}^{(h,l)}$ of the power function. These are handled separately for the low (l) and high mass (h) tails. A illustration of the double-sided Crystal Ball function can be see in Figure 6.2. The double-sided Crystal Ball function, $CB^{\mathrm{sig}}(m_{\gamma\gamma}; \Delta\mu_{\mathrm{CB}}, \sigma_{\mathrm{CB}}, \alpha_{\mathrm{CB}}^{(h,l)}, n_{\mathrm{CB}}^{(h,l)})$ is defined as

$$\mathcal{N}_c \begin{cases} e^{-t^2/2} & -\alpha^l_{\rm CB} \leq t \leq \alpha^h_{\rm CB} \\ \left(\frac{n^l_{\rm CB}}{|\alpha^l_{\rm CB}|}\right)^{n^l_{\rm CB}} e^{-|\alpha^l_{\rm CB}|^2/2} \left(\frac{n^l_{\rm CB}}{\alpha^l_{\rm CB}} - \alpha^l_{\rm CB} - t\right)^{-n^l_{\rm CB}} & t < -\alpha^l_{\rm CB} \\ \left(\frac{n^h_{\rm CB}}{|\alpha^h_{\rm CB}|}\right)^{n^h_{\rm CB}} e^{-|\alpha^h_{\rm CB}|^2/2} \left(\frac{n^h_{\rm CB}}{\alpha^h_{\rm CB}} - \alpha^h_{\rm CB} - t\right)^{-n^h_{\rm CB}} & t > \alpha^h_{\rm CB} \ ; \end{cases}$$

where $t = (m_{\gamma\gamma} - m_H - \Delta\mu_{\rm CB})/\sigma_{\rm CB}$, and $\mathcal{N}_c$ is a normalization factor. Each of these parameters, for all fiducial regions and differential bins, are determined by performing a signal PDF only fit to the simulated $m_H = 125$ $H \to \gamma\gamma$ process. This signal-only model, which is then fitted, is built by summing all the Higgs production modes described in Section 6.2.2.

6.4 Background Modeling

The following section examines the process used to model the background in each fiducial region and differential bin in the analysis. The modeling of the background must be as precise as possible in order to correctly extract the number of events coming from the Higgs. The main backgrounds of the $m_{\gamma\gamma}$ spectrum arise from non-resonant sources of $\gamma\gamma$, γj (γ-jet), jγ (jet-γ), and jj (jet-jet) production. In order to characterize this combination of backgrounds an analytic function is fit to the diphoton invariant mass spectrum in the mass range of $105 < m_{\gamma\gamma} < 160$ GeV. The background function is chosen by building a template of the $m_{\gamma\gamma}$ spectrum from the various sources and then testing different analytic functions to model it, choosing the one with the lowest number of parameters that minimizes any bias.

6.4.1 Background Decomposition

To determine the background composition, a method known as the 2x2D sideband method [199,200] is used. This method exploits the isolation and identification profile of the two photons in the event and is reliant on the correlation between the isolation and identification to be small. Each photon is identified as a *Tight* or "pseudo" photon, as described in Section 5.1.3, and is classified as non-isolated or isolated using the `FixedCutLoose` definition outlined in Section 5.1.4. The photon definition for the $H \to \gamma\gamma$ cross section search requires both photons to be *Tight* and isolated. Regions for the γj, jγ, and jj backgrounds can be created by reversing the ID and/or isolation requirements of the photon candidate.

One can write down the breakdown of the *Tight* + pseudo photon sample (no isolation requirement) as:

$$\mathrm{N_{total}} = \mathrm{Y}_{\gamma\gamma} + \mathrm{Y}_{\gamma j} + \mathrm{Y}_{j\gamma} + \mathrm{Y}_{jj} \ ; \tag{6.4}$$

where $\mathrm{N_{total}}$ is the total number of photons, and $\mathrm{Y_{process}}$ is the yield for a particular process.

The goal is to extract the yields of the distinct diphoton categories as broken down by process. This includes not only the yield of the two *Tight* and isolated photons, but also that of all the different combinations. The number of events in each category can be related to the sample of *Tight* + pseudo photons by efficiencies, jet-to-photon mis-identification rates, and correlation factors. Using simulation, photon identification efficiencies for both the leading and subleading photons (ϵ_1 and ϵ_2) and photon isolation efficiencies for both the leading and subleading photons (ξ_1 and ξ_2) are determined. The correlation between the identification and the isolation mis-identification rates for the leading and subleading jets (ρ_1 and ρ_2) are measured in data. For the inclusive fiducial region, Figure 6.3 shows the measurement of the efficiencies for both identification and isolation.

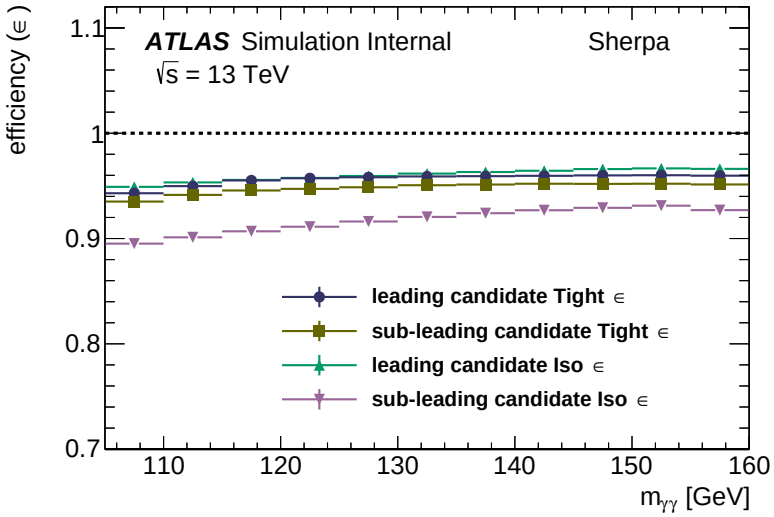

Figure 6.3: Photon identification and isolation efficiencies for both the leading and subleading photon candidates in the inclusive fiducial region.

Since the leading photon can be be in one of four categories in the 2D isolation-ID plane, the combination of leading and subleading photons produces 16 distinct categories. One can write down a system of linear equations and solve them for each region, deriving the yields of all the regions.

For instance the term for the category for both photons to be *Tight* and isolated is given by:

$$N_{AA} = Y_{\gamma\gamma}\epsilon_1\xi_1\epsilon_2\xi_2 + Y_{\gamma j}\epsilon_1\xi_1 f_2 g_2\rho_2 + Y_{j\gamma} f_1 g_1\epsilon_2\xi_2\rho_1 + Y_{jj} f_1 g_1 f_2 g_2\rho_1\rho_2\rho_{jj} \ . \quad (6.5)$$

The equations for all 16 regions can been seen in Refs. [199, 200]. The purity of isolated and *Tight* photon pairs are assessed by extrapolating the backgrounds from the other non-*Tight* or non-isolated regions to the region of interest. The method relies on the negligible correlation between these two variables for the jet background and that the sidebands (the regions where either the photon identification or isolation is looser) are essentially populated by jets. The small amount of *Tight*, isolated photons in the other regions is estimated using the Monte Carlo. The extracted yields and purities can be see in Figure 6.4. Figure 6.4a shows the raw yield in the inclusive region of $\gamma\gamma$, γj/jγ, and jj events. The remaining subfigures show the percentage of each background calculated by the 2x2D sideband method, in the inclusive region as a function of $m_{\gamma\gamma}$ and of the $p_{\mathrm{T}}^{\gamma\gamma}$ and $N_{\mathrm{jets}}^{\geq 30\ \mathrm{GeV}}$ differential variables. Table 6.4 contains these numbers for the fiducial regions and $p_{\mathrm{T}}^{\gamma\gamma}$, $N_{\mathrm{jets}}^{\geq 30\ \mathrm{GeV}}$, and $|y_{\gamma\gamma}|$ variables.

6.4.2 Building the Template

Using the yields and purities derived in Section 6.4.1, the background template can now be built. Because of the abundance of γj, jγ, and dijet events produced in ATLAS and rejection power of the photon ID, it is not possible to generate Monte Carlo of these processes with sufficient statistics. The $\gamma\gamma$ MC, for which high statistics are available, is reweighted using the results of the background decomposition in order to build a template with the $\gamma\gamma$ main background and smaller jet-to-photon fake components.

Figure 6.5a shows the $\gamma\gamma$ MC in black, and the normalized (scaled so the yields match to that of the $\gamma\gamma$ MC) data-driven components of the $\gamma\gamma$, γj/jγ, and jj shapes from the 2x2D sideband method. The construction of each background component is accomplished by reweighting the $\gamma\gamma$ MC by a fitted first order polynomial of the ratio of each data component to the $\gamma\gamma$ MC. This is to account for any shape difference of the components, and then the shape is normalized to the yield given by the 2x2D sideband method. The simulation tends to model the shape of the $\gamma\gamma$ component well, and does worse with the γj/γj and jj shapes. Once the components have been reweighted and normalized, one can simply add them together to obtain a template of the background for the given bin or fiducial region. Figure 6.5b shows the components of the different backgrounds and the data sidebands with the $120 < m_{\gamma\gamma} < 130$ window blinded. A background only fit of the data sidebands,

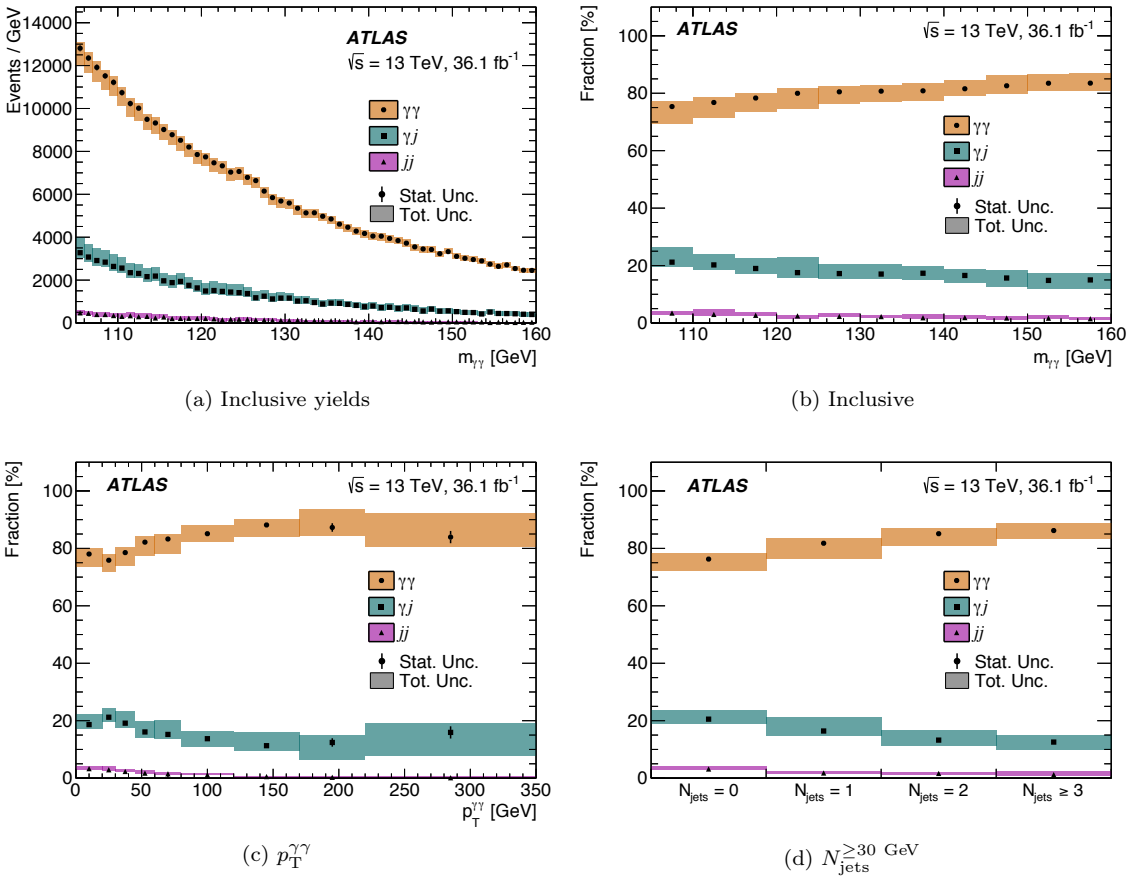

(a) Inclusive yields

(b) Inclusive

(c) $p_{\mathrm{T}}^{\gamma\gamma}$

(d) $N_{\mathrm{jets}}^{\geq 30\ \mathrm{GeV}}$

Figure 6.4: (a)Yields, and fractional composition of the $m_{\gamma\gamma}$ spectrum background components in the (b) inclusive fiducial region, as a function of (c) $p_{\mathrm{T}}^{\gamma\gamma}$, and (d) $N_{\mathrm{jets}}^{\geq 30\ \mathrm{GeV}}$ as determined by the 2x2D sideband method.

a fit of the template (not shown), and comparisons between the fit, template, and data can be see in the different χ^2 values and ratios shown. The process of choosing the function and various tests done with the constructed template will be discussed in the following sections.

This construction works for all differential bins and for the inclusive and VBF fiducial regions. For fiducial regions where Higgs bosons are produced in association with vector bosons, the $N_{\mathrm{lepton}} \geq 1$ and high $E_{\mathrm{T}}^{\mathrm{miss}}$ regions, additional $V\gamma\gamma$ samples are used in tandem with the $\gamma\gamma$ samples. The fraction of each component set initially by the relative Standard Model cross sections, and then the template is then normalized to the data sidebands. The $t\bar{t}H$-enhanced template is built via a data-driven approach in which the b-tagged requirements are removed and the photon is required to fail the identification or isolation criteria. This template is then normalized to the nominal

Table 6.4: 2x2D sideband yields and purities for the fiducial regions, $p_{\mathrm{T}}^{\gamma\gamma}$, $|y_{\gamma\gamma}|$, and $N_{\mathrm{jets}}^{\geq 30\ \mathrm{GeV}}$.

	Yield ± stat. ± syst.			Fraction ± stat. ± syst. [%]		
	$\gamma\gamma$	γ-jet	jet-jet	$\gamma\gamma$	γ-jet	jet-jet
Inclusive	$261469 \pm 718\ ^{+1254}_{-15117}$	$62307 \pm 448\ ^{+11538}_{-341}$	$8633 \pm 103\ ^{+3134}_{-604}$	$78.7 \pm 0.2\ ^{+0.3}_{-4.4}$	$18.7 \pm 0.2\ ^{+3.5}_{-0.1}$	$2.6 \pm 0.0\ ^{+0.9}_{-0.2}$
$\boldsymbol{N_{lep}}$						
0	$262559 \pm 720\ ^{+2625}_{-11845}$	$60822 \pm 453\ ^{+8735}_{-2316}$	$8427 \pm 104\ ^{+2668}_{-799}$	$79.1 \pm 0.2\ ^{+0.9}_{-3.5}$	$18.3 \pm 0.2\ ^{+2.7}_{-0.7}$	$2.5 \pm 0.0\ ^{+0.8}_{-0.2}$
≥ 1	$517 \pm 31\ ^{+0}_{-137}$	$72 \pm 19\ ^{+130}_{-0}$	$4 \pm 4\ ^{+8}_{-5}$	$87.2 \pm 3.5\ ^{+0.0}_{-23.1}$	$12.1 \pm 3.5\ ^{+22.0}_{-0.0}$	$0.7 \pm 0.7\ ^{+1.4}_{-0.8}$
VBF enriched						
underflow	$259781 \pm 711\ ^{+2450}_{-11974}$	$60214 \pm 451\ ^{+8996}_{-2077}$	$8351 \pm 104\ ^{+2525}_{-854}$	$79.1 \pm 0.2\ ^{+0.9}_{-3.5}$	$18.3 \pm 0.2\ ^{+2.8}_{-0.6}$	$2.5 \pm 0.0\ ^{+0.8}_{-0.3}$
VBF enriched	$3309 \pm 78\ ^{+72}_{-50}$	$669 \pm 45\ ^{+43}_{-78}$	$87 \pm 10\ ^{+61}_{-16}$	$81.4 \pm 1.3\ ^{+1.8}_{-1.3}$	$16.5 \pm 1.2\ ^{+1.0}_{-1.9}$	$2.1 \pm 0.3\ ^{+1.5}_{-0.4}$
$\boldsymbol{t\bar{t}H}$ **enriched**						
underflow	$262360 \pm 716\ ^{+2575}_{-11898}$	$60819 \pm 454\ ^{+8778}_{-2268}$	$8423 \pm 104\ ^{+2681}_{-795}$	$79.1 \pm 0.2\ ^{+0.9}_{-3.5}$	$18.3 \pm 0.2\ ^{+2.7}_{-0.7}$	$2.5 \pm 0.0\ ^{+0.8}_{-0.2}$
$t\bar{t}H$ enriched	$725 \pm 33\ ^{+6}_{-31}$	$69 \pm 16\ ^{+34}_{-2}$	$10 \pm 2\ ^{+0}_{-11}$	$90.1 \pm 2.2\ ^{+1.0}_{-3.4}$	$8.6 \pm 2.1\ ^{+4.3}_{-0.2}$	$1.3 \pm 0.3\ ^{+0.0}_{-1.4}$
High $\boldsymbol{E_{\mathrm{T}}^{\mathrm{miss}}}$						
underflow	$262661 \pm 723\ ^{+2529}_{-11986}$	$60731 \pm 454\ ^{+8850}_{-2237}$	$8416 \pm 104\ ^{+2689}_{-782}$	$79.2 \pm 0.2\ ^{+0.9}_{-3.5}$	$18.3 \pm 0.2\ ^{+2.7}_{-0.6}$	$2.5 \pm 0.0\ ^{+0.8}_{-0.2}$
High $E_{\mathrm{T}}^{\mathrm{miss}}$	$439 \pm 31\ ^{+50}_{-30}$	$143 \pm 19\ ^{+28}_{-29}$	$17 \pm 3\ ^{+2}_{-21}$	$73.2 \pm 3.7\ ^{+8.3}_{-5.0}$	$23.9 \pm 3.6\ ^{+4.7}_{-4.9}$	$2.8 \pm 0.7\ ^{+0.4}_{-3.5}$
$\boldsymbol{p_T^{\gamma\gamma}[GeV]}$						
0 - 20	$102780 \pm 456\ ^{+845}_{-5062}$	$24564 \pm 281\ ^{+3897}_{-584}$	$4370 \pm 51\ ^{+967}_{-572}$	$78.0 \pm 0.2\ ^{+0.8}_{-3.7}$	$18.6 \pm 0.2\ ^{+3.0}_{-0.4}$	$3.3 \pm 0.1\ ^{+0.7}_{-0.4}$
20 - 30	$43835 \pm 305\ ^{+524}_{-1901}$	$12256 \pm 200\ ^{+1148}_{-475}$	$1687 \pm 47\ ^{+646}_{-147}$	$75.9 \pm 0.4\ ^{+1.0}_{-3.2}$	$21.2 \pm 0.4\ ^{+2.0}_{-0.8}$	$2.9 \pm 0.1\ ^{+1.1}_{-0.3}$
30 - 45	$43886 \pm 296\ ^{+407}_{-2272}$	$10699 \pm 184\ ^{+1835}_{-425}$	$1301 \pm 41\ ^{+323}_{-81}$	$78.5 \pm 0.4\ ^{+0.9}_{-3.9}$	$19.1 \pm 0.4\ ^{+3.3}_{-0.7}$	$2.3 \pm 0.1\ ^{+0.6}_{-0.1}$
45 - 60	$27309 \pm 223\ ^{+220}_{-1420}$	$5346 \pm 129\ ^{+1016}_{-336}$	$582 \pm 27\ ^{+308}_{-28}$	$82.2 \pm 0.4\ ^{+0.9}_{-4.0}$	$16.1 \pm 0.4\ ^{+3.1}_{-1.0}$	$1.8 \pm 0.1\ ^{+0.9}_{-0.1}$
60 - 80	$21201 \pm 186\ ^{+66}_{-1167}$	$3876 \pm 109\ ^{+1057}_{-0}$	$387 \pm 22\ ^{+56}_{-98}$	$83.3 \pm 0.5\ ^{+0.3}_{-4.4}$	$15.2 \pm 0.5\ ^{+4.2}_{-0.0}$	$1.5 \pm 0.1\ ^{+0.2}_{-0.4}$
80 - 120	$16718 \pm 163\ ^{+387}_{-255}$	$2698 \pm 90\ ^{+131}_{-468}$	$227 \pm 17\ ^{+81}_{-13}$	$85.1 \pm 0.5\ ^{+2.2}_{-1.1}$	$13.7 \pm 0.5\ ^{+0.7}_{-2.4}$	$1.2 \pm 0.1\ ^{+0.4}_{-0.1}$
120 - 170	$5390 \pm 91\ ^{+0}_{-216}$	$691 \pm 43\ ^{+234}_{-0}$	$34 \pm 7\ ^{+5}_{-44}$	$88.1 \pm 0.8\ ^{+0.0}_{-3.3}$	$11.3 \pm 0.8\ ^{+3.9}_{-0.0}$	$0.6 \pm 0.1\ ^{+0.1}_{-0.7}$
170 - 220	$1466 \pm 47\ ^{+95}_{-2}$	$209 \pm 22\ ^{+3}_{-94}$	$5 \pm 3\ ^{+4}_{-7}$	$87.3 \pm 1.5\ ^{+6.0}_{-0.4}$	$12.4 \pm 1.5\ ^{+0.2}_{-5.6}$	$0.3 \pm 0.2\ ^{+0.3}_{-0.4}$
220 - 350	$747 \pm 34\ ^{+71}_{-0}$	$142 \pm 16\ ^{+0}_{-68}$	$1 \pm 2\ ^{+2}_{-2}$	$83.9 \pm 2.1\ ^{+7.8}_{-0.0}$	$15.9 \pm 2.1\ ^{+0.0}_{-7.7}$	$0.1 \pm 0.2\ ^{+0.2}_{-0.2}$
$\boldsymbol{|y_{\gamma\gamma}|}$						
0.0 - 0.1	$26026 \pm 228\ ^{+1244}_{-368}$	$6226 \pm 142\ ^{+182}_{-981}$	$979 \pm 33\ ^{+190}_{-262}$	$78.3 \pm 0.5\ ^{+3.7}_{-1.1}$	$18.7 \pm 0.5\ ^{+0.5}_{-3.0}$	$2.9 \pm 0.1\ ^{+0.6}_{-0.8}$
0.1 - 0.3	$25277 \pm 227\ ^{+1810}_{-0}$	$6308 \pm 143\ ^{+0}_{-1595}$	$912 \pm 33\ ^{+116}_{-214}$	$77.8 \pm 0.5\ ^{+5.5}_{-0.0}$	$19.4 \pm 0.5\ ^{+0.0}_{-4.9}$	$2.8 \pm 0.1\ ^{+0.4}_{-0.7}$
0.3 - 0.5	$24543 \pm 222\ ^{+1480}_{-81}$	$5720 \pm 141\ ^{+411}_{-948}$	$868 \pm 33\ ^{+0}_{-585}$	$78.8 \pm 0.5\ ^{+4.8}_{-0.3}$	$18.4 \pm 0.5\ ^{+1.3}_{-3.0}$	$2.8 \pm 0.1\ ^{+0.0}_{-1.9}$
0.5 - 0.6	$22852 \pm 212\ ^{+1309}_{-75}$	$5198 \pm 132\ ^{+65}_{-1012}$	$653 \pm 30\ ^{+66}_{-305}$	$79.6 \pm 0.5\ ^{+4.6}_{-0.4}$	$18.1 \pm 0.5\ ^{+0.2}_{-3.5}$	$2.3 \pm 0.1\ ^{+0.2}_{-1.1}$
0.6 - 0.8	$21818 \pm 206\ ^{+1083}_{-391}$	$4822 \pm 127\ ^{+322}_{-918}$	$727 \pm 30\ ^{+87}_{-213}$	$79.7 \pm 0.5\ ^{+4.1}_{-1.3}$	$17.6 \pm 0.5\ ^{+1.2}_{-3.3}$	$2.7 \pm 0.1\ ^{+0.3}_{-0.8}$
0.8 - 0.9	$21080 \pm 204\ ^{+284}_{-992}$	$4913 \pm 127\ ^{+893}_{-170}$	$724 \pm 30\ ^{+63}_{-166}$	$78.9 \pm 0.5\ ^{+1.2}_{-3.6}$	$18.4 \pm 0.5\ ^{+3.4}_{-0.6}$	$2.7 \pm 0.1\ ^{+0.2}_{-0.9}$
0.9 - 1.2	$40899 \pm 282\ ^{+0}_{-2167}$	$9107 \pm 174\ ^{+1100}_{-0}$	$1442 \pm 41\ ^{+1004}_{-258}$	$79.5 \pm 0.4\ ^{+0.0}_{-4.0}$	$17.7 \pm 0.4\ ^{+2.2}_{-0.0}$	$2.8 \pm 0.1\ ^{+2.0}_{-0.5}$
1.2 - 1.6	$46077 \pm 304\ ^{+0}_{-3677}$	$10791 \pm 193\ ^{+2497}_{-0}$	$1536 \pm 45\ ^{+1078}_{-326}$	$78.9 \pm 0.4\ ^{+0.0}_{-6.1}$	$18.5 \pm 0.4\ ^{+4.3}_{-0.0}$	$2.6 \pm 0.1\ ^{+1.9}_{-0.6}$
1.6 - 2.4	$34479 \pm 260\ ^{+717}_{-4690}$	$7867 \pm 157\ ^{+3993}_{-653}$	$526 \pm 30\ ^{+622}_{-42}$	$80.4 \pm 0.4\ ^{+1.6}_{-10.8}$	$18.3 \pm 0.4\ ^{+9.4}_{-1.5}$	$1.2 \pm 0.1\ ^{+1.5}_{-0.1}$
$\boldsymbol{N_{jets}\ [p_T^{jet} > 30\ GeV]}$						
$N_{jets} = 0$	$147124 \pm 554\ ^{+2427}_{-6289}$	$39621 \pm 345\ ^{+4397}_{-2130}$	$6157 \pm 60\ ^{+1633}_{-581}$	$76.3 \pm 0.2\ ^{+1.3}_{-3.2}$	$20.5 \pm 0.2\ ^{+2.3}_{-1.1}$	$3.2 \pm 0.0\ ^{+0.9}_{-0.3}$
$N_{jets} = 1$	$72676 \pm 367\ ^{+513}_{-4320}$	$14587 \pm 216\ ^{+3645}_{-339}$	$1601 \pm 46\ ^{+488}_{-312}$	$81.8 \pm 0.3\ ^{+0.4}_{-4.7}$	$16.4 \pm 0.3\ ^{+4.1}_{-0.4}$	$1.8 \pm 0.1\ ^{+0.6}_{-0.3}$
$N_{jets} = 2$	$29210 \pm 224\ ^{+205}_{-1074}$	$4545 \pm 124\ ^{+880}_{-276}$	$565 \pm 27\ ^{+160}_{-110}$	$85.1 \pm 0.4\ ^{+0.7}_{-3.0}$	$13.2 \pm 0.4\ ^{+2.6}_{-0.8}$	$1.6 \pm 0.1\ ^{+0.5}_{-0.3}$
$N_{jets} \geq 3$	$14112 \pm 150\ ^{+238}_{-293}$	$2056 \pm 81\ ^{+68}_{-347}$	$202 \pm 16\ ^{+213}_{-28}$	$86.2 \pm 0.6\ ^{+1.6}_{-1.7}$	$12.6 \pm 0.5\ ^{+0.4}_{-2.1}$	$1.2 \pm 0.1\ ^{+1.3}_{-0.2}$

$t\bar{t}H$-enhanced data sidebands.

6.4.3 Spurious Signal

Once the background template is built, a method is developed to measure any "spurious signal", i.e. bias in the extracted signal yield due to the different background functions. The template is a prediction of the pure background component so the spurious signal, defined by the signal extracted from signal + background fit of the template, should be zero. The total spurious signal is evaluated for a range of assumed $m_{\gamma\gamma}$ masses from 121 to 129 GeV, in 0.5 GeV steps. The signal yield extracted (N_{spur}) and the 1σ statistical error (Δ_{spur}) are then used to rank the different background functions. The following are requirements for functions passing the spurious signal test in a bin/region:

- $\mathrm{N}_{spur} \pm 2\Delta_{spur}$ is less than 10% of the expected number of signal events (S_{ref}) **OR**

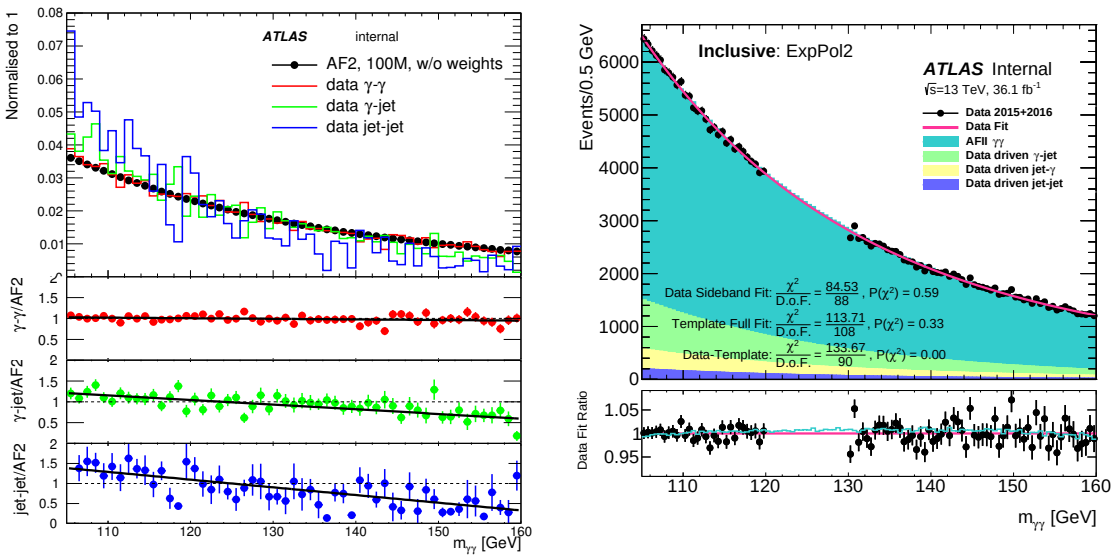

(a) Different components of $m_{\gamma\gamma}$ spectrum extracted from data

(b) Built template with reweighted $\gamma\gamma$ Monte Carlo

Figure 6.5: (a) Inclusive $m_{\gamma\gamma}$ spectrum with the fast simulation $\gamma\gamma$ MC (AFII, black) shape compared with the normalized (scaled so yield matches that of the $\gamma\gamma$ MC) data-driven $\gamma\gamma$, γj/jγ, and jj components and linear fits in of the ratios. These linear fits are then used to reweight the $\gamma\gamma$ MC to form the different γj/jγ/jj components of the full template. (b) Full template of the inclusive $m_{\gamma\gamma}$ spectrum built by reweighting the shapes of the fast simulation $\gamma\gamma$ MC by the ratios extracted in (a). The fitted data sidebands with ExpPol2 function is also shown as well as the χ^2 values between fits, template, and data.

- $N_{spur} \pm 2\Delta_{spur}$ is less than 20% of the background statistical uncertainty (δS)

In previous iterations of the analysis it was sufficient to look at only the value of N_{spur}, without the $\pm 2\Delta_{spur}$ for the function selection criteria. Recently, because of the increased data statistics, there are not enough computing resources to simulate even the AFII $\gamma\gamma$ sample. This results in statistical fluctuations when scaling the Monte Carlo to the data yield which can then manifest itself as an extracted signal during the test. If more Monte Carlo could be generated then some functions that currently fail due to these fluctuations would pass the test, so in order to account for this, the $\pm 2\Delta_{spur}$ leeway was added to the spurious signal criteria. This requirement avoids situations when the tests reject functions in regions it has limited statistical power. A cartoon of this requirement can be see in Figure 6.6. The figure shows the new spurious signal value ζ determined by the edge of the $\pm 2\Delta_{spur}$ statistical band closest to zero, or zero if the 2σ band is consistent with no signal.

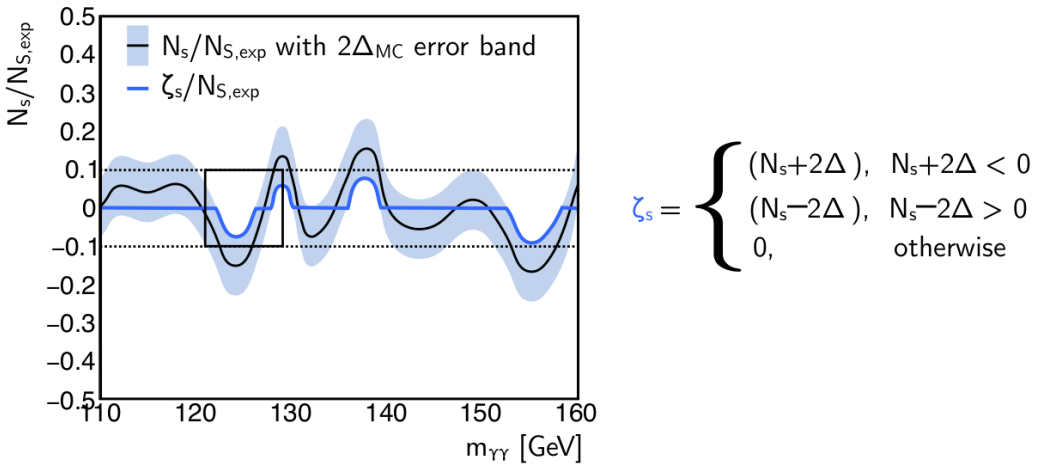

Figure 6.6: Cartoon illustrating the relaxed spurious signal method. ζ is defined as the edge of the 2σ band of N_{spur} closest to zero or zero if $N_{spur} \pm 2\Delta_{spur}$ is consistent with zero.

Additionally, there was a χ^2 goodness-of-fit condition, requiring the probability to be greater than 1%. This was instituted because some functions could have small spurious signal biases in the $121 < m_{\gamma\gamma} < 129$ GeV region, but could have poor descriptions of the data sidebands.

The functional families tested are:

- *Exponential polynomials* (ExpPol) of form $e^{c_n x^n + c_{n-1} x^{n-1} \ldots + c_1 x}$
- *Bernstein polynomials* (Bern) of form $B_n = \sum_{\nu=0}^{n} C_\nu b_{\nu,n}(x)$
  where $b_{\nu,n}(x) = \binom{n}{\nu} x^\nu (1-x)^{(n-\nu)}$, and $\binom{n}{\nu}$ is the binomial coefficient.
- *Power functions* (Pow) of form $P_n = \sum c_n x^n$

Most chosen functions are first or second degree exponential polynomials or first degree power functions. If multiple functions satisfy the spurious signal requirements, the one with the fewest degrees of freedom is chosen and if there are still multiple, the function with the smallest N_{spur} is selected. The spurious signal uncertainty ascribed to the selected function is the largest spurious signal yield in the $121 < m_{\gamma\gamma} < 129$ GeV window. An example of this spurious signal test can be seen in Figure 6.7 for $|y_{\gamma\gamma}| \in [0.00, 0.15)$ (bin 1). The right plots (a and c) show the S/S_{ref} where S is the N_{spur} and the left plots (b and d) show the $S/\delta S$. The function selected for this bin was the ExpPol2 function.

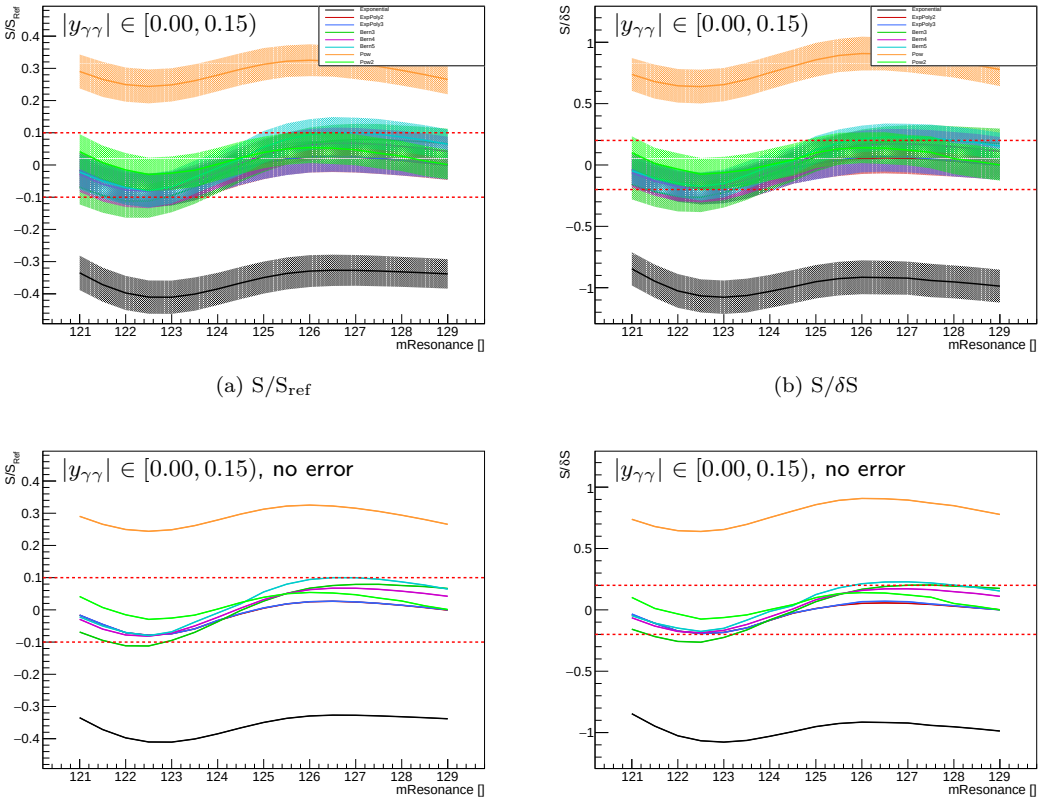

(a) S/S_{ref}

(b) $S/\delta S$

(c) S/S_{ref}, no error

(d) $S/\delta S$, no error

Figure 6.7: Spurious signal plots for $|y_{\gamma\gamma}| \in [0.00, 0.15)$. (a) and (c) show the S/S_{ref} values with and without errors, respectively. (b) and (d) show the $S/\delta S$ values with and without errors, respectively.

6.4.4 F-Tests

Once the functional form of the background is selected via the spurious signal criteria one final test, the F-test, is performed using the data sidebands. This test considers the possibility that the function chosen does not accurately describe the data and a function with more degrees of freedom would.

The F-test, named after the Fisher distribution of which it follows, compares the χ^2 fits between two functions of the same family. For families of embedded functions, there exists a function $g(x; c_n, ..., c_1)$ given a choice of $c_m, ..., c_1$ such that $f(x; c_m, ..., c_1) = g(x; c_n, ..., c_1)$ for $m > n$. Therefore, when performing a binned fit to the data sideband, the function with a greater number of degrees of freedom $f(x)$ will always have a smaller or equal χ^2.

One can then define a statistic F:

$$\mathrm{F}_{(1,2)} = \frac{\frac{\chi_1^2 - \chi_2^2}{d_2 - d_1}}{\frac{\chi_2^2}{n - d_2}} \; ; \tag{6.6}$$

where χ_1^2 and χ_2^2 are the χ^2 the two fits, d_1 and d_2 are the degrees of freedom for the different functions, and n is the number of bins used to compute the χ^2.

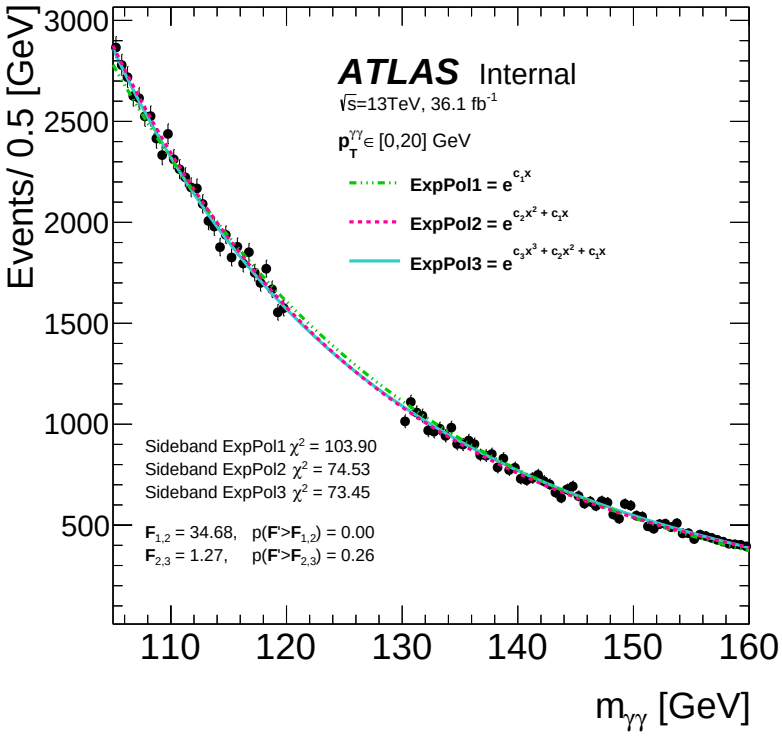

Figure 6.8: F-test for $p_{\mathrm{T}}^{\gamma\gamma} \in [0, 20)$ GeV (bin1). The ExpPol family of functions was tested as the spurious signal criteria selected the ExpPol2. The χ^2s,F values, and probabilities are also shown. From the F-test, the ExpPol2 is shown to be sufficient in modeling the sideband.

For the $H \to \gamma\gamma$ analysis, the test is executed with half GeV bins from $105 < m_{\gamma\gamma} < 160$ GeV, blinding the Higgs signal peak region $120 < m_{\gamma\gamma} < 130$ GeV. The statistic F has Fisher distribution $f(\mathrm{F}; d_2 - d_1, n - d_2)$ if an added degree of freedom does *not* improve the modeling of the sidebands. One can reject the hypothesis that an additional degree of freedom is *not* needed if $P(\mathrm{F}' \geq \mathrm{F}) < 0.05$, where P is the probability of observing an F' greater than or equal to the observed F when this F' is drawn from a Fisher distribution with the same degrees of freedom. In the case in which $P(\mathrm{F}' \geq \mathrm{F}) < 0.05$, the function with the higher number of parameters is chosen, and the process

is repeated for additional degrees of freedom. This procedure will ensure the function selected will have the lowest number of parameters while still accurately describing the data sidebands.

An example of this process can be seen in Figure 6.8, where the F-test is applied to $p_{\mathrm{T}}^{\gamma\gamma} \in [0, 20)$ GeV (bin 1). The function chosen by the spurious signal test was the ExpPol2. Judging purely from the χ^2 of the sideband fits, the ExpPol2 fits much better than the ExpPol1 though only slightly better than the ExpPol3. In this case calculating the F-statistic and its probability in the underlying Fisher distribution helps determine if one needs to fit with an ExpPol3 rather than an ExpPol2. In the example bin, there is no need to increase the number of parameter of the background function. The probability is taken from the exact Fisher distribution corresponding to $f(\mathrm{F}; d_2 - d_1, n - d_2) = f(34.68, 1, 88)$ for the ExpPol1 vs. ExpPol2 test and $f(1.27, 1, 87)$ for the ExpPol2 vs. ExpPol3 test. This was calculated using built in functions in the ROOT data analysis framework [201] developed by CERN, though not used for the final published result.

For the published result the Fisher distribution was built using pseudo-experiments. For example, if one were to build this distribution for comparing the ExpPol1 and ExpPol2, the following would be done. First the data sidebands would be fit with the ExpPol1 function to extract an Asimov dataset [202] with underlying ExpPol1 distribution. Next each bin in the distribution is Poisson fluctuated creating a new pseudo-distribution. This resulting pseudo-data is fit with the ExpPol1 and ExpPol2, and the F-statistic is calculated from the χ^2s of the fits to the pseudo-data. This value of F is filled in a histogram, and the process is repeated 10,000 times to create the Fisher distribution. The derived Fisher distribution should follow that of the ExpPol1 not needing an extra parameter as the underlying distribution of the pseudo-data was generated from an ExpPol1. Figure 6.9 shows the derived Fisher distributions for the $p_{\mathrm{T}}^{\gamma\gamma} \in [0, 20)$ GeV bin. Figure 6.9a shows the distribution for comparing ExpPol1 and ExpPol2, and Figure 6.9b shows the distribution for comparing ExpPol2 and ExpPol3. ExpPol2 is strongly preferred over ExpPol1 but the accuracy of the fit is not substantially improved going from ExpPol2 to ExpPol3. The probability obtained via pseudo-experiments is also commensurate with the calculation with the built in Fisher distributions as for $\mathrm{F}_{2,3}$ the obtained probability is 0.268 vs. the expected 0.262 from the exact distribution.

F-tests were performed in all 165 fiducial regions and differential bins in the $H \to \gamma\gamma$ analysis. Only 6 bins showed a preference of a higher function for describing the data sidebands. The final functions used to fit each fiducial region and differential bin is shown in Table 6.5.

	Bin1	Bin2	Bin3	Bin4	Bin5	Bin6	Bin7	Bin8	Bin9	Bin10	Bin11	Bin12	Bin13	Bin14
inclusive	ExpPol2													
catXS_{lepton}	ExpPol2	Exponential												
catXS_{ttH}	ExpPol2	Exponential												
catXS_{VBF}	ExpPol2	Exponential												
met_{TST}	ExpPol2	Exponential												
pT_{yy}	ExpPol2	ExpPol2	ExpPol2	ExpPol2	ExpPol2	ExpPol2	Pow	Exponential	Pow	Pow				
yAbs_{yy}	ExpPol2	ExpPol2	ExpPol2	ExpPol2	ExpPol2	ExpPol2	ExpPol2	ExpPol2	ExpPol2					
cosTS_{yy}	ExpPol2	ExpPol2	ExpPol2	ExpPol2	ExpPol2	ExpPol2	ExpPol2	ExpPol2	ExpPol2					
pTt_{yy}	ExpPol2	ExpPol2	ExpPol2	ExpPol2	ExpPol2	ExpPol2	ExpPol2	Bern3	ExpPol2	ExpPol2	ExpPol2	Exponential	Exponential	Exponential
Dy_{yy}	ExpPol2	ExpPol2	ExpPol2	ExpPol2	Pow	ExpPol2	ExpPol2	ExpPol2	ExpPol2	ExpPol2	Exponential			
N_{j}^{30}	ExpPol2	ExpPol2	ExpPol2	Exponential										
N_{j}^{50}	ExpPol2	Exponential	Exponential											
HT^{30}	ExpPol2	ExpPol2	ExpPol2	Exponential	Exponential	Exponential								
Dphi_{jj}^{30}	ExpPol2	Exponential	Exponential	ExpPol2										
Dphi_{jj}^{30}_signed	ExpPol2	ExpPol2	Exponential	Exponential	ExpPol2									
Dphi_{yyjj}^{30}	ExpPol2	Exponential	Exponential	ExpPol2										
Dy_{jj}^{30}	ExpPol2	ExpPol2	ExpPol2	ExpPol2										
maxTau_{yyj}^{30}	ExpPol2	ExpPol2	ExpPol2	Exponential	ExpPol2	Exponential	Exponential							
m_{jj}^{30}	ExpPol2	ExpPol2	ExpPol2	Exponential	Pow									
pT_{j1}^{30}	ExpPol2	ExpPol2	Exponential	ExpPol2	Pow	ExpPol2								
pT_{j2}^{30}	ExpPol2	ExpPol2	ExpPol2	Exponential	Exponential									
pT_{j3}^{30}	ExpPol2	ExpPol2	Exponential	Pow										
pT_{yyjj}^{30}	ExpPol2	ExpPol2	ExpPol2	Exponential										
sumTau_{yyj}^{30}	ExpPol2	ExpPol2	ExpPol2	Exponential	Exponential	Exponential	Exponential							
yAbs_{j1}^{30}	ExpPol2	ExpPol2	ExpPol2	ExpPol2	ExpPol2	ExpPol2	ExpPol2	ExpPol2						
yAbs_{j2}^{30}	ExpPol2	Exponential	Exponential	ExpPol2										
pT_{yy}^{0j}	ExpPol2	ExpPol2	ExpPol2	Exponential										
pT_{yy}^{1j}	ExpPol2	ExpPol2	ExpPol2	Exponential	ExpPol2									
pT_{yy}^{2j}	ExpPol2	Exponential	Pow	Exponential										
pT_{yy}^{3j}	Exponential	Pow	Pow											
$\text{pT}_{yy}^{cosTS_1}$	ExpPol3	ExpPol2	Pow	Exponential										
$\text{pT}_{yy}^{cosTS_2}$	ExpPol2	ExpPol2	Exponential	Exponential										

Table 6.5: Table of final selected functions used to model the background in each fiducial region and differential bin. Selected background functions pass the F-test on the functions selected by the spurious signal requirements. Functions in red are those in which the F-test recommended increasing the number of parameters of the selected function.

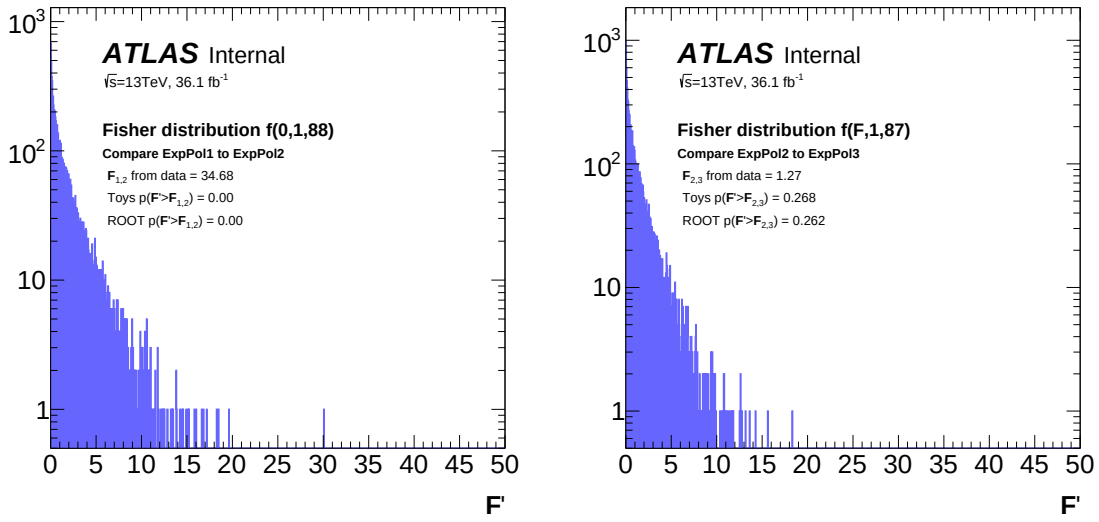

(a) Toys for $F_{1,2}$

(b) Toys for $F_{2,3}$

Figure 6.9: Toy distributions of the F-test calculated for $p_{\mathrm{T}}^{\gamma\gamma} \in [0, 20)$ GeV.

6.4.5 Mass and Yield Bias

After the final functions are selected by the spurious signal tests and F-tests, other bias tests are performed in order to assess the impact of the chosen functional form on the signal extraction. This assessment does not reject any function, though the amount of bias is added to the signal extraction fit in the form of additional nuisance parameters as described in Section 6.5.

Mass Bias

For the mass bias test, an Asimov signal sample was created from a nominal $m_H = 125$ GeV Monte Carlo sample, shifted so $m_H = 125.09$ GeV. This sample was then added to the constructed background template and a signal + background fit was performed using the double-sided Crystal Ball signal shape with the nominal fit parameters fixed with the exception of the m_H. The mass is allowed to float freely, and a mass-bias uncertainty:

$$\frac{m_{\mathrm{H,fit}} - 125.09 \text{ GeV}}{125.09 \text{ GeV}}, \tag{6.7}$$

is calculated. This uncertainty of the signal peak due the background function was determined to be less than 0.5% in all fiducial regions and differential bins.

Yield Bias

Another test was designed to gauge the output yield bias due to the signal + background choice. This is performed by fitting the data sidebands with the chosen background function and creating a background Asimov dataset. Signal Monte Carlo corresponding to the expected $H \to \gamma\gamma$ signal in the region/bin/ is injected into the smoothly falling Asimov background. The total number of signal events injected is known and compared to final extracted yield from the signal + background fit. This test demonstrated that any yield bias due to the background function was less than 1% of the injected signal.

6.5 Fitting Procedure

In obtaining the $H \to \gamma\gamma$ signal yield for every observable (differential variable or fiducial region), a simultaneous signal + background fit of the $m_{\gamma\gamma}$ distributions for each bin of the observable needs to be done. This is achieved using the Maximum Likelihood Estimator (MLE), where the likelihood for each bin is constructed and the product is maximized. The total likelihood maximized is:

$$\mathcal{L}(m_{\gamma\gamma}|\mathcal{N}^{\rm sig},\mathcal{N}^{\rm bkg}) = \prod_i \left\{ \frac{e^{-\mathcal{N}_i}}{n_i!} \prod_j^{n_i} \left[\mathcal{N}_i^{\rm sig}\,\mathcal{S}_i(m_{\gamma\gamma}^j|\theta_k) + \mathcal{N}_i^{\rm bkg}\,\mathcal{B}_i(m_{\gamma\gamma}^j) \right] \right\} \times \prod_k G_k\left(\theta_k - \theta\right) \;; \quad (6.8)$$

where $\mathcal{N}_i^{\rm sig}$ and $\mathcal{N}_i^{\rm bkg}$ are the extracted number of fitted signal and background events in the $i^{\rm th}$ bin, $\mathcal{N}_i = \mathcal{N}_i^{\rm sig} + \mathcal{N}_i^{\rm bkg}$ is the mean value of the underlying Poisson distribution for the n_i events in the bin, and $m_{\gamma\gamma}^j$ is the value of the diphoton invariant mass for event j. $\mathcal{S}_i(m_{\gamma\gamma}^j|\theta_k)$ and $\mathcal{B}_i(m_{\gamma\gamma}^j)$ are signal and background probability distribution functions. The signal probability distribution has a nuisance parameter for the uncertainty on the yield due to the spurious signal. The signal parameterization, apart from mean, is fixed by fits to Monte Carlo simulations as described in Section 6.3 while the background parameters of the function chosen in Section 6.4 are allowed to float in the fit.

The $\prod_k G_k\left(\theta_k\ - \theta\right)$ are Gaussian terms which constrain the Nuisance Parameters (NPs) of the uncertainty on the photon energy scale and photon energy resolution described in Section 6.5.1 as well as the uncertainty on the Higgs mass (240 MeV). The energy scale NPs are implemented as Gaussian asymmetric terms, while the energy resolution NPs are implemented as a log-normal asymmetric distribution. The uncertainty on the Higgs mass and spurious signal are treated as symmetric Gaussian terms. The central value is given by θ_k and the final value after likelihood maximization is θ. Note the product of constraint terms, aside from spurious signal which is built

into the signal PDF, is multiplied by the product over bins, ensuring the constraints are correlated across bins in an observables distribution. All the constraint terms are allowed to float, though non-zero values are penalized by a reduction in the likelihood. Uncertainties which do not affect the shape of the fit are not considered here, and are taken into account during the unfolding procedure described in Section 6.6.

In practice the likelihood in Equation 6.8 is not maximized, but the likelihood ratio is minimized. This technique is referred to as the profile likelihood ratio test [202], and the test statistic, λ, can be written as:

$$\lambda(\mathcal{N}) = -2\ln\frac{\mathcal{L}(\mathcal{N},\hat{\boldsymbol{\theta}}_{\mathcal{N}})}{\mathcal{L}(\hat{\mathcal{N}},\hat{\boldsymbol{\theta}})} \ ; \tag{6.9}$$

where $\hat{\mathcal{N}}$ and $\hat{\boldsymbol{\theta}}$ are the signal yield extracted and the nuisance parameters that maximize the likelihood. $\hat{\boldsymbol{\theta}}_{\mathcal{N}}$ are the values of the NPs that maximize the likelihood when the extracted signal yield is fixed to $\mathcal{N}$. This is the same in practice as the natural log is a monotonic function therefore the maximum of $\mathcal{L}$ will be the minimum of the likelihood ratio. Furthermore, this change is made as numerically the $-2\ln$ converts small positive values to large negative values as generally most computational extremizer tools compute minimums not maximums, and using the ratio makes allows for the easier computation of confidence intervals. Wilk's theorem [203] states in the large N limit, $\lambda(\mathcal{N})$ will be a χ^2 distribution with one degree of freedom. Thus the confidence intervals can be calculated by moving along the profile likelihood curve, increasing $\lambda(\mathcal{N})$ by 1 to get the 68.3% interval, increasing $\lambda(\mathcal{N})$ by 4 to get 95.5% interval, and so on and so forth.

For each observable the simultaneous fit is performed multiple times in order to break down the fit uncertainty into the statistical and systematic components. First the best-fit values of all nuisance parameters are obtained in the signal + background fit and an observed signal yield is extracted. This signal yield is not required to be positive. Next, an Asimov dataset is constructed using the observed signal yield, and best-fit values of the NPs. For the next fit, the NPs are fixed to the extracted values from the best-fit and the $\lambda(\mathcal{N})$ is scanned as a function of signal yield. The extracted signal value would be at the minimum of the $\lambda(\mathcal{N})$ and in the asymptotic limit the statistical uncertainty corresponding to the 68.3% confidence interval is given by values of $\mathcal{N}_i^{\text{sig}}$ in which $\lambda(\mathcal{N})$ is 1 unit higher than the minimum. This statistical uncertainty extracted is by construction asymmetric. One can then extract the systematic and theory errors by fixing all NPs except those of interest ("profiling"), refitting, and then recalculating the ±1 values on the profile likelihood curve.

Examples of these fits and extracted signal yields can be seen in Figure 6.10 for the inclusive fiducial region and in Figure 6.11 for the $p_{\mathrm{T}}^{\gamma\gamma}$ variable. Shown are the results of the simultaneous fits for each bin, the pulls of the nuisance parameters, and the comparisons to the Standard Model predictions.

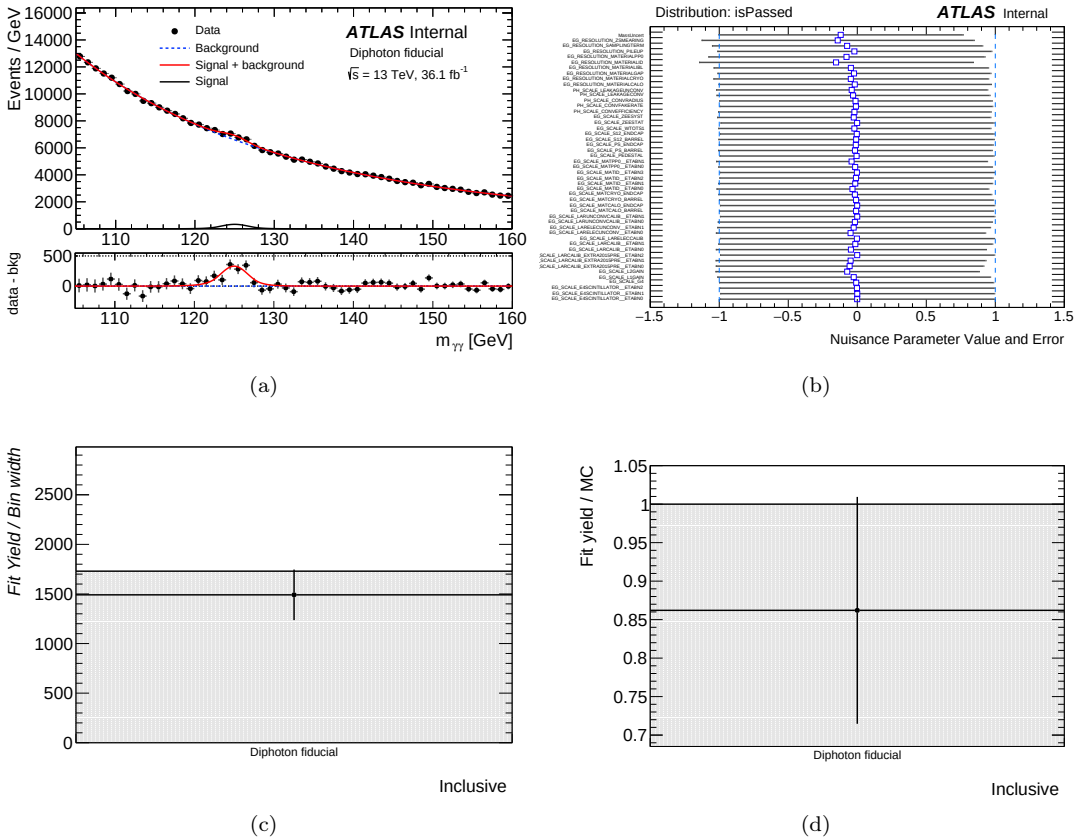

(a) (b)

(c) (d)

Figure 6.10: Signal extraction fit details for the inclusive region. (a) shows the fitted background and signal probability distribution functions, (b) shows the fitted NP pulls, and (c) and (d) show the measurement(in number of events) and ratio, respectively, of the signal yield over the Standard Model expectation.

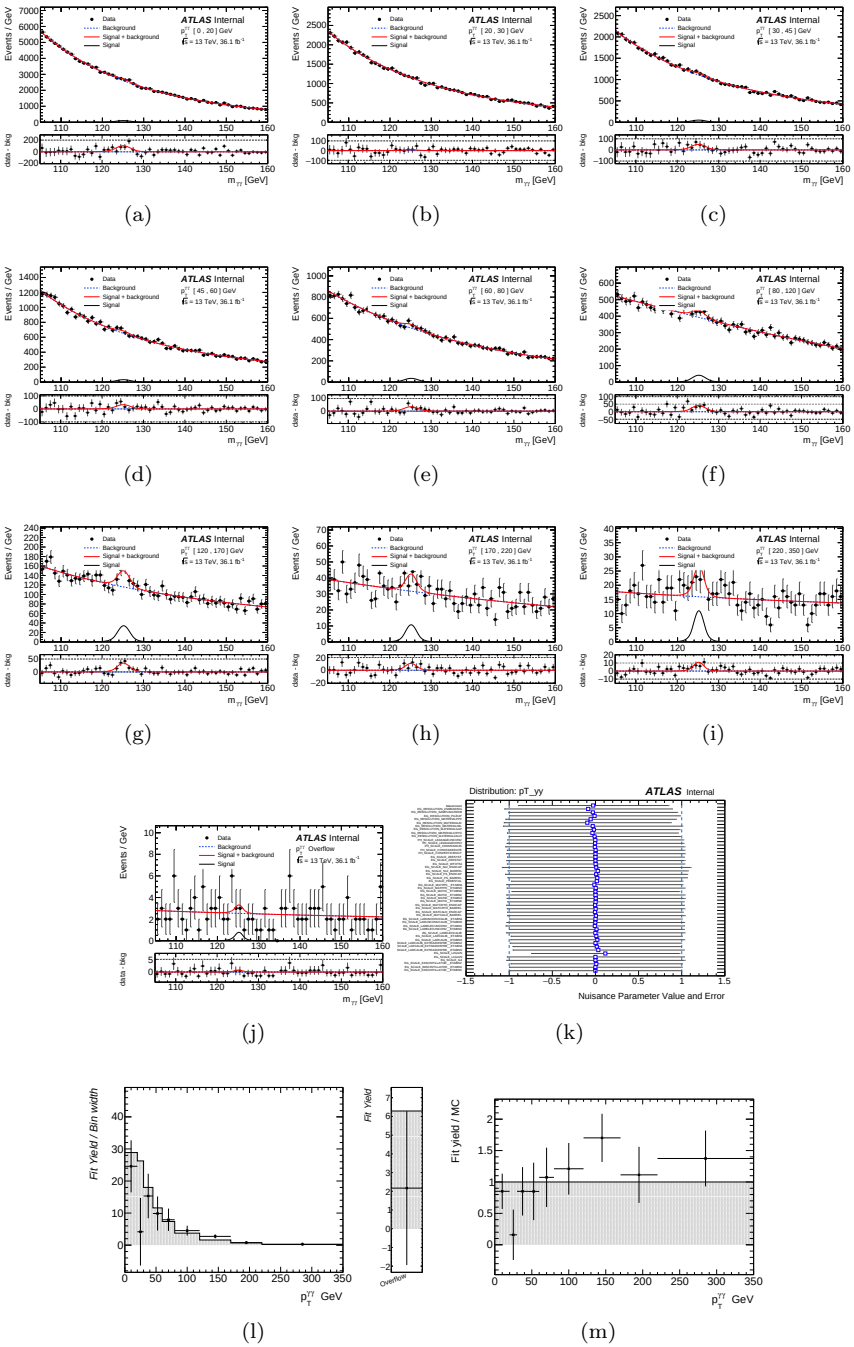

(a) (b) (c) (d) (e) (f) (g) (h) (i) (j) (k) (l) (m)

Figure 6.11: Signal extraction fit details for the $p_{\mathrm{T}}^{\gamma\gamma}$ observable. (a)-(j) show the fitted background and signal probability distribution functions, (k) shows the fitted NP pulls, and (l) and (m) show the measurement (in number of events) and ratio, respectively, of the signal yield over the Standard Model expectation.

6.5.1 Photon Energy Scale and Resolution

The Photon Energy Scale (PES) and Photon Energy Resolution (PER) uncertainties play an important role in the fitting procedure as well as in the unfolding back to truth particle level. In order to avoid overconstraints on the nuisance parameters, the total energy scale and resolution uncertainties are split into different components. This is completed following a prescription from ATLAS's Electron/Photon calibration group, recommending the full decorrelation scheme which contains 72 PES and 9 PER terms in different η bins. By adding in quadrature the PES terms of different η bins to create two sets of parameters (one for the barrel $[|\eta| < 1.37]$ and one for the endcap $[1.52 \leq |\eta| < 2.37]$), the final number of terms implemented in the fit was reduced to 40 PES and 9 PER nuisance parameters.

The different photon energy scale uncertainties considered are:

- $Z \to ee$ calibration: Statistical (`EG_SCALE_ZEESTAT`) and systematic (`EG_SCALE_ZEESYST`) uncertainties associated with the $Z \to ee$ calibration procedure of electrons.
- E4 scintillators calibration: Uncertainty (`EG_SCALE_E4SCINTILLATOR`) from the E4 scintillators calibration in $1.4 < |\eta| < 1.6$ barrel-endcap transition region.
- Calibration pedestal: Uncertainty (`EG_SCALE_PEDESTAL`) from mis-modeling of the pedestal calibration after pileup corrections.
- Electronic gain calibration: Uncertainties on the first layer (`EG_SCALE_L1GAIN`) and second layer (`EG_SCALE_L1GAIN`) due to gain non-linearity, derived from response measurements and special runs.
- Presampler scale: Uncertainty (`EG_SCALE_PS`) of the calibration of the presampler which remains unchanged from Run 1.
- E1/E2 scale: The scale uncertainty (`EG_SCALE_S12`) of the first and second layer calibration determined using muons.
- LAr: LAr uncertainties from calibrations and modeling of muons (`EG_SCALE_LARCALIB`), unconverted photons (`EG_SCALE_LARUNCONVCALIB`), converted photons and electrons (`EG_SCALE_LARELECUNCONV`), and electrons in the forward region (`EG_SCALE_LARELECCALIB`).

- Material: Uncertainties on the amount of material before the electromagnetic calorimeter due to the Inner Detector (`EG_SCALE_MATID`), the cryostat (`EG_SCALE_MATCRYO`), passive calorimeter material (`EG_SCALE_MATCALO`), and the IBL/Inner Detector patch panels (`EG_SCALE_MATPPO`).

- Geant4 modeling: Uncertainty (`EG_SCALE_G4`) from different shower shapes derived from modeling options in Geant4.

- Shower shape: Mis-modeling of the lateral shower shape (`EG_SCALE_WTOTS1`) dependent on the reconstructed energy and lateral shower width.

- Photon leakage: Uncertainty of the lateral energy leakage (`PH_SCALE_LEAKAGECONV`, `PH_SCALE_LEAKAGEUNCONV`) for converted and unconverted photons.

- Conversions: Uncertainty due to mis-modeling of the photon conversion inefficiency (`PH_SCALE_CONVEFFICIENCY`), conversion fake rate (`PH_SCALE_CONVFAKERATE`), and conversion radius ((`PH_SCALE_CONVRADIUS`).

The different photon energy resolution uncertainties considered are:

- $Z \to ee$ smearing: Resolution difference (`EG_RESOLUTION_ZSMEARING`) between data and simulation measured in 2015 and 2016 for $Z \to ee$ events.

- Sampling term: Sampling term uncertainty (`EG_RESOLUTION_SAMPLINGTERM`) from test-beam analysis of EM calorimeter modules. This was determined to be 10%.

- Pileup: Uncertainty (`EG_RESOLUTION_PILEUP`) due to the noise difference between data and simulation in randomly triggered events.

- Material: Uncertainties on the amount of material before the electromagnetic calorimeter due to the Inner Detector (`EG_RESOLUTION_MATERIALID`), the cryostat (`EG_RESOLUTION_MATERIALCRYO`), passive calorimeter material (`EG_RESOLUTION_MATERIALCALO`), the cryostat in the barrel-endcap region (`EG_RESOLUTION_MATERIALGAP`), the IBL (`EG_RESOLUTION_MATERIALIBL`), and the Inner Detector patch panels (`EG_RESOLUTION_MATERIALPPO`).

The first step to extracting the PES/PER uncertainties is building the signal model. All production modes of the $H \to \gamma\gamma$ process, described in Section 6.2, are simulated and combined by weighting them according to the Standard Model prediction. The resulting signal-only simulation

is fit in the $115 < m_{\gamma\gamma} < 135$ GeV mass window using the double-sided Crystal Ball function described in Section 6.3. The optimal fit parameters are then saved. The uncertainties are simulated and for each uncertainty an "up" and "down" $m_{\gamma\gamma}$ spectrum are built corresponding to 1σ possible deviations due to the uncertainty. For the photon energy scale, the up and down distributions are refit with parameters fixed to the saved nominal values, except the mean of the double-sided Crystal Ball is allowed to float freely. The percent difference of the calculated mean with respect to the nominal mean is taken as the uncertainty. The same technique is used for the photon energy resolution though instead of fixing all parameters except the mean, all parameters except the width (σ) of the double-sided Crystal Ball are fixed. This is done for each uncertainty component and each bin/region.

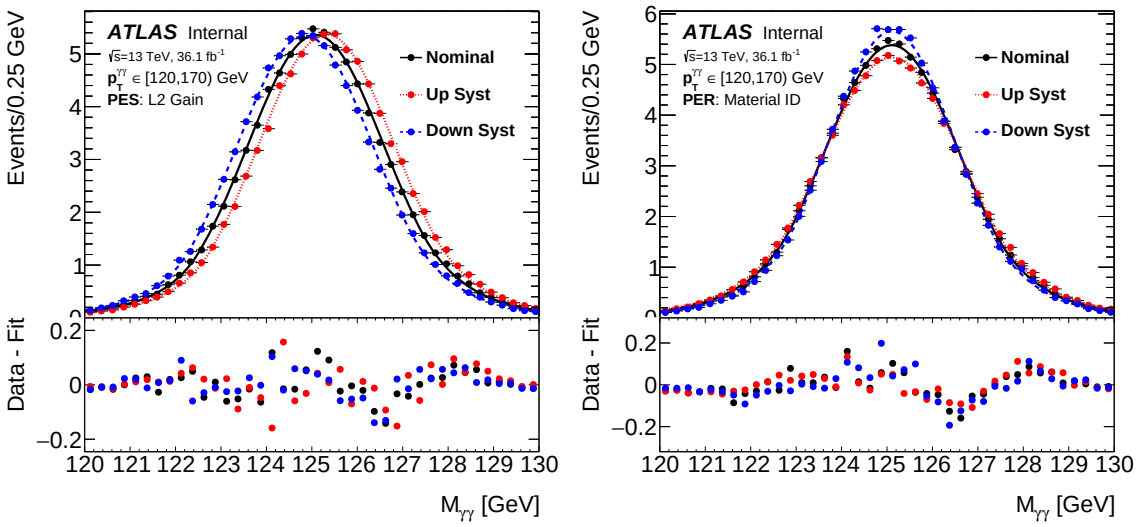

(a) Photon Energy Scale

(b) Photon Energy Resolution

Figure 6.12: (a) Photon energy scale and (b) photon energy resolution for $p_{\mathrm{T}}^{\gamma\gamma} \in [120, 170)$GeV. (a) shows the layer 2 gain uncertainty and the shifts in the mean value from the up and down components are seen. (b) shows the Material in the Inner Detector uncertainty and the effect of the width (σ) from it. These components were chosen so that the reader may see differences in scale/resolution as some uncertainty components are small. While the figure shows $120 < m_{\gamma\gamma} < 130$ GeV the fit was done in the $115 < m_{\gamma\gamma} < 135$GeV window as stated in the text.

Examples of the PES/PER extraction can be seen in Figure 6.12 which shows different uncertainty components for $p_{\mathrm{T}}^{\gamma\gamma} \in [120, 170)$, chosen so the reader can see the differences between the nominal $H \to \gamma\gamma$ shape and the uncertainty component. Figure 6.12a shows the `EG_SCALE_L2GAIN` component which arises from the non-linearity of the gain. A clear shift in measured invariant

mass of the diphoton system can be seen in the up and down distributions. Figure 6.12b shows the `EG_RESOLUTION_MATERIALID` component which is due to mis-modeling of the material in the Inner Detector. Once again, the width of the double-sided Crystal Ball function is obviously altered. For most bins/regions the total PES is about a $0.2-0.4\%$ effect and the PER is a $5-8\%$ effect. Table 6.6 shows the total PES and PER uncertainties for the fiducial regions and $p_{\mathrm{T}}^{\gamma\gamma}$, $|y_{\gamma\gamma}|$, and $N_{\mathrm{jets}}^{\geq 30\ \mathrm{GeV}}$ variables. The 40 PES and 9 PER terms are each added in quadrature in order to obtain the values in the table. To give some sense of scale of the different PES/PER components, Table 6.7 contains the breakdown of relative uncertainties for the inclusive region, and Figure 6.13 shows the *percent* uncertainty for different components for the $p_{\mathrm{T}}^{\gamma\gamma}$ spectrum.

Table 6.6: Total photon energy scale and resolution percent uncertainties for the fiducial regions, $p_{\mathrm{T}}^{\gamma\gamma}$, $|y_{\gamma\gamma}|$, and $N_{\mathrm{jets}}^{\geq 30\ \mathrm{GeV}}$. These are calculated by adding the different components in quadrature.

Bin	PES Up	PES Down	PER Up	PER Down
Inclusive	0.0025	0.0025	0.063	0.061
$\boldsymbol{N_{lep}} = 0$	0.0028	0.0030	0.073	0.061
$\boldsymbol{N_{lep}} \geq 1$	0.0028	0.0028	0.073	0.067
VBF underflow	0.0025	0.0025	0.062	0.060
VBF enriched	0.0029	0.0029	0.075	0.068
$\boldsymbol{t\bar{t}H}$ underflow	0.0027	0.0023	0.071	0.066
$\boldsymbol{t\bar{t}H}$ **enriched**	0.0029	0.0029	0.072	0.074
High $\boldsymbol{E_{\mathrm{T}}^{\mathrm{miss}}}$ underflow	0.0025	0.0025	0.062	0.061
High $\boldsymbol{E_{\mathrm{T}}^{\mathrm{miss}}}$	0.0032	0.0032	0.076	0.084
$p_{\mathrm{T}}^{\gamma\gamma} \in [0, 20)$ GeV	0.0024	0.0024	0.057	0.059
$p_{\mathrm{T}}^{\gamma\gamma} \in [20, 30)$ GeV	0.0024	0.0024	0.060	0.057
$p_{\mathrm{T}}^{\gamma\gamma} \in [30, 45)$ GeV	0.0024	0.0024	0.061	0.058
$p_{\mathrm{T}}^{\gamma\gamma} \in [45, 60)$ GeV	0.0025	0.0024	0.060	0.061
$p_{\mathrm{T}}^{\gamma\gamma} \in [60, 80)$ GeV	0.0025	0.0025	0.061	0.062
$p_{\mathrm{T}}^{\gamma\gamma} \in [80, 120)$ GeV	0.0028	0.0027	0.067	0.068
$p_{\mathrm{T}}^{\gamma\gamma} \in [120, 170)$ GeV	0.0031	0.0031	0.081	0.079
$p_{\mathrm{T}}^{\gamma\gamma} \in [170, 220)$ GeV	0.0035	0.0035	0.096	0.097
$p_{\mathrm{T}}^{\gamma\gamma} \in [220, 300)$ GeV	0.0040	0.0040	0.113	0.112
$N_{\mathrm{jets}}^{\geq 30\ \mathrm{GeV}} = 0$	0.0024	0.0024	0.059	0.058
$N_{\mathrm{jets}}^{\geq 30\ \mathrm{GeV}} = 1$	0.0026	0.0026	0.065	0.062
$N_{\mathrm{jets}}^{\geq 30\ \mathrm{GeV}} = 2$	0.0028	0.0028	0.070	0.068
$N_{\mathrm{jets}}^{\geq 30\ \mathrm{GeV}} \geq 3$	0.0029	0.0030	0.073	0.072
$\lvert y_{\gamma\gamma}\rvert \in [0.0, 0.1)$	0.0022	0.0022	0.056	0.055
$\lvert y_{\gamma\gamma}\rvert \in [0.1, 0.3)$	0.0022	0.0022	0.058	0.055
$\lvert y_{\gamma\gamma}\rvert \in [0.3, 0.5)$	0.0023	0.0023	0.056	0.054
$\lvert y_{\gamma\gamma}\rvert \in [0.5, 0.6)$	0.0023	0.0023	0.056	0.054
$\lvert y_{\gamma\gamma}\rvert \in [0.6, 0.8)$	0.0024	0.0024	0.060	0.056
$\lvert y_{\gamma\gamma}\rvert \in [0.8, 0.9)$	0.0026	0.0026	0.061	0.057
$\lvert y_{\gamma\gamma}\rvert \in [0.9, 1.2)$	0.0028	0.0028	0.063	0.065
$\lvert y_{\gamma\gamma}\rvert \in [1.2, 1.6)$	0.0038	0.0038	0.072	0.075
$\lvert y_{\gamma\gamma}\rvert \in [1.6, 2.4)$	0.0064	0.0065	0.093	0.102

Table 6.7: Breakdown of full photon energy scale/resolution decorrelation scheme percent errors that enter the fit for the inclusive fiducial region.

Component	Up	Down
EG_RESOLUTION_MATERIALCALO	0.0048802	0.0045121
EG_RESOLUTION_MATERIALCRYO	0.0114307	0.0118533
EG_RESOLUTION_MATERIALGAP	0.0061174	0.0058777
EG_RESOLUTION_MATERIALIBL	0.0113991	0.0116531
EG_RESOLUTION_MATERIALID	0.0352729	0.0378975
EG_RESOLUTION_MATERIALPP0	0.0180221	0.0196961
EG_RESOLUTION_PILEUP	0.0052656	0.0052048
EG_RESOLUTION_SAMPLINGTERM	0.0217894	0.0182997
EG_RESOLUTION_ZSMEARING	0.0390875	0.0351860
EG_SCALE_E4SCINTILLATOR__ETABIN0	0.0000110	0.0000110
EG_SCALE_E4SCINTILLATOR__ETABIN1	0.0000043	0.0000026
EG_SCALE_E4SCINTILLATOR__ETABIN2	0.0000321	0.0000386
EG_SCALE_G4	0.0001227	0.0001235
EG_SCALE_L1GAIN	0.0004103	0.0004064
EG_SCALE_L2GAIN	0.0011614	0.0011566
EG_SCALE_LARCALIB_EXTRA2015PRE__ETABIN0	0.0008923	0.0008794
EG_SCALE_LARCALIB_EXTRA2015PRE__ETABIN1	0.0007536	0.0007646
EG_SCALE_LARCALIB_EXTRA2015PRE__ETABIN2	0.0000101	0.0000101
EG_SCALE_LARCALIB__ETABIN0	0.0007261	0.0007299
EG_SCALE_LARCALIB__ETABIN1	0.0002223	0.0002265
EG_SCALE_LARELECCALIB	0.0000447	0.0000391
EG_SCALE_LARELECUNCONV__ETABIN0	0.0007781	0.0007714
EG_SCALE_LARELECUNCONV__ETABIN1	0.0004142	0.0004127
EG_SCALE_LARUNCONVCALIB__ETABIN0	0.0002643	0.0002726
EG_SCALE_LARUNCONVCALIB__ETABIN1	0.0000043	0.0000103
EG_SCALE_MATCALO_BARREL	0.0001369	0.0001359
EG_SCALE_MATCALO_ENDCAP	0.0000131	0.0000156
EG_SCALE_MATCRYO_BARREL	0.0001376	0.0001393
EG_SCALE_MATCRYO_ENDCAP	0.0002835	0.0002748
EG_SCALE_MATID__ETABIN0	0.0005532	0.0005535
EG_SCALE_MATID__ETABIN1	0.0002298	0.0002337
EG_SCALE_MATID__ETABIN2	0.0001569	0.0001482
EG_SCALE_MATID__ETABIN3	0.0000408	0.0000434
EG_SCALE_MATPP0__ETABIN0	0.0002441	0.0002446
EG_SCALE_MATPP0__ETABIN1	0.0006496	0.0006535
EG_SCALE_PEDESTAL	0.0000801	0.0000801
EG_SCALE_PS_BARREL	0.0002632	0.0002635
EG_SCALE_PS_ENDCAP	0.0001686	0.0001659
EG_SCALE_S12_BARREL	0.0001149	0.0001313
EG_SCALE_S12_ENDCAP	0.0000609	0.0000532
EG_SCALE_S12_ETABIN4	0.0000194	0.0000351
EG_SCALE_WTOTS1	0.0003484	0.0003330
EG_SCALE_ZEESTAT	0.0000255	0.0000151
EG_SCALE_ZEESYST	0.0003954	0.0004052
PH_SCALE_CONVEFFICIENCY	0.0003362	0.0003273
PH_SCALE_CONVFAKERATE	0.0001702	0.0001555
PH_SCALE_CONVRADIUS	0.0002146	0.0001994
PH_SCALE_LEAKAGECONV	0.0004701	0.0004823
PH_SCALE_LEAKAGEUNCONV	0.0006308	0.0006387

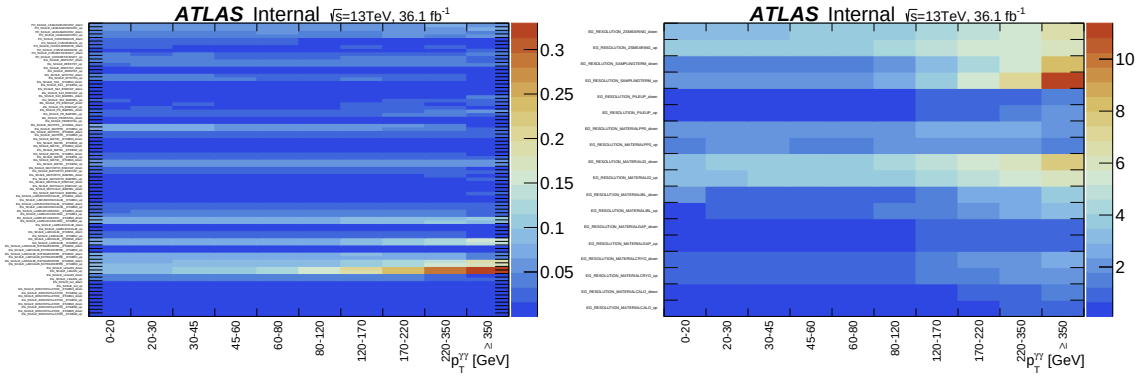

(a) PES $p_{\mathrm{T}}^{\gamma\gamma}$ (b) PER $p_{\mathrm{T}}^{\gamma\gamma}$

Figure 6.13: $p_{\mathrm{T}}^{\gamma\gamma}$: Percent uncertainty for each component of the full (a) photon energy scale and (b) photon energy resolution parameters.

6.6 Unfolding Procedure

Once the signal yields are extracted, they will need to be "unfolded" or "deconvoluted" back to their particle level or truth distributions to make comparisons with theoretical predictions. This is done to correct for the finite resolution and response of the ATLAS detector. If the detector had infinite precision and could collect a sample of infinite statistics, the truth distribution for a well understood process would match exactly to the reconstructed or "reco" distribution. Mathematically, unfolding can we written as:

$$f_{\mathrm{reco}}(x) = \int \mathcal{R}(x|y) \times f_{\mathrm{part}}(y)\, dy \; ; \tag{6.10}$$

where $f_{\mathrm{reco}}(x)$ is the reconstructed probability distribution function of measured values x, and $f_{\mathrm{part}}(y)$ is the PDF of the true underlying values y, which are then smeared out by a detector response term $\mathcal{R}(x|y)$. By measuring the observables in different bins, the integral is converted to a sum:

$$x_i = \sum \mathcal{R}_{ij} y_j \; ; \tag{6.11}$$

where now $\mathcal{R}_{ij}$ represents a response matrix of conditional probabilities. The i, j^{th} value of $\mathcal{R}_{ij}$ represents the probability of the reconstructed observable being in bin i given the true value of value residing in bin j. For a perfect detector the matrix would be the identity matrix. Because we measure the reconstructed distribution the unfolding procedure is to build the $\mathcal{R}_{ij}$ matrix with as little bias as possible and invert Equation 6.10 to calculate the true probability distribution function of the observable of interest.

In practice unfolding can be done via the correction factor method [204], Single Value Decomposition (SVD) [205], Iterative Bayesian [206], and Iteratively Dynamically Stabilized (IDS) [207] each with its own merits and flaws. There is a balance between simple methods which can be dependent on the underlying physics simulation of truth distributions versus more complicated methods which can result in large statistical uncertainties. Historically, the $H \to \gamma\gamma$ cross section analyses have used the bin-by-bin or correction factor approach as this is more justified when the measurements are dominated by statistical uncertainties rather than systematic ones. This is the method used for this analysis as the analysis is still statistically limited, though comparisons between the other methods have been studied.

6.6.1 Correction Factors

As described in Section 6.1.1, the differential cross section can be defined as:

$$\frac{d\sigma_{\text{fid}}}{dx} = \frac{n_{\text{reco}}}{C_{\text{i}}^{\text{fid}} \cdot \Delta x \cdot \mathcal{L}_{\text{int}}} \; ; \tag{6.12}$$

where $C_{\text{i}}^{\text{fid}}$ denotes the correction factor. The correction factor, derived in Monte Carlo, is defined to be the ratio of expected events reconstructed with a given detector level criteria n_{reco} to the expected events passing truth criteria n_{true}. This takes into account both the efficiency of the ATLAS trigger, reconstruction, identification, and isolation requirements of particles as well as any extrapolation between the detector and particle level regions of phase space. This can be written as:

$$C_{\text{i}}^{\text{fid}} = \frac{n_{\text{reco}}}{n_{\text{true}}} = \frac{\epsilon_{\text{fid}}}{\mathcal{P}_{\text{fid}}} \; ; \tag{6.13}$$

where one can define the efficiency $\epsilon_{\text{fid}} = \frac{n_{\text{reco}}^{\text{true}}}{n_{\text{true}}}$ and purity $\mathcal{P}_{\text{fid}} = \frac{n_{\text{reco}}^{\text{true}}}{n_{\text{reco}}}$ of each bin/region. The total number of events that are reconstructed in the fiducial region and satisfy the truth selection criteria is $n_{\text{reco}}^{\text{true}}$. The efficiency is sensitive to events which are reconstructed outside the fiducial criteria and the purity is sensitive to incorrectly reconstructed objects inside the fiducial region. Both are sensitive to migrations of events due to detector resolution. Most bins/regions in the analysis have purity greater than 50% and efficiency greater than 70%.

This method has a smaller variance during inversion than other methods but an unknown bias in the simulation can cause adverse effects. Generally the bias is estimated by assuming some baseline model (the Standard Model) and then the bias is parameterized by the maximum deviation from that model that one can expect (due to new physics, etc). This bias is treated as an added systematic uncertainty in the unfolding procedure.

The correction factors are built to be as model independent as possible, though some things can lead to potential model dependence. The truth level and reco level regions are chosen to be as close as possible though this implicitly assumes the PDFs of the observables follow Standard Model expectations. Second, the correction factors can be sensitive to Higgs production mode so there is an underlying assumption of the relative rates of these modes. Finally, the correction factors can be sensitive to hadronization effects and underlying event modeling of the simulation so there are additional uncertainties that need to be taken into account.

The correction factors for the fiducial region and the $p_{\mathrm{T}}^{\gamma\gamma}$, $|y_{\gamma\gamma}|$, and $N_{\mathrm{jets}}^{\geq 30\ \mathrm{GeV}}$ are shown in Table 6.8 for each production mode and the combination. The combined correction factor is calculated by weighting the individual production mode correction factors by their the Standard Model cross sections. Therefore the closer the correction factors are to each other, the lower the sensitivity to the assumptions made. Subdominant production modes like $b\bar{b}H$ and tHW are not included in the correction factors due to complicated interference with ggF which are not considered. These Higgs production mechanisms would only affect the correction factor by less than 0.01% and are consequently ignored.

6.6.2 Unfolding Uncertainties

Uncertainties on the correction factor can broadly be categorized into two types, physics modeling and experimental.

The physics modeling uncertainties can be summarized as the following:

- Higgs production mechanism: The relative contributions from different Higgs production mechanisms are varied within their measured experimental limits from the Run 1 couplings combination measurements from ATLAS and CMS.

- Higgs p_{T} and y corrections: In order to estimate the effect of different models and inherent MC assumptions, a reweighting of the MC to the observed, unfolded data PDFs of $p_{\mathrm{T}}^{\gamma\gamma}$ and $|y_{\gamma\gamma}|$ were done simultaneously. These variables are largely uncorrelated and a smooth reweighting function was extracted from the data/MC ratio.

- Underlying event: The uncertainty on the modeling of the underlying event was assessed by using varying MC tunes with the standard Pythia8 generator and comparisons with the Herwig7 generator.

Table 6.8: Correction factors for the fiducial regions $p_{\mathrm{T}}^{\gamma\gamma}$, $|y_{\gamma\gamma}|$, and $N_{\mathrm{jets}}^{\geq 30\ \mathrm{GeV}}$. WmH refers to HW^+ production, WpH refers to HW^- production, and ZH refers to quark initiated ZH production.

Inclusive								
Bin	ggF	VBF	WmH	WpH	ggZH	ZH	ttH	Combined.
Inclusive	0.751	0.756	0.746	0.746	0.762	0.747	0.737	0.752
$\boldsymbol{N_{lep}}$								
Bin	ggF	VBF	WmH	WpH	ggZH	ZH	ttH	Combined.
0	0.751	0.756	0.776	0.776	0.765	0.751	0.818	0.753
≥ 1	16.660	4.844	0.625	0.627	0.732	0.708	0.596	0.639
VBF enriched								
Bin	ggF	VBF	WmH	WpH	ggZH	ZH	ttH	Combined.
underflow	0.746	0.751	0.741	0.741	0.759	0.742	0.735	0.746
VBF enriched	1.069	0.763	1.150	1.190	0.825	1.188	0.779	0.866
$\boldsymbol{t\bar{t}H}$ **enriched**								
Bin	ggF	VBF	WmH	WpH	ggZH	ZH	ttH	Combined.
underflow	0.750	0.755	0.743	0.744	0.757	0.744	1.233	0.751
$t\bar{t}H$ enriched	0.954	1.064	1.411	1.213	0.888	0.898	0.611	0.657
High $\boldsymbol{E_{\mathrm{T}}^{\mathrm{miss}}}$								
Bin	ggF	VBF	WmH	WpH	ggZH	ZH	ttH	Combined.
underflow	0.750	0.753	0.740	0.740	0.757	0.745	0.710	0.750
High $E_{\mathrm{T}}^{\mathrm{miss}}$	1.0	1.0	0.829	0.821	0.792	0.776	0.865	1.068
$\boldsymbol{p_T^{\gamma\gamma}}$**[GeV]**								
Bin	ggF	VBF	WmH	WpH	ggZH	ZH	ttH	Combined.
$0-20$	0.755	0.753	0.748	0.754	0.750	0.745	0.721	0.755
$20-30$	0.750	0.750	0.757	0.735	0.757	0.734	0.711	0.750
$30-45$	0.743	0.746	0.728	0.746	0.710	0.737	0.703	0.743
$45-60$	0.744	0.744	0.729	0.724	0.747	0.735	0.706	0.743
$60-80$	0.742	0.738	0.731	0.732	0.734	0.733	0.703	0.741
$80-120$	0.751	0.754	0.750	0.741	0.756	0.738	0.721	0.750
$120-170$	0.776	0.773	0.762	0.759	0.763	0.768	0.752	0.773
$170-220$	0.790	0.783	0.757	0.773	0.778	0.784	0.770	0.785
$220-350$	0.793	0.795	0.793	0.783	0.793	0.788	0.785	0.792
$350-\infty$	0.807	0.816	0.781	0.805	0.790	0.806	0.799	0.807
$\boldsymbol{\lvert y_{\gamma\gamma}\rvert}$								
Bin	ggF	VBF	WmH	WpH	ggZH	ZH	ttH	Combined.
$0.00-0.15$	0.760	0.774	0.757	0.758	0.776	0.763	0.749	0.761
$0.15-0.30$	0.769	0.765	0.769	0.768	0.789	0.765	0.745	0.769
$0.30-0.45$	0.770	0.770	0.752	0.774	0.770	0.767	0.747	0.769
$0.45-0.60$	0.765	0.774	0.767	0.776	0.781	0.769	0.740	0.766
$0.60-0.75$	0.766	0.769	0.767	0.766	0.746	0.766	0.746	0.766
$0.75-0.90$	0.761	0.769	0.755	0.750	0.772	0.770	0.746	0.761
$0.90-1.20$	0.746	0.755	0.754	0.752	0.756	0.749	0.734	0.747
$1.20-1.60$	0.733	0.739	0.729	0.727	0.736	0.726	0.721	0.733
$1.60-2.40$	0.717	0.714	0.698	0.706	0.734	0.704	0.695	0.716
$\boldsymbol{N_{jets}[p_T^j > 30\ \mathrm{GeV}]}$								
Bin	ggF	VBF	WmH	WpH	ggZH	ZH	ttH	Combined.
$=0$	0.691	0.712	0.662	0.676	0.745	0.696	0.819	0.691
$=1$	0.811	0.708	0.720	0.712	0.737	0.708	0.672	0.797
$=2$	0.907	0.735	0.769	0.770	0.714	0.753	0.671	0.847
≥ 3	1.084	1.093	0.900	0.884	0.826	0.884	0.743	0.991

The experimental uncertainties can be summarized in the following text, though a more detailed description of these uncertainties can be seen in Section 7.5. A summary of uncertainties on the correction factor can be seen for the $p_{\mathrm{T}}^{\gamma\gamma}$ and $N_{\mathrm{jets}}^{\geq 30\ \mathrm{GeV}}$ variable in Figure 6.14.

- Photon energy scale and resolution: The correction factors, like the signal extraction, have some uncertainty due to migrations between bins from incorrect scale/resolution effects of the detector. Correlations between the signal extraction and correction factors are ignored as there are small. The total uncertainty of the photon energy scale and resolution on correction factors was generally 0.05% to 3% for higher and lower sample size bins, respectively.

- Photon and diphoton selection efficiencies: The trigger efficiency for the diphoton trigger used in analysis was 99.2 ± 0.4. This was measured using a bootstrap method, detailed in Ref. [208]. The uncertainties related to selection of the vertex using the diphoton pointing from were found to be less than 0.3%. The photon identification and isolation efficiencies were also considered and are each sub percent level effects. The total contribution from the combination of photon/diphoton selection efficiencies described range from 0.4% to 2.6% depending on the bin/region.

- Jet energy scale, resolution, and Jet Vertex Fraction (JVT): The fiducial regions and differential variables requiring jets in the event have additional uncertainties on the correction factor due to the jet energy scale and resolution. There is also an uncertainty due to the JVT. These uncertainties range between 1% and 16% depending on the bin/region.

- Pileup: There are two sources of uncertainties due to the pileup in events. The first is due to the MC modeling and designed to cover the uncertainty of the inelastic proton-proton cross section [209]. This uncertainty is less than 1.5% in all bins. The next is due to mis-identification of pileup jets and is found to be a less than 5% effect.

- Luminosity:The uncertainty on the luminosity collected for the 2015–2016 dataset was 3.2%. It is derived using a technique outlined in Ref. [210], using a van der Meer scan [211] performed in August 2015.

6.7 Total Uncertainties

Detailed in Section 6.5.1 and Section 6.6.2 are the uncertainties for the signal extraction and correction factors. Summarized briefly here are the total uncertainties for the entire cross section

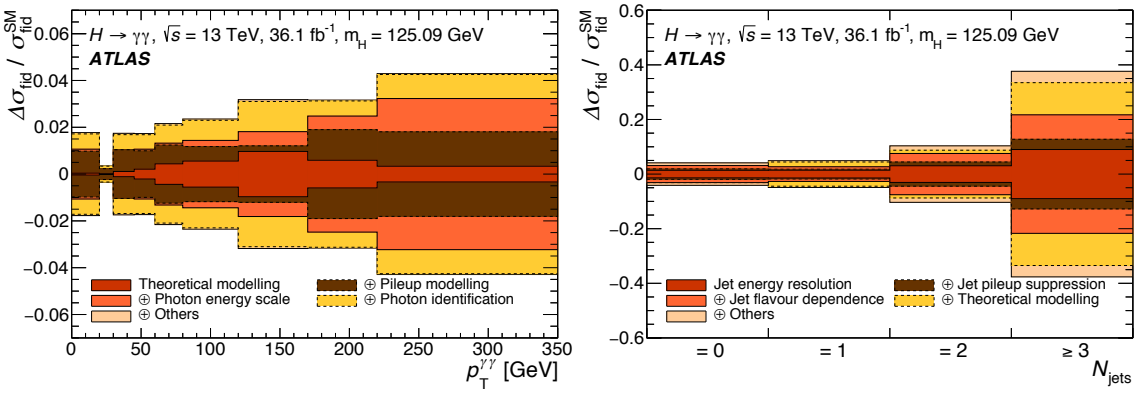

(a) $p_{\mathrm{T}}^{\gamma\gamma}$ (b) $N_{\mathrm{jets}}^{\geq 30\ \mathrm{GeV}}$

Figure 6.14: Summary of different uncertainties, sequentially summed in quadrature, on the correction factor for the (a) $p_{\mathrm{T}}^{\gamma\gamma}$ and (b) $N_{\mathrm{jets}}^{\geq 30\ \mathrm{GeV}}$ observables. Note the larger jet uncertainties for $N_{\mathrm{jets}}^{\geq 30\ \mathrm{GeV}}$.

extraction. Figure 6.15 shows the total uncertainties associated with the signal extraction, correction factors, luminosity, and statistics for all bins for the $p_{\mathrm{T}}^{\gamma\gamma}$ and $N_{\mathrm{jets}}^{\geq 30\ \mathrm{GeV}}$ differential distributions. The result is still dominated by statistical errors.

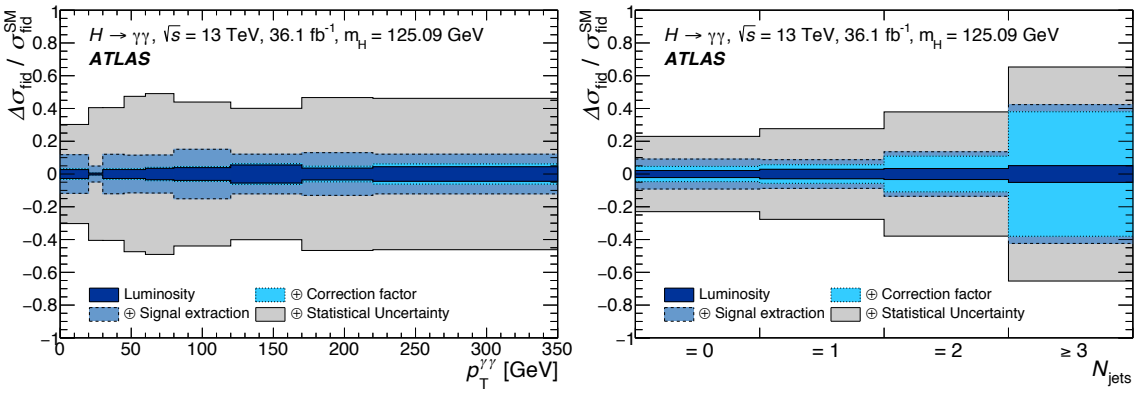

(a) $p_{\mathrm{T}}^{\gamma\gamma}$ (b) $N_{\mathrm{jets}}^{\geq 30\ \mathrm{GeV}}$

Figure 6.15: Signal extraction, correction factor, luminosity and statistical errors (sequentially summed in quadrature) are shown for the (a) $p_{\mathrm{T}}^{\gamma\gamma}$ and (b) $N_{\mathrm{jets}}^{\geq 30\ \mathrm{GeV}}$ observables.

6.8 Results

Unfolded measured fiducial regions and selected differential distributions results are presented in this section while Appendix C contains the remaining measured differential spectra. They are then compared with different SM truth level theoretical predictions. For different differential measurements, ggF predictions are combined with standard non-ggF predictions, referred to as $XH = \text{VBF} + VH + t\bar{t}H + b\bar{b}H$ in the figures. For a description of of the default simulations, refer to Section 6.2.2. The measured differential PDFs are then used to investigate BSM physics with an effective field theory framework

6.8.1 Measured Fiducial Regions and Differential Distributions

Figure 6.16 and Table 6.9 summarize the fiducial region measurements and comparisons with different theoretical predictions. The inclusive diphoton cross section is measured to be:

$$55 \pm 9\,(\text{stat.}) \pm 4\,(\text{syst.}) \pm 0.1\,(\text{theo.})\,\text{fb}\ , \tag{6.14}$$

compared with the Standard model prediction of 64 ± 2 fb. The inclusive cross section is compared with the N^{3}LO QCD calculation with NLO electroweak corrections and the Powheg NNLOPS prediction without electroweak corrections. The VBF-enhanced cross section is measured to be:

$$3.7 \pm 0.8\,(\text{stat.}) \pm 0.5\,(\text{syst.}) \pm 0.2\,(\text{theo.})\,\text{fb}\ , \tag{6.15}$$

compared with the predicted 2.3 ± 0.1 fb. This is compared with the default simulation, the Powheg NNLOPS prediction without corrections, and the Sherpa(Meps@Nlo) prediction which is a fixed order calculation at NLO for Higgs $+0, 1, 2, 3$ jets which are then merged with the Meps@Nlo merging scheme [192, 193, 212–221]. For the $N_{\text{lepton}} \geq 1$, High $E_{\text{T}}^{\text{miss}}$, and $t\bar{t}H$-enhanced regions in the absence of signals, 95% Confidence Level (CL) limits on the cross section were set.

Table 6.9: Table of measured cross sections for the diphoton inclusive and VBF-enhanced fiducial regions as well as 95% CL limits on the cross sections for the $N_{\text{lepton}} \geq 1$, High $E_{\text{T}}^{\text{miss}}$, and $t\bar{t}H$-enhanced fiducial regions. The measurements are done using the 36.1 fb^{-1}dataset collected in 2015–2016. Comparisons to the Standard Model predictions are shown.

Fiducial region	Measured cross section	SM prediction	
Diphoton fiducial	$55 \pm 9\,(\text{stat.}) \pm 4\,(\text{syst.}) \pm 0.1\,(\text{theo.})$ fb	64 ± 2 fb	[N^{3}LO + XH]
VBF-enhanced	$3.7 \pm 0.8\,(\text{stat.}) \pm 0.5\,(\text{syst.}) \pm 0.2\,(\text{theo.})$ fb	2.3 ± 0.1 fb	[default MC + XH]
$N_{\text{lepton}} \geq 1$	≤ 1.39 fb 95% CL	0.57 ± 0.03 fb	[default MC + XH]
High $E_{\text{T}}^{\text{miss}}$	≤ 1.00 fb 95% CL	0.30 ± 0.02 fb	[default MC + XH]
$t\bar{t}H$-enhanced	≤ 1.27 fb 95% CL	0.55 ± 0.06 fb	[default MC + XH]

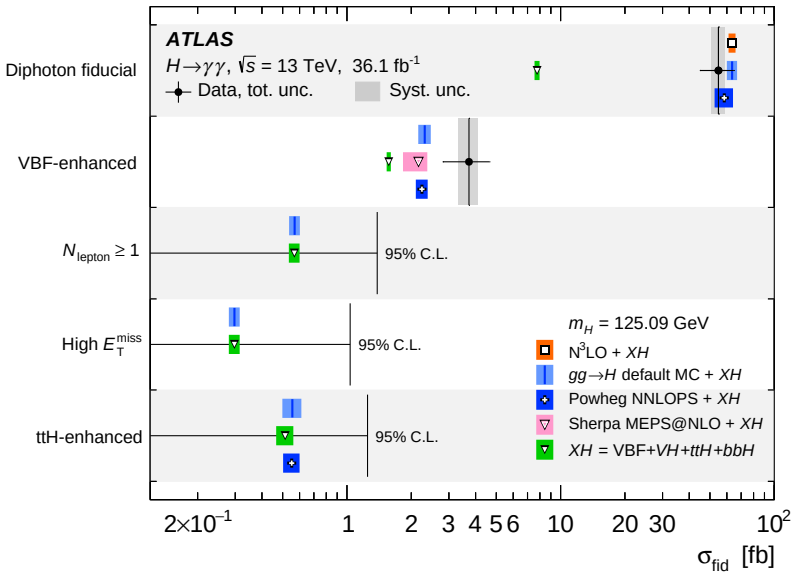

Figure 6.16: Measured cross sections for the diphoton inclusive and VBF-enhanced fiducial regions as well as 95% CL limits on the cross sections for the $N_{\text{lepton}} \geq 1$, High $E_{\text{T}}^{\text{miss}}$, and $t\bar{t}H$-enhanced fiducial regions. The measurements are done using the 36.1 fb^{-1}dataset collected in 2015–2016. Comparisons to multiple theoretical predictions are shown and summarized in the text.

The differential distributions for $p_{\text{T}}^{\gamma\gamma}$, $|y_{\gamma\gamma}|$, as well as inclusive and exclusive $N_{\text{jets}}^{\geq 30\text{ GeV}}$ can be seen in Figure 6.17. The $p_{\text{T}}^{\gamma\gamma}$ is sensitive to perturbative QCD modeling and at higher p_{T}, BSM physics. The $|y_{\gamma\gamma}|$ distribution is sensitive to ggF production mode and the $N_{\text{jets}}^{\geq 30\text{ GeV}}$ distribution can elucidate the nature of QCD modeling and rates of the different Higgs production mechanisms. The binning is chosen such that the expected signal significance is at least 2σ while trying to bin as fine as possible to extract meaningful shape information. The $|y_{\gamma\gamma}|$ is binned to be consistent with the binning structure in the photon identification as the identification cuts change as a function of η. The predictions are compared with the default MC simulation and others described in the following text.

For $p_{\text{T}}^{\gamma\gamma}$, the measured spectra is also compared with Hres [222, 223] which includes the prediction for $p_{\text{T}}^{\gamma\gamma}$ at NNLO with p_{T}^{H} resummation at next-to-next-to-leading logarithmic (NNLL) and RadISH+NNLOjet [224] which provides a $p_{\text{T}}^{\gamma\gamma}$ PDF prediction using a p_{T}^{H} resummation to NNLL and matching to the 1 jet NNLO differential spectrum from NNLOjet [225, 226]. Both contain corrections from finite top and bottom quark masses though Hres also includes charm quarks.

The $|y_{\gamma\gamma}|$ PDF is compared with the SCETlib+MCFM8 prediction which predicts the $|y_{\gamma\gamma}|$

shape at NNLO+NNLL′$_\varphi$[11] with applying a resummation of the virtual corrections to the gluon form factor [227, 228]. The NNLO predictions are derived from MCFM8 with zero-jettiness subtractions [229, 230].

The $N_{\text{jets}}^{\geq 30\ \text{GeV}}$ as seen in Figure 6.17c contains many other theoretical predictions for the inclusive and exclusive jet multiplicity. Aside from those mentioned above, the JVE+N^{3}LO 1 jet inclusive prediction [231] contains NNLL resummation in QCD of the p_{T} of the leading jet and then it is matched to the N^{3}LO total cross section. The STWZ-BLPTW prediction [232, 233] includes the NNLL′+NNLO[12] resummation for the p_{T} of the leading jet, and NLL′+NLO resummation for the subleading jet. The STWZ-BLPTW prediction is shown for both the inclusive and exclusive 0 and 1 jet cross sections and inclusive 2 jet cross section. The GoSam prediction [219,234] provides fixed-order loop contributions at NLO for the inclusive Higgs $+0, 1, 2, 3$ jet regions though is shown only for inclusive and exclusive regions where there is at least one jet. The MadGraph5_aMC@NLO prediction [175, 235], shown for all inclusive and exclusive multiplicity, is a calculation for up to two jets at NLO using the FxFx merging scheme [236] where the central merging scale is taken to be 30 GeV.

6.8.1.1 2017 Update

With the 2017 dataset adding 43.7 fb^{-1}, a small analysis was done with updates to $p_{\text{T}}^{\gamma\gamma}$, $|y_{\gamma\gamma}|$, $p_{\text{T}}^{j_1}$, and measuring the number of b-tagged jets produced in association with the Higgs boson. This is roughly consistent with a 50% improvement in the statistical precision of the analysis for regions and variables which were not rebinned. The total measured inclusive cross section is:

$$60.4 \pm 6.1\,(\text{stat.}) \pm 6.0\,(\text{syst.}) \pm 0.3\,(\text{theo.})\,\text{fb}\ . \tag{6.16}$$

The differential spectra for $p_{\text{T}}^{\gamma\gamma}$ and $|y_{\gamma\gamma}|$ are shown in Figure 6.18 with $p_{\text{T}}^{\gamma\gamma}$ being binned finer this time to probe the shape at lower transverse momentum. The $p_{\text{T}}^{\gamma\gamma}$ is compared to a new theoretical prediction, NNLOjet+SCET [237], which predicts the $p_{\text{T}}^{\gamma\gamma}$ spectra using a N^{3}LL resummation matched to an NNLO fixed-order calculation in the heavy top limit. The $p_{\text{T}}^{j_1}$ and number of b-tagged jets are shown in Appendix C.

[11] The subscript φ refers to the fact that the applied resummation is to the gluon form factor.

[12] The prime mark indicates the leading contributions from N^{3}LL (NNLL) are included as well as the full NNLL (NLL) corrections.

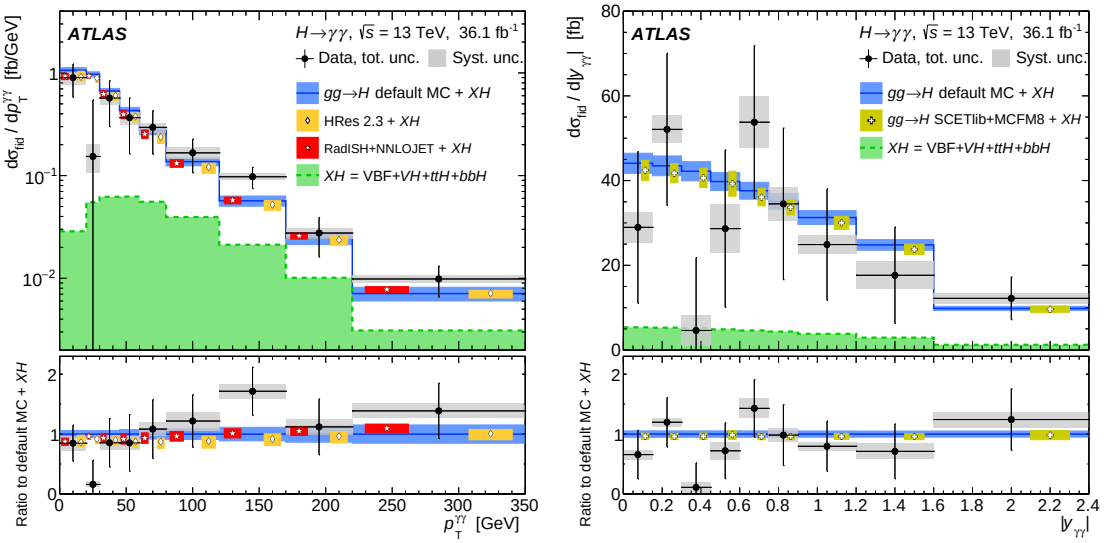

(a) $p_{\mathrm{T}}^{\gamma\gamma}$ (b) $|y_{\gamma\gamma}|$

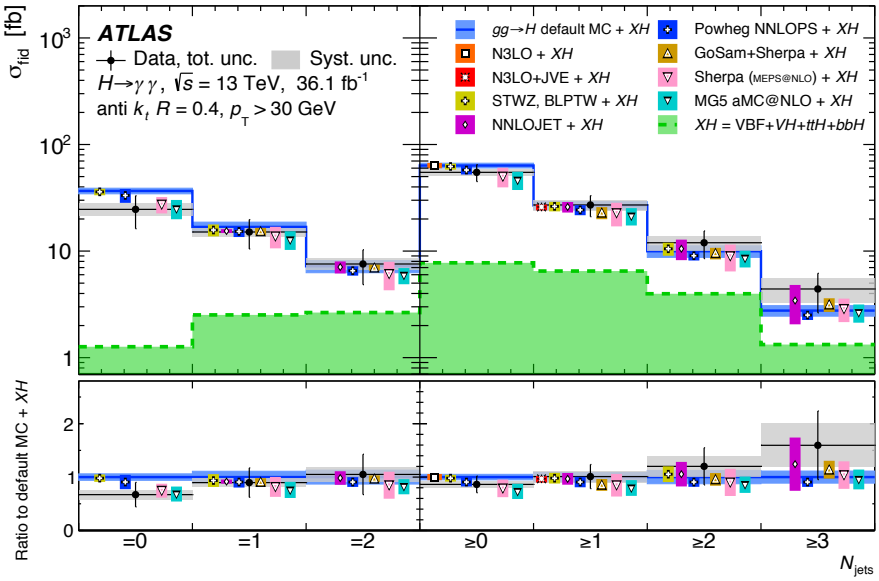

(c) $N_{\mathrm{jets}}^{\geq 30\ \mathrm{GeV}}$

Figure 6.17: Measured differential spectra for (a) $p_{\mathrm{T}}^{\gamma\gamma}$, (b) $|y_{\gamma\gamma}|$, and (c) $N_{\mathrm{jets}}^{\geq 30\ \mathrm{GeV}}$ compared with different theoretical predictions using the 36.1 fb^{-1}dataset collected in 2015–2016. The data are shown as filled black circles. The vertical error bar on each data point represents the total uncertainty in the measured cross section and the shaded gray band is the systematic component. The small contribution from VBF$+VH+t\bar{t}H+b\bar{b}H$ is also shown as a (green) histogram and denoted as XH.

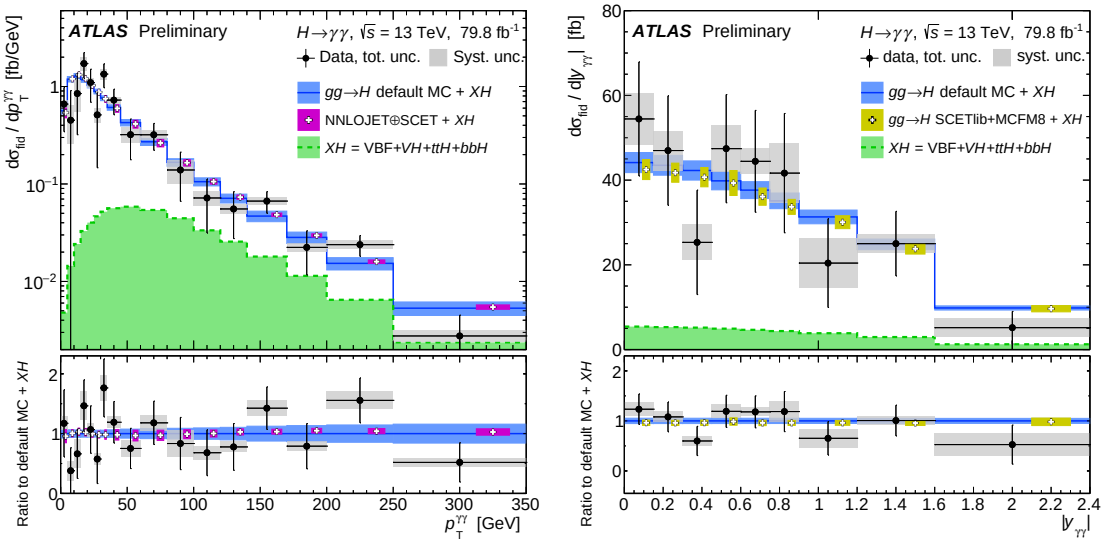

(a) $p_{\mathrm{T}}^{\gamma\gamma}$ (b) $|y_{\gamma\gamma}|$

Figure 6.18: Measured differential spectra for (a) $p_{\mathrm{T}}^{\gamma\gamma}$ and (b) $|y_{\gamma\gamma}|$ compared with different theoretical predictions using the 79.8 fb^{-1}dataset collected in 2015–2017.

6.9 Effective Field Theory Interpretations

While the results in the previous section were consistent with SM values, these can then be utilized to set limits on BSM physics in an effective field theory approach. Previously, ATLAS and CMS used a κ-framework, where couplings strengths were allowed to vary from the SM values. In this framework the strengths of the Higgs production and decay channels could differ, but the Higgs boson's kinematics would remain unchanged. Using an effective field theory approach, the BSM physics is parameterized by the addition of dimension-six operators ($\mathcal{O}_i$) with Wilson coefficients ($\bar{c}_i$), that fix the strength of the interaction to the SM Lagrangian:

$$\mathcal{L} = \mathcal{L}_{\mathrm{SM}} + \sum_i \bar{c}_i \mathcal{O}_i \ . \tag{6.17}$$

These new operators can specify new interactions between the Higgs boson and SM particles which can change the shapes of measured differential distributions as well as the rates.

A key assumption of this framework is that the interaction terms are low-energy effects from the new physics, which exists at a much higher energy scale. This is akin to the Fermi theory of beta decay [238], where weak decays of nuclei were studied at the scale of $\sim$ 10 MeV. The theory worked well to describe the low energy manifestations of the underlying gauge theory of

electroweak interactions, decades before the formation of the gauge theory because the true scale of the interaction (the W boson) was at 80 GeV.

6.9.1 Parameterization of the Effective Field Theory

The Effective Field Theory Lagrangian can be written as [239–242]:

$$\mathcal{L} = \mathcal{L}_{\text{SM}} + \sum_i c_i \mathcal{O}_i = \mathcal{L}_{\text{SM}} + \mathcal{L}_{\text{SILH}} + \mathcal{L}_{CP} + \mathcal{L}_{F_1} + \mathcal{L}_{F_2} + \mathcal{L}_G \ ; \tag{6.18}$$

where the six-dimensional operators have now been organized by the types of physics the new interactions produce. The terms $\mathcal{L}_{\text{SILH}}$ (Strongly Interacting Light Higgs) and $\mathcal{L}_{CP}$ (Charge conjugation-Parity) contain the interactions of interest to this analysis. $\mathcal{L}_{\text{SILH}}$ contains all CP even 3-point interactions of the Higgs boson with a pair of gauge bosons or an fermion-antifermion-fermion pair. The six-dimensional operators in $\mathcal{L}_{CP}$ contain the complementary CP-odd 3-point interactions. The other operators, which are not considered in the interpretation, produce triple and quartic anomalous couplings, and 4-point interactions between fermion-antifermion pairs and two Higgs bosons or a Higgs boson and an gauge boson. The $\mathcal{L}_{\text{SILH}}$ is defined as

$$\begin{aligned}
\mathcal{L}_{\text{SILH}} = {} & \frac{\bar{c}_H}{2v^2}\partial^\mu\big[\Phi^\dagger\Phi\big]\partial_\mu\big[\Phi^\dagger\Phi\big] + \frac{\bar{c}_T}{2v^2}\big[\Phi^\dagger \overleftrightarrow{D}^\mu \Phi\big]\big[\Phi^\dagger \overleftrightarrow{D}_\mu \Phi\big] - \frac{\bar{c}_6\lambda}{v^2}\big[\Phi^\dagger\Phi\big]^3 \\
& - \left[\frac{\bar{c}_u}{v^2} y_u \Phi^\dagger\Phi\ \Phi^\dagger \cdot Q_L u_R + \frac{\bar{c}_d}{v^2} y_d \Phi^\dagger\Phi\ \Phi Q_L d_R + \frac{\bar{c}_l}{v^2} y_\ell\ \Phi^\dagger\Phi\ \Phi L_L e_R + \text{h.}c.\right] \\
& + \frac{ig\ \bar{c}_W}{m_W^2}\big[\Phi^\dagger \frac{\sigma_k}{2} \overleftrightarrow{D}^\mu \Phi\big] D^\nu W^k_{\mu\nu} + \frac{ig'\ \bar{c}_B}{2m_W^2}\big[\Phi^\dagger \overleftrightarrow{D}^\mu \Phi\big]\partial^\nu B_{\mu\nu} \\
& + \frac{2ig\ \bar{c}_{HW}}{m_W^2}\big[D^\mu\Phi^\dagger \frac{\sigma_k}{2} D^\nu \Phi\big] W^k_{\mu\nu} + \frac{ig'\ \bar{c}_{HB}}{m_W^2}\big[D^\mu\Phi^\dagger D^\nu\Phi\big] B_{\mu\nu} \\
& + \frac{g'^2\ \bar{c}_\gamma}{m_W^2}\Phi^\dagger\Phi B_{\mu\nu}B^{\mu\nu} + \frac{g_s^2\ \bar{c}_g}{m_W^2}\Phi^\dagger\Phi G^a_{\mu\nu}G_a^{\mu\nu} \ ;
\end{aligned} \tag{6.19}$$

where Φ is the Higgs doublet, $G_{\mu\nu}$, $W_{\mu\nu}$ and $B_{\mu\nu}$ are gauge fields for the gluon, weak, and photon, respectively. The Wilson coefficients, $\bar{c}$, are free parameters, λ stands for the Higgs quartic coupling and y_u, y_d and y_ℓ are the Yukawa coupling matrices in flavor space. The $U(1)_Y$, $SU(2)_L$ and $SU(3)_c$ coupling constants are denoted by g', g, and g_s. The Pauli matrices of $SU(2)_L$ are denoted by σ^k.

The $\mathcal{L}_{CP}$ is defined as

$$\begin{aligned}
\mathcal{L}_{CP} = {} & \frac{ig\ \tilde{c}_{HW}}{m_W^2} D^\mu\Phi^\dagger \frac{\sigma_k}{2} D^\nu\Phi \widetilde{W}^k_{\mu\nu} + \frac{ig'\ \tilde{c}_{HB}}{m_W^2} D^\mu\Phi^\dagger D^\nu\Phi \widetilde{B}_{\mu\nu} + \frac{g'^2\ \tilde{c}_\gamma}{m_W^2}\Phi^\dagger\Phi B_{\mu\nu}\widetilde{B}^{\mu\nu} \\
& + \frac{g_s^2\ \tilde{c}_g}{m_W^2}\Phi^\dagger\Phi G^a_{\mu\nu}\widetilde{G}_a^{\mu\nu} + \frac{g^3\ \tilde{c}_{3W}}{m_W^2}\epsilon_{ijk} W^i_{\mu\nu} W^{\nu j}_{\ \ \rho}\widetilde{W}^{\rho\mu k} + \frac{g_s^3\ \tilde{c}_{3G}}{m_W^2} f_{abc} G^a_{\mu\nu} G^{\nu b}_{\ \ \rho}\widetilde{G}^{\rho\mu c} \ ;
\end{aligned} \tag{6.20}$$

where the $\widetilde{G}_{\mu\nu}$, $\widetilde{W}_{\mu\nu}$ and $\widetilde{B}_{\mu\nu}$ are dual fields defined as $\widetilde{X}_{\mu\nu} = \frac{1}{2}\,\epsilon_{\mu\nu\rho\sigma}\,X^{\rho\sigma}$, f_{abc} are the structure constants of the Gell-Mann matrices, and ϵ_{ijk} is the Levi-Civita symbol.

While the Lagrangians above may seem complex, the analysis can be distilled by using the measured distributions to constrain the twelve Wilson coefficients from the above $\mathcal{L}_{\text{SILH}}$ and $\mathcal{L}_{\text{CP}}$. Furthermore, the $\bar{c}_T$, combination of $\bar{c}_T$ and $\bar{c}_\gamma$, and combination of $\bar{c}_W$ and $\bar{c}_B$ have been constrained by LEP or Z mass measurements [241, 243–245]. Additionally, the $\bar{c}_H$ and $\bar{c}_\gamma$ (and its CP conjugate operator) operators have very small effects on the observed cross sections and therefore disregarded.

This leaves only the $\bar{c}_g$, $\bar{c}_{HW}$, $\bar{c}_{HB}$ terms, and their CP conjugate operators, as the contributions to the effective theory that would induce observable effects in the differential measurements. The $\bar{c}_g$ terms add new interactions between Higgs bosons and gluons, which modifies the $gg \to H$ process and produces interference with SM diagrams. The conjugate operator does not interfere but both operators can modify the total cross section and produce small changes in the kinematics of Higgs bosons produced by ggF. The $\bar{c}_{HW}$ and $\bar{c}_{HB}$ (and complex conjugates) terms modify the interactions between the Higgs and vector bosons. These interactions can affect the total cross section and can greatly change the kinematic distributions sensitive to the VBF and VH productions modes. This includes modifications to the Higgs p_{T} spectrum and jet sensitive variables such as $N_{\text{jets}}^{\geq 30\ \text{GeV}}$, m_{jj}, $|\Delta\phi_{jj}|$, or $p_{\text{T}}^{j_1}$.

In the $H \to \gamma\gamma$ EFT framework, the new effective Lagrangian can now be written as:

$$\mathcal{L}_{\text{eff}} = \bar{c}_g\mathcal{O}_g + \bar{c}_{HW}\mathcal{O}_{HW} + \bar{c}_{HB}\mathcal{O}_{HB} + \tilde{c}_g\tilde{\mathcal{O}}_g + \tilde{c}_{HW}\tilde{\mathcal{O}}_{HW} + \tilde{c}_{HB}\tilde{\mathcal{O}}_{HB}\ , \tag{6.21}$$

where now only the relevant terms are presented. The effects of these operators on the measured differential cross sections can be seen in Figure 6.19, where the Wilson coefficients are set to different values and the ratio to the SM prediction is shown. The new gluon operators lead to large increases in total cross section and the additional Higgs-boson operators result in very different kinematics, with more boosted Higgs and an increase in the number of events when the Higgs boson is produced with no accompanying jets.

6.9.2 Results

The effective Lagrangian was implemented in FEYNRULES [243] and event samples were produced for varying values of a Wilson coefficient. The PROFESSOR method [246] is used to interpolate between these samples. This is performed for each bin of a given differential distribution, providing a parameterization of the effective Lagrangian prediction. After the unblinding of the differential

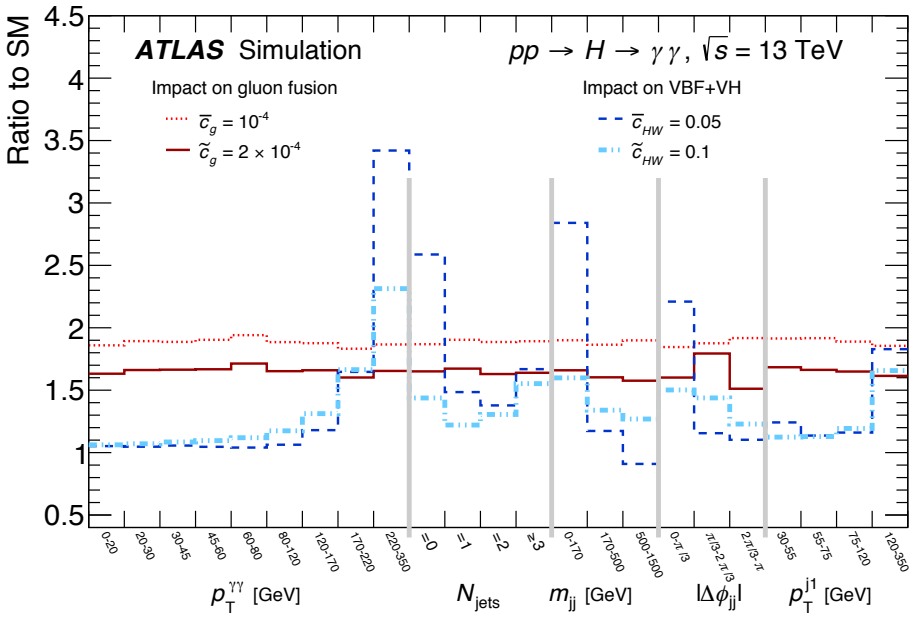

Figure 6.19: Ratios of differential cross sections with non-zero Wilson coefficients to the differential cross sections predicted by the SM. The impact of non-zero $\bar{c}_g$ and $\tilde{c}_g$ is shown relative to the SM ggF prediction, which lies at ratio = 1. The impact of a nonzero $\bar{c}_{HW}$ or $\tilde{c}_{HW}$ is shown relative to the SM VBF and VH expectations.

cross section data, Figure 6.20 shows the cross sections compared with the SM hypothesis and to two BSM hypotheses where $\tilde{c}_g = 1 \times 10^{-4}$ and $\bar{c}_{HW} = 0.05$ for the 5 analyzed observables of $p_{\mathrm{T}}^{\gamma\gamma}$, $N_{\mathrm{jets}}^{\geq 30\ \mathrm{GeV}}$, m_{jj}, $|\Delta\phi_{jj}|$, and $p_{\mathrm{T}}^{j_1}$. Limits on Wilson coefficients are then set by constructing a likelihood function using the measured and predicted differential cross sections of the five analyzed variables.

Table 6.10 displays the observed and expected 95% CL limits for the four Wilson coefficients of interest. Limits on $\bar{c}_g$ and $\tilde{c}_g$ are calculated when all other Wilson coefficients are set to zero. Limits on $\bar{c}_{HW}$ and $\tilde{c}_{HW}$ are derived with $\bar{c}_{HB} = \bar{c}_{HW}$ and $\tilde{c}_{HB} = \tilde{c}_{HW}$, respectively, with all other Wilson coefficients set to zero. This is to ensure the partial width for $H \to Z\gamma$ remains unchanged as value of $|\bar{c}_{HW} - \tilde{c}_{HW}| > 0.03$ lead to large widths of $Z\gamma$, which is constrained by experimental limits.

Figure 6.21 shows the 68% and 95% confidence intervals obtained from scanning $\bar{c}_{HW}$ and $\tilde{c}_{HW}$ simultaneously. All other Wilson coefficients, except for $\bar{c}_{HB} = \bar{c}_{HW}$ and $\tilde{c}_{HB} = \tilde{c}_{HW}$, are set to zero. This result is produced using the information of the $p_{\mathrm{T}}^{\gamma\gamma}$, $N_{\mathrm{jets}}^{\geq 30\ \mathrm{GeV}}$, m_{jj}, $|\Delta\phi_{jj}|$, and $p_{\mathrm{T}}^{j_1}$ spectra. The shape deformation of the observed 68% confidence interval results from both shape and yield differences between data and expectations. This is due to the six-dimensional operators of

Table 6.10: Observed and expected intervals at 95% CL for the $\bar{c}_g$ and $\bar{c}_{HW}$ Wilson coefficients and their conjugate coefficients. Limits on $\bar{c}_g$ and $\tilde{c}_g$ are calculated when all other Wilson coefficients are set to zero. Limits on $\bar{c}_{HW}$ and $\tilde{c}_{HW}$ are derived with $\bar{c}_{HB} = \bar{c}_{HW}$ and $\tilde{c}_{HB} = \tilde{c}_{HW}$, respectively.

Coefficient	Observed 95% CL limit	Expected 95% CL limit
$\bar{c}_g$	$[-0.8, 0.1] \times 10^{-4} \cup [-4.6, -3.8] \times 10^{-4}$	$[-0.4, 0.5] \times 10^{-4} \cup [-4.9, -4.1] \times 10^{-4}$
$\tilde{c}_g$	$[-1.0, 0.9] \times 10^{-4}$	$[-1.4, 1.3] \times 10^{-4}$
$\bar{c}_{HW}$	$[-5.7, 5.1] \times 10^{-2}$	$[-5.0, 5.0] \times 10^{-2}$
$\tilde{c}_{HW}$	$[-0.16, 0.16]$	$[-0.14, 0.14]$

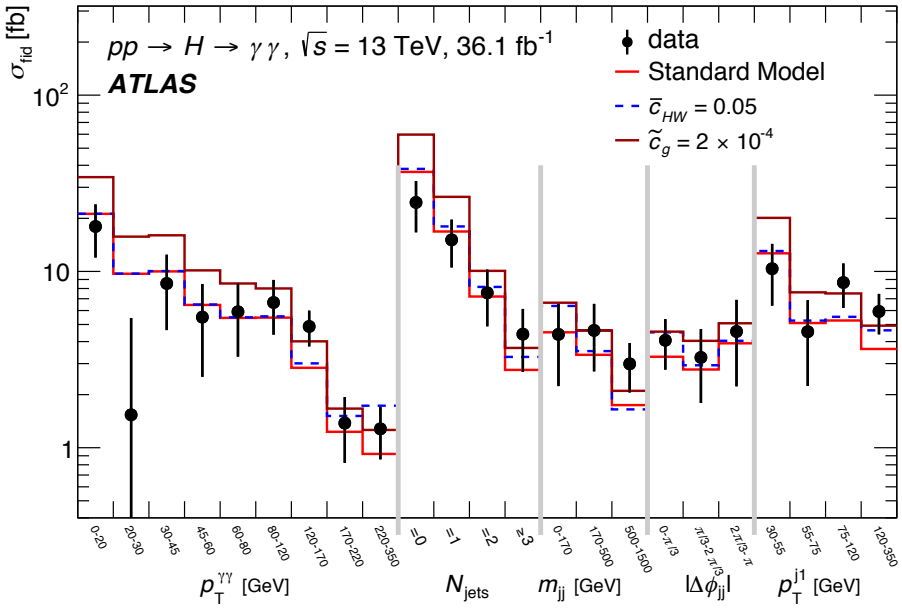

Figure 6.20: Measured differential cross sections as a function of $p_{\mathrm{T}}^{\gamma\gamma}$, $N_{\mathrm{jets}}^{\geq 30\ \mathrm{GeV}}$, jj, $|\Delta\phi_{jj}|$, and $p_{\mathrm{T}}^{j_1}$ are compared to the SM hypothesis and two BSM hypotheses with $\tilde{c}_g = 1 \times 10^{-4}$ and $\bar{c}_{HW} = 0.05$. In this plot, the effects of the $\bar{c}_{HW}$ coefficient due to VBF and VH are much less (fractionally) than in Figure 6.19 due to the large contribution from ggF Higgs production.

the $\bar{c}_{HW}$ Wilson coefficient can destructively interfere with the SM contributions. A negative value of $\bar{c}_{HW}$ reduces the overall predicted cross section in the zero jet and low m_{jj} bins, where deficits are observed in the data. The operators of the of the $\tilde{c}_{HW}$ Wilson coefficient only increase the cross section from its SM value and can enhance the predicted cross sections in the higher jet multiplicity bins, which is also observed in the data.

These results improve upon the ATLAS Run 1 results [143] by a factor of ~ 2.

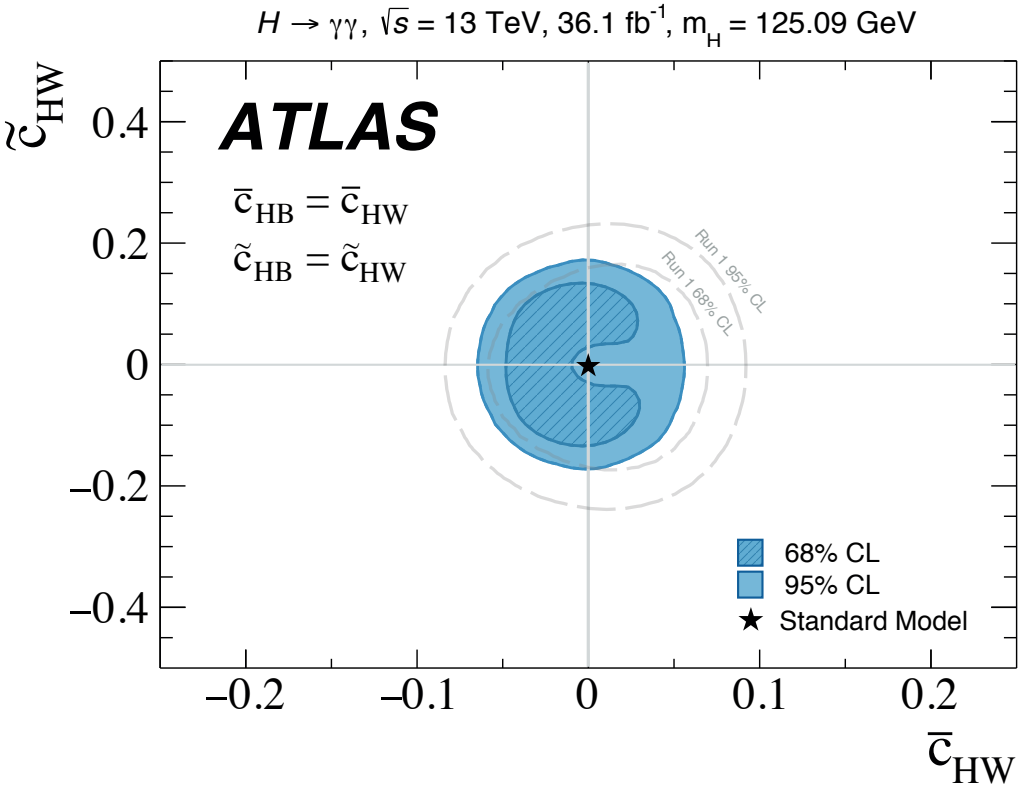

Figure 6.21: The observed 68% (dark) and 95% (light) confidence level intervals for the $\bar{c}_{HW}$ and $\tilde{c}_{HW}$ Wilson coefficients. Limits on $\bar{c}_{HW}$ and $\tilde{c}_{HW}$ are derived with $\bar{c}_{HB} = \bar{c}_{HW}$ and $\tilde{c}_{HB} = \tilde{c}_{HW}$, respectively. Additionally, the SM expectation at (0,0) is shown, along with with the Run 1 confidence intervals [143].

Chapter 7

Search for Exotic Higgs Decays

"If God came down and told me where to look for Supersymmetry, he'd say to look in the diphoton + $E_{\mathrm{T}}^{\mathrm{miss}}$ channel."

— H. H. 'Brig' Williams,

At visiting day in 2013 to the author.[13]

7.1 Introduction

In the previous chapter a precision measurement of Higgs boson properties was discussed. To this date no significant deviation from SM predictions have been observed in combined Higgs measurements from ATLAS and CMS. With minimal model assumptions, the Branching Fraction (BF) of the Higgs boson to new processes Beyond the Standard Model (BSM) is constrained to be less than 34% at the 95% confidence level [247, 248]. This chapter will focus on using the Higgs boson as a tool to probe beyond the Standard Model physics.

As discussed in Section 2.4, a wide variety of theories predict decays of the Higgs boson to BSM particles [54]. In a class of SUSY models called Gauge Mediated Supersymmetry Breaking (GMSB) [55–59] (discussed in detail in Section 2.4.2), there are some mechanisms that produce a 125 GeV Higgs boson consistent with current measurements [63–67]. In GMSB models, the Higgs boson can decay to a very light gravitino $\tilde{G}$ (the Lightest Supersymmetric Particle (LSP)) and a neutralino $\tilde{\chi}_1^0$ (the next-to-lightest supersymmetric particle (NLSP)) [76]. A diagram of this process is shown in Figure 7.1a. The neutralino in turn decays to a photon (γ) and a gravitino ($\tilde{G}$), leading to a photon and missing transverse momentum in the final state. This process can also be realized in the context of the Next-to-Minimal Supersymmetric Standard Model (NMSSM) [83, 249], where the Higgs boson decays to a singlino $\tilde{\chi}_1^0$ (LSP) and Bino $\tilde{\chi}_2^0$ (NLSP) which in turn decays to a photon

[13] There may or may not have been alcohol involved before this statement was made.

and $\tilde{\chi}_1^0$. In NMSSM scenarios the LSP mass is less constrained than in GMSB models where the gravitino is nearly massless.

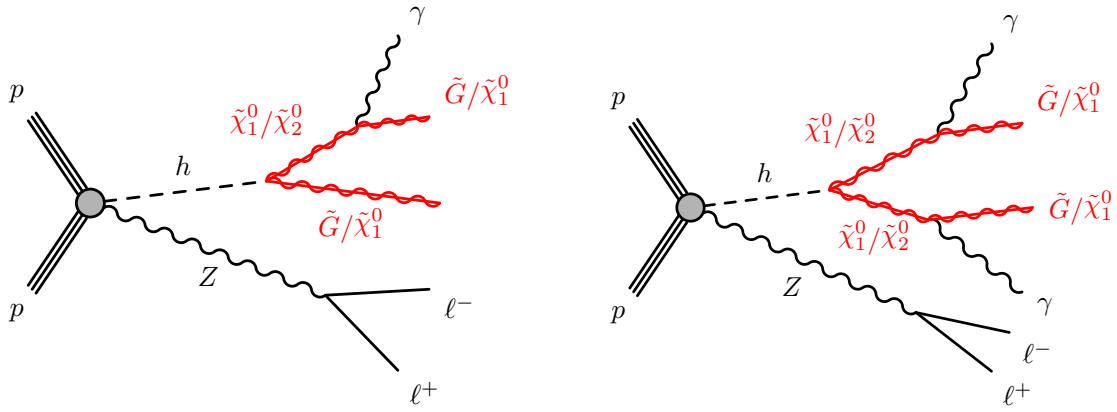

(a) $h \to \tilde{\chi}_1^0\tilde{G} \to \gamma\tilde{G}\tilde{G}$ / $h \to \tilde{\chi}_2^0\tilde{\chi}_1^0 \to \gamma\tilde{\chi}_1^0\tilde{\chi}_1^0$

(b) $h \to \tilde{\chi}_1^0\tilde{\chi}_1^0 \to \gamma\tilde{G}\gamma\tilde{G}$ / $h \to \tilde{\chi}_2^0\tilde{\chi}_2^0 \to \gamma\tilde{\chi}_1^0\gamma\tilde{\chi}_1^0$

Figure 7.1: Diagrams for the production, in association with a Z, and GMSB/NMSSM decay of the Higgs boson leading to a final state of two leptons + (a) $\gamma + E_{\mathrm{T}}^{\mathrm{miss}}$ and (b) $\gamma\gamma + E_{\mathrm{T}}^{\mathrm{miss}}$. The $\gamma + E_{\mathrm{T}}^{\mathrm{miss}}$ final state is produced when $m_h/2 < m_{\tilde{\chi}_1^0}(m_{\tilde{\chi}_2^0}) < m_h$, while the $\gamma\gamma + E_{\mathrm{T}}^{\mathrm{miss}}$ final state is realized when $m_{\tilde{\chi}_1^0}(m_{\tilde{\chi}_2^0}) < m_h/2$.

In GMSB models, the Higgs boson can decay to an $\tilde{\chi}_1^0$ and $\tilde{G}$ in the case when $m_h/2 < m_{\tilde{\chi}_1^0} < m_h$ as this is the only kinematically allowed decay. When $m_{\tilde{\chi}_1^0} < m_h/2$, the Higgs boson is allowed to decay directly to two NLSP neutralinos , each decaying to a photon and LSP gravitino [78](Figure 7.1a). Alternatively, in NMSSM models the Higgs can decay to an $\tilde{\chi}_2^0$ and $\tilde{\chi}_1^0$ directly in the case when $m_h/2 < m_{\tilde{\chi}_2^0} < m_h$ and into two NLSP Bino-like with each decaying to a singlino-like LSP neutralino and a photon when $m_{\tilde{\chi}_2^0} < m_h/2$. A diagram of this process can be seen in Figure 7.1b. This two photon final state is expected to dominate when $m_{\tilde{\chi}_1^0}(m_{\tilde{\chi}_2^0}) < m_h/2$.

Higgs bosons produced in association with a Z boson decaying to muons or electrons are considered in order to reduce backgrounds and provide clean kinematic handles on the Higgs boson decay products. This chapter presents a search using events containing two same flavor opposite-sign, isolated electrons or muons, at least one isolated photon and missing transverse momentum. The search is performed using $79.8\,\mathrm{fb}^{-1}$of proton-proton collisions collected at $\sqrt{s} = 13\,\mathrm{TeV}$ with the ATLAS detector at the LHC in 2015, 2016, and 2017 and is available as a conference note [5]. In the absence of a significant excess over the SM background processes prediction, the total number of expected and observed events in the signal region is used to set limits on $(\sigma/\sigma_{SM}) \times \mathrm{BF}$ (Section 7.7). Here, σ refers to the cross section of a Higgs boson produced in association with a Z from

pp collisions at $\sqrt{s} = 13\,\text{TeV}$, and BF is the branching fraction of the Higgs boson to a $\gamma + E_{\text{T}}^{\text{miss}}$ or $\gamma\gamma + E_{\text{T}}^{\text{miss}}$ final state.

The ATLAS experiment sought these processes in Run 1 by probing the VBF production mode of the Higgs boson [250]. An exclusion of $(\sigma/\sigma_{SM}) \times \text{BF}(h \to \tilde{\chi}_1^0\tilde{\chi}_1^0 \to \gamma\tilde{G}\gamma\tilde{G})$ above $20-35\%$ and $(\sigma/\sigma_{SM}) \times \text{BF}(h \to \tilde{\chi}_1^0\tilde{G} \to \gamma\tilde{G}\tilde{G})$ above $25-80\%$ was derived at the 95% confidence level for the majority of phase space, depending on the masses of the NLSP and LSP. The CMS experiment sought a similar signature using the ggF and ZH production modes, and excluded $(\sigma/\sigma_{SM}) \times$ BFs above $7-15\%$ at the 95% CL for models with massless gravitinos [251]. Other monophoton/diphoton + missing transverse momentum searches [252–257] are not sensitive to this model since p_{T} and $E_{\text{T}}^{\text{miss}}$ cuts exceed those kinematically possible from a Higgs decay. The goal of this analysis from the inception was to be sensitive to Higgs boson branching fractions to this process at the sub 10% level for *all* NLSP/LSP masses.

The analysis is performed in a single bin signal region, known as a "cut and count" analysis. The signal-background discriminating power lies in the kinematics of constructed four-vectors of the $\gamma + E_{\text{T}}^{\text{miss}}$ and dileptons. Because the resolution of the physics objects is important and the signal has a low $E_{\text{T}}^{\text{miss}}$ signature, events with any jets are vetoed. Events are also vetoed if more than two leptons are present. The major backgrounds in this phase space are $WZ \to e\nu\ell\ell$[14] where the electron from the W fakes a photon and $Z+\text{jets}$ where a jet is mis-identified as a photon. Therefore understanding and using data-driven techniques to estimate these backgrounds are key to having a meaningful result. These fake analyses can be reviewed in Section 7.4.1 and 7.4.2 for electron-to-photon and photon-to-jet fakes, respectively.

In addition to the analysis, Section 7.8 includes an optimization for the full Run 2 dataset.

7.2 Dataset and Simulation

7.2.1 Dataset

The analysis was performed with $\sqrt{s} = 13\,\text{TeV}$ pp collisions recorded in 2015–2017 corresponding to $79.8\,\text{fb}^{-1}$. Discussion regarding the pileup and luminosity delivered of the dataset can be seen in Section 3.1.

[14] ℓ in this chapter refers to electron and muons only, not taus.

7.2.2 Monte Carlo Signal Samples

Signal events for the $Z \to \ell\ell$ and $h \to \tilde{\chi}_1^0\tilde{\chi}_1^0 \to \gamma\tilde{G}\gamma\tilde{G}$ or $h \to \tilde{\chi}_1^0\tilde{G} \to \gamma\tilde{G}\tilde{G}$ processes were produced at leading order with MadGraph5_aMC@NLO using the SUSY simplified model framework [258, 259]. In this framework the MSSM is used as the BSM model so the processes generated are actually the $h \to \tilde{\chi}_2^0\tilde{\chi}_1^0 \to \gamma\tilde{\chi}_1^0\tilde{\chi}_1^0$ and $h \to \tilde{\chi}_2^0\tilde{\chi}_2^0 \to \gamma\tilde{\chi}_1^0\gamma\tilde{\chi}_1^0$ processes. Fifty-five equally spaced points of interest were generated across the NLSP/LSP phase space allowed by the $m_H = 125$ GeV Higgs. This corresponds to roughly 10 GeV spacing for NLSP and LSP masses. The Z boson was forced to decay to electrons and muons in equal amounts. Samples were generated with the NNPDF2.3LO PDF set, using the A14 set of tuned parameters of Pythia8 for the parton-shower and hadronization simulation. The remaining stable particles that have a lifetime longer than 10 ps are processed through a fast detector simulation based on a parameterization of the performance of the calorimeters [195]. The cross section for a SM Higgs boson produced in association with the $Z \to \ell\ell$ process, is taken from Ref. [32].

7.2.3 Monte Carlo Background Samples

While the dominant background processes are derived from data-driven control regions (see Section 7.4), the $Z\gamma$, $Z\gamma\gamma$, $W\gamma\gamma$, $t\bar{t}\gamma$, and other small contributions are modeled with Monte Carlo simulation. Events in an electron rich control region are also compared with WZ MC simulation.

Events containing a vector boson decaying leptonically and one (two) photons are simulated with the Sherpa [192] event generator which emphasizes matrix-element/parton-shower merging. Matrix elements including all diagrams with 3 (4) electroweak couplings are calculated with up to 3 (4) partons at next-to-leading order and merged with the parton shower according to the ME+PS@NLO prescription [214]. Events containing a single vector boson, dibosons, or tribosons are all generated with the Sherpa+ ME+PS@NLO prescription as well. The NNPDF3.0 NNLO PDF set [176] is used in conjunction with a dedicated parton shower tuning developed by the Sherpa authors [193].

Top-antitop quark pair with a photon or Z boson events were generated using MadGraph5_aMC@NLO [175] at LO. This setup was also used to generate 3 top, 4 top, $t\bar{t} + W$, and $t\bar{t} + WW$ events. Samples were generated with the NNPDF2.3LO PDF set [260], using the A14 set of tuned parameters [177] of Pythia8 [156–158] for the parton-shower and hadronization simulation.

Events with a single top-antitop quark pair, a single top or antitop quark, W + a single top

or antitop, and Z's produced in association with a Higgs boson decaying to $Z\gamma$, $\tau\tau$, or WW are generated and showered using Powheg+Pythia8 [164–166] with the NNPDF3.0 NNLO PDF set.

The generated events were passed through a full detector simulation based on Geant4 [190,191]. Events are then overlaid with multiple proton-proton collisions which are simulated with the soft QCD processes of Pythia8 using the A2 set of tuned parameters [197] and the MSTW2008LO PDF set. The simulated events are weighted to reproduce the distribution of average number of interactions per bunch crossing observed in data. This pileup includes minimum bias, cavern backgrounds, and beam gas and halo effects.

7.3 Event Selection

7.3.1 Signal Region Selection Criteria

Signal events are characterized by moderate missing transverse momentum, and the $Z \to \ell\ell$ pair balancing the $h \to \gamma E_{\mathrm{T}}^{\mathrm{miss}}$ system in the transverse plane. Only isolated photons passing the *Tight* identification criteria with $p_{\mathrm{T}} > 25\,\mathrm{GeV}$ are considered, and the vector sum of the two highest p_{T} photons (or one if two are not present in the event) with the $E_{\mathrm{T}}^{\mathrm{miss}}$ defines the $\gamma E_{\mathrm{T}}^{\mathrm{miss}}$ system. The signal photon p_{T} spectrum depends on the NLSP and LSP masses. For fixed NLSP mass, photon transverse momentum increases as LSP mass decreases, although this does not translate into higher signal efficiency as the $E_{\mathrm{T}}^{\mathrm{miss}}$ distribution becomes softer. Therefore there is a careful balance of decreasing the $E_{\mathrm{T}}^{\mathrm{miss}}$ requirement and tighter selection criteria of other variables.

The Z boson system is composed of two opposite-sign electrons or muons, where the highest (second highest) p_{T} lepton must have $p_{\mathrm{T}} > 25$ (20) GeV. The reconstructed dilepton invariant mass must be within 10 GeV of the Z boson mass, and the ϕ separation of the leptons is required to be less than 1.4 rad[15]. In order to reduce contamination from diboson processes the event must have exactly 2 leptons.

Background rejection is achieved predominately by selecting events with $E_{\mathrm{T}}^{\mathrm{miss}} > 95\,\mathrm{GeV}$. To improve the resolution of the $E_{\mathrm{T}}^{\mathrm{miss}}$, and to reduce contamination from background processes containing top quarks or vector bosons with associated jets, events containing jets with $p_{\mathrm{T}} > 30\,\mathrm{GeV}$ are also rejected. In addition, two variables are defined to exploit the balance of the Z and $\gamma E_{\mathrm{T}}^{\mathrm{miss}}$ systems and reject Z + jet events.

[15] This is primarily to select boosted Z bosons, and optimization studies suggested this cut performed better than a $p_{\mathrm{T}}^{\ell\ell}$ cut.

1. $\Delta\phi_{\ell\ell,\gamma E_{\mathrm{T}}^{\mathrm{miss}}}$: the absolute ϕ separation of the two lepton system and the $\gamma E_{\mathrm{T}}^{\mathrm{miss}}$ system.

2. $\mathrm{Bal}_{p_{\mathrm{T}}}$: the scalar p_{T} asymmetry of the $\ell\ell$ and $\gamma E_{\mathrm{T}}^{\mathrm{miss}}$ systems, $\frac{|p_{\mathrm{T}}^{\ell\ell} - p_{\mathrm{T}}^{\gamma E_{\mathrm{T}}^{\mathrm{miss}}}|}{p_{\mathrm{T}}^{\gamma E_{\mathrm{T}}^{\mathrm{miss}}}}$.

A modest improvement in the signal-to-background ratio is achieved by selecting events with $\mathrm{Bal}_{p_{\mathrm{T}}} < 0.2$ and $\Delta\phi_{\ell\ell,\gamma E_{\mathrm{T}}^{\mathrm{miss}}} > 2.8$. In order to select events from the collisions, 140M events were selected by the single and dilepton triggers shown in Table 7.1.

Table 7.1: Lepton triggers and p_{T} trigger thresholds for electrons and muons, requiring one or two leptons. In a given year the logical OR of electron and muon triggers, for both one and two objects, is taken.

	Single lepton	Threshold [GeV]	Two lepton	Thresholds [GeV]
Electron trigger year				
2015	HLT_e24_lhmedium_L1EM20VH	24	HLT_2e12_lhloose_L12EM10VH	12, 12
2016	HLT_e24_lhmedium_L1EM20VH	24	HLT_2e12_lhloose_L12EM10VH	12, 12
2017	HLT_e26_lhtight_nod0_ivarloose	26	HLT_2e17_lhvloose_nod0[16]	17, 17
2017			HLT_2e24_lhvloose_nod0	24, 24
Muon trigger year				
2015	HLT_mu20_iloose_L1MU15	20	HLT_mu18_mu8noL1	18, 8
2016	HLT_mu26_ivarmedium	26	HLT_mu22_mu8noL1	22, 8
2017	HLT_mu26_ivarmedium	26	HLT_mu22_mu8noL1	22, 8

The selection described above and summarized in Table 7.2 is designed to optimize the search over the full phase space of NLSP/LSP masses for both monophoton and diphoton final states. Dedicated signal regions for different NLSP/LSP splitting or final states could improve the sensitivity of the analysis though adds additional complexity. This is briefly explored in the optimization for the Run 2 dataset outlined in Section 7.8.

Optimization of Signal Region

In order to determine the optimal selection criteria as detailed in the previous text, iterative studies and scans of the defined variables and others were performed. Understanding the most likely potential Standard Model processes which look signal-like can shed light on the approach taken by this analysis. Minor backgrounds like $t\bar{t}\gamma$, Standard Model Higgs boson decays, double fakes (one lepton faked as well as the photon), and triboson processes are taken to be negligible at first order.

As stated in the Introduction, the goal of this analysis was to be sensitive to Higgs branching fractions at the sub 10% level. This means at a 10% BF of Higgs to neutralinos or neutralino/gravitino produced in association with a Z boson decaying to electrons or muons, the predicted cross section

[16] In 2017 the dielectron trigger was accidentally prescaled for part of the data taking, so the next unprescaled trigger was used in addition to the prescaled trigger.

Table 7.2: Summary of the optimized signal region selection criteria for the ZH search using 79.8 fb^{-1}of data.

Objects
Photons: $p_{\mathrm{T}} > 25$ GeV, $\lvert\eta\rvert < 1.37$ or $1.52 < \lvert\eta\rvert < 2.37$, *Tight* ID, `FixedCutTight` Isolation
Electrons: $p_{\mathrm{T}}^{e_1} > 25$ GeV, $p_{\mathrm{T}}^{e_2} > 20$ GeV, $\lvert\eta\rvert < 1.37$ or $1.52 < \lvert\eta\rvert < 2.47$ *Medium* ID, `GradientLoose` Isolation
Muons: $p_{\mathrm{T}}^{\mu_1} > 25$ GeV, $p_{\mathrm{T}}^{\mu_2} > 20$ GeV, $\lvert\eta\rvert < 2.7$, *Medium* ID, `GradientLoose` Isolation
Jets: anti-k_t, $R = 0.4$, $p_{\mathrm{T}} > 30$ GeV, $\lvert y\rvert < 4.4$
Preselection
Single or dilepton unprescaled trigger with trigger matching
Jet veto
Require exactly two leptons
Require at least one photon
Event Topology
***Z* window**: $\lvert m_Z - m_{\ell\ell}\rvert < 10$ GeV
Missing transverse momentum: $E_{\mathrm{T}}^{\mathrm{miss}} > 95$ GeV
Event p_{T} balance: $\frac{\lvert p_{\mathrm{T}}^{\ell\ell} - p_{\mathrm{T}}^{\gamma E_{\mathrm{T}}^{\mathrm{miss}}}\rvert}{p_{\mathrm{T}}^{\gamma E_{\mathrm{T}}^{\mathrm{miss}}}} < 0.2$
Event ϕ balance: $\Delta\phi_{\ell\ell,\gamma E_{\mathrm{T}}^{\mathrm{miss}}} > 2.8$
$\ell\ell$ separation: $\Delta\phi(\ell,\ell) < 1.4$

would be 6.0 fb! A brief discussion of the major backgrounds and how they led to the shaping of the analysis variables follow, though the majority of the background estimation is discussed in Section 7.4.

The first major background is the production of the Standard Model $Z\gamma$, which has a cross section (calculated with Sherpa) of over 80 pb for Z's decaying to electrons or muons and $p_{\mathrm{T}}^{\gamma_1} > 15$ GeV. With a perfect detector, SM $Z\gamma$ events with no associated jets coming from the hard scatter should have no missing transverse momentum as the momentum of the photon and Z boson should balance perfectly. Because of this, the kinematics of the constructed 4-vector of the $\gamma E_{\mathrm{T}}^{\mathrm{miss}}$ system and a high $E_{\mathrm{T}}^{\mathrm{miss}}$ requirement can reduce the background from $Z\gamma$. However if one cuts too high on $E_{\mathrm{T}}^{\mathrm{miss}}$, signal efficiency is lost.

The next major background considered is electrons mis-identified as photons, coming primarily from Standard Model WZ. At $\sqrt{s} = 13$ TeV, the diboson cross section according to the latest theory prediction [261] is $48.2^{+1.1}_{-1.0}$ pb and requiring the Z decaying to electrons or muons and the W decaying to $e\nu$, the cross section is roughly 200 fb. With a boosted Z recoiling off of a electron and neutrino, this process looks very much like the signal process. Understanding the electron to photon fake rate and trying to get a handle on the kinematics of the $\gamma E_{\mathrm{T}}^{\mathrm{miss}}$ systems are vital to reducing this background.

The last background considered in the optimization process is jets mis-identified as photons, mostly arising from Standard Model $Z+$jets. These jets generally contain light mesons or π^0's that decay to photons are mis-identified as prompt photons. Because these events have jets calibrated as photons the balance of the $\gamma E_{\mathrm{T}}^{\mathrm{miss}}$ and dilepton system is generally skewed as there is fake detector $E_{\mathrm{T}}^{\mathrm{miss}}$ introduced into the event by the mis-measured fake photon. The cross section of this process is on the order of $10-100$s of fbs as the $Z \to \ell\ell$ cross section is 1.89 ± 0.05 nb [262] and the jet-to-photon mis-identification rate is roughly 1 in $10,000$. Both a high $E_{\mathrm{T}}^{\mathrm{miss}}$ cut or balance in ϕ/p_{T} of the dilepton and $\gamma E_{\mathrm{T}}^{\mathrm{miss}}$ system can help reduce this background. Understanding this fake rate and process is vital as strong QCD processes are produced at the LHC in exorbitant quantities.

The optimization is performed on three grid points corresponding to NLSP-LSP masses of 70-40, 120-0, and 40-0 GeV in order to probe the whole phase space. The $m_{\mathrm{NLSP}} = 70$, $m_{\mathrm{LSP}} = 40$ GeV point was chosen as according to initial studies it had one of the worst sensitivities of the monophoton region, excluding points closest to the kinematic edge where the NLSP mass approaches the LSP mass. After the baseline objects were chosen to maximize signal acceptance, intermediate cuts of other event topology values were chosen. This baseline event topology criteria involved selecting two leptons with an invariant mass within 15 GeV of the Z mass, one signal photon with $p_{\mathrm{T}} > 25$ GeV, $E_{\mathrm{T}}^{\mathrm{miss}} > 55$ GeV, and $\mathrm{Bal}_{p_{\mathrm{T}}}$ of less than 0.4. Iterative scans over pairs of $E_{\mathrm{T}}^{\mathrm{miss}}$, $\Delta\phi_{\ell\ell,\gamma E_{\mathrm{T}}^{\mathrm{miss}}}$, $\mathrm{Bal}_{p_{\mathrm{T}}}$, $p_{\mathrm{T}}^{\ell\ell}$, $\Delta\phi(\ell,\ell)$were performed, changing the cut value and recording the Z-score. The Z-score value is defined as the significance of a signal observation in one-sided Gaussian standard deviations. For each cut iteration the number of signal events and background events are found and assumed to be from a double Poisson counting experiment. A 30% uncertainty on the background was assumed and together with the number of events a useful approximation of the significance (the Z-score) can be extracted from the incomplete β-function and inverse error function [263, 264].

After this initial scan was performed and an optimal selection criteria was defined, a second scan was performed over each set of two variables, this time fixing all other cuts to their newly "optimized" value. The process was then done iteratively, relaxing different variables and re-doing scans until the optimized values were constant. This was done for the three signal points and the selection criteria chosen was the one that had the best acceptance in all areas of phase space, and not necessarily the most optimal for a specific grid point. The values of selected 2D scans over different variables can be see in Figures 7.2–7.5. Each figure shows two different variable scans for the three different grid points.

In addition to the final variables which make up the final selection criteria, other strategies and variables were considered. The cut of the $\Delta\phi(\ell,\ell)$ is analogous to a cut on the $p_{\mathrm{T}}^{\ell\ell}$, and thus both

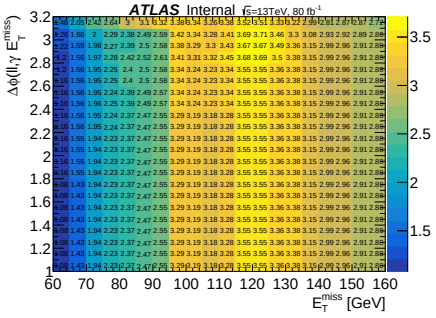

(a) $E_{\mathrm{T}}^{\mathrm{miss}}$ vs.$\Delta\phi_{\ell\ell,\gamma E_{\mathrm{T}}^{\mathrm{miss}}}$, GP: 70, 40 GeV

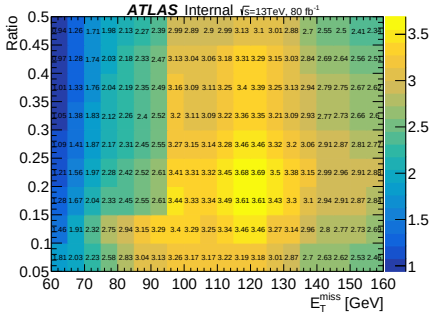

(b) $E_{\mathrm{T}}^{\mathrm{miss}}$ vs.$\mathrm{Bal}_{p_{\mathrm{T}}}$, GP: 70, 40 GeV

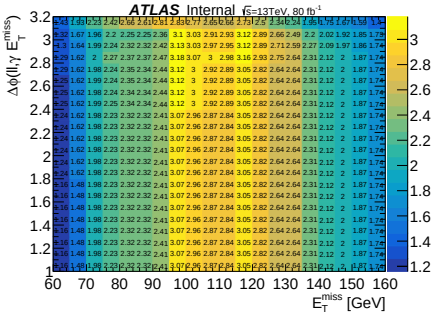

(c) $E_{\mathrm{T}}^{\mathrm{miss}}$ vs.$\Delta\phi_{\ell\ell,\gamma E_{\mathrm{T}}^{\mathrm{miss}}}$, GP: 120, 0 GeV

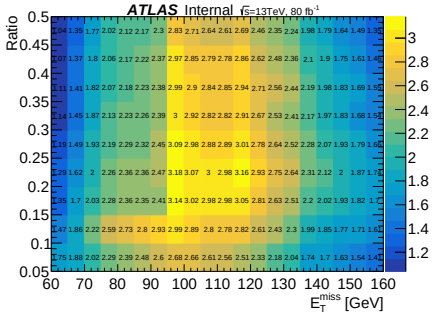

(d) $E_{\mathrm{T}}^{\mathrm{miss}}$ vs.$\mathrm{Bal}_{p_{\mathrm{T}}}$, GP: 120, 0 GeV

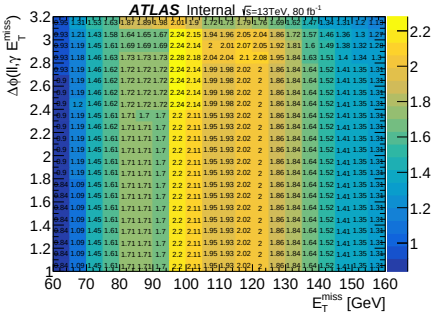

(e) $E_{\mathrm{T}}^{\mathrm{miss}}$ vs.$\Delta\phi_{\ell\ell,\gamma E_{\mathrm{T}}^{\mathrm{miss}}}$, GP: 40, 0 GeV

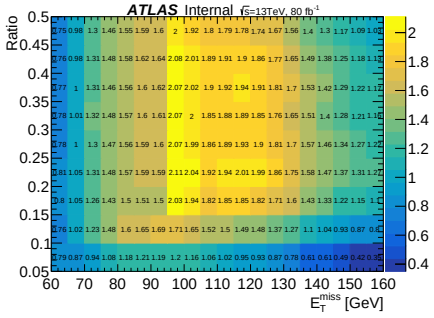

(f) $E_{\mathrm{T}}^{\mathrm{miss}}$ vs.$\mathrm{Bal}_{p_{\mathrm{T}}}$, GP: 40, 0 GeV

Figure 7.2: 2D optimization scans over $E_{\mathrm{T}}^{\mathrm{miss}}$ vs. $\Delta\phi_{\ell\ell,\gamma E_{\mathrm{T}}^{\mathrm{miss}}}$ and $E_{\mathrm{T}}^{\mathrm{miss}}$ vs. $\mathrm{Bal}_{p_{\mathrm{T}}}$(Ratio). The Z score metric (defined in the text) is used with a flat 30% background uncertainty. All selection criteria are applied except the two cuts scanned over. The three grid points (GP) scanned are $m_{\mathrm{NLSP}} = 70$ GeV, $m_{\mathrm{LSP}} = 40$ GeV (a) and (b), $m_{\mathrm{NLSP}} = 120$ GeV, $m_{\mathrm{LSP}} = 0$ GeV (c) and (d), $m_{\mathrm{NLSP}} = 40$ GeV, $m_{\mathrm{LSP}} = 0$ GeV (e) and (f).

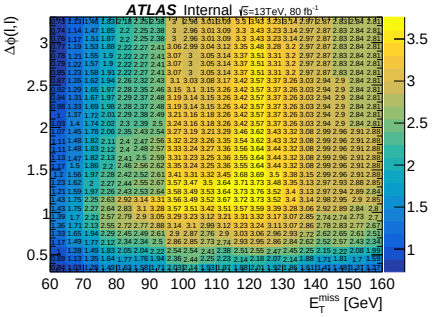

(a) $E_{\mathrm{T}}^{\mathrm{miss}}$ vs. $\Delta\phi(\ell,\ell)$, GP: $70, 40$ GeV

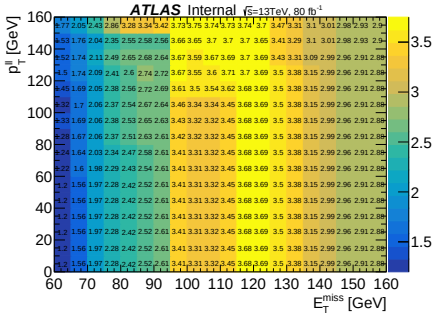

(b) $E_{\mathrm{T}}^{\mathrm{miss}}$ vs. $p_{\mathrm{T}}^{\ell\ell}$, GP: $70, 40$ GeV

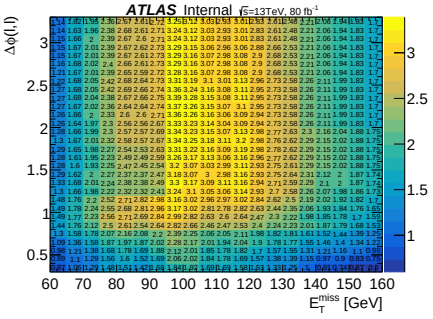

(c) $E_{\mathrm{T}}^{\mathrm{miss}}$ vs. $\Delta\phi(\ell,\ell)$, GP: $120, 0$ GeV

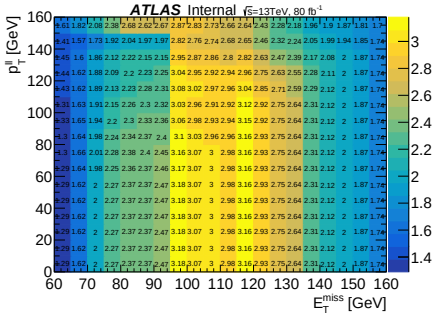

(d) $E_{\mathrm{T}}^{\mathrm{miss}}$ vs. $p_{\mathrm{T}}^{\ell\ell}$, GP: $120, 0$ GeV

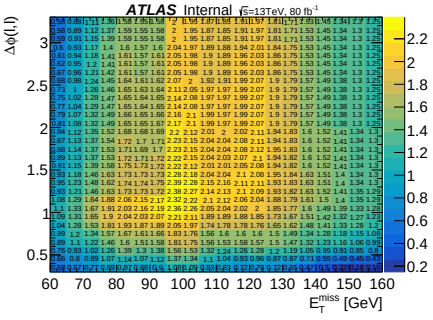

(e) $E_{\mathrm{T}}^{\mathrm{miss}}$ vs. $\Delta\phi(\ell,\ell)$, GP: $40, 0$ GeV

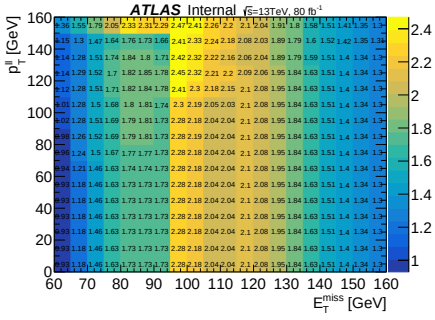

(f) $E_{\mathrm{T}}^{\mathrm{miss}}$ vs. $p_{\mathrm{T}}^{\ell\ell}$, GP: $40, 0$ GeV

Figure 7.3: 2D optimization scans over $E_{\mathrm{T}}^{\mathrm{miss}}$ vs. $\Delta\phi(\ell,\ell)$ and $E_{\mathrm{T}}^{\mathrm{miss}}$ vs. $p_{\mathrm{T}}^{\ell\ell}$. The Z score metric (defined in the text) is used with a flat 30% background uncertainty. All selection criteria are applied except the two cuts scanned over. The three grid points (GP) scanned are $m_{\mathrm{NLSP}} = 70$ GeV, $m_{\mathrm{LSP}} = 40$ GeV (a) and (b), $m_{\mathrm{NLSP}} = 120$ GeV, $m_{\mathrm{LSP}} = 0$ GeV (c) and (d), $m_{\mathrm{NLSP}} = 40$ GeV, $m_{\mathrm{LSP}} = 0$ GeV (e) and (f).

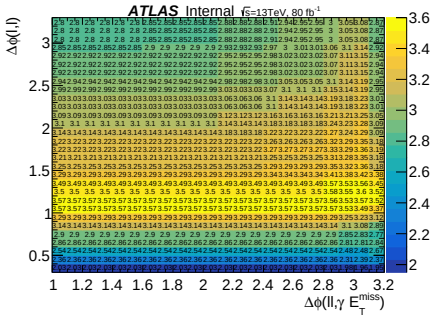

(a) $\Delta\phi_{\ell\ell,\gamma E_{\mathrm{T}}^{\mathrm{miss}}}$ vs. $\Delta\phi(\ell,\ell)$, GP: 70, 40 GeV

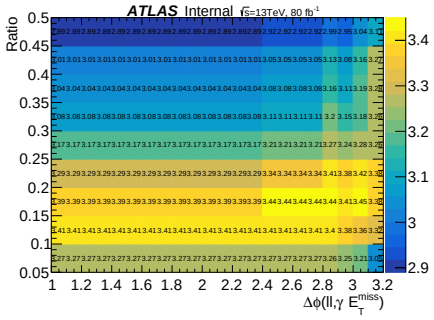

(b) $\Delta\phi_{\ell\ell,\gamma E_{\mathrm{T}}^{\mathrm{miss}}}$ vs. $\mathrm{Bal}_{p_{\mathrm{T}}}$, GP: 70, 40 GeV

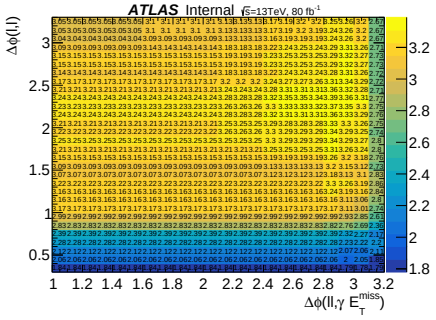

(c) $\Delta\phi_{\ell\ell,\gamma E_{\mathrm{T}}^{\mathrm{miss}}}$ vs. $\Delta\phi(\ell,\ell)$, GP: 120, 0 GeV

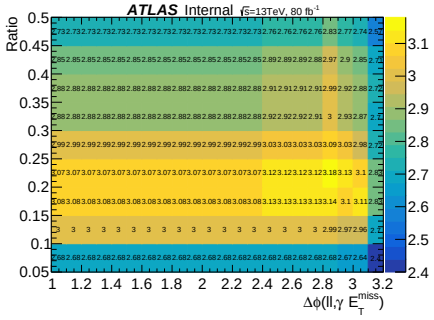

(d) $\Delta\phi_{\ell\ell,\gamma E_{\mathrm{T}}^{\mathrm{miss}}}$ vs. $\mathrm{Bal}_{p_{\mathrm{T}}}$, GP: 120, 0 GeV

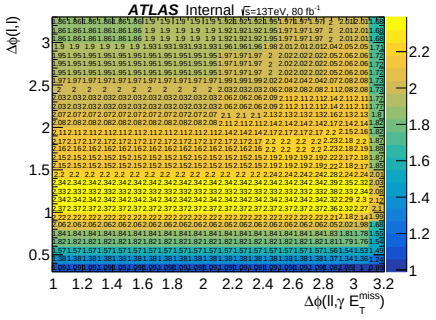

(e) $\Delta\phi_{\ell\ell,\gamma E_{\mathrm{T}}^{\mathrm{miss}}}$ vs. $\Delta\phi(\ell,\ell)$, GP: 40, 0 GeV

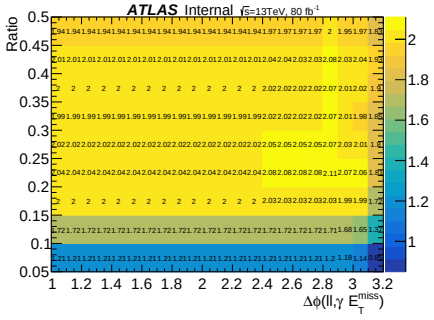

(f) $\Delta\phi_{\ell\ell,\gamma E_{\mathrm{T}}^{\mathrm{miss}}}$ vs. $\mathrm{Bal}_{p_{\mathrm{T}}}$, GP: 40, 0 GeV

Figure 7.4: 2D optimization scans over $\Delta\phi_{\ell\ell,\gamma E_{\mathrm{T}}^{\mathrm{miss}}}$ vs. $\Delta\phi(\ell,\ell)$ and $\Delta\phi_{\ell\ell,\gamma E_{\mathrm{T}}^{\mathrm{miss}}}$ vs. $\mathrm{Bal}_{p_{\mathrm{T}}}$(Ratio). The Z score metric (defined in the text) is used with a flat 30% background uncertainty. All selection criteria are applied except the two cuts scanned over. The three grid points (GP) scanned are $m_{\mathrm{NLSP}} = 70$ GeV, $m_{\mathrm{LSP}} = 40$ GeV (a) and (b), $m_{\mathrm{NLSP}} = 120$ GeV, $m_{\mathrm{LSP}} = 0$ GeV (c) and (d), $m_{\mathrm{NLSP}} = 40$ GeV, $m_{\mathrm{LSP}} = 0$ GeV (e) and (f).

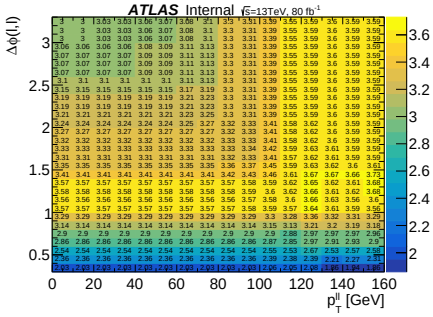

(a) $\Delta\phi(\ell,\ell)$ vs. $p_{\mathrm{T}}^{\ell\ell}$, GP: 70, 40 GeV

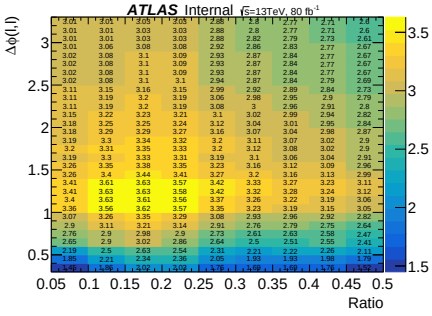

(b) $\mathrm{Bal}_{p_{\mathrm{T}}}$ vs. $\Delta\phi(\ell,\ell)$, GP: 70, 40 GeV

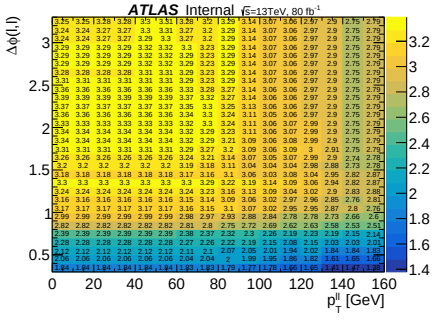

(c) $\Delta\phi(\ell,\ell)$ vs. $p_{\mathrm{T}}^{\ell\ell}$, GP: 120, 0 GeV

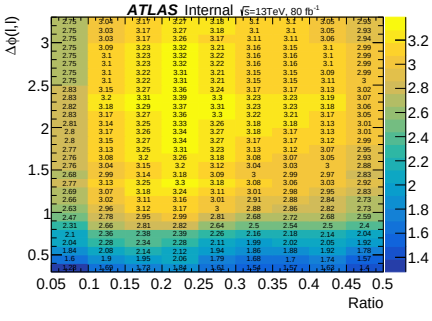

(d) $\mathrm{Bal}_{p_{\mathrm{T}}}$ vs. $\Delta\phi(\ell,\ell)$, GP: 120, 0 GeV

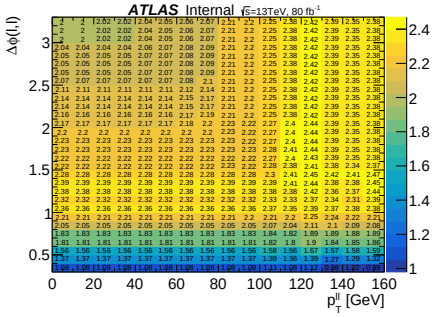

(e) $\Delta\phi(\ell,\ell)$ vs. $p_{\mathrm{T}}^{\ell\ell}$, GP: 40, 0 GeV

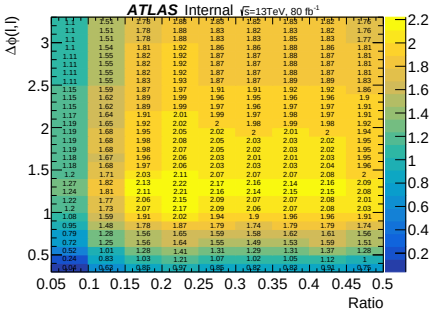

(f) $\mathrm{Bal}_{p_{\mathrm{T}}}$ vs. $\Delta\phi(\ell,\ell)$, GP: 40, 0 GeV

Figure 7.5: 2D optimization scans over $\Delta\phi(\ell,\ell)$ vs. $p_{\mathrm{T}}^{\ell\ell}$ and $\mathrm{Bal}_{p_{\mathrm{T}}}$ (Ratio) vs. $\Delta\phi(\ell,\ell)$. The Z score metric (defined in the text) is used with a flat 30% background uncertainty. All selection criteria are applied except the two cuts scanned over. The three grid points (GP) scanned are $m_{\mathrm{NLSP}} = 70$ GeV, $m_{\mathrm{LSP}} = 40$ GeV (a) and (b), $m_{\mathrm{NLSP}} = 120$ GeV, $m_{\mathrm{LSP}} = 0$ GeV (c) and (d), $m_{\mathrm{NLSP}} = 40$ GeV, $m_{\mathrm{LSP}} = 0$ GeV (e) and (f).

were not needed. Exploiting the properties of the $\gamma E_{\mathrm{T}}^{\mathrm{miss}}$ system also can improve the sensitivity of the analysis. The $m_T^{\gamma, E_{\mathrm{T}}^{\mathrm{miss}}}$ of the system has an endpoint near the NLSP mass while the $W \to e\nu$ has an endpoint at m_W. Because there is one signal region, no explicit cut on this can be made or sensitivity to the different neutralino masses is greatly reduced. Using a multi-bin fit of this variable to extract significance can improve the sensitivity of the analysis for next iterations, though a deeper understanding of the background modeling is needed. The shape of the $\Delta\phi(E_{\mathrm{T}}^{\mathrm{miss}}, \gamma)$ distribution also has the same problem of depending of the NLSP/LSP masses, and likewise is not used as a discriminating variable. Other variables studied included $m_{\ell\ell\gamma}$, boosting in the $\gamma E_{\mathrm{T}}^{\mathrm{miss}}$ system and building variables in its frame, total sum p_{T} of hard objects in the event, and object based $E_{\mathrm{T}}^{\mathrm{miss}}$-significance.

For certain variables, at more extreme cut values there is a higher significance in the single photon region but the significance degrades in the diphoton region. For instance it may be beneficial for higher NLSP masses to cut harder on $E_{\mathrm{T}}^{\mathrm{miss}}$ and softer on $\Delta\phi(\ell, \ell)$ (because the $\mathrm{Bal}_{p_{\mathrm{T}}}$ cut keeps things balanced), but if one does so the significance in the $h \to \tilde{\chi}_1^0\tilde{\chi}_1^0 \to \gamma\tilde{G}\gamma\tilde{G}$ region is significantly degraded due to the softer $E_{\mathrm{T}}^{\mathrm{miss}}$ signature of the diphoton region. There is also noticeable shape in the η^{γ_1} distribution. The signal is overwhelmingly in the barrel because higher q^2 processes tend to be more central. Since sensitivity is driven by the barrel region, investigations of requiring only central photons or using a two bin shape fit in the η distribution were performed though they did not improve the expected significance by more than a few percent and the simpler approach was chosen.

Kinematic and event topology variable distributions can be seen after applying all of the selection criteria in Figure 7.6. This includes all the minor backgrounds discussed in the "other" category. The shape of the $\Delta\phi(E_{\mathrm{T}}^{\mathrm{miss}}, \gamma)$ and $m_T^{\gamma, E_{\mathrm{T}}^{\mathrm{miss}}}$ can be seen in Figures 7.6f and 7.6g respectively. There are 2.1 total background events with over 70% of the background expected from electron-to-photon fakes. Across most of the $h \to \tilde{\chi}_1^0\tilde{G} \to \gamma\tilde{G}\tilde{G}$ region, there is greater than 8 signal events. An example cutflow of the background processes and signal point for $m_{\mathrm{NLSP}} = 70$ GeV, $m_{\mathrm{LSP}} = 40$ GeV can be seen in Table 7.3.

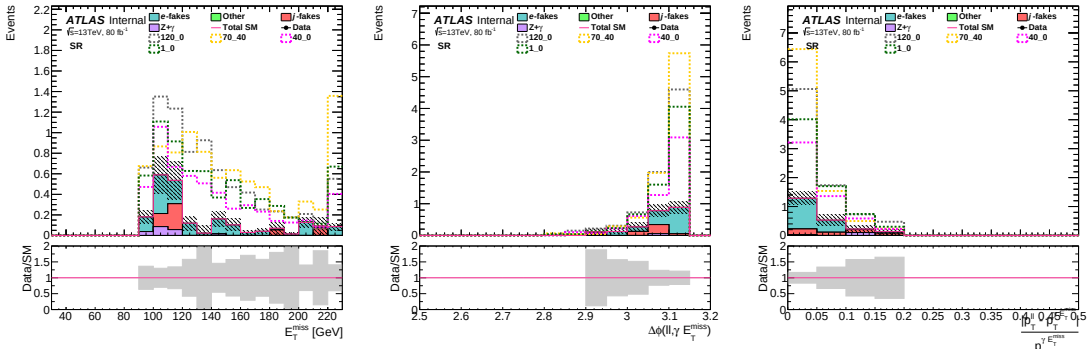

(a) $E_{\mathrm{T}}^{\mathrm{miss}}$ (b) $\Delta\phi_{\ell\ell,\gamma E_{\mathrm{T}}^{\mathrm{miss}}}$ (c) $\mathrm{Bal}_{p_{\mathrm{T}}}$

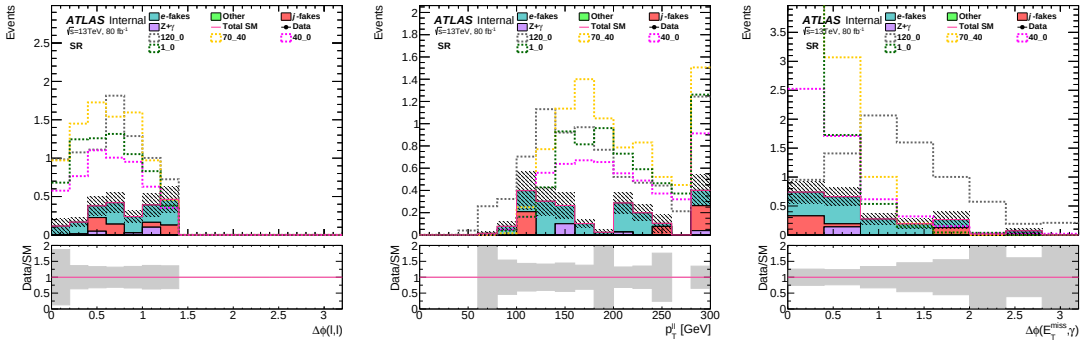

(d) $\Delta\phi(\ell,\ell)$ (e) $p_{\mathrm{T}}^{\ell\ell\,\dagger}$ (f) $\Delta\phi(E_{\mathrm{T}}^{\mathrm{miss}},\gamma)^{\dagger}$

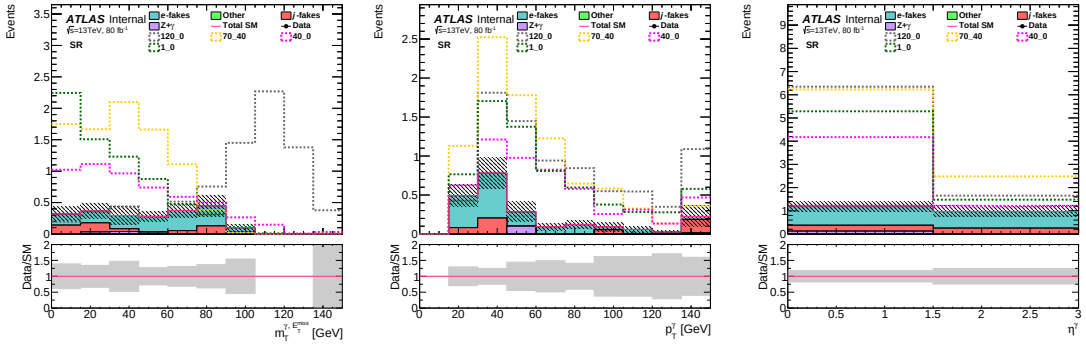

(g) $m_T^{\gamma,E_{\mathrm{T}}^{\mathrm{miss}}\,\dagger}$ (h) $p_{\mathrm{T}}^{\gamma_1}$ (i) η^{γ_1}

Figure 7.6: Distributions of (a) $E_{\mathrm{T}}^{\mathrm{miss}}$, (b) $\Delta\phi_{\ell\ell,\gamma E_{\mathrm{T}}^{\mathrm{miss}}}$, (c) $\mathrm{Bal}_{p_{\mathrm{T}}}$, (d) $\Delta\phi(\ell,\ell)$, (e) $p_{\mathrm{T}}^{\ell\ell\,\dagger}$, (f) $\Delta\phi(E_{\mathrm{T}}^{\mathrm{miss}},\gamma)^{\dagger}$, (g) $m_T^{\gamma,E_{\mathrm{T}}^{\mathrm{miss}}\,\dagger}$, (h) $p_{\mathrm{T}}^{\gamma_1}$, and (i) η^{γ_1} in the signal region with data-driven backgrounds. Four grid points of $m_{\mathrm{NLSP}} = 70$ GeV, $m_{\mathrm{LSP}} = 40$ GeV, $m_{\mathrm{NLSP}} = 120$ GeV, $m_{\mathrm{LSP}} = 0$ GeV, $m_{\mathrm{NLSP}} = 40$ GeV, $m_{\mathrm{LSP}} = 0$ GeV, and $m_{\mathrm{NLSP}} = 1$ GeV, $m_{\mathrm{LSP}} = 0$ GeV are overlaid. † denotes variables not used to define the signal region definition.

Table 7.3: Signal region cutflow for backgrounds and signal point with $m_{\text{NLSP}} = 70$ GeV and $m_{\text{LSP}} = 40$ GeV. Error quoted is statistical only.

Cut	Signal	$Z\gamma$	$e \to \gamma$	j $\to \gamma$	Other
$\lvert m_{\ell\ell} - m_Z \rvert < 10$ GeV	85.92 ± 1.39	599385 ± 1398	-	-	336.8 ± 27.25
$p_{\text{T}}^{\gamma_1} > 25$ GeV	28.17 ± 0.79	34677 ± 245	79.51 ± 1.59	3698 ± 18	9.55 ± 1.05
$E_{\text{T}}^{\text{miss}} > 95$ GeV	9.32 ± 0.45	1.08 ± 0.36	2.29 ± 0.26	4.18 ± 0.59	0.01 ± 0.004
$\text{Bal}_{p_{\text{T}}} < 0.2$	9.09 ± 0.44	0.16 ± 0.14	1.97 ± 0.24	1.45 ± 0.35	0 ± 0
$\Delta\phi_{\ell\ell,\gamma E_{\text{T}}^{\text{miss}}} > 2.8$	9.07 ± 0.44	0.05 ± 0.09	1.91 ± 0.24	1.10 ± 0.30	0 ± 0
$\Delta\phi(\ell,\ell) < 1.4$	8.71 ± 0.42	0.03 ± 0.08	1.55 ± 0.21	0.55 ± 0.20	0 ± 0

7.3.2 Control and Validation Regions

In addition to the signal region several orthogonal control and validation regions were defined to help understand and validate different backgrounds. These regions are constructed to isolate a single background with high purity. Generally a control region is used to compare the background prediction to the data, tweaking parameters like normalization factors and in more complicated situations, the shape, so that the control region background models the data well. In the validation region the background is then adjusted in the same way as the control region and compared with the data. If all is well in the validation region, the same tweaks are done to the prediction in the signal region to give a background estimate. The regions defined in this section are used for the analysis in order to construct background estimates for the signal region. There are other control and validation regions used to determine the different data-driven mis-identification rates which are outlined in the sections for electron-to-photon fakes, Section 7.4.1.1, and jet-to-photon fakes, Section 7.4.2.1. A summary of these regions, including the signal region, can be seen in Table 7.4.

Table 7.4: Selection criteria for the different control, validation, and signal regions used in the analysis. The '(electron)' in the WZ control region signifies the condition of an *Medium* electron being required in place of the signal photon. The '(pseudo γ)' in the jet control region signifies the condition of a pseudo photon being required in place of the signal photon.

Cut	Control Reg. WZ	Control Reg. jets	Valid. Reg. jets	Control Reg. $Z\gamma$	Valid. Reg. $Z\gamma$	Signal Reg.
Pass triggers and vetoes	✓	✓	✓	✓	✓	✓
2 signal leptons	✓	✓	✓	✓	✓	✓
At least 1 signal photon	> 25 GeV(electron)	> 25 GeV(pseudo γ)	> 25 GeV	> 25 GeV	> 25 GeV	> 25 GeV
$m_{\ell\ell}^{\text{win}}$	$81 - 101$ GeV	$81 - 101$ GeV	$85 - 120$ GeV	$81 - 101$ GeV	$81 - 101$ GeV	$81 - 101$GeV
$E_{\text{T}}^{\text{miss}}$	> 95 GeV	> 95 GeV	> 35 GeV	$20 - 35$ GeV	$35 - 70$ GeV	> 95 GeV
$\text{Bal}_{p_{\text{T}}}$	< 0.2	< 0.2	-	< 0.2	< 0.2	< 0.2
$\Delta\phi_{\ell\ell,\gamma E_{\text{T}}^{\text{miss}}}$	> 2.8	> 2.8	< 2.2	-	-	> 2.8
$\Delta\phi(\ell,\ell)$	< 1.4	< 1.4	-	< 2.0	< 2.0	< 1.4

For the electron-to-photon fakes, a control region is defined in the same way as the signal region

except that instead of requiring a signal photon, a *Medium* electron is required with the same signal region kinematic topology selections. Eventually, the electron-to-photon mis-identification rate is applied to this region in order to estimate the background in the control region. A validation region with similar kinematics is very hard to carve out while having meaningful statistics and low signal contamination. This is because the $WZ \to e\nu\ell\ell$ kinematics match the signal region kinematics. Thus a validation region, without a Z boson in the event, was defined as a region with two photons and exactly one electron. This region contains a small amount of $W\gamma\gamma$ contamination but most of the events come from $Z\gamma$ events where one of the electrons from the Z is mis-identified as a second photon.

Analogously, there is a control region for the jet-to-photon fakes which is constructed in the same way as the signal region though rather than a signal photon, a pseudo photon is required. The jet-to-photon mis-identification rate is then applied in order to get a signal region background estimate. A validation region is defined using unbalanced events containing a signal photon + two leptons in an asymmetric invariant mass window. This asymmetric window is utilized in order to remove the radiative $Z\gamma$ contamination. The $\text{Bal}_{p_{\text{T}}}$ and $\Delta\phi(\ell,\ell)$ cuts are dropped, the $E_{\text{T}}^{\text{miss}}$ requirement is relaxed, and the $\Delta\phi_{\ell\ell,\gamma E_{\text{T}}^{\text{miss}}}$ cut is inverted such that events are required to have the dilepton system unbalanced with the $\gamma E_{\text{T}}^{\text{miss}}$ system.

The $Z\gamma$ background shape is taken from simulation, while the normalization is derived from a control region. This control region is similar to the signal region, but with relaxing the $\Delta\phi(\ell,\ell)$ requirement, dropping the $\Delta\phi_{\ell\ell,\gamma E_{\text{T}}^{\text{miss}}}$ criterion, and requiring substantially less missing transverse momentum in the event. The validation region is then defined in the same way but requiring the missing transverse momentum to be in an intermediate range, greater than the control region but less than the signal region.

Composition and Signal Leakage of Control and Validation Regions

Aside from the mis-identified objects control regions, which will be discussed in depth in Section 7.4, the composition and purity of the three other regions can be seen in Figure 7.7. The purity of targeted background is over 50% for all regions, though the validation region for the jet-to-photon fakes has lower purity than other regions. This is due to the contribution from $Z\gamma$ with real photons and because the photon identification of ATLAS detector is excellent at rejecting mis-identified photons.

These control and validation regions were also designed to have as little signal leakage as possible in order to avoid prematurely "unblinding" the analysis. The percentage of signal events entering

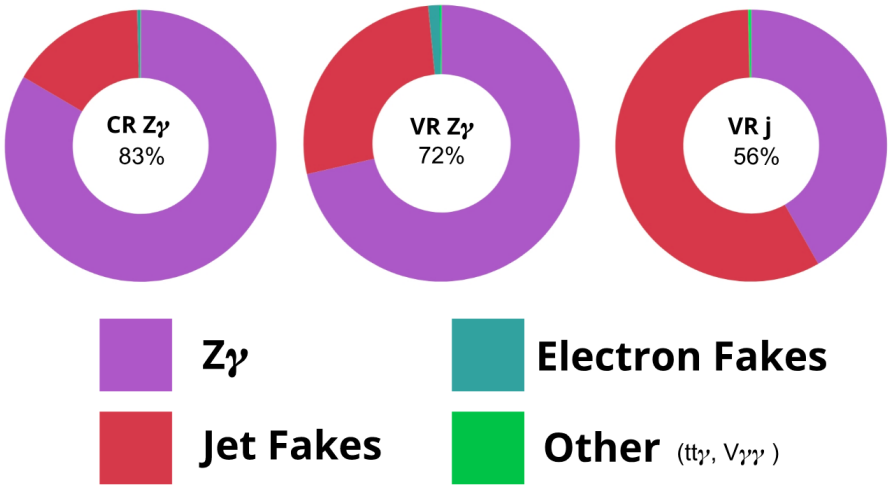

Figure 7.7: Composition of the control and validation regions mentioned in the text. The purity of the desired background is noted in as a percentage of total events.

each region can be seen in Figure 7.8. The highest percentage of signal leakage is less than 2.5% in the $Z\gamma$ validation region. This is due to that region being closest, kinematically to the signal region. The other regions have less than 0.5% of events due to signal processes. This holds true for the mis-identification control regions used for the signal region fake background estimates.

7.4 Background Estimation

There are four main background sources which can leave signatures in the detector similar to the signal process. These can be broadly grouped into:

- Backgrounds where an electron is mis-identified as a photon, primarily coming from $WZ \to e\nu\ell\ell$.
- Backgrounds with resonant Z bosons that contain a real photon, coming largely from Standard Model $Z\gamma$.
- Backgrounds generally coming from $Z+$jets where a jet is mis-identified as a photon.
- Backgrounds with non-resonant leptons, consistent with the Z mass, that contain a real photon.

Section 7.4.1 discusses the background estimation from electrons mis-identified as photons ($e \to \gamma$) using a data-driven method. These fakes predominantly come from $WZ \to e\nu\ell\ell$ events where

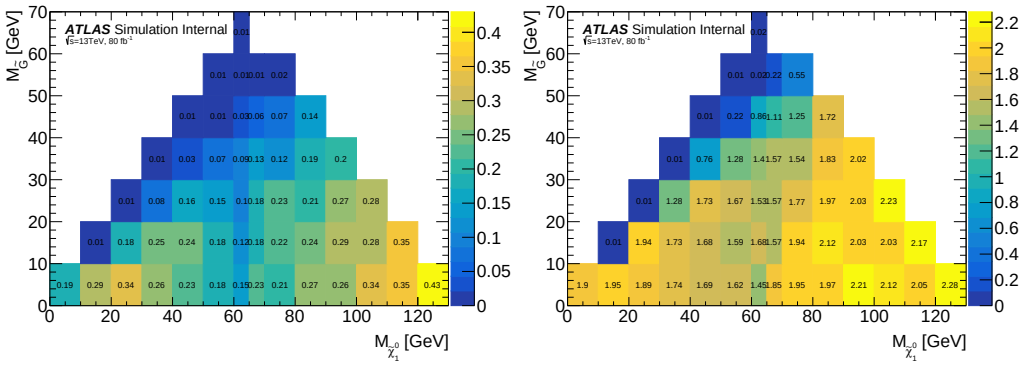

(a) Leakage in $Z\gamma$ control region

(b) Leakage in $Z\gamma$ validation region

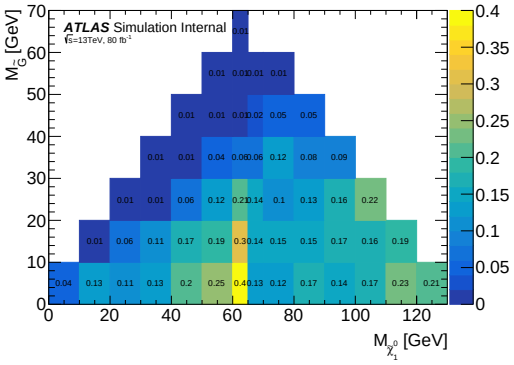

(c) Leakage in jet validation region

Figure 7.8: Signal leakage percentage in the (a) $Z\gamma$ control region, (b) $Z\gamma$ validation region, and (c) $Z+$jets validation region. The grid points are generally given by the bin edges. The exceptions are along the left diagonal, where the grid points are m_{NLSP}-m_{LSP}(GeV) = 1-0, 11-10, 21-20, ..., 61-60.

the electron is mis-identified as a photon. Section 7.4.2 expands upon the background estimation of jets mis-identified as photons (j $\to \gamma$). These events mostly come from $Z+$jets events but other processes such as diboson and $t\bar{t}$ production may also contribute. The method to estimate the j $\to \gamma$ background is validated in a region with unbalanced events ($\Delta\phi_{\ell\ell,\gamma E_{\text{T}}^{\text{miss}}} < 2.2$) and enforces a higher, asymmetric dilepton mass window to remove the radiative $Z\gamma$ contamination. The shape of the background from Standard Model $Z\gamma$ production is estimated using simulated events while the normalization is obtained from a control region with lower $E_{\text{T}}^{\text{miss}}$, as described in Section 7.4.3. This estimation is then validated in an intermediate $E_{\text{T}}^{\text{miss}}$ region. Finally, Section 7.4.4 outlines the small and almost negligible remaining backgrounds with non-resonant leptons with real photons.

In the following background sections, all plots will be presented with statistical uncertainties only. The systematic errors will be discussed in the next section (Section 7.5). All the systematic

errors will be propagated and handled in the fitting procedure, where the $Z\gamma$ background will also be normalized in the control region. This is explained in Section 7.6.

7.4.1 Backgrounds with an Electron Mis-identified as a Photon

Electrons and photons leave a very similar signature in the calorimeter; the primary distinction between the two is the existence of a track originating from the primary vertex for an electron. A small fraction of electrons, e.g. those which undergo hard bremsstrahlung at very small radius, may end up reconstructed as photons. If real electrons have been reconstructed as photons, there can be significant backgrounds arising from fake photons in searches with photon final states.

In this analysis, these electron-to-photon fakes manifest themselves as the background from a resonant Z boson with an additional electron mis-identified as a photon. These events come primarily from Standard Model diboson processes. The dominant process is $WZ \to e\nu\ell\ell$, although there are smaller cross section processes such as $ZZ \to 4\ell$ in which one electron is out of the detector acceptance or mis-reconstructed.

In order to assess these electron-to-photon fakes, a WZ control region is defined in the same way as the signal region except instead of requiring a signal photon, a *Medium* electron is required with the same signal region kinematic topology selections. This region isolates the WZ very well as according to simulation 93% of events arise from the WZ process. This region is denoted "CR WZ" or "eCR" in the following figures. The prediction of the background in the signal region is then the electron-to-photon mis-identification rate, denoted as $\xi^{e\to\gamma}_{data}$, multiplied by the number of events in the control region. This can be written as:

$$N_{e\to\gamma}(p_{\mathrm{T}},\eta) = \xi^{e\to\gamma}_{data}(p_{\mathrm{T}},\eta) \times N_e^{\text{replace }\gamma}(p_{\mathrm{T}},\eta)\ ; \tag{7.1}$$

where $N_{e\to\gamma}(p_{\mathrm{T}},\eta)$ is the background prediction of the signal region, and $N_e^{\text{replace }\gamma}(p_{\mathrm{T}},\eta)$ is the number of events in the control region constructed where the photons are replaced with an electron.

The $E_{\mathrm{T}}^{\mathrm{miss}}$ distribution of the data and WZ (and other processes) simulation in the control region is shown in Figure 7.9a. The modeling of the control region agrees well with the SM expectation and the data are then used to derive the signal region prediction. Figure 7.9b shows the expected background from $e \to \gamma$ in the signal region as modeled by the simulation (WZ + other), the data in the control region scaled by $\xi^{e\to\gamma}_{data}$(open triangles), and the simulation in the control region scaled by the mis-identification rate calculated in $Z \to ee$ Monte Carlo, $\xi^{e\to\gamma}_{MC}$, (closed squares, denoted MC closure).

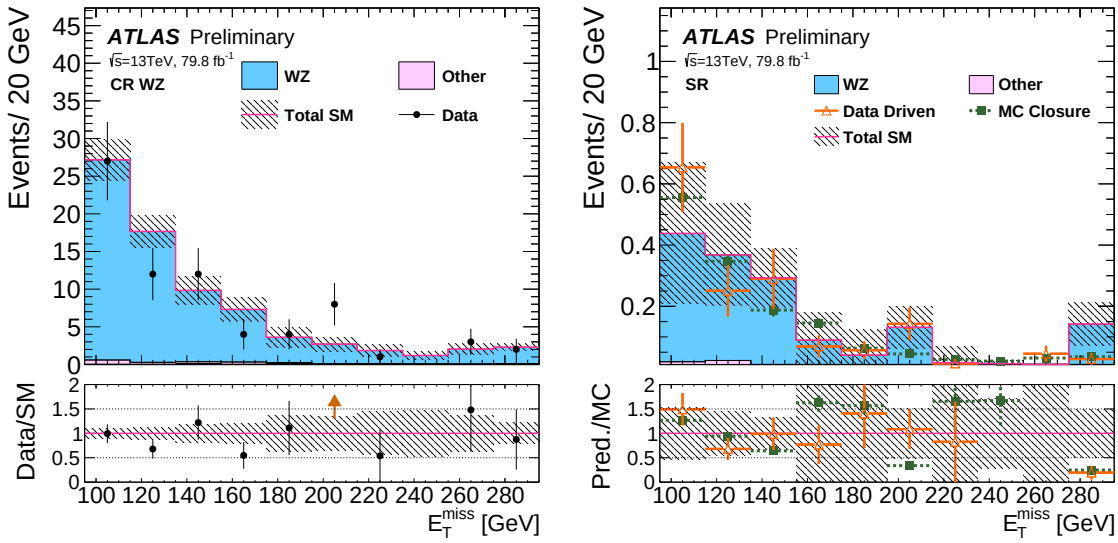

(a) $E_{\mathrm{T}}^{\mathrm{miss}}$ in the WZ control region

(b) $E_{\mathrm{T}}^{\mathrm{miss}}$ in the signal region

Figure 7.9: Distribution of $E_{\mathrm{T}}^{\mathrm{miss}}$ in (a) the WZ control region and (b) signal region for the $e \to \gamma$ background. Both regions are rich in WZ events. The other backgrounds include $Z+$jets, $t\bar{t}$, and other diboson processes. In (a) the black points are the data in the region selecting an electron instead of a signal photon in the "Higgs system". The WZ and other are the simulated SM processes. In (b) the data from (a) are scaled by the data-derived $e \to \gamma$ mis-identification rate in order to obtain the data-driven prediction (open triangles). This is compared with MC simulation (WZ + other) and the Monte Carlo closure test (closed squares). The closure test involves calculating a $e \to \gamma$ mis-identification rate with $Z \to ee$ Monte Carlo and applying this to the simulated control region, which is the WZ + other background in (a), in order to derive a "data-driven" prediction using only simulation. In both cases the uncertainty bands display the statistical error only.

The spectra of other variables are shown in Figures 7.10 and 7.11. Distributions of $\Delta\phi_{\ell\ell,\gamma E_{\mathrm{T}}^{\mathrm{miss}}}$, $\mathrm{Bal}_{p_{\mathrm{T}}}$, $\Delta\phi(\ell,\ell)$, $p_{\mathrm{T}}^{\ell\ell}$, $\Delta\phi(E_{\mathrm{T}}^{\mathrm{miss}},\gamma)$, $m_T^{\gamma,E_{\mathrm{T}}^{\mathrm{miss}}}$, $p_{\mathrm{T}}^{\gamma_1}$, and η^{γ_1} are shown in the WZ control region in both linear and log scales. In Figure 7.10, the extrapolation from the control region to the signal region is shown as a the data-driven (orange) lines. This corresponds to applying the $\xi_{data}^{e\to\gamma}$ to the data events in the WZ control region. The signal region distributions also contain the Monte Carlo closure test (green). This is obtained by applying the mis-identification rate calculated from Monte Carlo only to the Monte Carlo in the WZ control region. The blue and pink distributions, labeled WZ and other, are the simulation predictions for the electron-to-photon mis-identified events, this is not expected to be modeled well in the simulation and therefore the data-driven estimate is used. The final signal region prediction is given by the extrapolation of data events in the control region (orange) and the final electron-to-photon fake event yield is 1.5 ± 0.3.

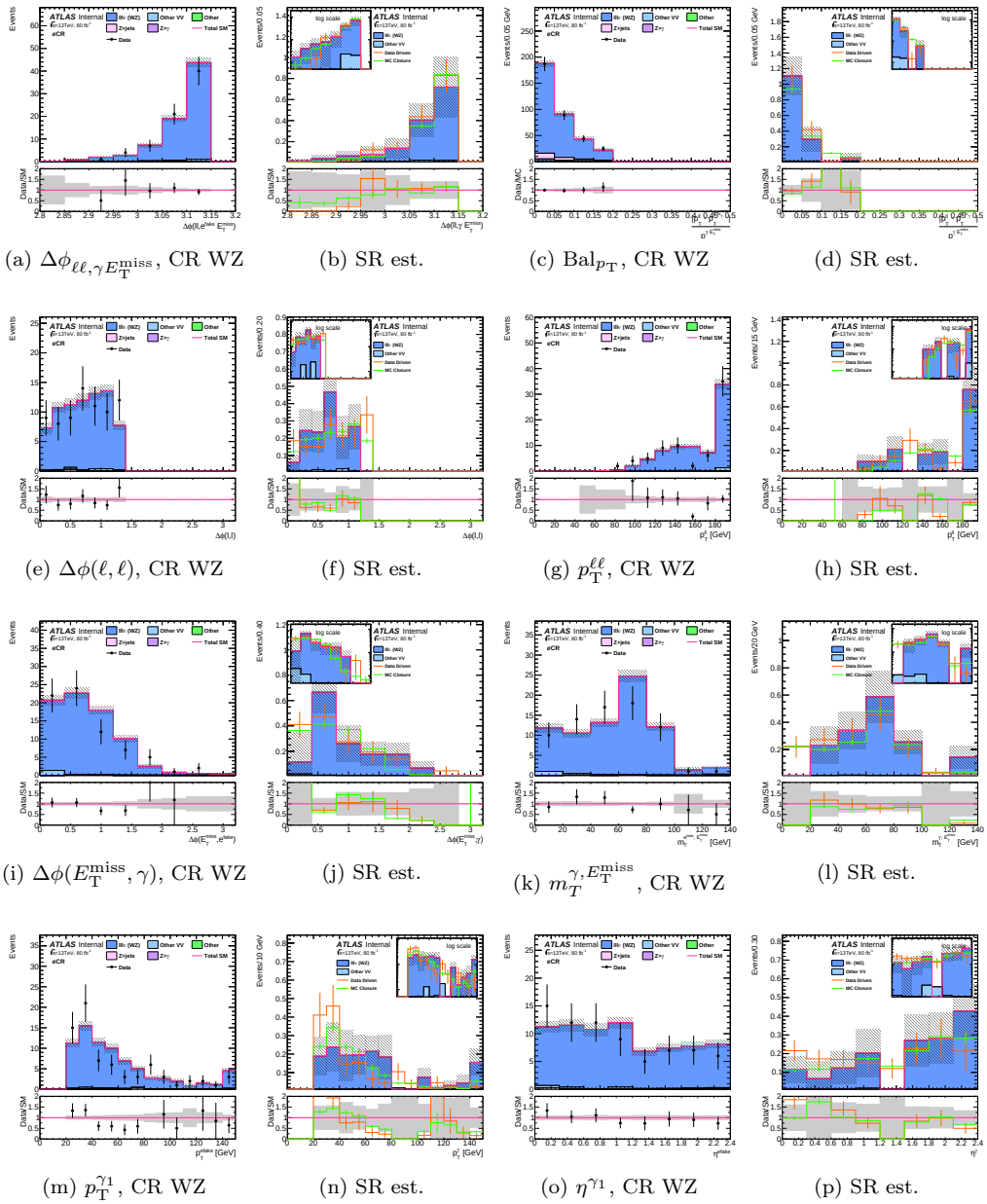

(a) $\Delta\phi_{\ell\ell,\gamma E_{\mathrm{T}}^{\mathrm{miss}}}$, CR WZ (b) SR est. (c) $\mathrm{Bal}_{p_{\mathrm{T}}}$, CR WZ (d) SR est.

(e) $\Delta\phi(\ell,\ell)$, CR WZ (f) SR est. (g) $p_{\mathrm{T}}^{\ell\ell}$, CR WZ (h) SR est.

(i) $\Delta\phi(E_{\mathrm{T}}^{\mathrm{miss}},\gamma)$, CR WZ (j) SR est. (k) $m_T^{\gamma,E_{\mathrm{T}}^{\mathrm{miss}}}$, CR WZ (l) SR est.

(m) $p_{\mathrm{T}}^{\gamma_1}$, CR WZ (n) SR est. (o) η^{γ_1}, CR WZ (p) SR est.

Figure 7.10: Distributions of (a) $\Delta\phi_{\ell\ell,\gamma E_{\mathrm{T}}^{\mathrm{miss}}}$, (c) $\mathrm{Bal}_{p_{\mathrm{T}}}$, (e) $\Delta\phi(\ell,\ell)$, (g) $p_{\mathrm{T}}^{\ell\ell}$, (i) $\Delta\phi(E_{\mathrm{T}}^{\mathrm{miss}},\gamma)$, (k) $m_T^{\gamma,E_{\mathrm{T}}^{\mathrm{miss}}}$, (m) $p_{\mathrm{T}}^{\gamma_1}$, and (o) η^{γ_1} in the WZ control region. The black points are the data in the control region selecting an electron instead of a signal photon in the "Higgs system". The WZ and other colored histograms are the simulated SM processes. To the left (b,d,...etc) is the signal region estimate (SR est.) obtained from the control region. The Monte Carlo estimation (blue) is compared with the data-driven technique (orange) and the MC closure (green). These are explained in the text or in Figure 7.9.

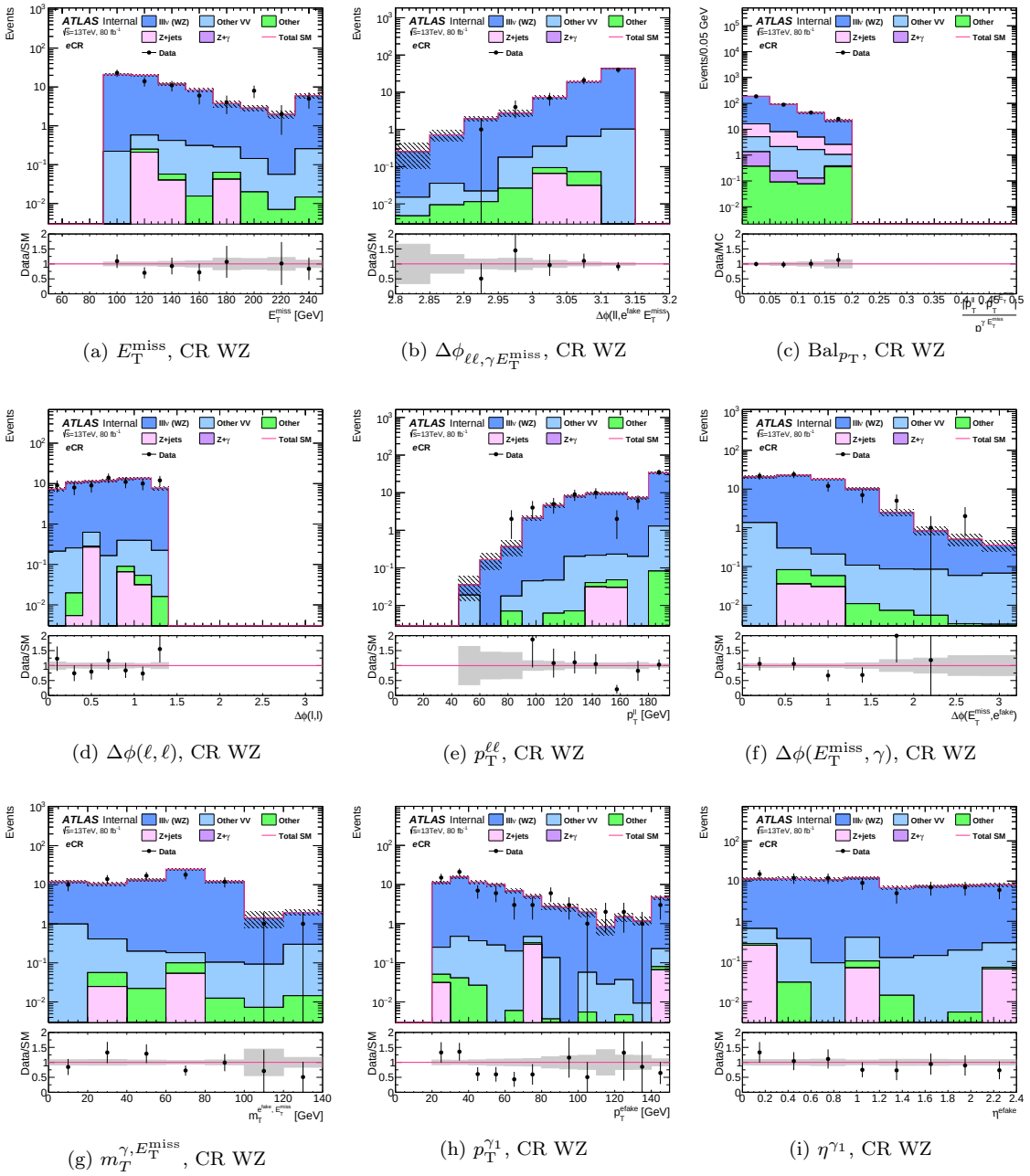

(a) $E_{\mathrm{T}}^{\mathrm{miss}}$, CR WZ (b) $\Delta\phi_{\ell\ell,\gamma E_{\mathrm{T}}^{\mathrm{miss}}}$, CR WZ (c) $\mathrm{Bal}_{p_{\mathrm{T}}}$, CR WZ

(d) $\Delta\phi(\ell,\ell)$, CR WZ (e) $p_{\mathrm{T}}^{\ell\ell}$, CR WZ (f) $\Delta\phi(E_{\mathrm{T}}^{\mathrm{miss}},\gamma)$, CR WZ

(g) $m_T^{\gamma,E_{\mathrm{T}}^{\mathrm{miss}}}$, CR WZ (h) $p_{\mathrm{T}}^{\gamma_1}$, CR WZ (i) η^{γ_1}, CR WZ

Figure 7.11: Distributions of (a) $E_{\mathrm{T}}^{\mathrm{miss}}$, (b) $\Delta\phi_{\ell\ell,\gamma E_{\mathrm{T}}^{\mathrm{miss}}}$, (c) $\mathrm{Bal}_{p_{\mathrm{T}}}$, (d) $\Delta\phi(\ell,\ell)$, (e) $p_{\mathrm{T}}^{\ell\ell}$, (f) $\Delta\phi(E_{\mathrm{T}}^{\mathrm{miss}},\gamma)$, (g) $m_T^{\gamma,E_{\mathrm{T}}^{\mathrm{miss}}}$, (h) $p_{\mathrm{T}}^{\gamma_1}$, and (i) η^{γ_1} in the WZ control region in log scale.

7.4.1.1 Derivation of the Electron to Photon Mis-identification Rate

This section outlines the derivation of the electron-to-photon fake rate. The basic definition of the electron-to-photon fake event is an event in which a reconstructed photon actually comes from a true electron. By studying the Z boson decay to e^+e^-, the fake rate can be extracted as sometimes one of these electrons can be reconstructed as a photon. In the past, this measurement has been performed with the "tag and probe" method [131, 132] in which there are strict identification and isolation requirements on the leading electron (the "tag"), and looser requirements on the second objects which can be an electron or photon (the "probe"). The electron to photon fake rate would them just be:

$$F_{e\to\gamma} = \frac{N^{e\gamma}}{2 * N^{ee}} \ ; \tag{7.2}$$

where $F_{e\to\gamma}$ is the fake rate, $N^{e\gamma}$ is the number of events with a reconstructed tag electron and probe photon, and N^{ee} is the number of events with two reconstructed electrons.

Instead of using the tag and probe method, a new method developed on the ATLAS experiment is used; dubbed the "tag and tag" method. This method uses the objects with the same identification and isolation criteria. The electron-to-photon mis-identification rate is measured as a function of the transverse momentum and absolute value of the pseudorapidity of the photon candidate.

The 2015–2017 dataset is used to derive the mis-identification rate used in the final background estimation, though a mis-identification rate is also calculated using $Z \to ee$ Monte Carlo only and is employed for cross-checks. Instead of using the triggers outlined in Section 7.3.1, dielectron triggers or photon-electron triggers, shown in Table 7.5, are used to select the events. The electron and photon selection criteria are required to be the same as in the analysis, shown in Table 7.2. This is to ensure the mis-identification rate computed can be used directly in the main analysis. Overlap removal of the selected photons and electrons is performed, removing the photon candidate if a photon object and electron object are within a cone of $\Delta R = 0.4$. This overlap procedure is chosen to reduce the overall electron to photon fake rate, and is the same overlap removal procedure used in the analysis. After selecting events with a reconstructed e^+e^- and/or $e\gamma$ pairs, the invariant mass of the pair(s) are calculated. If there are multiple $e^+e^-/e\gamma$ pairs, only the invariant mass closest to the Z boson mass is stored.

At this point the analysis is divided between the e^+e^- and $e\gamma$ pairs and then performed in two steps. The first step involves fitting the invariant mass distributions of the pairs and extracting a "signal fraction" which will be defined in the following subsection. Next, the mis-identification rate is calculated in different p_{T} and η bins using the calculated signal fraction.

Table 7.5: Triggers and trigger p_{T} trigger thresholds for electrons and photons, requiring two electrons or one electron and one photon. In a given year the logical `OR` of dielectron and photon-electron triggers is taken.

	Trigger Name	**Thresholds [GeV]**
Dilepton trigger year		
2015	`HLT_2e12_lhloose_L12EM10VH`	12, 12
2016	`HLT_2e17_lhvloose_nod0`	17, 17
2017	`HLT_2e17_lhvloose_nod0_L12EM15VHI`	17, 17
Photon-electron trigger year		
2015	`HLT_e24_lhmedium_nod0_L1EM15VH_g25_medium`	24(e), 25(γ)
2016	`HLT_e24_lhmedium_nod0_L1EM15VH_g25_medium`	24(e), 25(γ)
2017	`HLT_e24_lhmedium_nod0_L1EM20VH_g25_medium`	24(e), 25(γ)

Signal Fraction Extraction

First, the invariant mass pairs of the e^+e^- and $e\gamma$ are roughly binned by the η and p_{T} of the objects. For dielectron events, 9 bins are defined by combinatorics of two unordered electrons, split by the $p_{\mathrm{T}}^{e_{1,2}}/m_{ee}$ (0-0.5,0.5-∞) and the $|\eta^{e_{1,2}}|$ (0.0-1.37, 1.52-2.37). For electron-photon events $|\eta^{e,\gamma}|$ and $p_{\mathrm{T}}^{e,\gamma}/m_{e\gamma}$ defines 16 different regions as the photon and electron can be distinguished.

The invariant mass is then fit in each of these $m_{ee}/m_{e\gamma}$ spectra between 65 and 200 GeV. The signal model used is the same as in the $H \to \gamma\gamma$ analysis, the double-sided Crystal Ball, defined in Section 6.3. The background model is a exponential of the form Ne^{Ax^2+Bx}, where N is a normalization parameter and A, B are constants. The fits of the e^+e^- and $e\gamma$ distributions can be seen in Figures 7.12 and 7.14. The double-sided Crystal Ball component is shown by the solid, red line and the background exponential can be seen as the dashed, green line. The combined PDF is shown as the solid, blue line.

After the fit a signal fraction is calculated in 1 GeV bins as the number of signal events divided by the number of total events. This fraction is calculated using the PDFs of the fits and depends on the invariant mass and p_{T}/η of both objects. The weight can then be written as:

$$\mathrm{w}(m_{12},\eta^1,\eta^2,\frac{p_{\mathrm{T}}^1}{m_{12}},\frac{p_{\mathrm{T}}^2}{m_{12}}) = \frac{\mathcal{N}_{\mathrm{S}} f_{\mathrm{S}}(m_{12},\eta^1,\eta^2,\frac{p_{\mathrm{T}}^1}{m_{12}},\frac{p_{\mathrm{T}}^2}{m_{12}})}{\mathcal{N}_{\mathrm{S}} f_{\mathrm{S}}(m_{12},\eta^1,\eta^2,\frac{p_{\mathrm{T}}^1}{m_{12}},\frac{p_{\mathrm{T}}^2}{m_{12}}) + \mathcal{N}_{\mathrm{B}} f_{\mathrm{B}}(m_{12},\eta^1,\eta^2,\frac{p_{\mathrm{T}}^1}{m_{12}},\frac{p_{\mathrm{T}}^2}{m_{12}})} \; ; \tag{7.3}$$

where $\mathcal{N}_{\mathrm{S}}$ is the number of signal events, $\mathcal{N}_{\mathrm{B}}$ is the number of background events, f_{S} is the signal PDF, f_{B} is the background PDF. The weights from 60 to 120 GeV can be see in Figures 7.13 and 7.15. The weight distribution for the e^+e^- pairs are wider, indicating less background contamination in

the sample. For both dielectron and photon-electron events, the weights near the Z mass are close to unity.

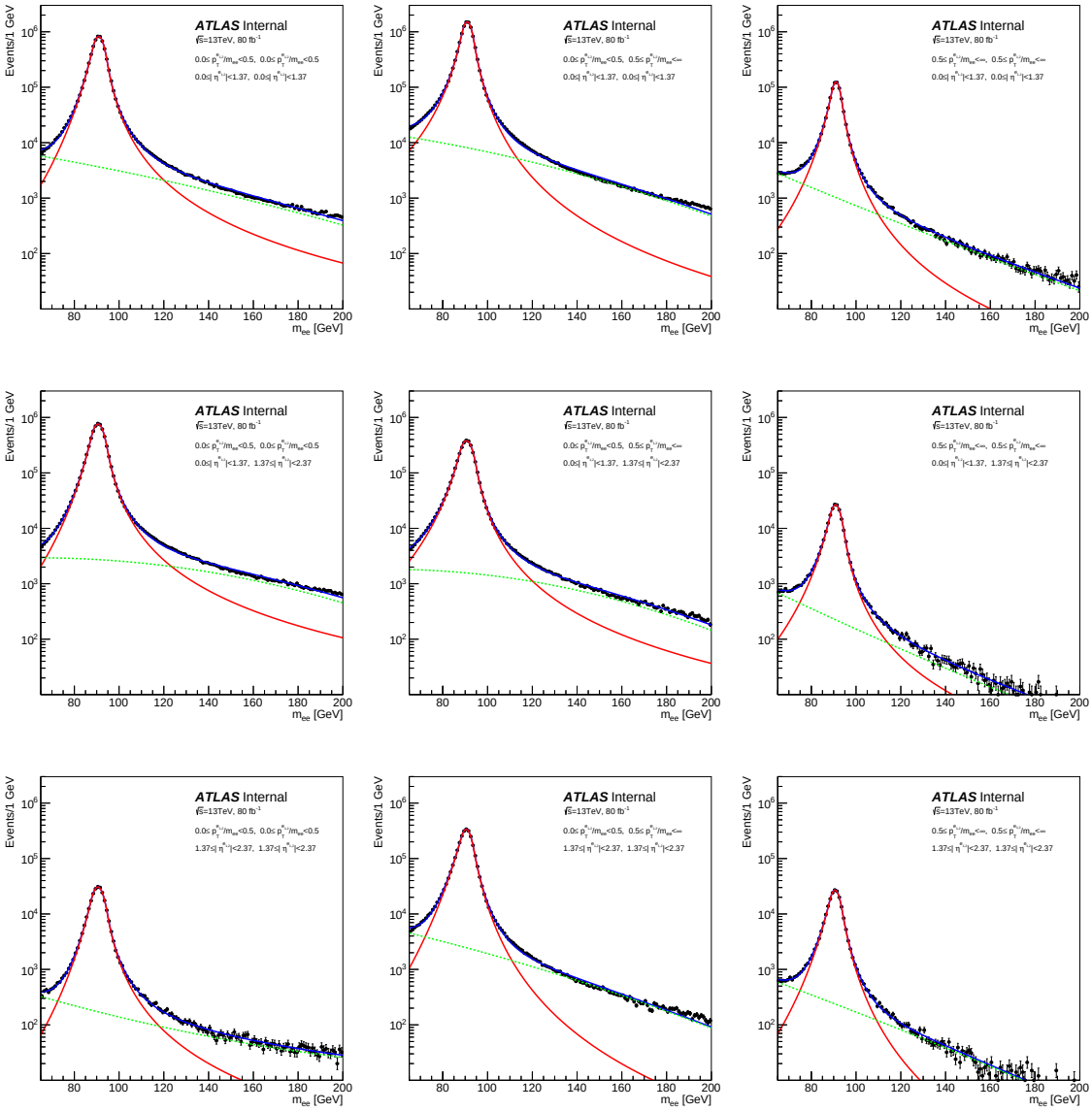

Figure 7.12: Signal plus background model fit to the invariant mass distributions of the e^+e^- pairs selected sample. Distributions are split up by all unordered combinations of $|\eta^{e_{1,2}}|$ (0.0-1.37, 1.52-2.37) and $p_{\mathrm{T}}^{e_{1,2}}/m_{ee}$ (0-0.5,0.5-∞). The signal and background fits are shown by the red and green lines respectively, while the blue line shows the combined fit.

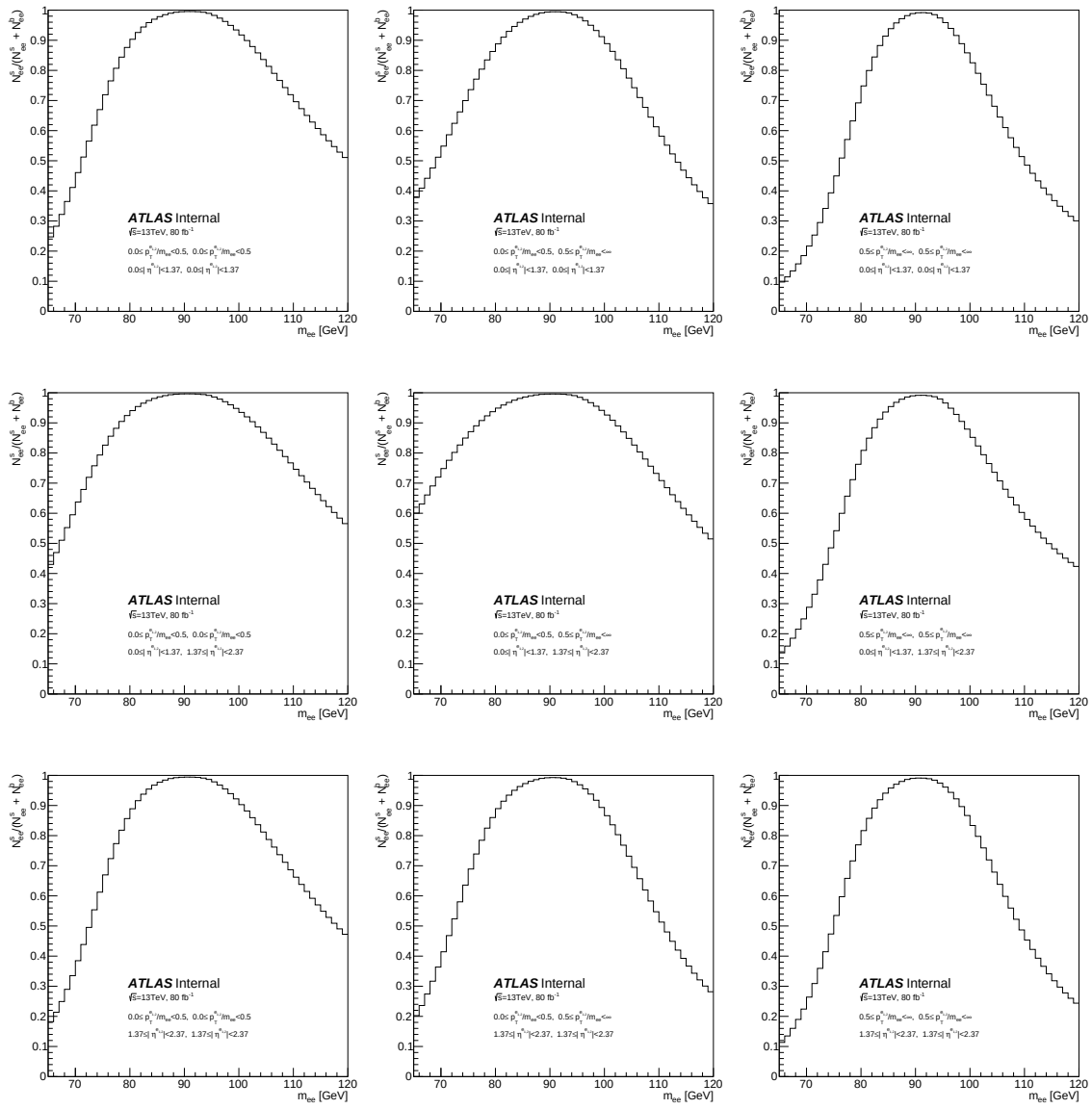

Figure 7.13: Signal fraction weights computed from the e^+e^- pair fits. Distributions are split up by all unordered combinations of $|\eta^{e_{1,2}}|$ (0.0-1.37, 1.52-2.37) and $p_{\mathrm{T}}^{e_{1,2}}/m_{ee}$ (0-0.5,0.5-∞).

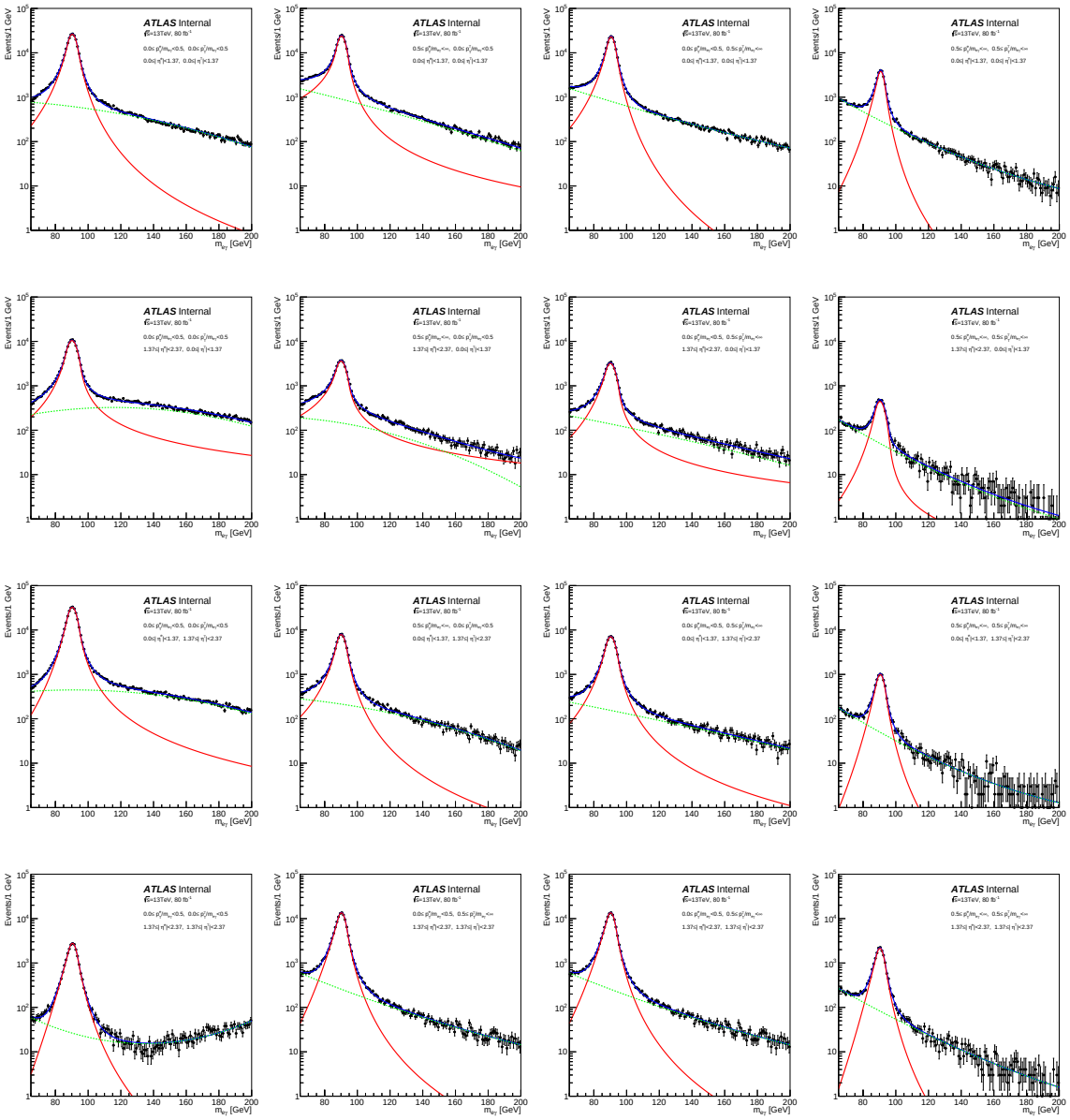

Figure 7.14: Signal plus background model fit to the invariant mass distributions of the $e\gamma$ pairs selected sample. Distributions are split up by all combinations of $|\eta^{e,\gamma}|$ (0.0-1.37, 1.52-2.37) and $p_{\mathrm{T}}^{e,\gamma}/m_{e\gamma}$ (0-0.5,0.5-∞). The signal and background fits are shown by the red and green lines respectively, while the blue line shows the combined fit.

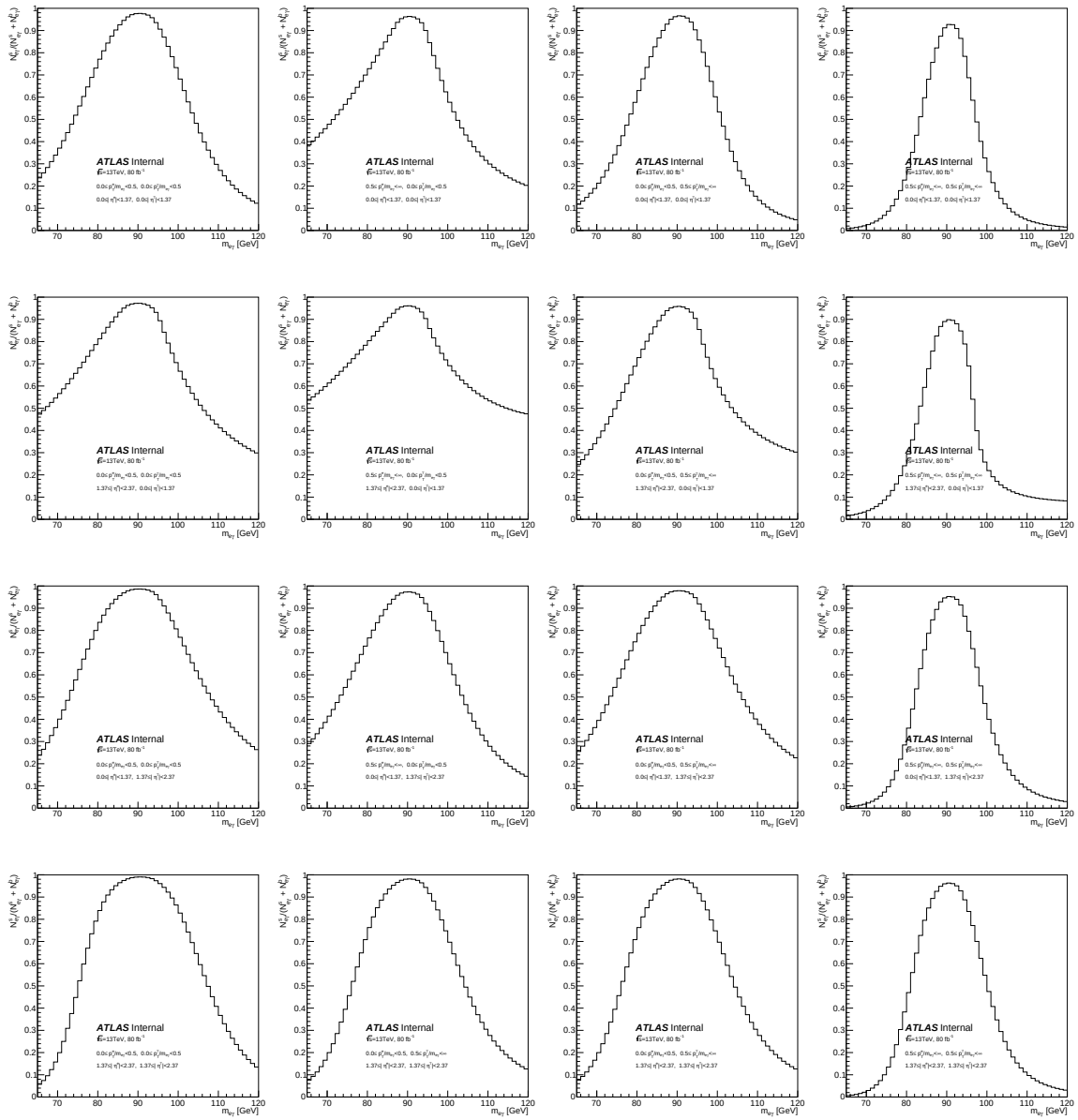

Figure 7.15: Signal fraction weights computed from the $e\gamma$ pair fits. Distributions are split up by all combinations of $|\eta^{e,\gamma}|$ (0.0-1.37, 1.52-2.37) and $p_{\mathrm{T}}^{e,\gamma}/m_{e\gamma}$ (0-0.5,0.5-∞).

Mis-Identification Rate Calculation

Once the signal fraction weights are calculated the events are iterated over again, this time only keeping the event if it passes all criteria mentioned above and if the invariant mass of the objects is between 86 and 96 GeV. A histogram (one for e^+e^- event, and one for $e\gamma$ events) is then filled, weighted by the corresponding signal fraction of the event. This histogram is segmented in 7 bins of $|\eta|$: 0.0-0.6, 0.6-0.8, 0.8-1.15, 1.15-1.37, 1.52-1.81, 1.81-2.01, 2.01-2.37 (the bin from 1.37 to 1.52 is excluded) and 9 bins in p_{T}:25-35, 35-45, 45-55, 55-65, 65-75, 75-90, 90-120, 120-180, 180-∞ GeV. For each e^+e^- event, the weight is stored twice; once in the bin corresponding to the first electron's p_{T} and η and then in the bin for the second electron's p_{T} and η. For the $e\gamma$ pairs, the $e\gamma$ histogram is filled once corresponding to the p_{T} and η of the photon only. A cartoon of the procedure can be seen in Figure 7.16.

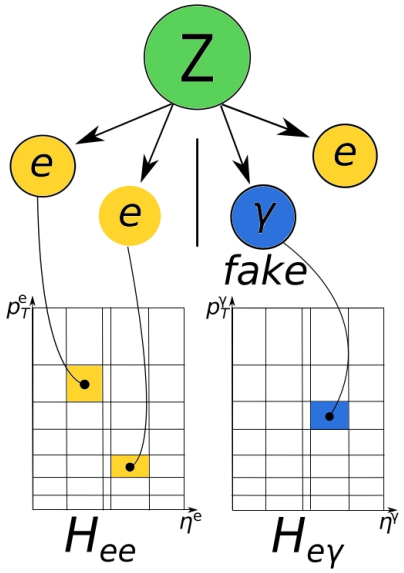

Figure 7.16: Cartoon of the procedure used to fill the histograms for the determination of the electron-to-photon fake rate.

In order to get the mis-identification rate, the $e\gamma$ histogram is just divided by the e^+e^- histogram. The total mis-identification rates as a function of p_{T} and η can be seen in Figure 7.17 and seen in Table 7.6. Only the statistical uncertainties are shown in the figure. The systematics of this measurement are discussed in Section 7.5. The $e \to \gamma$ mis-identification rate is approximately 1-2.5% in the barrel region of the detector. It increases to 2.5-5.5% in the endcap region because of the larger amount of material in front of the electromagnetic calorimeter.

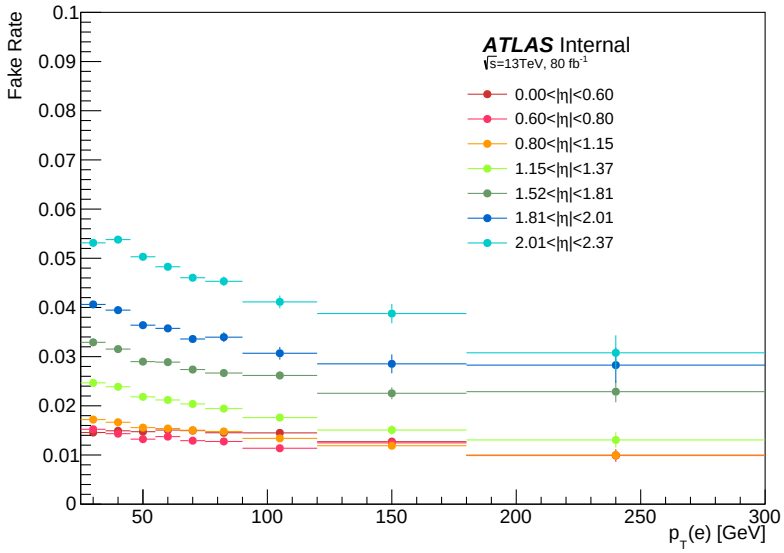

Figure 7.17: The $e \to \gamma$ mis-identification rates as a function of p_{T} split into different $|\eta|$ bins. These are the rates used in the ZH analysis.

Table 7.6: The $e \to \gamma$ mis-identification rates as a function of p_{T} split into different $|\eta|$ bins. These are the rates used in the ZH analysis. The $|\eta|$ bins are 0.0-0.6, 0.6-0.8, 0.8-1.15, 1.15-1.37, 1.52-1.81, 1.81-2.01, 2.01-2.37.

p_{T}Bin [GeV]	η Bin 1	Stat. Err.	η Bin 2	Stat. Err.	η Bin 3	Stat. Err.	η Bin 4	Stat. Err.	η Bin 5	Stat. Err.	η Bin 6	Stat. Err.	η Bin 7	Stat. Err.
$25 \leq p_{\mathrm{T}} < 35$	0.0146	0.0001	0.0152	0.0001	0.0172	0.0001	0.0247	0.0002	0.0329	0.0002	0.0406	0.0002	0.0531	0.0002
$35 \leq p_{\mathrm{T}} < 45$	0.0149	0.0000	0.0143	0.0001	0.0167	0.0001	0.0239	0.0001	0.0315	0.0001	0.0395	0.0002	0.0538	0.0002
$45 \leq p_{\mathrm{T}} < 55$	0.0147	0.0001	0.0132	0.0001	0.0156	0.0001	0.0218	0.0001	0.0290	0.0002	0.0364	0.0002	0.0503	0.0002
$55 \leq p_{\mathrm{T}} < 65$	0.0151	0.0001	0.0137	0.0002	0.0154	0.0002	0.0212	0.0003	0.0289	0.0003	0.0357	0.0005	0.0483	0.0005
$65 \leq p_{\mathrm{T}} < 75$	0.0150	0.0002	0.0129	0.0003	0.0150	0.0003	0.0204	0.0004	0.0274	0.0005	0.0336	0.0008	0.0460	0.0008
$75 \leq p_{\mathrm{T}} < 90$	0.0145	0.0003	0.0127	0.0004	0.0148	0.0004	0.0194	0.0006	0.0267	0.0007	0.0340	0.0010	0.0453	0.0010
$90 \leq p_{\mathrm{T}} < 120$	0.0145	0.0003	0.0114	0.0005	0.0134	0.0005	0.0176	0.0007	0.0262	0.0009	0.0307	0.0013	0.0411	0.0013
$120 \leq p_{\mathrm{T}} < 180$	0.0127	0.0005	0.0125	0.0008	0.0119	0.0006	0.0151	0.0010	0.0225	0.0012	0.0285	0.0019	0.0388	0.0020
$180 \leq p_{\mathrm{T}} < \infty$	0.0099	0.0007	0.0099	0.0013	0.0100	0.0010	0.0131	0.0016	0.0229	0.0022	0.0283	0.0035	0.0308	0.0036

Ambiguity Bit

As discussed previously, the electron and photon closely resemble each other and identifying an unambiguous object during reconstruction is not trivial. In the process, there is a bit assigned known as the "ambiguity bit", to alert analyzers about how unambiguous the object is classified. This bit is defined as:

- **Bit 0**: defined as ambiguous electron (most likely electron).
- **Bit 1**: defined as ambiguous electron with the track E over P better than vertex E over P.
- **Bit 2**: defined as ambiguous object with the p_{T} of the track less than 2.0 GeV.

- **Bit 3**: defined as ambiguous object with the E over P less than 10.
- **Bit 4**: defined as ambiguous object with no pixel hits.
- **Bit 5**: defined as ambiguous object with the vertex E over P better than track E over P.
- **Bit 6**: defined as ambiguous photon (most likely photon).
- **Bit 7**: defined as unknown object.

In previous versions of the ATLAS reconstruction and identification software, there was no requirements on the ambiguous objects and the object was classified as both a photon and electron. It was up to the analyzer to decide, via overlap removal procedures and their own criteria, if they wanted to classify the object as a photon or electron. In the newest release of the software, *Medium* and *Loose* electrons were rejected if they were classified as bits 5-7, and the electron is not *Tight* if classified as bits 2-7. This change was detrimental to this analysis and photon analyses in general as this bit essentially performs the overlap removal. The ambiguous electrons are removed if they appear more photon-like, and this choice to remove the electron from its container will in turn increase the electron-to-photon fake rate. One can see this effect explored in Figure 7.18. This plot was made with different object selection criteria, so the rates calculated without the ambiguity bit do not correspond the previous plot and table or mis-identification rates used in the analysis. One can clearly see a change in p_{T} shape dependence and the overall mis-identification.

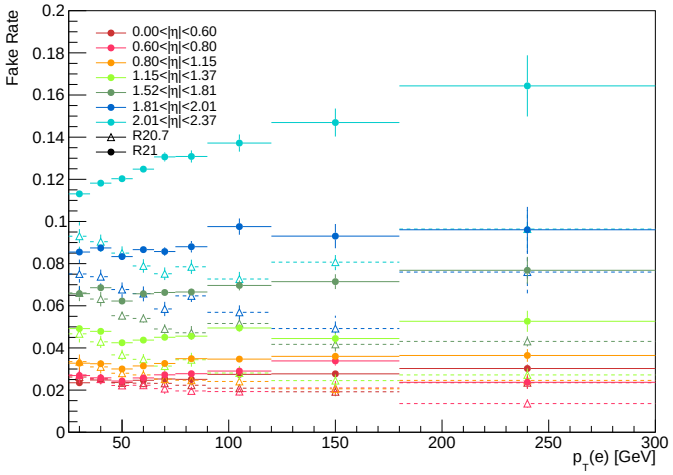

Figure 7.18: The $e \to \gamma$ mis-identification rates with (closed circles) and without (open triangles) the ambiguity bit, as a function of p_{T} split into different $|\eta|$ bins.

The effect of this ambiguity bit on the ZH analysis can be very drastic. There is a two-fold effect; first the derived mis-identification rate is measured to be higher as the photons that would be removed as fake electrons enter the calculation and second, there would be more fake electrons in the photon containers as they were no longer removed in the overlap procedure. This was investigated early in the design of the analysis when the signal region definition had a $E_{\mathrm{T}}^{\mathrm{miss}}$ cut of 70 GeV rather than 95 GeV. Figure 7.19a shows the signal region selection for electron-to-photon fake backgrounds with the ambiguity bit in the default state. The Monte Carlo (blue) is compared with the data-driven approach (orange) and the Monte Carlo is shown only above 70 GeV to draw attention in the signal region only. With the ambiguity bit turned off and performing the overlap removal in the desired way, the total fakes are reduced by a factor of two as shown in Figure 7.19b.

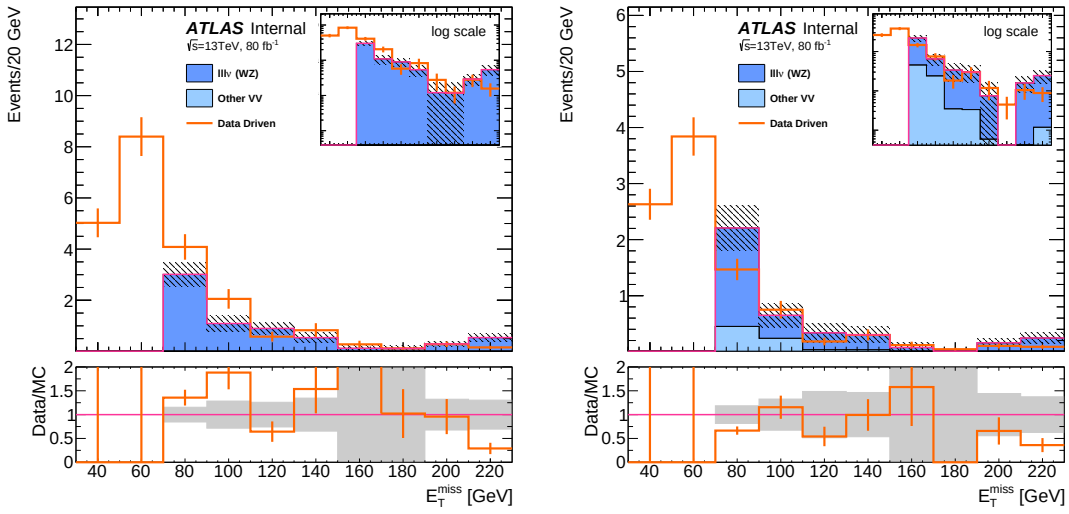

(a) Ambiguity bit on

(b) Ambiguity bit off

Figure 7.19: Distributions of $E_{\mathrm{T}}^{\mathrm{miss}}$ in the signal region, as compared with the predictions from Monte Carlo (blue) and the data-driven technique (orange). In (a) the ambiguity bit is in the default configuration and in (b) the ambiguity bit is turned off.

7.4.2 Backgrounds with a Jet Mis-identified as a Photon

Backgrounds from jets mis-identified as prompt photons come from two distinct sources. The large majority come from jets containing π^0's, η's, ρ's, and other light mesons decaying to final states of photons. A small fraction come from jets containing neutral hadrons depositing a considerable amount of energy in the electromagnetic calorimeter, imitating that of real prompt photons. Though

the detector, identification criteria, and isolation criteria were designed in order to reject jet-to-photon fakes, the immense amount of jets produced by QCD processes and slight inefficiency of each component leads to a significant number of jet-to-photon fakes.

In this analysis, the background arising from jets mis-identified as a photon comes primarily from $Z+$jets events and to a lesser extent, diboson/$t\bar{t}$ events with jets. The mis-identification rate ($\kappa_{\text{tight}}^{\text{j}\to\gamma}$) is obtained by the ABCD method (Section 7.4.2.1), which is similar to the 2x2D sideband method employed in the $H\to\gamma\gamma$ analysis and described in Section 6.4.1. To first order, the mis-identification rate is defined as the number of jets mis-identified as *Tight* photons divided by the number of pseudo (as outlined in Section 5.1.3) photons (jet-like non-*Tight* photon objects), measured in a non-isolated (jet-rich) region. These rates are calculated as a function of p_{T} separately for the barrel and endcap η regions. Once this rate is calculated the background estimation of different regions is constructed by choosing events with the same kinematics selection, though the signal photon is replaced with an isolated pseudo photon.

Unlike the excellent Monte Carlo modeling of the electron-to-photon background, the modeling of the jets mis-identified as photons is not expected to be predicted precisely. Figure 7.20 shows the kinematic variables of objects in a region selecting a signal photon, two leptons with $|m_{\ell\ell}-m_Z|<10\,\text{GeV}$, $E_{\text{T}}^{\text{miss}}>20$ GeV, and $\Delta\phi(\ell,\ell)<2.0$. The region is expected to be dominated by Standard Model $Z\gamma$ events with some amount of $Z+$jets. The data and other predictions are not plotted in the Figure and only the comparison between the $Z+$jets estimate from Monte Carlo and the data-driven procedure of selecting pseudo photons and scaling by the photon fake rate is shown. The distributions corroborate the hypothesis of poor MC modeling as the shapes and normalization greatly differ from the data-driven estimate. Additionally, the Monte Carlo statistical error is seen to be enormous. The Monte Carlo does confirm the expected configuration of fakes, as approximately 82% photons originated from a truth π^0 or light meson. About 17% of photons originated from strange and charm hadrons, and less than 1% from from heavy flavor hadrons.

In order to confirm the validity of the data-driven fake estimate, a validation region is constructed. This region is a sample of $Z+$jets events, where the jet is very "photon-like" (mis-identified as a photon candidate), and yet the contamination from $Z+$ real photons is small. This is constructed with p_{T} unbalanced events ($\text{Bal}_{p_{\text{T}}}$ criteria relaxed) containing two leptons consistent with a Z boson and a candidate signal photon. This domain is difficult to design as the ATLAS photon identification is very good at rejecting jet-to-photon fakes and thus a sizable amount of events with a Z and photon candidate encompass Standard Model $Z\gamma$ events. In this validation region the invariant mass of the dilepton pair is required to be between 85 and 120 GeV instead of the signal region norm of a 10 GeV

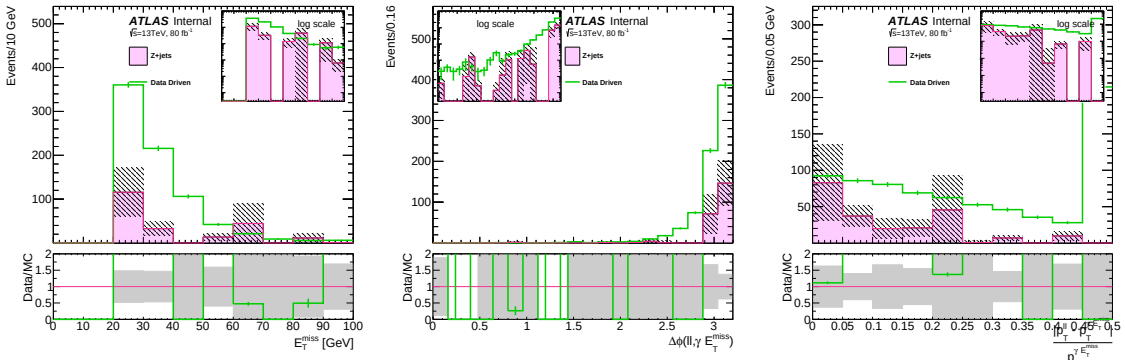

(a) $E_{\mathrm{T}}^{\mathrm{miss}}$

(b) $\Delta\phi_{\ell\ell,\gamma E_{\mathrm{T}}^{\mathrm{miss}}}$

(c) $\mathrm{Bal}_{p_{\mathrm{T}}}$

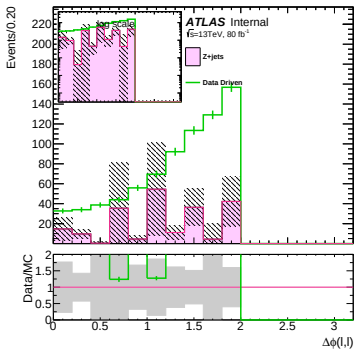

(d) $\Delta\phi(\ell,\ell)$

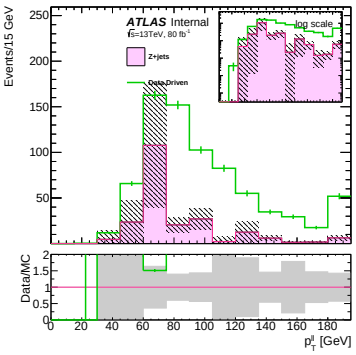

(e) $p_{\mathrm{T}}^{\ell\ell}$

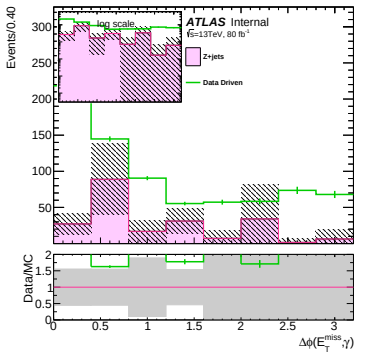

(f) $\Delta\phi(E_{\mathrm{T}}^{\mathrm{miss}},\gamma)$

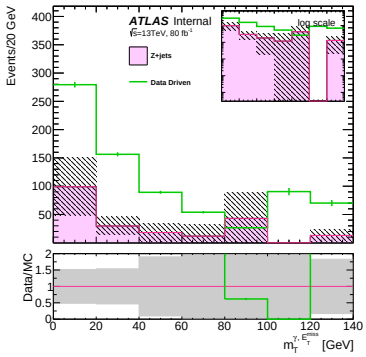

(g) $m_T^{\gamma,E_{\mathrm{T}}^{\mathrm{miss}}}$

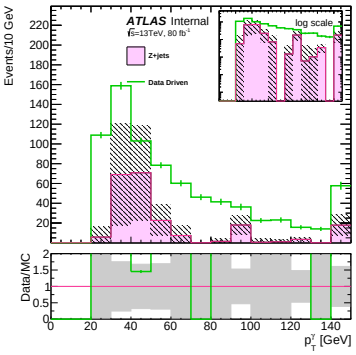

(h) $p_{\mathrm{T}}^{\gamma_1}$

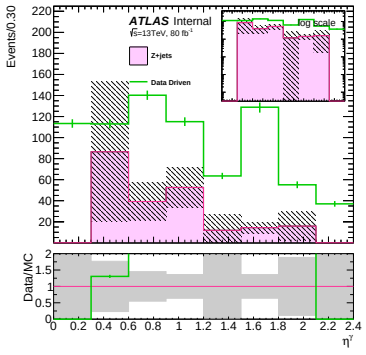

(i) η^{γ_1}

Figure 7.20: Predicted $Z+$jets background distributions derived using the data-driven method (green) and Monte Carlo. Distributions include (a) $E_{\mathrm{T}}^{\mathrm{miss}}$, (b) $\Delta\phi_{\ell\ell,\gamma E_{\mathrm{T}}^{\mathrm{miss}}}$, (c) $\mathrm{Bal}_{p_{\mathrm{T}}}$, (d) $\Delta\phi(\ell,\ell)$, (e) $p_{\mathrm{T}}^{\ell\ell}$, (f) $\Delta\phi(E_{\mathrm{T}}^{\mathrm{miss}},\gamma)$, (g) $m_T^{\gamma,E_{\mathrm{T}}^{\mathrm{miss}}}$, (h) $p_{\mathrm{T}}^{\gamma_1}$, and (i) η^{γ_1} in the relaxed region described in the text. The hatched band is the statistical uncertainty of the $Z+$jets MC. This shows the poor modeling and statistics of the $Z+$jets MC component and compared with a data-driven approach.

window around the Z mass. Employing this asymmetric window reduces the amount of radiative $Z\gamma$, increasing the purity of the $Z+$jets sample. The missing momentum is required to be over 35 GeV, further reducing the $Z\gamma$ background while keeping sufficient statistics. The $\Delta\phi_{\ell\ell,\gamma E_{\mathrm{T}}^{\mathrm{miss}}}$ (γ candidate) is also restricted to be less than 2.2 radians, retaining unbalanced events and forming a sector orthogonal to the signal region cut of $\Delta\phi_{\ell\ell,\gamma E_{\mathrm{T}}^{\mathrm{miss}}} > 2.9$. With this selection criteria, the contamination from $Z\gamma$ is still present though now over half of the events (56%) originate from the $Z+$jets background.

Pseudo Photon Scaling Factor

In order to estimate the jet to photon mis-identification background in a given region, isolated photon candidates passing the pseudo photon criterion are scaled by photon fake factor. This method, extrapolating in the identification variables, shows good agreement in validation regions but with large statistical uncertainties, especially in the signal region. A novel technique was developed in this analysis, additionally extrapolating in isolation in order to reduce this statistical error.

The fraction of isolated pseudo photons to all pseudo photons was measured in different domains. This ratio is measured in a looser version of the $Z\gamma$ control region, where the $\Delta\phi(\ell,\ell)$ cut is relaxed, and the $Z+$jets validation region. Figure 7.21 presents this fraction as a function of different kinematic variables in the looser $Z\gamma$ region, and Figure 7.22 shows the ratio in the $Z+$jets validation region. In both cases, there is a noticeable dependence of the ratio on the $\Delta\phi(\ell,\ell)$ variable, thus events have distinctive features when the Z boson is boosted in the event. This is further illustrated by Figure 7.23a where the scaling factor as a function of p_{T} is shown in the looser $Z\gamma$ region described and then in Figure 7.23b where the fraction is presented after requiring $\Delta\phi(\ell,\ell) < 2.0$ which then defines the $Z\gamma$ control region. These plots are made by applying all selection criteria except in the variable of interest, and then measuring the fraction of isolated pseudo photons to all pseudo photons in bins. In practice there is a very small contribution from real photons to the pseudo photon selection, though this has a negligible in the calculations. The fraction for the loose $Z\gamma$ region, measured to be 0.17, is stable when restricting the $\Delta\phi(\ell,\ell)$ to lower values. Furthermore, the ratio is unchanging as a function of other variables, and therefore is very similar in the $Z\gamma$ validation region and signal region. The ratio for the $Z+$jets region is measured to be 0.35 as the majority of events lay in the $\Delta\phi(\ell,\ell) > 2.5$ bin.

With the scaling factor of the isolated to non-isolated pseudo photons understood, backgrounds from $Z+$jets are then predicted by selecting all pseudo photons and then scaling by $\kappa_{\mathrm{tight}}^{\mathrm{j}\to\gamma} \times 0.17$

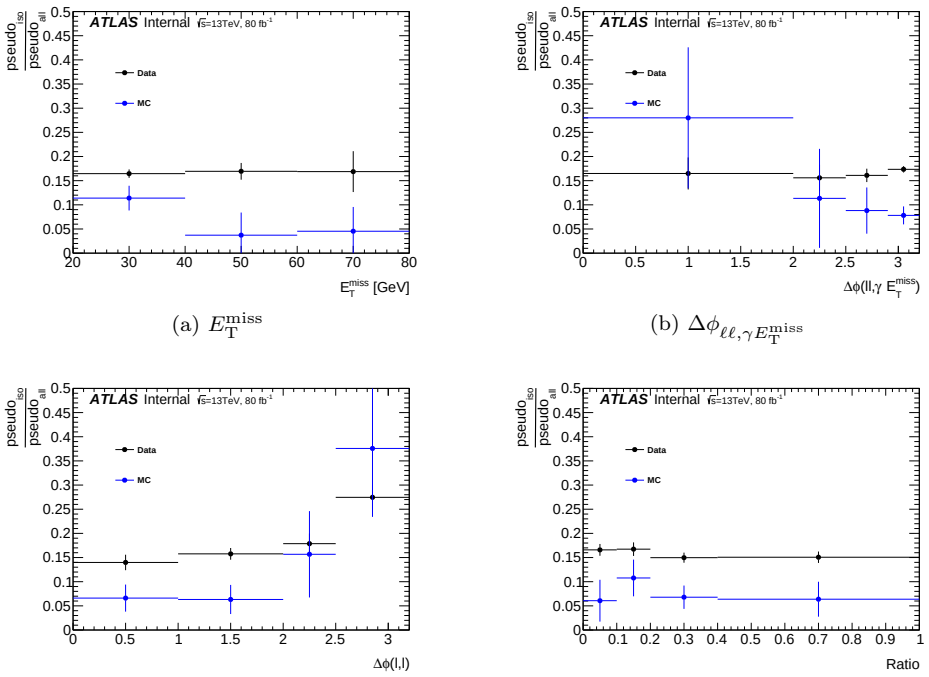

(a) $E_{\mathrm{T}}^{\mathrm{miss}}$ (b) $\Delta\phi_{\ell\ell,\gamma E_{\mathrm{T}}^{\mathrm{miss}}}$

(c) $\Delta\phi(\ell,\ell)$ (d) $\mathrm{Bal}_{p_{\mathrm{T}}}$

Figure 7.21: Dependence of the fraction of isolated pseudo photons to all pseudo photons in the data (black) and Monte Carlo (blue) as a function of: $E_{\mathrm{T}}^{\mathrm{miss}}$, $\Delta\phi_{\ell\ell,\gamma E_{\mathrm{T}}^{\mathrm{miss}}}$, $\Delta\phi(\ell,\ell)$, and $\mathrm{Bal}_{p_{\mathrm{T}}}$. This scaling factor, calculated in the "loose $Z\gamma$ region" is used as an additional extrapolation factor in the $Z\gamma$ control and validation regions and signal region. The Monte Carlo is not expected to model fakes well and is not used.

for the $Z\gamma$ regions and signal region. For the $Z+$jets validation region, the same technique is used but with a $\kappa_{\mathrm{tight}}^{\mathrm{j}\to\gamma} \times 0.35$ scaling factor. This technique introduces more systematic uncertainty due to the extrapolation in both isolation and identification, nevertheless the overall error of the $Z+$jets background estimate was reduced due to the diminished statistical uncertainty. Figure 7.24 demonstrates the effect of utilizing all scaled pseudo photons in comparison to only using isolated pseudo photons. The plot of the $E_{\mathrm{T}}^{\mathrm{miss}}$ spectra shows the jet-to-photon background estimation in the $Z\gamma$ validation region where statistics are already lacking. Using all scaled pseudo photons makes the background more akin to the smoothly falling distribution expected. The agreement between the scaled pseudo photons and the isolated pseudo photons is very good and the statistical uncertainties are *greatly* reduced. This gives us great confidence in this newly developed technique given the additional extrapolation.

With this technique Figures 7.25 and 7.26 show the kinematic variables in the $Z+$jets validation

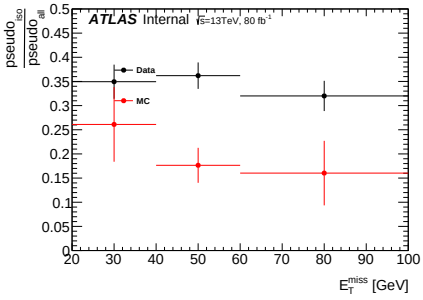

(a) $E_{\mathrm{T}}^{\mathrm{miss}}$

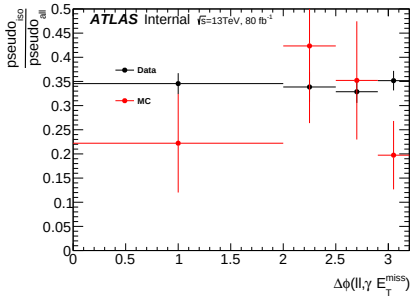

(b) $\Delta\phi_{\ell\ell,\gamma E_{\mathrm{T}}^{\mathrm{miss}}}$

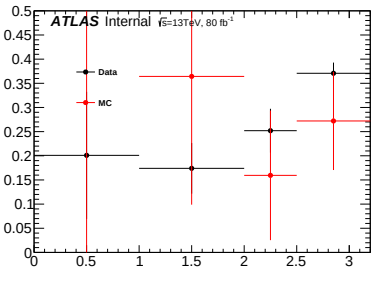

(c) $\Delta\phi(\ell,\ell)$

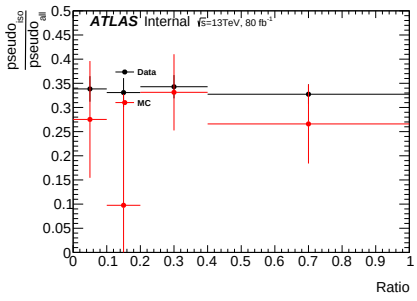

(d) $\mathrm{Bal}_{p_{\mathrm{T}}}$

Figure 7.22: Dependence of the fraction of isolated pseudo photons to all pseudo photons in the data (black) and Monte Carlo (red) as a function of: $E_{\mathrm{T}}^{\mathrm{miss}}$, $\Delta\phi_{\ell\ell,\gamma E_{\mathrm{T}}^{\mathrm{miss}}}$, $\Delta\phi(\ell,\ell)$, and $\mathrm{Bal}_{p_{\mathrm{T}}}$ for the $Z+$jets validation region. The Monte Carlo is not expected to model fakes well and is not used.

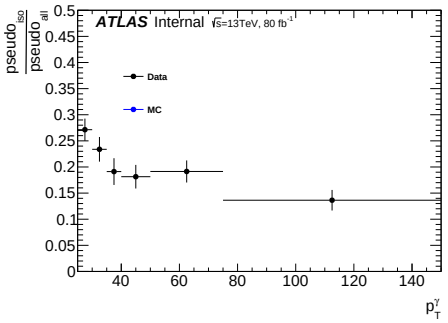

(a) p_{T} in loose $Z\gamma$ region

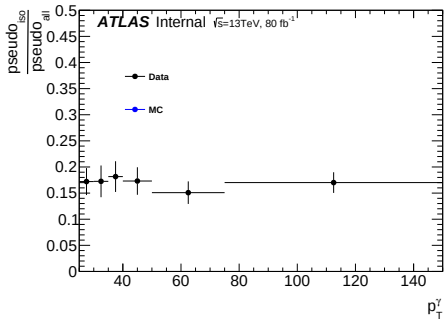

(b) p_{T} in loose $Z\gamma$ region with $\Delta\phi(\ell,\ell) < 2.0$

Figure 7.23: p_{T} dependence of the fraction of isolated pseudo photons to all pseudo photons measured in the data for (a) the loose $Z\gamma$ region and (b) with the $\Delta\phi(\ell,\ell) < 2.0$ cut which then makes the $Z\gamma$ control region.

region. Overall a 1.03 data/prediction ratio is observed which is well within the statistical and systematics errors. Extending the approach to the signal region by selecting events with pseudo photons (not signal photons) satisfying all other signal region criteria and scaling by $\kappa_{\text{tight}}^{\text{j}\to\gamma} \times 0.17$, this technique predicts 0.6 ± 0.3 jet-to-photon fake events in the signal region.

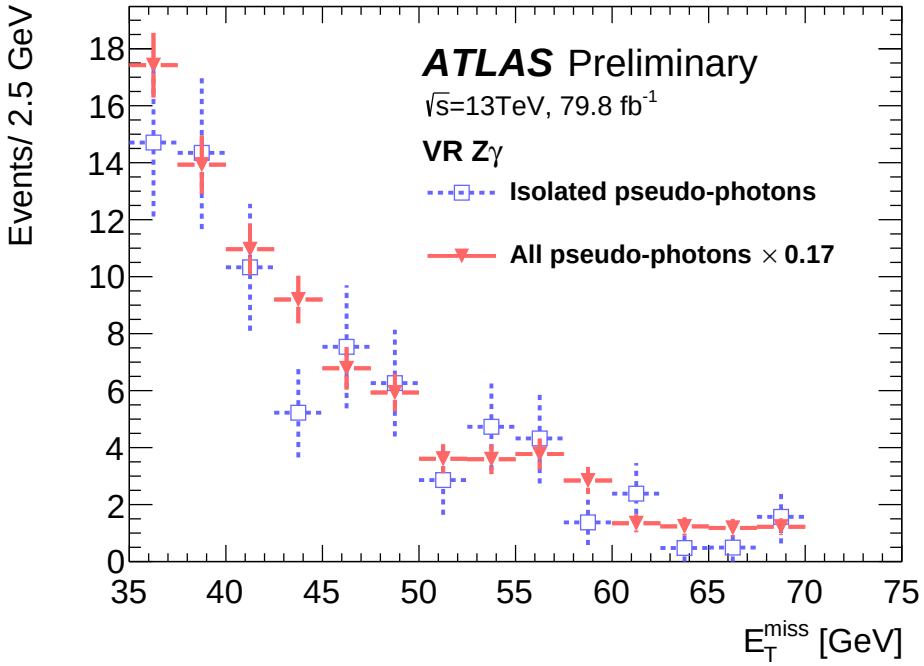

Figure 7.24: Distribution of $E_{\text{T}}^{\text{miss}}$ in the $Z\gamma$ validation region for the j $\to \gamma$ background utilizing all scaled pseudo photons (closed triangles) compared with only using isolated pseudo photons (open squares). Only the statistical uncertainty of the prediction is shown. The agreement between the scaled pseudo photons and the isolated pseudo photons is very good and the statistical uncertainties are *greatly* reduced.

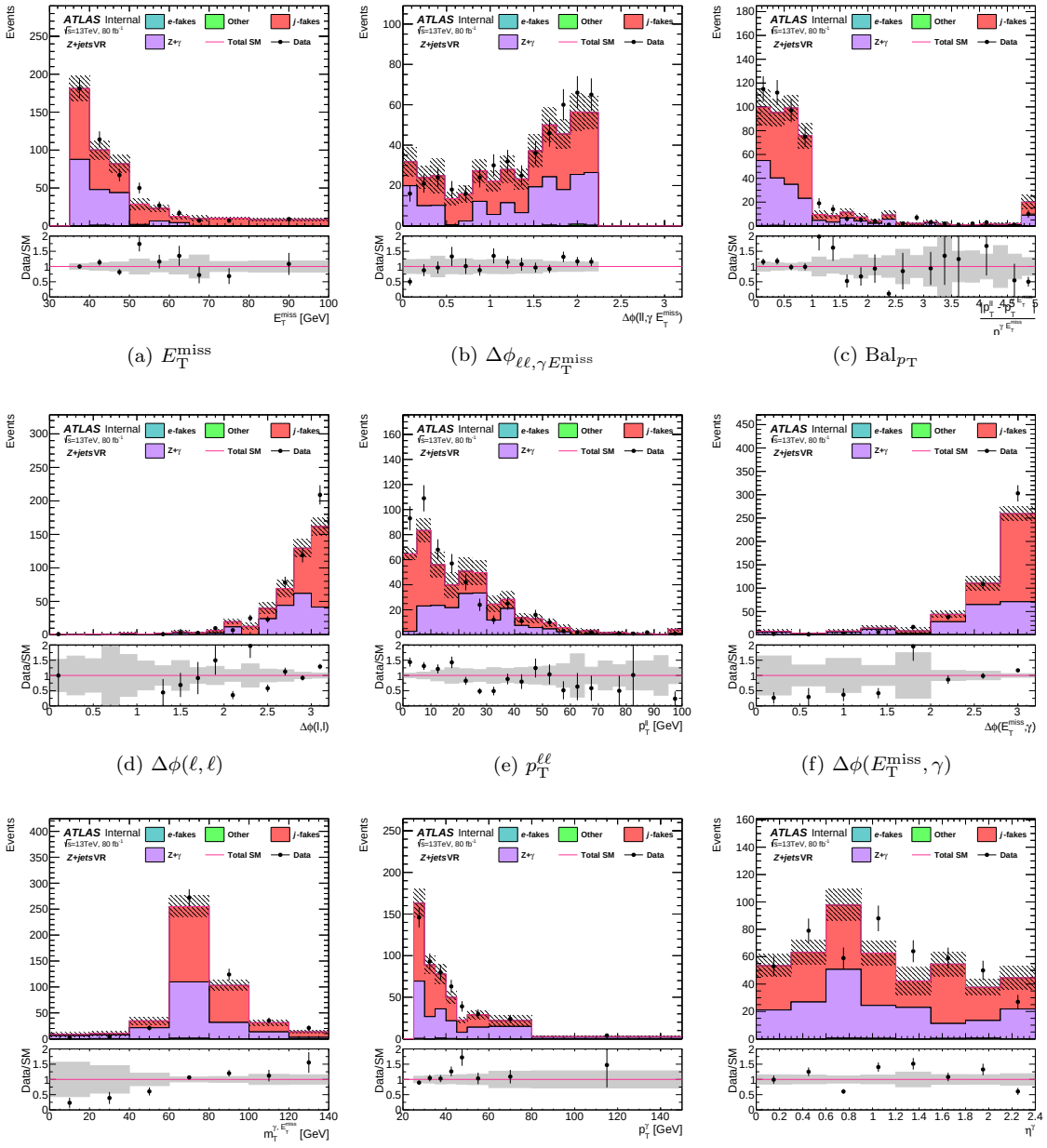

(a) $E_{\mathrm{T}}^{\mathrm{miss}}$ (b) $\Delta\phi_{\ell\ell,\gamma E_{\mathrm{T}}^{\mathrm{miss}}}$ (c) $\mathrm{Bal}_{p_{\mathrm{T}}}$

(d) $\Delta\phi(\ell,\ell)$ (e) $p_{\mathrm{T}}^{\ell\ell}$ (f) $\Delta\phi(E_{\mathrm{T}}^{\mathrm{miss}},\gamma)$

(g) $m_T^{\gamma,E_{\mathrm{T}}^{\mathrm{miss}}}$ (h) $p_{\mathrm{T}}^{\gamma_1}$ (i) η^{γ_1}

Figure 7.25: Distributions of (a) $E_{\mathrm{T}}^{\mathrm{miss}}$, (b) $\Delta\phi_{\ell\ell,\gamma E_{\mathrm{T}}^{\mathrm{miss}}}$, (c) $\mathrm{Bal}_{p_{\mathrm{T}}}$, (d) $\Delta\phi(\ell,\ell)$, (e) $p_{\mathrm{T}}^{\ell\ell}$, (f) $\Delta\phi(E_{\mathrm{T}}^{\mathrm{miss}},\gamma)$, (g) $m_T^{\gamma,E_{\mathrm{T}}^{\mathrm{miss}}}$, (h) $p_{\mathrm{T}}^{\gamma_1}$, and (i) η^{γ_1} in the $Z+$jets validation region. The red histogram is the data-driven j $\to \gamma$ background, which makes up $\sim 56\%$ of the event yield. The other contributions, except for the $e \to \gamma$ background are modeled by simulation. The region is used to validate the technique to derive the j $\to \gamma$ background as a function of many variables.

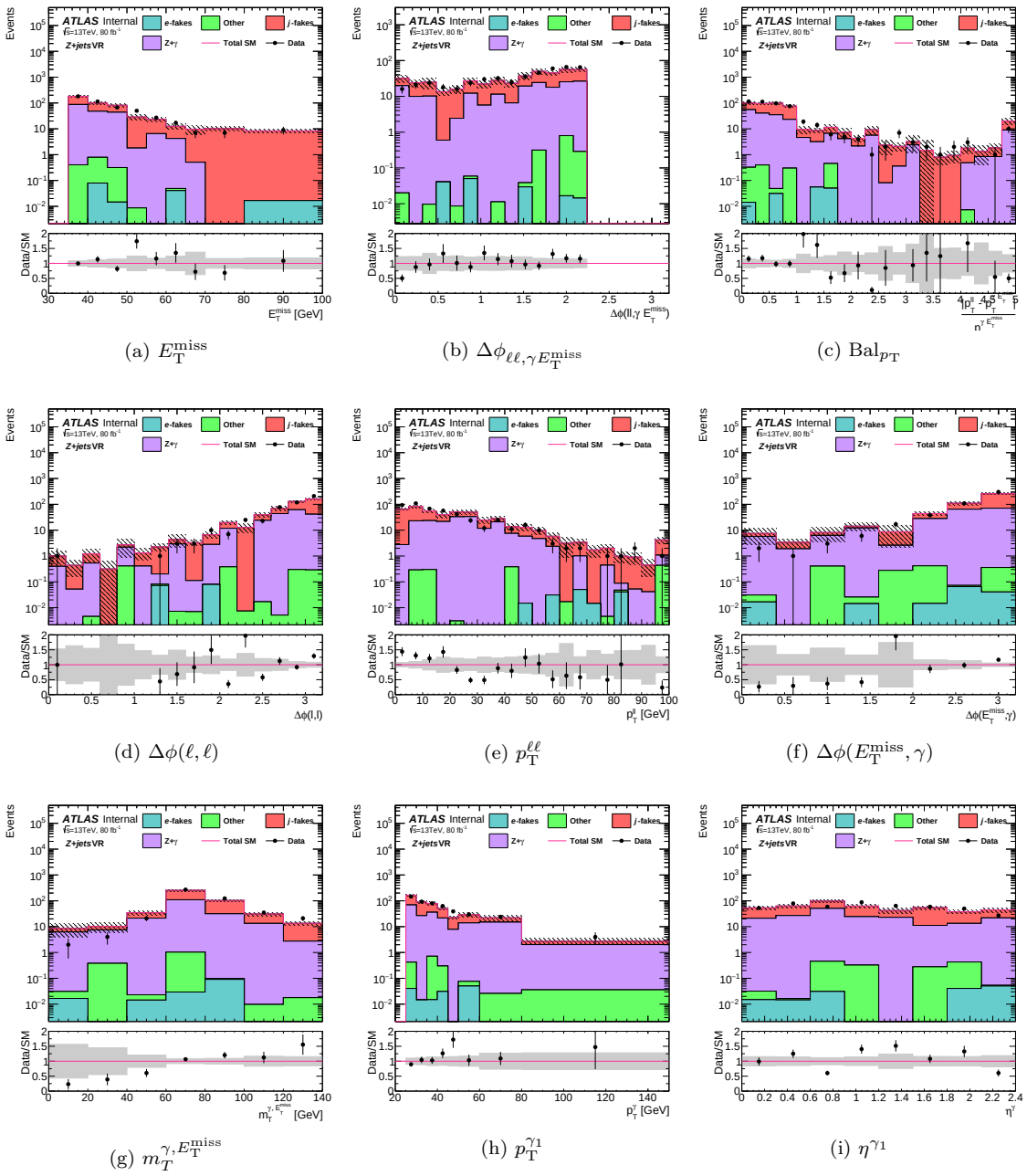

(a) $E_{\mathrm{T}}^{\mathrm{miss}}$ (b) $\Delta\phi_{\ell\ell,\gamma E_{\mathrm{T}}^{\mathrm{miss}}}$ (c) $\mathrm{Bal}_{p_{\mathrm{T}}}$

(d) $\Delta\phi(\ell,\ell)$ (e) $p_{\mathrm{T}}^{\ell\ell}$ (f) $\Delta\phi(E_{\mathrm{T}}^{\mathrm{miss}},\gamma)$

(g) $m_T^{\gamma,E_{\mathrm{T}}^{\mathrm{miss}}}$ (h) $p_{\mathrm{T}}^{\gamma_1}$ (i) η^{γ_1}

Figure 7.26: Log scale distributions of (a) $E_{\mathrm{T}}^{\mathrm{miss}}$, (b) $\Delta\phi_{\ell\ell,\gamma E_{\mathrm{T}}^{\mathrm{miss}}}$, (c) $\mathrm{Bal}_{p_{\mathrm{T}}}$, (d) $\Delta\phi(\ell,\ell)$, (e) $p_{\mathrm{T}}^{\ell\ell}$, (f) $\Delta\phi(E_{\mathrm{T}}^{\mathrm{miss}},\gamma)$, (g) $m_T^{\gamma,E_{\mathrm{T}}^{\mathrm{miss}}}$, (h) $p_{\mathrm{T}}^{\gamma_1}$, and (i) η^{γ_1} in the $Z+$jets validation region. The red histogram is the data-driven j $\to \gamma$ background, which makes up $\sim 56\%$ of the event yield. The other contributions, except for the $e \to \gamma$ background are modeled by simulation. The region is used to validate the technique to derive the j $\to \gamma$ background as a function of many variables.

7.4.2.1 Derivation of the Jet to Photon Mis-identification Rate

The method employed to derive the photon fake factors, called the ABCD method, makes use of the isolation profiles expected for real and mis-identified photons. Similarly to the 2x2D sideband method, a two dimensional plane is constructed with identification and isolation variables. The difference, other than only requiring one signal photon, between this and the 2x2D sideband method is that only the number of jet-to-photon fakes in the signal region is desired. The photon is identified as either *Tight* or "pseudo", which is *Loose-but-not-Tight* and defined in a way to be less correlated with isolation variables, as described in Section 5.1.3. In the isolation axis, the photon candidate can either be isolated or non-isolated, as determined by the "corrected topocone40" = topoetcone40$-0.022p_{\mathrm{T}}$, where the topoetcone40 is the transverse energy in a cone of radius $\Delta R = 0.4$ around the photon. This leads to four distinct areas of phase space described below or illustrated in Figure 7.27.

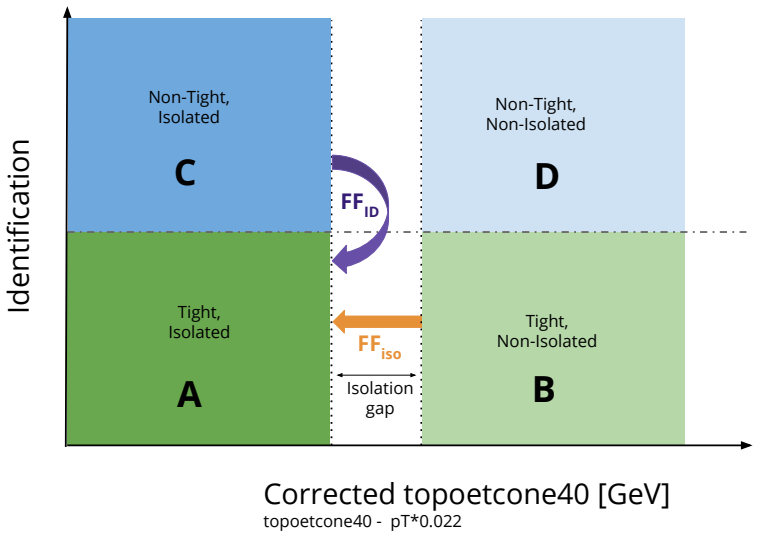

Figure 7.27: Cartoon of the ABCD regions in the two dimensional plane of identification and isolation.

- **A**: *Tight* ID photon with track isolation and corrected topocone40 < 0 GeV
- **B**: *Tight* ID photon with corrected topocone40 > 8 GeV
- **C**: Pseudo photon with track isolation and corrected topocone40 < 0 GeV
- **D**: Pseudo photon with corrected topocone40 > 8 GeV

The ABCD method establishes three control regions (denoted B,C,D), which are composed of the mis-identified and looser photons(referred to as background photons), and a "signal region" in A. Assuming no signal contamination and correlation in the regions (this is a first order conjecture), the following holds: $\frac{N_B^b}{N_A^b} = \frac{N_D^b}{N_C^b}$, that is the ratio of background events in B to A is the same as D to C. Thus two photon fake factors can be written:

$$\mathrm{FF_{Iso}} = \frac{N_C}{N_D}, \qquad \mathrm{FF_{ID}} = \frac{N_B}{N_D} \ . \tag{7.4}$$

With these factors designated, to estimate the number of jet-to-photon events in region A, the different fake factors can be applied in regions B or C:

$$N_{j\to\gamma}(p_{\mathrm{T}},\eta) = N_A^b = \mathrm{FF_{Iso}}(p_{\mathrm{T}},\eta) \times N_B = \mathrm{FF_{ID}}(p_{\mathrm{T}},\eta) \times N_C \tag{7.5}$$

By construction, using either $\mathrm{FF_{Iso}}$ or $\mathrm{FF_{ID}}$ will give the same prediction for the signal region. The choice is up to the analyzer. In this analysis the isolation fake factors were larger than one in some important areas of phase space. This implies one event in control regions would be used to predict more than one signal region event, leading to large statistical errors of the final prediction. Therefore the ID fake factors were chosen to be used in the analysis. To be explicit, in order to infer the $Z+$jets background in a given region, isolated pseudo photons would be selected and the $\mathrm{FF_{ID}}$ would be applied. The signal contamination in the control regions can be quantified and the fake factors are modified:

$$N_{j\to\gamma}(p_{\mathrm{T}},\eta) = N_A^b = \frac{N_B - N_B^s}{N_D - N_D^s} \times (N_C - N_C^s) = \mathrm{FF_{ID}^{corr}}(p_{\mathrm{T}},\eta) \times (N_C - N_C^s) \ ; \tag{7.6}$$

where N^s denotes the number of real prompt photons in each region. This number is extracted from truth matched photons in Monte Carlo. Lastly, to gauge the correlation of the regions (R), one can calculate:

$$R = \frac{N_A^b N_D^b}{N_B^b N_C^b} \ , \tag{7.7}$$

which will equal 1 in the case of no correlation. Unfortunately R cannot be measured in data as background photons cannot be distinguished, therefore a similarly defined $R^{'}$ is computed in a data region rich in background:

$$R' = \frac{N_A^{'} N_D^{'}}{N_B^{'} N_C^{'}} \ ; \tag{7.8}$$

where the primed regions are:

- $\mathbf{A}^{'}$: *Tight* ID photon with track isolation and $9 <$ corrected topocone40 < 15 GeV

- $\mathbf{B}^{'}$: *Tight* ID photon with $15 <$ corrected topocone40 < 27 GeV
- $\mathbf{C}^{'}$: Pseudo photon with track isolation and $9 <$ corrected topocone40 < 15 GeV
- $\mathbf{D}^{'}$: Pseudo photon with $15 <$ corrected topocone40 < 27 GeV

The 9 GeV choice to start the $R^{'}$ regions is arbitrary but aims to define a background enriched region for measuring the correlation while retaining sufficient statistics. The final formula for the estimated jet-to-photon events in a signal region with the correlation included would then be:

$$N_{j\to\gamma}(p_{\mathrm{T}},\eta) = N_A^b = \left\{R^{'}\frac{N_B - N_B^s}{N_D - N_D^s}\right\} \times (N_C - N_C^s) = \left\{R^{'}\frac{N_B - N_B^s}{N_D - N_D^s}(\frac{1 - N_C^s}{N_C})\right\} \times N_C = \mathrm{FF}_{\mathrm{ID}}^{\mathrm{corr}}(p_{\mathrm{T}},\eta) \times N_C \ . \quad (7.9)$$

In the analysis, the jet-to-photon mis-identified background arises from mostly $Z+$jets so naturally the fake factors should be measured in a $Z+$jets region distinct from the signal region. Unfortunately, with photon like objects, the region is dominated by Standard Model $Z\gamma$ leading to enormous subtractions of the signal photon contamination and large statistical uncertainties. Instead, the measurement is performed in a diphoton topology, tagging the first photon as *Tight* and isolated, and allowing the second photon to be *Tight* or pseudo. To further complicate matters, the 2017 trigger used to collect the sample was tighter and contained an additional calorimeter requirement, changing the composition of the *Loose-but-not-Tight* photons. In order to expedite the analysis further studies were left for the full Run 2 search, and it was decided to perform the photon fake factor extraction with the 2015–2016 diphoton sample collected with the same trigger as the $H\to\gamma\gamma$ analysis (detailed in Section 6.2.1).

A comparison between the $Z+$jets fake factor calculated with $79.8\,\mathrm{fb}^{-1}$ of data and the diphoton fake factor determined with $36.1\,\mathrm{fb}^{-1}$ of data in a different dataset is shown in Figure 7.28. The fake factors are calculated independently for the barrel (red) and endcap (blue) regions for the following studies. The shapes of the distributions are similar to each other and although the uncertainties in the fake factor determined from the $Z+$jets samples are large, they are consistent with the magnitude and dependence on p_{T}seen in the diphoton derivation. As long as the $Z+$jets fake factors were not contingent on the topology of the event, then the fake factors derived in the diphoton region could be employed for the final calculation. Figure 7.29 shows the $Z+$jets fake factors as a function of $p_{\mathrm{T}}^{\ell\ell}$ and $E_{\mathrm{T}}^{\mathrm{miss}}$. The values are relatively constant.

The diphoton fake factors were then investigated for reliance on kinematic variables. The fake factors as a function of $E_{\mathrm{T}}^{\mathrm{miss}}$, $\Delta\phi(E_{\mathrm{T}}^{\mathrm{miss}},\gamma)$, $m_T^{\gamma,E_{\mathrm{T}}^{\mathrm{miss}}}$ are shown in Figure 7.30. Considering the fake factors are not sensitive to most important kinematic variables, the fake factors parameterized by p_{T} will used in the analysis. The full breakdown of the ID fake factors can be seen in Table 7.7. The

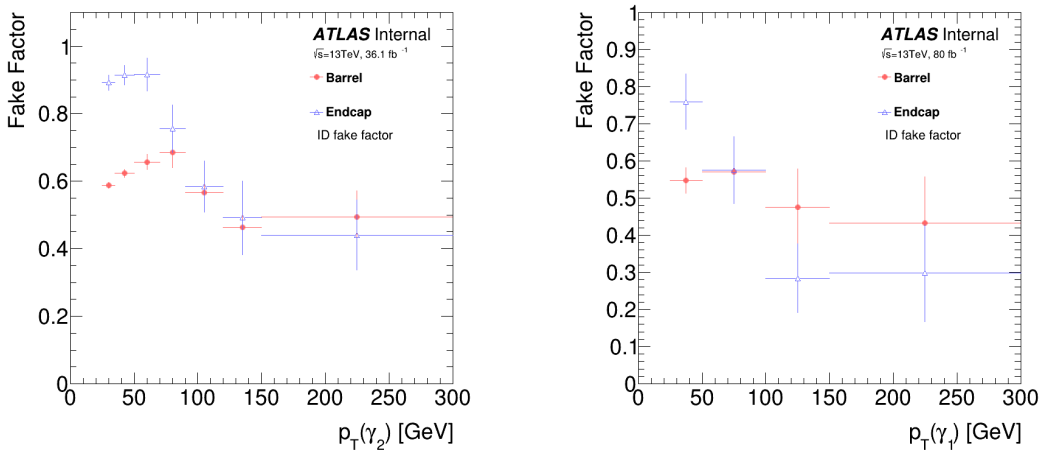

(a) Diphoton (b) $Z+\text{jets}$

Figure 7.28: (a) Diphoton and (b) $Z+\text{jets}$ jet-to-photon ID fake factors as a function of p_{T}. The measurements are split between barrel (red) and endcap objects (blue). The diphoton fake factors were calculated using $36.1\,\text{fb}^{-1}$ of 2015–2016 data while the $Z+\text{jets}$ fake factors were derived utilizing $79.8\,\text{fb}^{-1}$ of data collected in 2015–2017.

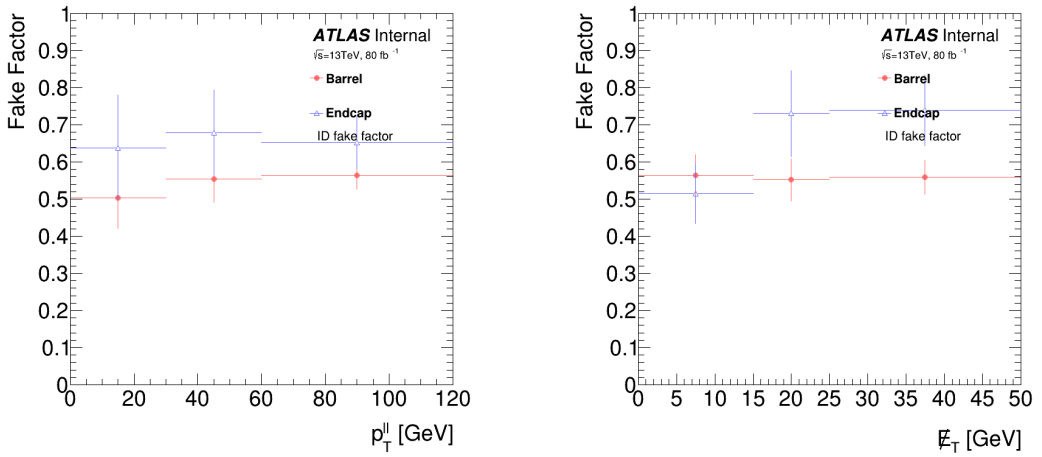

(a) $p_{\mathrm{T}}^{\ell\ell}$ (b) $E_{\mathrm{T}}^{\mathrm{miss}}$

Figure 7.29: Jet-to-photon ID fake factor as a function of (a) $p_{\mathrm{T}}^{\ell\ell}$ and (b) $E_{\mathrm{T}}^{\mathrm{miss}}$ in the $Z+\text{jets}$ region. The fake factors are derived in the barrel (red) and endcap (blue) regions.

factors, statistical errors, and $R^{'}$ parameters are presented in p_{T} bins for both the barrel and endcap regions. This factor is measured to be 0.4-0.7 in the barrel region and 0.45-0.95 in the endcap region of the detector, depending on the p_{T} of the photon. The correlation R' derived in the data was within 15% of 1.0 (no correlation) for most bins.

Table 7.7: Jet-to-photon ID fake factors, binned in p_{T} and split between barrel and endcap regions.

p_{T}Bin [GeV]	$0.0 < \lvert\eta\rvert < 1.37$	Stat. Err.	$R^{'}$	$1.52 < \lvert\eta\rvert < 2.37$	Stat. Err.	$R^{'}$
$25 \leq p_{\mathrm{T}} < 35$	0.59	0.01	0.86	0.87	0.02	0.86
$35 \leq p_{\mathrm{T}} < 50$	0.63	0.01	0.85	0.91	0.02	0.83
$50 \leq p_{\mathrm{T}} < 65$	0.66	0.02	0.93	0.92	0.05	0.90
$65 \leq p_{\mathrm{T}} < 80$	0.69	0.04	0.90	0.76	0.06	0.92
$80 \leq p_{\mathrm{T}} < 100$	0.57	0.05	0.90	0.58	0.07	0.90
$100 \leq p_{\mathrm{T}} < 150$	0.46	0.05	0.86	0.50	0.08	1.09
$150 \leq p_{\mathrm{T}} < \infty$	0.51	0.07	1.16	0.45	0.10	1.02

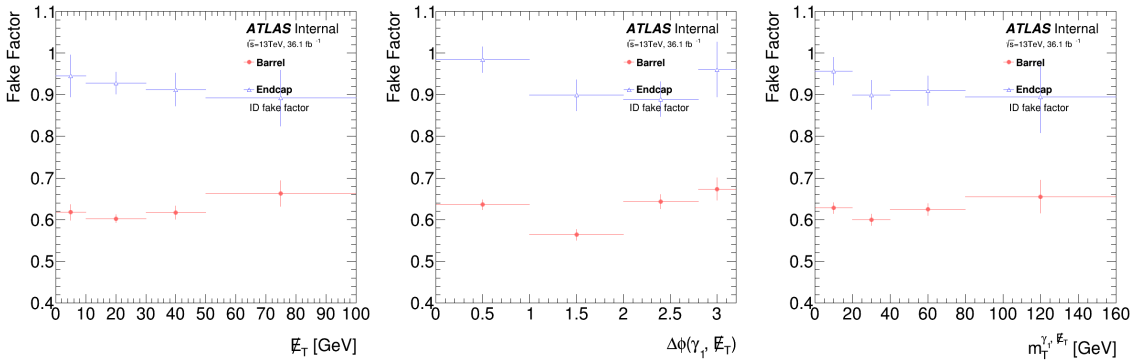

(a) $E_{\mathrm{T}}^{\mathrm{miss}}$ (b) $\Delta\phi(E_{\mathrm{T}}^{\mathrm{miss}}, \gamma)$ (c) $m_T^{\gamma, E_{\mathrm{T}}^{\mathrm{miss}}}$

Figure 7.30: Diphoton photon-to-jet ID fake factors as a function of (a) $E_{\mathrm{T}}^{\mathrm{miss}}$, (b) $\Delta\phi(E_{\mathrm{T}}^{\mathrm{miss}}, \gamma)$, (c) $m_T^{\gamma, E_{\mathrm{T}}^{\mathrm{miss}}}$. The fake factors are calculated in the barrel (red) and endcap (blue) regions.

Correlation Measurements

The previous section details the photon fake factors derived in the data. In $Z+$jets and γj Monte Carlo one can do the same calculations and confirm the assumptions are reasonable. The R' parameter, which measures the correlation of the regions, in the fake rate calculation is measured in primed regions rather than the actual ABCD regions. As a simple check, the actual $R = \frac{N_A^b N_D^b}{N_B^b N_C^b}$ is calculated in Monte Carlo and compared with the R' used in the fake rate derivation. Table 7.8

shows the comparison between data and Monte Carlo correlation factors, binned coarser to compare the correlation in both $Z+$jets and γj events. The majority of R' and R parameters are consistent with each other and 1.0.

Table 7.8: R and R' parameters measured in the $Z+$jets and γj Monte Carlo and data.

	Barrel $Z+$jets		**Barrel Diphoton**		**Endcap $Z+$jets**		**Endcap Diphoton**	
p_{T} **[GeV]**	R'	R	R'	R	R'	R	R'	R
$25 \leq p_{\mathrm{T}} < 50$	0.99± 0.03	1.16± 0.06	1.12±0.09	1.30 ± 0.06	0.83±0.07	1.23± 0.07	0.87 ±0.15	1.13 ± 0.10
$50 \leq p_{\mathrm{T}} < 100$	0.96± 0.05	1.22± 0.08	0.99±0.11	1.15 ± 0.09	0.94±0.11	0.88± 0.17	0.94 ±0.14	1.32 ± 0.16
$100 \leq p_{\mathrm{T}} < 150$	0.98± 0.11	1.07± 0.16	1.04±0.15	0.93 ± 0.18	1.16±0.17	0.79± 0.21	0.77 ±0.21	0.85 ± 0.32
$150 \leq p_{\mathrm{T}} < \infty$	0.96± 0.06	1.18± 0.23	1.07±0.06	1.01 ± 0.10	0.89±0.07	1.59± 0.61	1.11 ±0.23	1.17 ± 0.23

7.4.3 Backgrounds from Standard Model $Z\gamma$

Ideally, Standard Model $Z\gamma$ events with no associated jets originating from the hard scatter should have no $E_{\mathrm{T}}^{\mathrm{miss}}$ as the momentum of the γ and Z boson should balance perfectly. Due to detector resolution, pileup of the underlying event and soft jets from multiple vertices, as well as heavy flavor quark decays in jets with $20 < p_{\mathrm{T}} < 30$ GeV, missing transverse momentum is introduced into the event. Requiring large $E_{\mathrm{T}}^{\mathrm{miss}}$ is an effective strategy to reduce this background although due to the kinematics of the Higgs boson decay, cutting very hard on $E_{\mathrm{T}}^{\mathrm{miss}}$ greatly diminishes the signal acceptance. This is especially true in the $h \to \tilde{\chi}_1^0\tilde{\chi}_1^0 \to \gamma\tilde{G}\gamma\tilde{G}$ decay channel and therefore is not feasible.

A sample enriched with $Z\gamma$ events is defined at lower $E_{\mathrm{T}}^{\mathrm{miss}}$ requiring no cut on $\Delta\phi_{\ell\ell,\gamma E_{\mathrm{T}}^{\mathrm{miss}}}$, and a slightly looser cut on $\Delta\phi(\ell,\ell)$ in order to increase the event yield. This phase space is partitioned into two regions: $20 < E_{\mathrm{T}}^{\mathrm{miss}} < 35$ GeV for the control region and $35 < E_{\mathrm{T}}^{\mathrm{miss}} < 70$ GeV for the validation region. This control region has 1,203 data events and is used to constrain the normalization of the $Z\gamma$ Monte Carlo. The shape and normalization of different variables are validated in the intermediate $E_{\mathrm{T}}^{\mathrm{miss}}$ domain.

In Figure 7.31 the missing transverse momentum distribution is shown for events in the $Z\gamma$ control region. The other kinematic variables in the control region are presented in Figures 7.33 and 7.34 with linear and log scales, respectively. Overall the modeling is excellent in the region. Because these regions also have electrons and jets mis-identified as photons, the distributions are more accurately characterized with data-driven estimates of the mis-identified objects rather than the Monte Carlo only prediction. In addition to the shape description, these data-driven estimates also reduce the

statistical uncertainties of the estimation. The following figures show the $Z\gamma$ background regions with MC only estimates and estimates with fake backgrounds predicted with techniques outlines in the previous two sections.

After the fitting procedure, the normalization of the $Z\gamma$ Monte Carlo is determined to be $\mu_{Z\gamma} = 1.04 \pm 0.13$. The plots shown for the control and validation regions have the $Z\gamma$ component multiplied by this factor. The process of extracting this factor with a simultaneous fit to all control and signal regions is described in Section 7.6. Likewise, Figure 7.32, shows the $E_{\mathrm{T}}^{\mathrm{miss}}$ distribution in the $Z\gamma$ validation region and Figures 7.35 (linear) and 7.36 (log) show the other kinematic variables. The data-to-MC agreement is once again very good.

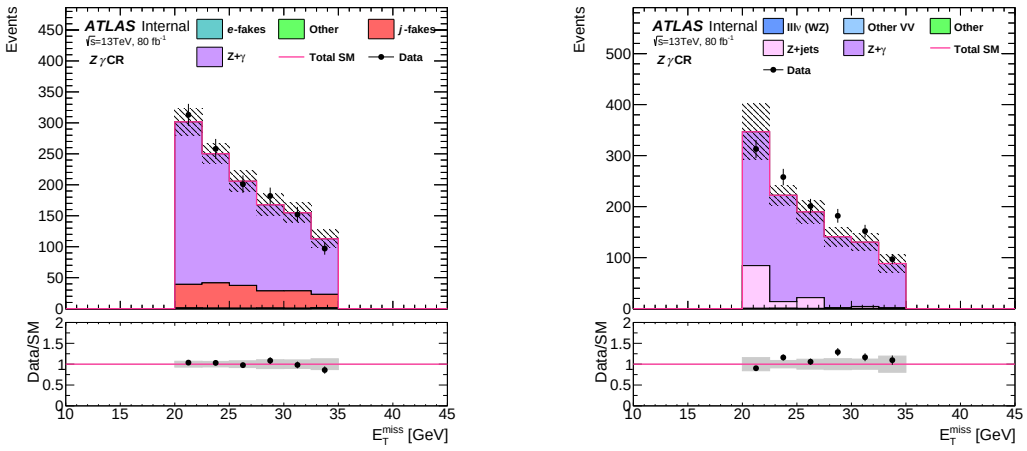

(a) data-driven

(b) MC only

Figure 7.31: Distribution of $E_{\mathrm{T}}^{\mathrm{miss}}$ in the $Z\gamma$ control region using (a) the data-driven estimate or (b) Monte Carlo only. In data-driven (a) approach all objects mis-identified as photons are labeled as e-fakes (electron) or j-fakes (jet) and their calculations are outlined in the previous sections. The $Z\gamma$ background component is predicted using only simulation, shown in purple, and is the same for both plots.

In both the control and validation regions, there is a slight slope in the data-MC ratio due to mis-modeling of the $m_T^{\gamma,E_{\mathrm{T}}^{\mathrm{miss}}}$ spectrum. This is ignored for now as it is a small effect as the $Z\gamma$ background is the signal region is very small. Additionally, no shape fit is performed and the signal region criteria is a single bin with no $m_T^{\gamma,E_{\mathrm{T}}^{\mathrm{miss}}}$ selection criterion. As mentioned earlier, in future iterations of the analysis hopefully this can be understood and corrected, allowing for a multi-bin fit of the $m_T^{\gamma,E_{\mathrm{T}}^{\mathrm{miss}}}$ distribution in order to increase sensitivity of the analysis. The final predicted signal region event yield arising from the $Z\gamma$ background is $0.03^{+0.15}_{-0.03}$ events. This error contains

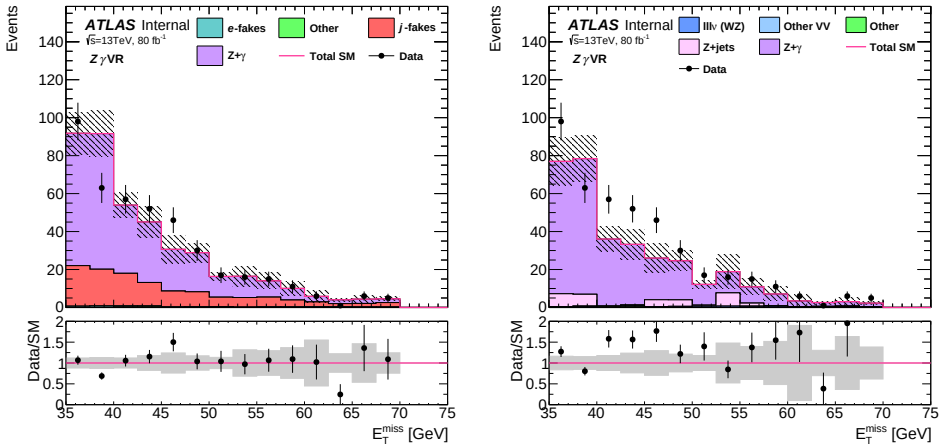

(a) data-driven (b) MC only

Figure 7.32: Distribution of $E_{\mathrm{T}}^{\mathrm{miss}}$ in the $Z\gamma$ validation region using (a) the data-driven estimate or (b) Monte Carlo only. In data-driven (a) approach all objects mis-identified as photons are labeled as e-fakes (electron) or j-fakes (jet) and their calculations are outlined in the previous sections. The $Z\gamma$ background component is predicted using only simulation, shown in purple, and is the same for both plots.

both the statistical and systematic uncertainties (described in the next section). The $Z\gamma$ Monte Carlo estimate arises from 11 unweighted events[17].

7.4.4 Backgrounds from Other Standard Model Processes Containing Real Photons

Backgrounds from $t\bar{t}\gamma$, $W\gamma\gamma$, and $Z\gamma\gamma$ are estimated with Monte Carlo simulation to be negligible. The number of background events from Standard Model Higgs boson decays ($h \to \gamma\gamma, WW, \tau\tau$) is also insignificant. The cross section of $ZH \to \ell\ell Z\gamma \to \ell\ell\nu\nu\gamma$ is 0.018 fb [32, 50] and is therefore neglected. The upper limit on the production cross section for $h \to Z\gamma \to \ell\ell\gamma$ is measured to be 6.6 times the SM prediction [265], making this background negligible as well. These small backgrounds are then predicted using Monte Carlo. They can be seen in the plots, denoted "Other". They can be observed in the control and validation regions, but no Monte Carlo events enter in the signal region. The final prediction in the signal region with systematic uncertainties is $0^{+0.01}_{-0.00}$ events.

[17] Of which one is removed as the photon is truth matched to a π^0meson. Keeping this event would double count part of the jet-to-photon fake background.

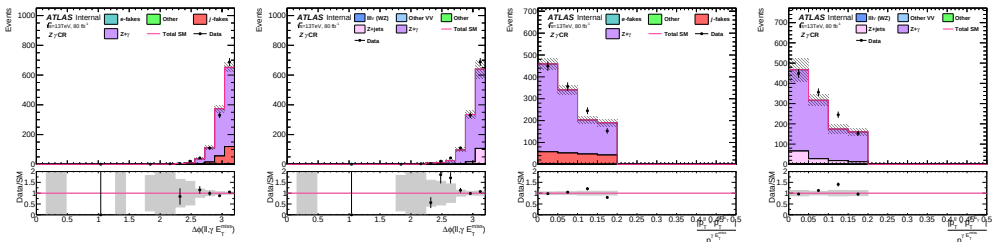

(a) $\Delta\phi_{\ell\ell,\gamma E_{\mathrm{T}}^{\mathrm{miss}}}$, data-driven (b) MC only (c) $\mathrm{Bal}_{p_{\mathrm{T}}}$, data-driven (d) MC only

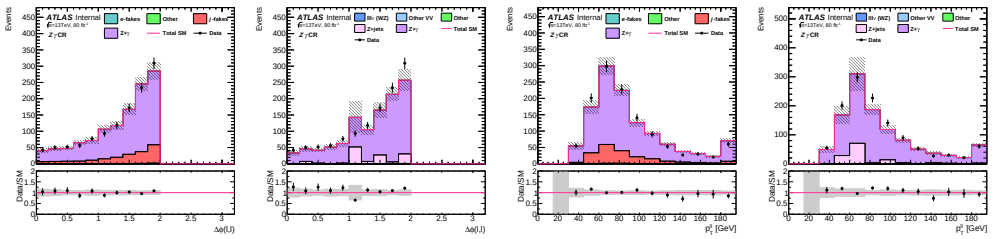

(e) $\Delta\phi(\ell,\ell)$, data-driven (f) MC only (g) $p_{\mathrm{T}}^{\ell\ell}$, data-driven (h) MC only

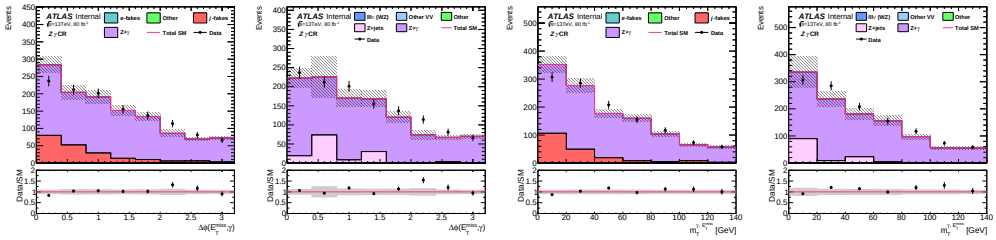

(i) $\Delta\phi(E_{\mathrm{T}}^{\mathrm{miss}},\gamma)$, data-driven (j) MC only (k) $m_T^{\gamma,E_{\mathrm{T}}^{\mathrm{miss}}}$, data-driven (l) MC only

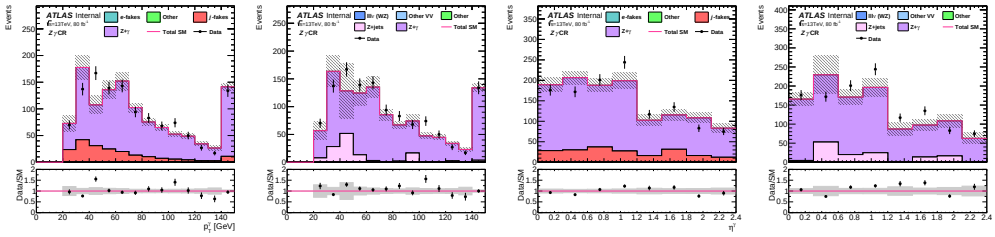

(m) $p_{\mathrm{T}}^{\gamma_1}$, data-driven (n) MC only (o) η^{γ_1}, data-driven (p) MC only

Figure 7.33: Distributions of (a) $\Delta\phi_{\ell\ell,\gamma E_{\mathrm{T}}^{\mathrm{miss}}}$, (c) $\mathrm{Bal}_{p_{\mathrm{T}}}$, (e) $\Delta\phi(\ell,\ell)$, (g) $p_{\mathrm{T}}^{\ell\ell}$, (i) $\Delta\phi(E_{\mathrm{T}}^{\mathrm{miss}},\gamma)$, (k) $m_T^{\gamma,E_{\mathrm{T}}^{\mathrm{miss}}}$, (m) $p_{\mathrm{T}}^{\gamma_1}$, and (o) η^{γ_1} in the $Z\gamma$ control region with data-driven backgrounds for the electron and jet fakes. Subfigures (b, d, ..., p) contain the same distributions as the subfigures to the right ((b) contains same distribution as (a)) but with the Monte Carlo only predictions. In the data-driven approach all objects mis-identified as photons are labeled as e-fakes (electron) or j-fakes (jet) and their calculations are outlined in the previous sections. The $Z\gamma$ background component is predicted using only simulation, shown in purple, and is the same for both plots.

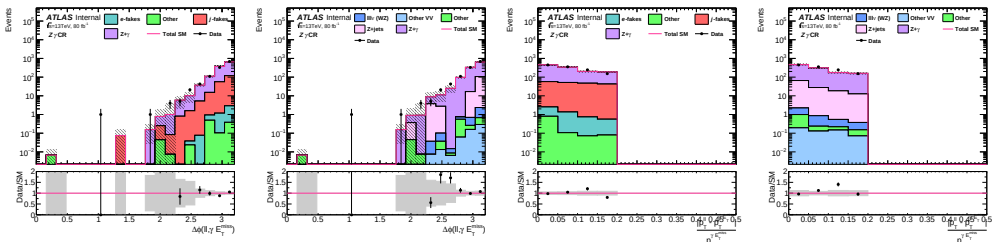

(a) $\Delta\phi_{\ell\ell,\gamma E_{\mathrm{T}}^{\mathrm{miss}}}$, data-driven (b) MC only (c) $\mathrm{Bal}_{p_{\mathrm{T}}}$, data-driven (d) MC only

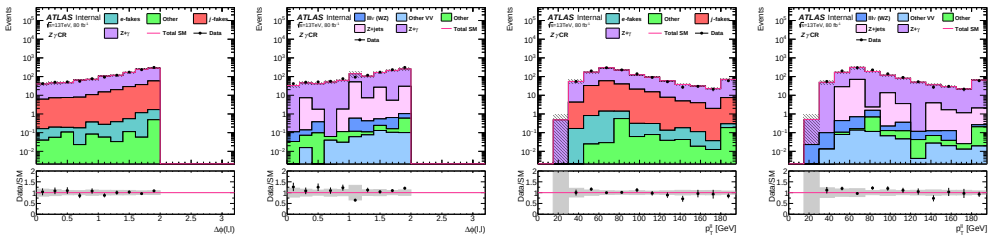

(e) $\Delta\phi(\ell,\ell)$, data-driven (f) MC only (g) $p_{\mathrm{T}}^{\ell\ell}$, data-driven (h) MC only

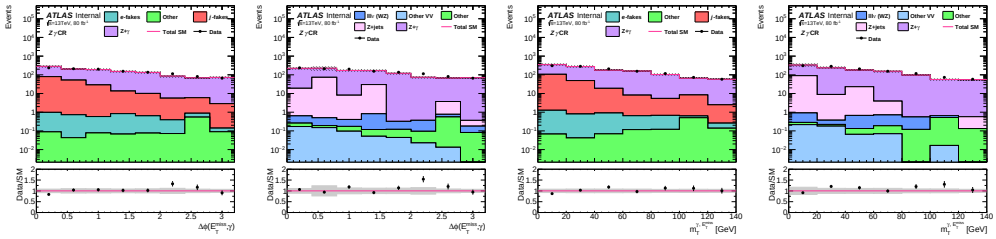

(i) $\Delta\phi(E_{\mathrm{T}}^{\mathrm{miss}},\gamma)$, data-driven (j) MC only (k) $m_T^{\gamma,E_{\mathrm{T}}^{\mathrm{miss}}}$, data-driven (l) MC only

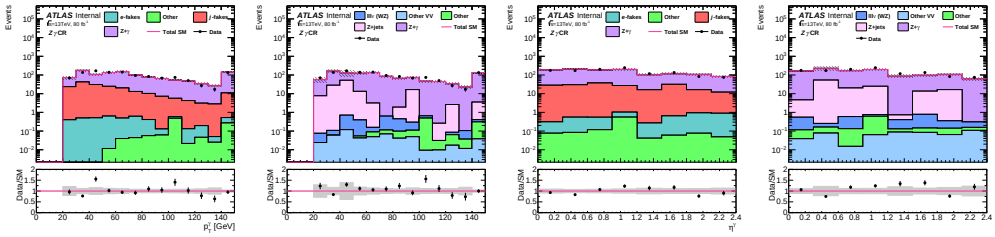

(m) $p_{\mathrm{T}}^{\gamma_1}$, data-driven (n) MC only (o) η^{γ_1}, data-driven (p) MC only

Figure 7.34: Distributions of (a) $\Delta\phi_{\ell\ell,\gamma E_{\mathrm{T}}^{\mathrm{miss}}}$, (c) $\mathrm{Bal}_{p_{\mathrm{T}}}$, (e) $\Delta\phi(\ell,\ell)$, (g) $p_{\mathrm{T}}^{\ell\ell}$, (i) $\Delta\phi(E_{\mathrm{T}}^{\mathrm{miss}},\gamma)$, (k) $m_T^{\gamma,E_{\mathrm{T}}^{\mathrm{miss}}}$, (m) $p_{\mathrm{T}}^{\gamma_1}$, and (o) η^{γ_1} in the $Z\gamma$ control region with data-driven backgrounds for the electron and jet fakes in the log scale. Subfigures (b, d, ..., p) contain the same distributions as to the right ((b) contains same distribution as (a)) but with the Monte Carlo only predictions. In the data-driven approach all objects mis-identified as photons are labeled as e-fakes (electron) or j-fakes (jet) and their calculations are outlined in the previous sections. The $Z\gamma$ background component is predicted using only simulation, shown in purple, and is the same for both plots.

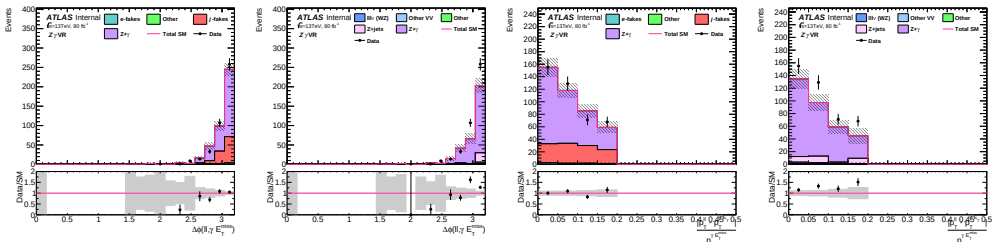

(a) $\Delta\phi_{\ell\ell,\gamma E_{\mathrm{T}}^{\mathrm{miss}}}$, data-driven (b) MC only (c) $\mathrm{Bal}_{p_{\mathrm{T}}}$, data-driven (d) MC only

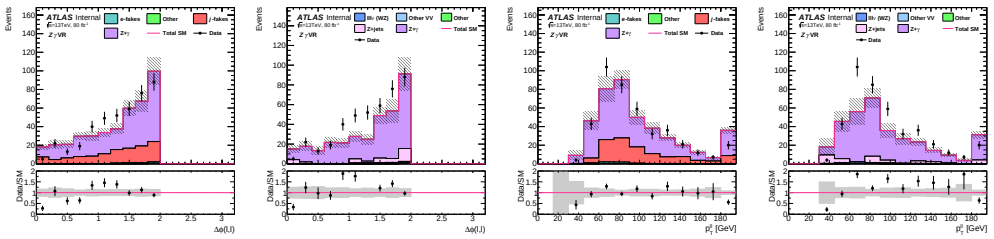

(e) $\Delta\phi(\ell,\ell)$, data-driven (f) MC only (g) $p_{\mathrm{T}}^{\ell\ell}$, data-driven (h) MC only

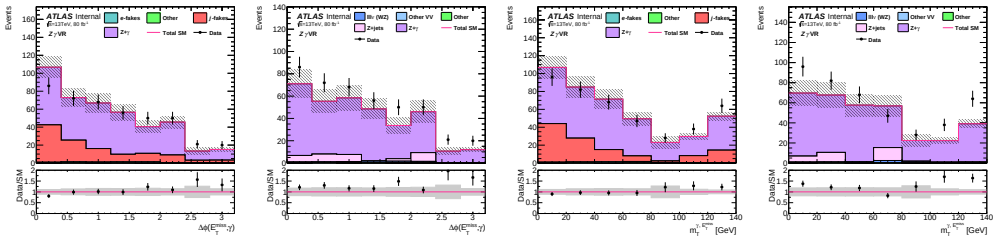

(i) $\Delta\phi(E_{\mathrm{T}}^{\mathrm{miss}},\gamma)$, data-driven (j) MC only (k) $m_T^{\gamma,E_{\mathrm{T}}^{\mathrm{miss}}}$, data-driven (l) MC only

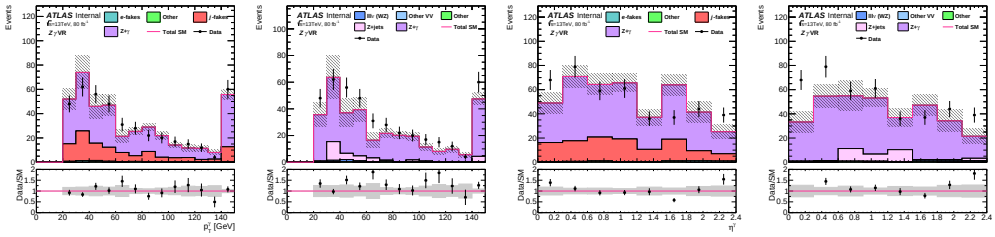

(m) $p_{\mathrm{T}}^{\gamma_1}$, data-driven (n) MC only (o) η^{γ_1}, data-driven (p) MC only

Figure 7.35: Distributions of (a) $\Delta\phi_{\ell\ell,\gamma E_{\mathrm{T}}^{\mathrm{miss}}}$, (c) $\mathrm{Bal}_{p_{\mathrm{T}}}$, (e) $\Delta\phi(\ell,\ell)$, (g) $p_{\mathrm{T}}^{\ell\ell}$, (i) $\Delta\phi(E_{\mathrm{T}}^{\mathrm{miss}},\gamma)$, (k) $m_T^{\gamma,E_{\mathrm{T}}^{\mathrm{miss}}}$, (m) $p_{\mathrm{T}}^{\gamma_1}$, and (o) η^{γ_1} in the $Z\gamma$ validation region with data-driven backgrounds for the electron and jet fakes. Subfigures (b, d, ..., p) contain the same distributions as to the right but with the Monte Carlo only predictions. In the data-driven approach all objects mis-identified as photons are labeled as e-fakes (electron) or j-fakes (jet) and their calculations are outlined in the previous sections. The $Z\gamma$ background component is predicted using only simulation, shown in purple, and is the same for both plots.

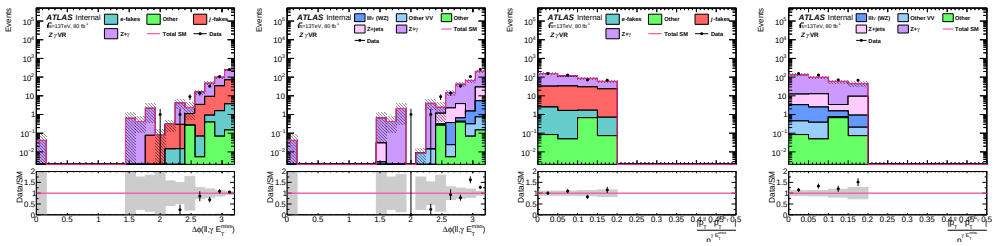

(a) $\Delta\phi_{\ell\ell,\gamma E_{\mathrm{T}}^{\mathrm{miss}}}$, data-driven (b) MC only (c) $\mathrm{Bal}_{p_{\mathrm{T}}}$, data-driven (d) MC only

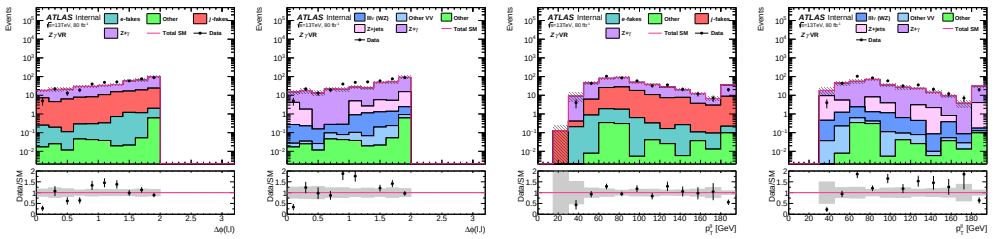

(e) $\Delta\phi(\ell,\ell)$, data-driven (f) MC only (g) $p_{\mathrm{T}}^{\ell\ell}$, data-driven (h) MC only

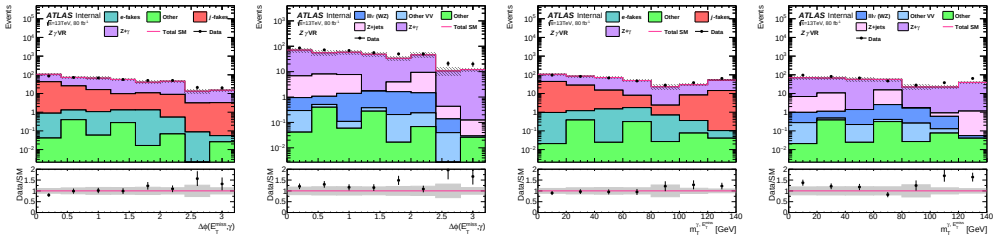

(i) $\Delta\phi(E_{\mathrm{T}}^{\mathrm{miss}},\gamma)$, data-driven (j) MC only (k) $m_T^{\gamma,E_{\mathrm{T}}^{\mathrm{miss}}}$, data-driven (l) MC only

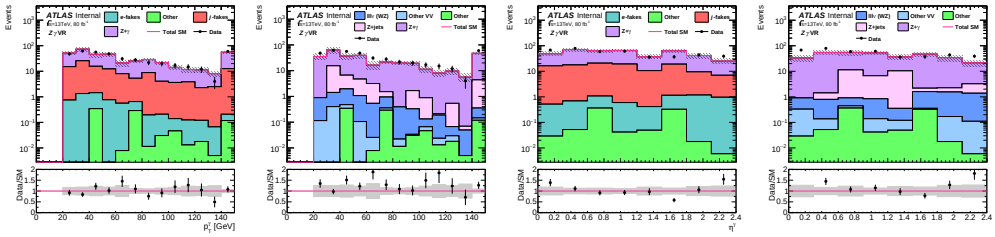

(m) $p_{\mathrm{T}}^{\gamma_1}$, data-driven (n) MC only (o) η^{γ_1}, data-driven (p) MC only

Figure 7.36: Distributions of (a) $\Delta\phi_{\ell\ell,\gamma E_{\mathrm{T}}^{\mathrm{miss}}}$, (c) $\mathrm{Bal}_{p_{\mathrm{T}}}$, (e) $\Delta\phi(\ell,\ell)$, (g) $p_{\mathrm{T}}^{\ell\ell}$, (i) $\Delta\phi(E_{\mathrm{T}}^{\mathrm{miss}},\gamma)$, (k) $m_T^{\gamma,E_{\mathrm{T}}^{\mathrm{miss}}}$, (m) $p_{\mathrm{T}}^{\gamma_1}$, and (o) η^{γ_1} in the $Z\gamma$ validation region with data-driven backgrounds for the electron and jet fakes in the log scale. Subfigures (b, d, ..., p) contain the same distributions as to the right but with the Monte Carlo only predictions. In the data-driven approach all objects mis-identified as photons are labeled as e-fakes (electron) or j-fakes (jet) and their calculations are outlined in the previous sections. The $Z\gamma$ background component is predicted using only simulation, shown in purple, and is the same for both plots.

7.5 Systematic Uncertainties

7.5.1 Simulation and Experimental uncertainties

The signal and background predictions are affected by uncertainties from experimental sources, such as those on data-driven background estimation techniques, and uncertainties from the theoretical modeling of the simulated samples. This section describes the sources of the uncertainties and their effects on the background estimation, while the next section(Section 7.5) about the fitting procedure will detail the largest sources of these uncertainties in the final result.

Luminosity

The uncertainty on the combined 2015–2017 integrated luminosity is 2.0%. It is derived from a preliminary calibration of the luminosity scale using x-y beam-separation scans, employing a method similar to that detailed in Ref. [266].

Photon Uncertainties

The photon uncertainties are summarized below, and for more information please refer to Refs. [128, 267, 268].

- `EG_SCALE_ALL_{UP,DOWN}`: Photon momentum scale uncertainty of $\pm 1\sigma$ variations in the scale of the measured photon momentum.
- `EG_RESOLUTION_ALL_{UP,DOWN}`: Photon momentum resolution uncertainty of $\pm 1\sigma$ variations in the resolution of the measured photon momentum.
- `PH_EFF_ID_Uncertainty_{UP,DOWN}`: Photon identification efficiency uncertainty of $\pm 1\sigma$ variations in the error on the photon identification scale factors.
- `PH_EFF_ISO_Uncertainty_{UP,DOWN}`: Photon isolation efficiency uncertainty of $\pm 1\sigma$ variations in the error on the photon isolation scale factors.

Lepton Uncertainties

Electron

The electron uncertainties are summarized below, and for more information please refer to Refs. [128, 267, 268].

- `EG_SCALE_ALL_{UP,DOWN}`: Electron momentum scale uncertainty of $\pm 1\sigma$ variations in the scale of the measured electron momentum.
- `EG_RESOLUTION_ALL_{UP,DOWN}`: Electron momentum resolution uncertainty of $\pm 1\sigma$ variations in the resolution of the measured electron momentum.
- `EL_EFF_ID_{UP,DOWN}`: Electron identification efficiency uncertainty of $\pm 1\sigma$ variations in the error on the electron identification scale factors.
- `EL_EFF_RECO_{UP,DOWN}`: Electron reconstruction efficiency uncertainty of $\pm 1\sigma$ variations in the error on the electron reconstruction scale factors.
- `EL_EFF_ISO_{UP,DOWN}`: Electron isolation efficiency uncertainty of $\pm 1\sigma$ variations in the error on the electron isolation scale factors.
- `EL_EFF_TRIGGER_{UP,DOWN}`: Electron trigger efficiency uncertainty of $\pm 1\sigma$ variations in the error on the electron trigger scale factors.
- `EL_EFF_TRIGGEREFF_{UP,DOWN}`: Electron trigger combined statistical and systematic uncertainty of $\pm 1\sigma$ variations in the error on the electron trigger scale factors.

Muon

The muon uncertainties are summarized below, and for more information please refer to Refs. [133, 269].

- `MUON_ID_{UP,DOWN}`: Muon momentum resolution uncertainty of $\pm 1\sigma$ variations in the smearing of the Inner Detector track.
- `MUON_MS_{UP,DOWN}`: Muon momentum resolution uncertainty of $\pm 1\sigma$ variations in the smearing of the Muon Spectrometer track.
- `MUON_SCALE_{UP,DOWN}`: Muon momentum scale uncertainty of $\pm 1\sigma$ variations in the scale of the measured muon momentum.
- `MUON_EFF_RECO_{STAT,STAT_LOWPT,SYS,SYS_LOWPT}_{UP,DOWN}`: Muon reconstruction efficiency uncertainty of $\pm 1\sigma$ variations of the statistical (systematic) error on the reconstruction scale factors.
- `MUON_EFF_ISO_{SYS,STAT}_{UP,DOWN}`: Muon isolation efficiency uncertainty of $\pm 1\sigma$ variations in the statistical (systematic) error on the muon isolation scale factors.

- `MUON_EFF_TTVA_{STAT,SYS}_{UP,DOWN}`: Muon track-to-vertex-association uncertainty of $\pm 1\sigma$ variations in the statistical (systematic) error on the muon TTVA scale factors.
- `MUON_EFF_TRIG{STAT,SYS}UNCERTAINTY_{UP,DOWN}`: Muon trigger statistical (systematic) uncertainty of $\pm 1\sigma$ variations in the error on the muon trigger scale factors.

Jet Uncertainties

The jet uncertainties are summarized below, and for more information please refer to Refs. [137, 270, 271].

- `JET_JER_SINGLE_NP_{UP,DOWN}`:Jet momentum resolution uncertainty of $\pm 1\sigma$ variations in the resolution of the measured jet momentum.
- `JET_JES_GROUPEDNP_{1,2,3}_{UP,DOWN}`: Jet momentum scale uncertainty of $\pm 1\sigma$ variations in the scale of the measured jet momentum.
- `JET_ETAINTERCALIBRATION_NONCLOSURE_{UP,DOWN}`: Jet momentum scale uncertainty of $\pm 1\sigma$ variations in the scale of the measured jet momentum.
- `JET_(f)JVTEff_{UP,DOWN}`: (Forward) Jet Vertex Fraction uncertainty of $\pm 1\sigma$ variations which account for the residual contamination from pileup jets after pileup suppression and the MC generator choice.

Missing Transverse Momentum

The missing transverse momentum uncertainties are summarized below, and for more information please refer to Refs. [272, 273].

- `MET_SOFTTRK_RESO{PARA,PERP}_{UP,DOWN}`: $E_{\mathrm{T}}^{\mathrm{miss}}$ soft-term resolution uncertainty of $\pm 1\sigma$ variations in the $E_{\mathrm{T}}^{\mathrm{miss}}$ resolution derived from comparisons of 2015 data to MC, with generator (Powheg+Pythia8 vs. MadGraph5_aMC@NLO) and simulation (Fullsim vs. AFII) comparisons.
- `MET_SOFTTRK_SCALE{UP,DOWN}`: $E_{\mathrm{T}}^{\mathrm{miss}}$ soft-term scale uncertainty of $\pm 1\sigma$ variations in the $E_{\mathrm{T}}^{\mathrm{miss}}$ scale derived from comparisons of 2015 data to MC, with generator (Powheg+Pythia8 vs. MadGraph5_aMC@NLO) and simulation (Fullsim vs. AFII) comparisons.

Pileup

The nominal pileup reweighting factor is defined to match average interactions per crossing of Monte Carlo to that of the data. This factor is scaled by 1/1.03 in order to take into account the matching of the number of vertices. The uncertainty on the reweighting is evaluated by changing the scale factor to 1.0/0.94 (up variation) to 1/1.12 (down variation).

7.5.2 Data-driven Uncertainties

The largest uncertainties are from the data-driven background estimations and control region sample sizes. Each component of data-driven uncertainties examined are outlined in the following text.

Electron-to-photon fake uncertainties

For the $e \to \gamma$ background, uncertainties are assigned to account for differences in the event topology and kinematic distributions between the domain in which the fake rate was measured and the signal region. These include the dependence of the fake rate as a function of $E_{\mathrm{T}}^{\mathrm{miss}}$, $\langle\mu\rangle$ and the size of the Z mass window used. The electron fake background yield in the signal region was calculated with systematically varied mis-identification rates, and the maximal deviations were chosen to bracket the nominal estimate as a total symmetric systematic uncertainty.

The mis-identification rate was calculated in four $\langle\mu\rangle$ bins to control for the amount of pileup in the event. A maximal deviation of 2.4% was assessed as the uncertainty. Next the window for the Z mass was altered, changing the ratio of the background to signal in the fake rate calculation. Tightening or widening the window caused a 2.6% difference in the signal region prediction. In order to account for $E_{\mathrm{T}}^{\mathrm{miss}}$ in the event, the fake rate was measured in bins of missing transverse momentum. A maximum change of 7.7% was observed and taken as the variation. Finally an Monte Carlo closure test was assessed, repeating the fake rate derivation and extrapolation procedure in the Monte Carlo. The 5.4% difference in yield was assessed as a symmetric uncertainty. Table 7.9 details the systematic variations considered and the percentage change of the signal region yield due to each change.

Jet-to-photon fake uncertainties

The systematic uncertainties of the j $\to \gamma$ background come from the number of events in the region used to measure the fake rates, the correlation in control regions used for the fake factor measurement, and the pseudo-photon scaling factor. The systematic error is assessed in the same

Nominal	1.5 ± 0.3 events						
$0 < \langle\mu\rangle < 20$	2.4%	7.5 GeV Window	1.4%	$0 < E_{\mathrm{T}}^{\mathrm{miss}} < 20$ GeV	−2.1%	MC Closure	6.5%
$20 < \langle\mu\rangle < 30$	−1.0%	2.5 GeV Window	−2.6%	$20 < E_{\mathrm{T}}^{\mathrm{miss}} < 40$ GeV	1.2%		
$30 < \langle\mu\rangle < 40$	−1.8%			$40 < E_{\mathrm{T}}^{\mathrm{miss}} < \mathrm{inf}$ GeV	7.7%		
$40 < \langle\mu\rangle$	1.8%						

Table 7.9: Electron mis-identification rate systematics variations and the percentage change of the signal region yield due to each variation.

way as the electron-to-photon fakes, where the maximum deviation of the variation is taken as a symmetric uncertainty.

The isolation gap between the tight and non-tight calorimeter isolation variable used to defined the regions was varied by 1 GeV and a 0.7% uncertainty was assessed to cover the difference in yield. Next, the R' factor utilized to control the correlation in regions was disabled, calculating the fake rate with no assumptions about the correlation between ABCD regions. This resulted in a 9.5% change of the jet background in the signal region. Finally the change in yield of all defined analysis regions using scaled pseudo photons was compared with using only isolated pseudo photons. A maximal difference of 9.1% was observed in $Z\gamma$ control region and taken as the uncertainty. Table 7.10 shows a summary of these uncertainties.

Nominal	0.6 ± 0.3 events				
Iso Gap variation (up)	0.7%	R' correlation	9.5%	pseudo-γ extr. CRz	9.1%
Iso Gap variation (dn)	−0.5%			pseudo-γ extr. VRz	3.7%
				pseudo-γ extr. VRj	−5.4%

Table 7.10: Jet mis-identification fake factor systematics variations and the percentage change of the signal region yield due to each variation.

7.5.3 Theory Uncertainties

Theoretical uncertainties on the cross section of different processes are taken into account. The ZH production cross section uncertainty of 4% [32] is assessed on the signal Monte Carlo. For the background process, Standard Model $Z\gamma$ cross section has a theory uncertainty of 8% [274] and the $t\bar{t}\gamma$ calculation has a 21% error [275].

7.6 Statistical Framework

The details of the interplay between control, validation, and signal regions as well as the overall analysis structure can be seen in Ref. [276]. This section will briefly touch on some of these concepts and explore how results are extracted and uncertainties are assessed.

After the predictions of the control and signal regions compositions, the Standard Model hypothesis can be tested by unblinding the signal region. A likelihood function is defined for the signal region as the product of Poisson probability distributions for the signal region and control region and Gaussian constraint nuisance parameters for the systematic uncertainties. This can be written as:

$$\mathcal{L}(\boldsymbol{n}, \boldsymbol{\theta'}|\mu_{\text{sig}}, \mathcal{B}, \boldsymbol{\theta}) = \text{P}_{\text{SR}} \times \text{P}_{\text{CR}}^{Z\gamma} \times \prod_k G_k\left(\boldsymbol{\theta'} - \boldsymbol{\theta}\right) \ ; \tag{7.10}$$

where the $\text{P}_{\text{SR}} = \text{P}_{\text{SR}}\left(\text{n}_{\text{SR}}|\lambda_{\text{SR}}\left(\mu_{\text{sig}}, \mathcal{B}, \boldsymbol{\theta}\right)\right)$ and $\text{P}_{\text{CR}}^{Z\gamma} = \text{P}_{\text{CR}}^{Z\gamma}\left(\text{n}_{\text{CR}}|\lambda_{\text{CR}}\left(\mu_{\text{sig}}, \mu_{\text{CR}}^{Z\gamma}, \mathcal{B}, \boldsymbol{\theta}\right)\right)$[18]are the Poisson probabilities of the observed events (n), with expected number of events (λ). The expected number of events depends on the background predictions, $\mathcal{B}$, background and signal normalization factors, μ, and nuisance parameters, $\boldsymbol{\theta}$. The signal normalization factor, also referred to as the signal strength, will be the parameter of interest used in the hypothesis testing. Signal strength $\mu_{\text{sig}} = 0$ corresponds to the SM hypothesis while $\mu_{\text{sig}} = 1$ corresponds to the signal expected from the SUSY simplified model.

The systematic uncertainties are implemented as $\prod_k G_k\left(\boldsymbol{\theta'} - \boldsymbol{\theta}\right)$, which are Gaussian terms that constrain the NPs of the uncertainties. The term is parameterized as a Gaussian distribution with mean $\boldsymbol{\theta'}$ and allowed to vary to value $\boldsymbol{\theta}$ in the likelihood maximization. The constraint terms are treated as uncorrelated and allowed to float with reductions to the likelihood for non-zero values. The values that maximize the likelihood will be labeled as $\hat{\boldsymbol{\theta}}$, $\hat{\mu_{\text{sig}}}$, $\hat{\mu}_{\text{CR}}^{\hat{Z}\gamma}$.

Profile Likelihood and CL_s Method

In order to determine the level of exclusion for μ_{sig}, the profile likelihood ratio test statistic is constructed. The statistic is defined for a fixed value of μ_{sig} as:

$$q_{\tilde{\mu_{\text{sig}}}} = -2\ln\frac{\mathcal{L}(\tilde{\mu_{\text{sig}}}, \tilde{\boldsymbol{\theta}})}{\mathcal{L}(\hat{\mu_{\text{sig}}}, \hat{\boldsymbol{\theta}})} \ ; \tag{7.11}$$

where the values with the $\hat{}$ maximize the likelihood function, while the $\tilde{}$ parameters maximize the likelihood for the specific value of $\tilde{\mu_{\text{sig}}}$. The distribution of this statistic is given by $f(q|\tilde{\mu_{\text{sig}}}, \tilde{\boldsymbol{\theta}})$

[18]In analyses with multiple signal and control regions, these terms turn into products of the Poisson distributions in for each region.

and is obtained by building many pseudo experiments based on the observed events. By generating many pseudo experiments, the distribution approaches the asymptotic regime where it resembles a χ^2 distribution with one degree of freedom. The p-value of the signal+background hypothesis is defined as:

$$p_{\tilde{\mu_{\rm sig}}} = \int_{q_{\rm obs}}^{\infty} f(q_{\tilde{\mu_{\rm sig}}}|\tilde{\mu_{\rm sig}}, \boldsymbol{\theta}) dq_{\tilde{\mu_{\rm sig}}} \ . \tag{7.12}$$

If p-value is lower than some predetermined threshold, corresponding to a specific Confidence Level (CL), the signal+background hypothesis is said to be excluded. The p-value for the Standard Model background-only hypothesis is then written as:

$$p_{\rm SM} = \int_{0}^{q_{\rm obs}} f(q_{\tilde{\mu_{\rm sig}}}|\tilde{\mu_{\rm sig}} = 0, \boldsymbol{\theta}) dq_{\tilde{\mu_{\rm sig}}} \ . \tag{7.13}$$

If the p-value for the null hypothesis is lower than the threshold, the Standard Model background-only hypothesis is then excluded. This p-value can be equivalently described as the statistical significance Z. This is the number of standard deviations of a Gaussian corresponding to integrating the Gaussian high tail and obtaining the same probability as the p-value. The p-value is converted to this Z by:

$$Z = \Phi^{-1}(1 - p) \ ; \tag{7.14}$$

where Φ is the cumulative function of the Gaussian. In particle physics the convention for evidence of new particles corresponds to $Z > 3$, $p_{\rm SM} < 0.0013$ and the discovery is declared with $Z > 5$, $p_{\rm SM} < .000000287$.

In the scenario where there is a non-significant excess of the observed events compared to the background-only prediction, the $\rm CL_s$ method [277,278] is utilized to calculate intervals. This method is a modified version of the confidence levels described above, and particularly useful for BSM searches where the number of signal events is small. The expected distributions for the background only hypothesis and

$$\rm CL_s = \frac{CL_{s+b}}{CL_b} = \frac{p_{\tilde{\mu_{\rm sig}}}}{1 - p_{\rm SM}} \ . \tag{7.15}$$

Effectively, the $\rm CL_s$ technique tries to fix the problem of excluding models to which one is not sensitive to by penalizing the p-value. The $\rm CL_s$ approaches the regular confidence interval p-value in the limit of negligible background (when $p_{\rm SM}$ is small). For the following results, the $\rm CL_s$ method is employed and the signal+background hypothesis is excluded at 95% CL if $\rm CL_s \ < 0.05$.

HistFitter

Once the profile likelihood is constructed, there are several different types of fits implemented and performed with the HistFitter package [276]. A **Background-Only** fit is used to determine background yields in the validation and signal regions. This fit only utilizes the constraints from the control regions and assumes no BSM contributions($\mu_{\text{sig}} = 0$). Statistical and systematic uncertainties are included in the fit as prescribed by the previous subsection. A **Model-Independent** fit is used to evaluate the agreement between the predicted and observed event yield in the signal region. Similarly to the background-only, this fit assumes no BSM contribution to the control region ($\mu_{\text{sig}} = 0$ in the control region), though the number of observed events in the signal region is included in the fit. The BSM physics signal is constrained to be non-negative and allowed to freely float in the fit. The observed and expected number of events in the signal region are used to set 95% CL upper limits on the visible BSM cross section and a p-value of the background-only hypothesis is calculated. The third and final fit type is the **Model-Dependent** fit. This is used to set exclusion limits on $(\sigma/\sigma_{SM}) \times \text{BF}(h \to \tilde{\chi}_1^0\tilde{\chi}_1^0 \to \gamma\tilde{G}\gamma\tilde{G})$. In this fit signal contamination in the control region and experimental/theoretical uncertainties on the signal production are taken into account. The confidence interval given by $\mu_{\text{sig}} = 1$ is calculated. Next, a scan over μ_{sig} is performed, in essence varying the $(\sigma/\sigma_{SM}) \times \text{BF}(h \to \tilde{\chi}_1^0\tilde{\chi}_1^0 \to \gamma\tilde{G}\gamma\tilde{G})$ until the desired CL_s threshold of 0.05 is reached. This corresponds to the value of μ_{sig} at which the process can be excluded at the 95% confidence level.

7.7 Results

In the following section, results for the different fits discussed in the previous section are shown. In the first subsection, the background-only fits in the control and validation regions are explored. Once again, these are then used to predict the yields and the size of the systematic uncertainties in the signal region. Finally the signal region is unblinded and the results are explored.

Control and Validation Regions

The background-only fit in this analysis is simple as there is only one $Z\gamma$ control region. The normalization of the $Z\gamma$ Monte Carlo is scaled in order for the simulation to match the data. In the data, 1,203 events were used to constrain this normalization factor to be 1.04 ± 0.13. Note, in this region all other backgrounds are fixed and only the $Z\gamma$ normalization is allowed to float. A table of the control region yields before and after the fit can be seen in Table 7.11.

Table 7.11: The results of the background-only fit in the $Z\gamma$ control region. The errors shown are the statistical plus systematic uncertainties. Note, in this region all other background are fixed and only the $Z\gamma$ normalization is allowed to float.

Yields	**Control Region $Z\gamma$**
Observed events	1203
Fitted bkg events	1203 ± 35
Fitted MC V$\gamma\gamma$	0.60 ± 0.06
Fitted MC $t\bar{t}\gamma$	0.00 ± 0.00
Fitted Data-Driven $e \to \gamma$	4.1 ± 0.5
Fitted Data-Driven j $\to \gamma$	196 ± 47
Fitted MC $Z\gamma$	1003 ± 59
MC exp. SM events	1164.9
Before Fit MC exp. V$\gamma\gamma$	0.60
Before Fit MC exp. $t\bar{t}\gamma$	0.00
Before Fit Data-Driven $e \to \gamma$	4.11
Before Fit Data-Driven j $\to \gamma$	195.4
Before Fit MC exp. $Z\gamma$	964.9

Figure 7.37 shows the $E_{\mathrm{T}}^{\mathrm{miss}}$, $\Delta\phi_{\ell\ell,\gamma E_{\mathrm{T}}^{\mathrm{miss}}}$, $\mathrm{Bal}_{p_{\mathrm{T}}}$, and $\Delta\phi(\ell,\ell)$ spectra in the control region after the normalization factor has been applied. By construction the normalized total yield of the control region SM predictions match exactly the measured data. This fitting procedure does not include any shape corrections, but overall there is excellent agreement in the shape predictions.

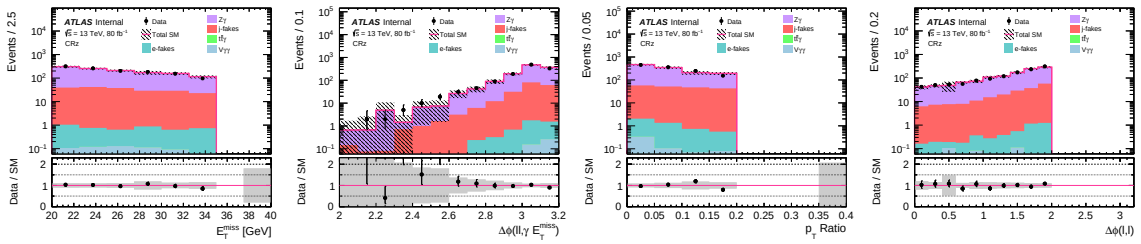

(a) $E_{\mathrm{T}}^{\mathrm{miss}}$ (b) $\Delta\phi_{\ell\ell,\gamma E_{\mathrm{T}}^{\mathrm{miss}}}$ (c) $\mathrm{Bal}_{p_{\mathrm{T}}}$ (d) $\Delta\phi(\ell,\ell)$

Figure 7.37: Distributions of (a) $E_{\mathrm{T}}^{\mathrm{miss}}$, (b) $\Delta\phi_{\ell\ell,\gamma E_{\mathrm{T}}^{\mathrm{miss}}}$, (c) $\mathrm{Bal}_{p_{\mathrm{T}}}$, and (d) $\Delta\phi(\ell,\ell)$, after the background-only fit in the $Z\gamma$ control region. The errors bars shown include both the statistical and systematic components.

Next, the normalization factor of the $Z\gamma$ background and the modeling of the $Z+$jets background is validated. Table 7.12 shows the prefit and postfit yields in the $Z\gamma$ and $Z+$jets validation regions.

These regions are not constrained in the fitting procedure. The background estimate includes the $Z\gamma$ with the normalization factor applied, and the systematic uncertainties propagated. For the $Z\gamma$ validation region, there are 422 ± 46 events predicted, compared with 423 observed. In the $Z+$jets validation region, 479 events are observed in the data, while 466 ± 65 are predicted. Both of these regions show excellent overall agreement in event yields. Figures 7.38 and 7.39 show the kinematic distributions of $E_{\mathrm{T}}^{\mathrm{miss}}$, $\Delta\phi_{\ell\ell,\gamma E_{\mathrm{T}}^{\mathrm{miss}}}$, $\mathrm{Bal}_{p_{\mathrm{T}}}$, and $\Delta\phi(\ell,\ell)$. The agreement is very good, but some bins have large Monte Carlo statistical errors.

Table 7.12: The results of the background-only fit in the $Z\gamma$ control region, shown in the validation regions for $Z\gamma$ and $Z+$jets. The errors shown are the statistical plus systematic uncertainties.

Yields	**Validation Region $Z\gamma$**	**Validation Region $Z+$jets**
Observed events	423	479
Fitted bkg events	422 ± 46	466 ± 65
Fitted MC V$\gamma\gamma$	0.32 ± 0.04	0.09 ± 0.03
Fitted MC $t\bar{t}\gamma$	0.60 ± 0.2	1.9 ± 0.6
Fitted Data-Driven $e \to \gamma$	5.7 ± 0.7	1.7 ± 0.2
Fitted Data-Driven j $\to \gamma$	114 ± 25	264 ± 40
Fitted MC $Z\gamma$	301 ± 44	198 ± 54
MC exp. SM events	409.79	458.82
Before Fit MC exp. V$\gamma\gamma$	0.32	0.09
Before Fit MC exp. $t\bar{t}\gamma$	0.61	1.86
Before Fit Data-Driven $e \to \gamma$	5.68	1.69
Before Fit Data-Driven j $\to \gamma$	113.90	263.81
Before Fit MC exp. $Z\gamma$	289.28	191.38

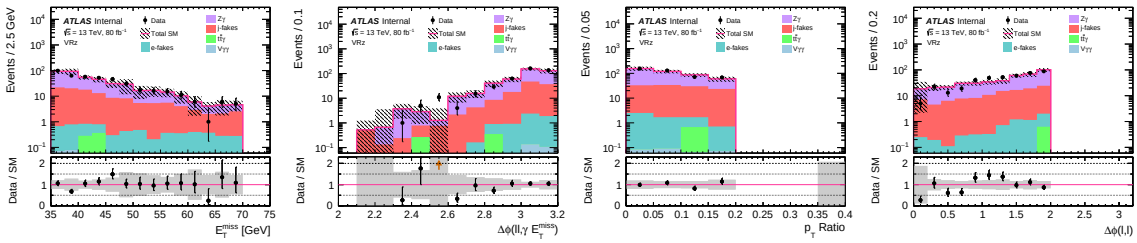

(a) $E_{\mathrm{T}}^{\mathrm{miss}}$ (b) $\Delta\phi_{\ell\ell,\gamma E_{\mathrm{T}}^{\mathrm{miss}}}$ (c) $\mathrm{Bal}_{p_{\mathrm{T}}}$ (d) $\Delta\phi(\ell,\ell)$

Figure 7.38: Distributions of (a) $E_{\mathrm{T}}^{\mathrm{miss}}$, (b) $\Delta\phi_{\ell\ell,\gamma E_{\mathrm{T}}^{\mathrm{miss}}}$, (c) $\mathrm{Bal}_{p_{\mathrm{T}}}$, and (d) $\Delta\phi(\ell,\ell)$, after the background-only fit in the $Z\gamma$ control region in the $Z\gamma$ validation region. The errors bars shown include both the statistical and systematic components.

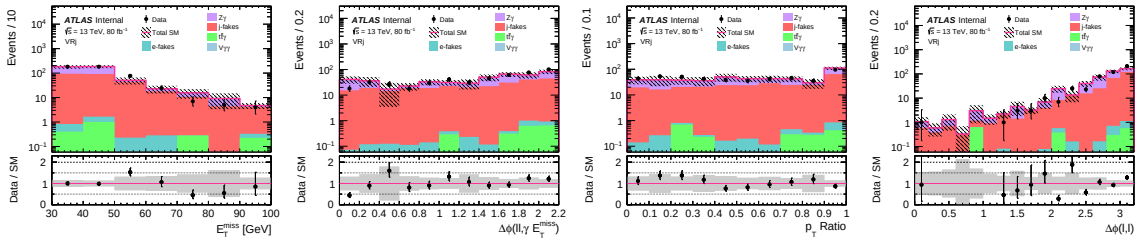

(a) $E_{\mathrm{T}}^{\mathrm{miss}}$ (b) $\Delta\phi_{\ell\ell,\gamma E_{\mathrm{T}}^{\mathrm{miss}}}$ (c) $\mathrm{Bal}_{p_{\mathrm{T}}}$ (d) $\Delta\phi(\ell,\ell)$

Figure 7.39: Distributions of (a) $E_{\mathrm{T}}^{\mathrm{miss}}$, (b) $\Delta\phi_{\ell\ell,\gamma E_{\mathrm{T}}^{\mathrm{miss}}}$, (c) $\mathrm{Bal}_{p_{\mathrm{T}}}$, and (d) $\Delta\phi(\ell,\ell)$, after the background-only fit in the $Z\gamma$ control region in the $Z+$jets validation region. The errors bars shown include both the statistical and systematic components.

Unblinded Signal Region

After unblinding the signal region, three events are observed compared with the expected 2.1 background events. The probability of the three observed events to be consistent with the expected background of 2.1 ± 0.5 is $p_0 = 0.32$ ($< 1\ \sigma$). These results are summarized in Table 7.13, as well as illustrated in Figure 7.40, with the expected number of background events broken down into its various components. The table shows the final breakdown of the predicted background, uncertainties, and the expected events from a BSM signal model. Figure 7.40 displays the full $E_{\mathrm{T}}^{\mathrm{miss}}$ distribution where all signal region selection criteria are applied, except for the missing transverse momentum requirement. The $E_{\mathrm{T}}^{\mathrm{miss}}$ cut requirement is denoted by the orange arrow, forming the signal region. No significant excess above the Standard Model expectation is observed.

Table 7.13: Table of the expected and observed number of events in the signal region. For comparison, the yield from a signal with Higgs branching fraction of 10% and $m_{\tilde{\chi}_1^0}, m_{\tilde{G}} = 80, 0\,\mathrm{GeV}$ is shown.

Observed events	3
Expected background events	2.1 ± 0.5
Expected signal events $m_{NLSP}, m_{LSP} = 80, 0$ GeV	8.1
$e \to \gamma$ fakes	1.5 ± 0.3
j $\to \gamma$ fakes	0.6 ± 0.3
SM $Z\gamma$	$0.03^{+0.15}_{-0.03}$
Other	$0.00^{+0.01}_{-0.00}$

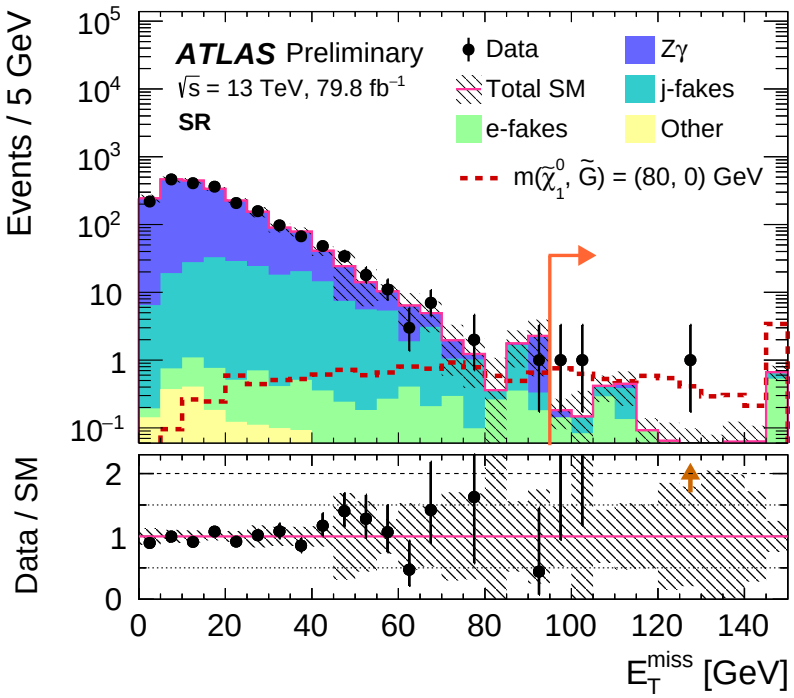

Figure 7.40: Distribution of $E_{\mathrm{T}}^{\mathrm{miss}}$ in the signal region. The orange arrow indicates the signal region. The contribution from $Z\gamma$ and other ($t\bar{t}\gamma$, $V\gamma\gamma$) sources is expected to be 0.03 events in the signal region. The red dashed line overlays the predictions from a signal with Higgs branching fraction of 10% and $m_{\tilde{\chi}_1^0}, m_{\tilde{G}} = 80, 0\,\mathrm{GeV}$. The uncertainty bands plotted include all statistical and systematic uncertainties.

The observed and expected number of events in the signal region is used to set upper limits on model-independent properties of BSM processes and the model-dependent branching fraction of the $h \to \tilde{\chi}_1^0\tilde{\chi}_1^0 \to \gamma\tilde{G}\gamma\tilde{G}$ and $h \to \tilde{\chi}_1^0\tilde{G} \to \gamma\tilde{G}\tilde{G}$ processes assuming a SM ZH production. As described previously, following the $\mathrm{CL_s}$ method, a one-side profile likelihood ratio test statistic is utilized to set upper limits at the 95% Confidence Level (CL). The test statistics' estimator is derived with pseudo-experiments. The model-independent limit provides an upper limit, independent of a specific signal model, on the number of events beyond the SM expectation in the signal region. Table 7.14 shows the limits from the model-independent fit in the signal region. The upper limit on the visible cross section $\langle\epsilon\sigma\rangle_{\mathrm{obs}}^{95}$ is obtained by dividing the number of signal events S_{obs}^{95} by the integrated luminosity of $79.8\,\mathrm{fb}^{-1}$. The expected number of signal events S_{exp}^{95} and p-value, quantifying the probability for the background hypothesis to fluctuate at or above the observed number of events, are also given.

With the model-dependent fit, the 95% CL upper limits on the $h \to \tilde{\chi}_1^0\tilde{\chi}_1^0 \to \gamma\tilde{G}\gamma\tilde{G}$ ($h \to$

$\tilde{\chi}_1^0\tilde{G} \to \gamma\tilde{G}\tilde{G}$) branching fractions as a function of m_{NLSP}, m_{LSP} are calculated and can be seen in Figure 7.41 (7.42) and Table 7.15 (7.16). For the $h \to \tilde{\chi}_1^0\tilde{\chi}_1^0 \to \gamma\tilde{G}\gamma\tilde{G}$ signature, BF($h \to \tilde{\chi}_1^0\tilde{G} \to \gamma\tilde{G}\tilde{G}$) is assumed to be zero and vice versa. The observed upper limits of the branching fraction of Higgs boson decays to one or two photons plus $E_{\mathrm{T}}^{\mathrm{miss}}$ range from 5-18% depending on NLSP and LSP masses.

Table 7.14: Table of the model-independent 95% CL upper limits on the visible cross section $\langle\epsilon\sigma\rangle_{\mathrm{obs}}^{95}$ and on the number of signal events S_{obs}^{95}. The third column (S_{exp}^{95}) shows the 95% CL upper limit on the number of signal events, given the expected number (and $\pm 1\sigma$ excursions on the expectation) of background events. The last column indicates the background-only hypothesis p-value $p(\mu_{\mathrm{sig}} = 0)$.

$\langle\epsilon\sigma\rangle_{\mathrm{obs}}^{95}$[fb]	S_{obs}^{95}	S_{exp}^{95}	$p(s=0)$
0.06	5.1	$4.5^{+1.9}_{-1.0}$	0.32

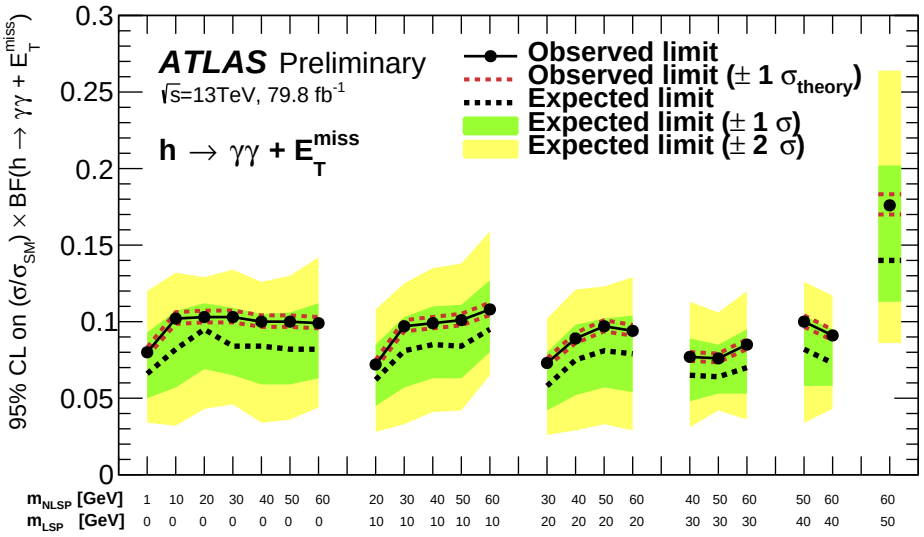

Figure 7.41: 95% CL observed and expected limits of $(\sigma/\sigma_{SM}) \times$ BF($h \to \gamma\gamma + E_{\mathrm{T}}^{\mathrm{miss}}$) for various NLSP and LSP masses. The inner and outer bands show the $\pm 1\sigma$ and $\pm 2\sigma$ excursions of the expected limits respectively. These limits are for the case $0 < m_{\mathrm{NLSP}} < m_h/2$ and the Higgs boson is assumed to decay to a $\gamma\gamma + E_{\mathrm{T}}^{\mathrm{miss}}$ final state.

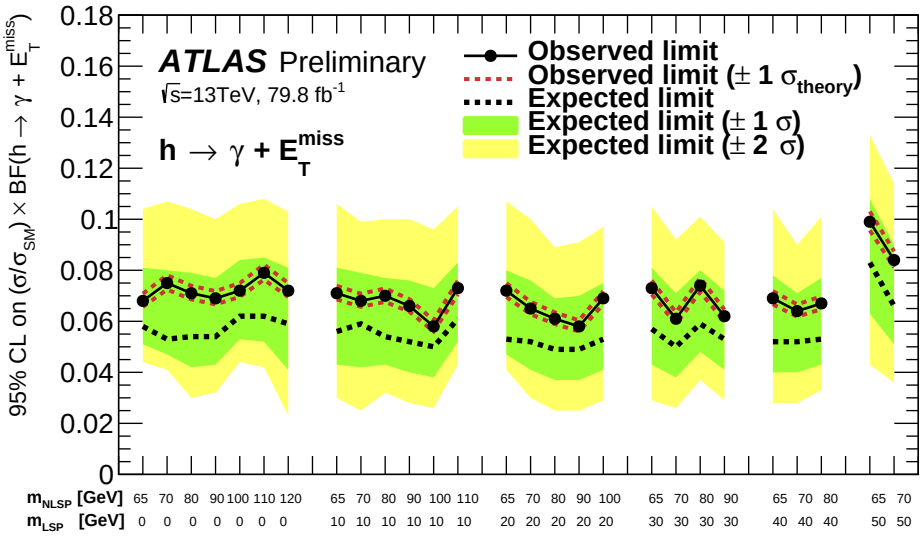

Figure 7.42: 95% CL observed and expected limits of $(\sigma/\sigma_{SM}) \times \mathrm{BF}(h \to \gamma + E_{\mathrm{T}}^{\mathrm{miss}})$ for various NLSP and LSP masses. The inner and outer bands show the $\pm 1\sigma$ and $\pm 2\sigma$ excursions of the expected limits respectively. These limits are for the case $m_h/2 < m_{\mathrm{NLSP}} < m_h$ and the Higgs boson is assumed to decay to a $\gamma + E_{\mathrm{T}}^{\mathrm{miss}}$ final state.

Table 7.15: 95% CL upper limits on the BF($h \to \gamma\gamma + E_{\mathrm{T}}^{\mathrm{miss}}$) assuming a SM Higgs boson production cross section. The second column (BF($h \to \gamma\gamma + E_{\mathrm{T}}^{\mathrm{miss}})_{\mathrm{exp}}^{95}$) shows the 95% CL upper limit on the BF($h \to \gamma\gamma + E_{\mathrm{T}}^{\mathrm{miss}}$) given the expected number (and $\pm 1\sigma$ excursions on the expectation) of background events. These limits are for the case $0 < m_{\mathrm{NLSP}} < m_h/2$ and the Higgs boson is assumed to decay to a $\gamma\gamma + E_{\mathrm{T}}^{\mathrm{miss}}$ final state.

Signal channel	BF($h \to \gamma\gamma + E_{\mathrm{T}}^{\mathrm{miss}})_{\mathrm{obs}}^{95}$	BF($h \to \gamma\gamma + E_{\mathrm{T}}^{\mathrm{miss}})_{\mathrm{exp}}^{95}$
$m_{NLSP}, m_{LSP} = 1, 0$ GeV	0.080	$0.066^{+0.027}_{-0.016}$
$m_{NLSP}, m_{LSP} = 10, 0$ GeV	0.102	$0.081^{+0.025}_{-0.025}$
$m_{NLSP}, m_{LSP} = 11, 10$ GeV	0.359	$0.292^{+0.175}_{-0.103}$
$m_{NLSP}, m_{LSP} = 20, 0$ GeV	0.103	$0.095^{+0.017}_{-0.026}$
$m_{NLSP}, m_{LSP} = 20, 10$ GeV	0.072	$0.062^{+0.023}_{-0.017}$
$m_{NLSP}, m_{LSP} = 21, 20$ GeV	3.618	$2.939^{+1.842}_{-1.047}$
$m_{NLSP}, m_{LSP} = 30, 0$ GeV	0.103	$0.084^{+0.025}_{-0.019}$
$m_{NLSP}, m_{LSP} = 30, 10$ GeV	0.097	$0.081^{+0.022}_{-0.024}$
$m_{NLSP}, m_{LSP} = 30, 20$ GeV	0.073	$0.058^{+0.022}_{-0.016}$
$m_{NLSP}, m_{LSP} = 31, 30$ GeV	5.744	$4.426^{+1.574}_{-2.102}$
$m_{NLSP}, m_{LSP} = 40, 0$ GeV	0.100	$0.084^{+0.021}_{-0.025}$
$m_{NLSP}, m_{LSP} = 40, 10$ GeV	0.099	$0.085^{+0.025}_{-0.022}$
$m_{NLSP}, m_{LSP} = 40, 20$ GeV	0.089	$0.075^{+0.023}_{-0.023}$
$m_{NLSP}, m_{LSP} = 40, 30$ GeV	0.077	$0.065^{+0.024}_{-0.017}$
$m_{NLSP}, m_{LSP} = 41, 40$ GeV	17.203	$12.986^{+7.014}_{-7.039}$
$m_{NLSP}, m_{LSP} = 50, 0$ GeV	0.100	$0.082^{+0.024}_{-0.023}$
$m_{NLSP}, m_{LSP} = 50, 10$ GeV	0.101	$0.084^{+0.027}_{-0.021}$
$m_{NLSP}, m_{LSP} = 50, 20$ GeV	0.097	$0.081^{+0.021}_{-0.024}$
$m_{NLSP}, m_{LSP} = 50, 30$ GeV	0.076	$0.064^{+0.021}_{-0.011}$
$m_{NLSP}, m_{LSP} = 50, 40$ GeV	0.100	$0.082^{+0.022}_{-0.024}$
$m_{NLSP}, m_{LSP} = 51, 50$ GeV	4.430	$3.590^{+2.318}_{-1.294}$
$m_{NLSP}, m_{LSP} = 60, 0$ GeV	0.099	$0.082^{+0.030}_{-0.019}$
$m_{NLSP}, m_{LSP} = 60, 10$ GeV	0.108	$0.095^{+0.015}_{-0.032}$
$m_{NLSP}, m_{LSP} = 60, 20$ GeV	0.094	$0.079^{+0.025}_{-0.025}$
$m_{NLSP}, m_{LSP} = 60, 30$ GeV	0.085	$0.070^{+0.025}_{-0.017}$
$m_{NLSP}, m_{LSP} = 60, 40$ GeV	0.091	$0.073^{+0.022}_{-0.015}$
$m_{NLSP}, m_{LSP} = 60, 50$ GeV	0.176	$0.140^{+0.062}_{-0.027}$
$m_{NLSP}, m_{LSP} = 61, 60$ GeV	8.601	$6.948^{+4.730}_{-2.560}$

Table 7.16: 95% CL upper limits on the BF($h \to \gamma + E_{\mathrm{T}}^{\mathrm{miss}}$) assuming a SM Higgs boson production cross section. The second column (BF($h \to \gamma + E_{\mathrm{T}}^{\mathrm{miss}})^{95}_{\mathrm{exp}}$) shows the 95% CL upper limit on the BF($h \to \gamma + E_{\mathrm{T}}^{\mathrm{miss}}$) given the expected number (and $\pm 1\sigma$ excursions on the expectation) of background events. These limits are for the case $m_h/2 < m_{\mathrm{NLSP}} < m_h$ and the Higgs boson is assumed to decay to a $\gamma + E_{\mathrm{T}}^{\mathrm{miss}}$ final state.

Signal channel	BF($h \to \gamma + E_{\mathrm{T}}^{\mathrm{miss}})^{95}_{\mathrm{obs}}$	BF($h \to \gamma + E_{\mathrm{T}}^{\mathrm{miss}})^{95}_{\mathrm{exp}}$
$m_{NLSP}, m_{LSP} = 65, 0$ GeV	0.068	$0.058^{+0.023}_{-0.007}$
$m_{NLSP}, m_{LSP} = 65, 10$ GeV	0.071	$0.056^{+0.025}_{-0.013}$
$m_{NLSP}, m_{LSP} = 65, 20$ GeV	0.072	$0.053^{+0.027}_{-0.006}$
$m_{NLSP}, m_{LSP} = 65, 30$ GeV	0.073	$0.057^{+0.024}_{-0.014}$
$m_{NLSP}, m_{LSP} = 65, 40$ GeV	0.069	$0.052^{+0.026}_{-0.012}$
$m_{NLSP}, m_{LSP} = 65, 50$ GeV	0.099	$0.083^{+0.025}_{-0.020}$
$m_{NLSP}, m_{LSP} = 70, 0$ GeV	0.075	$0.053^{+0.027}_{-0.006}$
$m_{NLSP}, m_{LSP} = 70, 10$ GeV	0.068	$0.059^{+0.020}_{-0.017}$
$m_{NLSP}, m_{LSP} = 70, 20$ GeV	0.065	$0.052^{+0.024}_{-0.011}$
$m_{NLSP}, m_{LSP} = 70, 30$ GeV	0.061	$0.050^{+0.021}_{-0.012}$
$m_{NLSP}, m_{LSP} = 70, 40$ GeV	0.064	$0.052^{+0.019}_{-0.012}$
$m_{NLSP}, m_{LSP} = 70, 50$ GeV	0.084	$0.066^{+0.024}_{-0.015}$
$m_{NLSP}, m_{LSP} = 80, 0$ GeV	0.071	$0.054^{+0.025}_{-0.012}$
$m_{NLSP}, m_{LSP} = 80, 10$ GeV	0.070	$0.054^{+0.023}_{-0.011}$
$m_{NLSP}, m_{LSP} = 80, 20$ GeV	0.061	$0.049^{+0.020}_{-0.012}$
$m_{NLSP}, m_{LSP} = 80, 30$ GeV	0.074	$0.059^{+0.021}_{-0.011}$
$m_{NLSP}, m_{LSP} = 80, 40$ GeV	0.067	$0.053^{+0.024}_{-0.010}$
$m_{NLSP}, m_{LSP} = 90, 0$ GeV	0.069	$0.054^{+0.023}_{-0.011}$
$m_{NLSP}, m_{LSP} = 90, 10$ GeV	0.066	$0.052^{+0.024}_{-0.012}$
$m_{NLSP}, m_{LSP} = 90, 20$ GeV	0.058	$0.049^{+0.021}_{-0.012}$
$m_{NLSP}, m_{LSP} = 90, 30$ GeV	0.062	$0.053^{+0.019}_{-0.012}$
$m_{NLSP}, m_{LSP} = 100, 0$ GeV	0.072	$0.062^{+0.022}_{-0.009}$
$m_{NLSP}, m_{LSP} = 100, 10$ GeV	0.058	$0.050^{+0.023}_{-0.012}$
$m_{NLSP}, m_{LSP} = 100, 20$ GeV	0.069	$0.053^{+0.022}_{-0.012}$
$m_{NLSP}, m_{LSP} = 110, 0$ GeV	0.079	$0.062^{+0.023}_{-0.010}$
$m_{NLSP}, m_{LSP} = 110, 10$ GeV	0.073	$0.061^{+0.022}_{-0.009}$
$m_{NLSP}, m_{LSP} = 120, 0$ GeV	0.072	$0.059^{+0.022}_{-0.018}$

7.8 Optimization and Design of the Full Run 2 Search

While the analysis completed using the $79.8\,\text{fb}^{-1}$ dataset currently has some of the best limits for the branching fraction of Higgs decays to both massive and light gravitinos, there is room for improvement.

In the ZH channel, the most obvious thing to do is separate the one and two photon signatures. Preliminary studies have shown much simpler cut and count regions can be designed for both signatures. These optimization exercises follow the procedures outlined in Section 7.3.1. For the one photon final state it was found cutting slightly harder on missing transverse momentum, allowing up to one jet in the event, and requiring the missing transverse momentum to be separated in ϕ from any lepton increased the expected sensitivity for the full Run 2 dataset. The full set of selection criteria can be found in Table 7.17. The expected sensitivity for different signal points can be seen

Table 7.17: Summary of the optimized signal region selection criteria for the ZH search using $140\,\text{fb}^{-1}$of data.

Objects
Photons: $p_{\text{T}} > 40$ GeV, $\lvert\eta\rvert < 1.37$ or $1.52 < \lvert\eta\rvert < 2.37$, *Tight* ID, `FixedCutTight` Isolation
Electrons: $p_{\text{T}}^{e_1} > 40$ GeV, $p_{\text{T}}^{e_2} > 20$ GeV, $\lvert\eta\rvert < 1.37$ or $1.52 < \lvert\eta\rvert < 2.47$ *Medium* ID, `GradientLoose` Isolation
Muons: $p_{\text{T}}^{\mu_1} > 25$ GeV, $p_{\text{T}}^{\mu_2} > 20$ GeV, $\lvert\eta\rvert < 2.7$, *Medium* ID, `GradientLoose` Isolation
Jets: anti-k_t, $R = 0.4$, $p_{\text{T}} > 30$ GeV, $\lvert y\rvert < 4.4$
Preselection
Single or dilepton unprescaled trigger with trigger matching
2+ jet veto
Require exactly two leptons
Require at least one photon
Event Topology
***Z* window**: $\lvert m_Z - m_{\ell\ell}\rvert < 15$ GeV
Missing transverse momentum: $E_{\text{T}}^{\text{miss}} > 100$ GeV
Event p_{T} balance: $\frac{\lvert p_{\text{T}}^{\ell\ell} - p_{\text{T}}^{\gamma E_{\text{T}}^{\text{miss}}}\rvert}{p_{\text{T}}^{\gamma E_{\text{T}}^{\text{miss}}}} < 0.15$
Lepton,$E_{\text{T}}^{\text{miss}}$ separation: $\min(\Delta\phi(E_{\text{T}}^{\text{miss}}, \ell)) > \pi$

in Figure 7.43, where the expected upper limit (in percentage) on the $(\sigma/\sigma_{SM}) \times \text{BF}(h \to \gamma + E_{\text{T}}^{\text{miss}})$ is shown. This limits can further be improved by employing a multi-bin "shape" fit with the $m_T^{\gamma, E_{\text{T}}^{\text{miss}}}$ variable. This variable is shown in Figure 7.44, where clear separation in bins can be seen. The lower bin is more sensitive to smaller mass splittings between the NLSP and LSP while the higher region is sensitive to higher mass NLSPs. Employing a shape fit in this region could push the expected sensitivity of this channel towards BFs of 1-1.5%. Very simple studies have shown for

the grid point $m_{\text{NLSP}} = 120$, $m_{\text{LSP}} = 0$ GeV, the expected upper limit is around 1.45%.

Due to the relatively simple nature of the signal process, this analysis would also be a good candidate for multivariate techniques. Utilizing a boosted decision tree or neural net with inputs such as the p_{T}, E_{T}, ϕ, and η of the leptons/photon as well as the ϕ and E_{T} of the missing transverse momentum could very well lead to large gains.

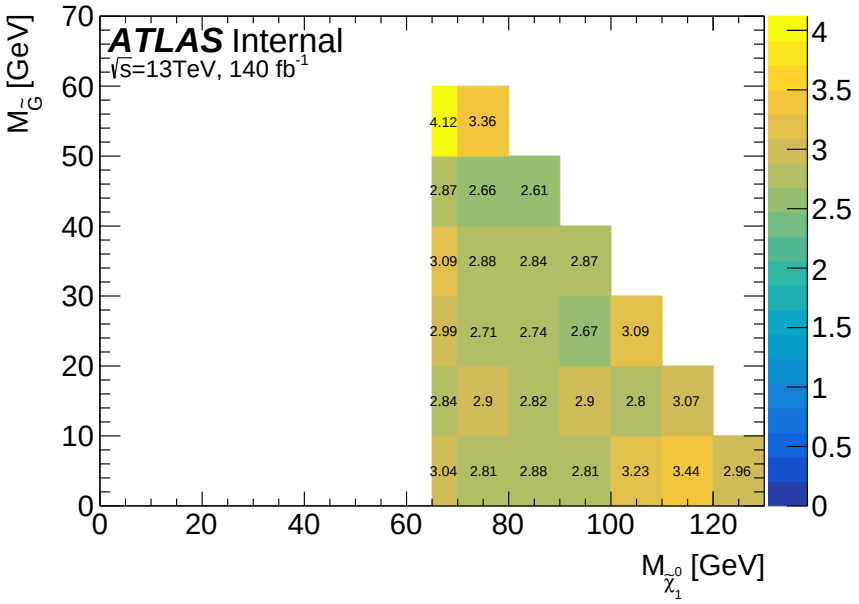

Figure 7.43: Expected 95% CL upper limits (in percentage) on $(\sigma/\sigma_{SM}) \times \text{BF}(h \to \gamma + E_{\text{T}}^{\text{miss}})$ for the 140 fb^{-1}dataset. This is calculated with the selection criteria shown in Table 7.17.

When requiring a second photon in the event, the backgrounds drop substantially. With basic selections of the preselection in Table 7.17 (dropping the lepton p_{T} cut to 25 GeV), $E_{\text{T}}^{\text{miss}} > 40$ GeV, $|m_Z - m_{\ell\ell}| < 15$ GeV, and $\text{Bal}_{p_{\text{T}}} < 0.5$, there is less than 0.02 expected background events. For the diphoton phase space, the expected sensitivity for $(\sigma/\sigma_{SM}) \times \text{BF}(h \to \gamma\gamma + E_{\text{T}}^{\text{miss}})$ is already below 1.5% with the described cuts and only further tuning in order to keep as many signal events is needed.

In addition to the optimization of the selection criteria, there are other key aspects to the analysis which can be enhanced. Handling the backgrounds from mis-identified objects is going to be a key moving forward with shape fits. Further examinations of the jet-to-photon fakes are needed in order to define a purer validation region. Additionally, categorizing and understanding quark-initiated vs. gluon-initiated mis-identified photons could be an interesting avenue to probe, which would also benefit other analyses using photons on ATLAS. While there was high confidence in the mis-

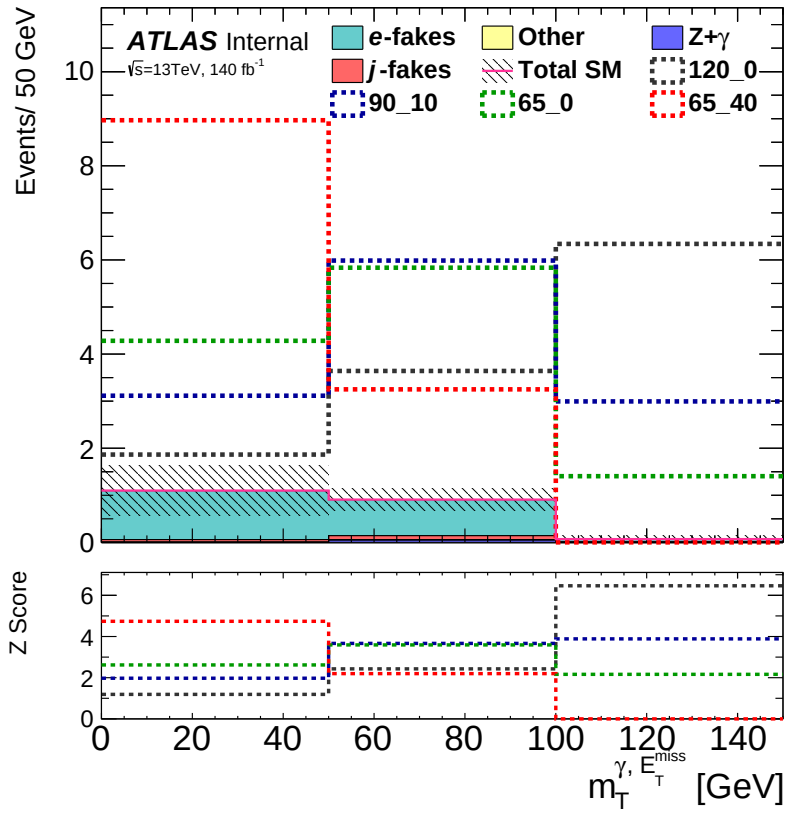

Figure 7.44: $m_T^{\gamma,E_{\mathrm{T}}^{\mathrm{miss}}}$ variable in the 140 fb^{-1} optimized single photon signal region. This variable can be utilized in a "shape" fit to boost the sensitivity of the analysis. The backgrounds are denoted by the colored histograms. Different signals, with Higgs branching fraction of 10%, are denoted by the dashed lines. The total uncertainty of the SM is given by the hatched band. The bottom plot shows the Z-score (defined in Section 7.3.1) for each bin.

identified electron-to-photon background, a validation region would be nice for the next iteration of the analysis. Furthermore, distinguishing between bremsstrahlung photons vs. true electron-deposit fakes could help with better ambiguity definitions which played an important role in the analysis. Supplementary inspections of different $E_{\mathrm{T}}^{\mathrm{miss}}$ terms could also help improve the rejection of fake detector $E_{\mathrm{T}}^{\mathrm{miss}}$ events and with the new signal region allowing for one jet, $E_{\mathrm{T}}^{\mathrm{miss}}$ significance could be beneficial. Overall, there are many new techniques being developed and investigations into the different backgrounds which would increase the power of this search.

This chapter has laid the groundwork for searches in the ZH channel aiming to probe Higgs decays leading to a final state of photon(s) + missing transverse momentum. But this is not the only place to look. Preliminary studies were performed utilizing the VBF production mode, which

seems encouraging. Inspired by the Run 1 conference note [250], this production mode is promising due to its larger production cross section of 3.8 pb, rather than the ZH (where $Z \to e^+e^- or \mu^+\mu^-$) cross section of 59 fb. The Run 1 ATLAS search can be improved upon with dedicated photon + VBF triggers (for Run 3). Additionally, it did not exploit the $h \to \tilde{\chi}_1^0\tilde{\chi}_1^0 \to \gamma\tilde{G}\gamma\tilde{G}$ decay kinematics of $\Delta\phi(\gamma\gamma)$ and $p_{\mathrm{T}}^{\gamma\gamma}$. Both of these variables, along with a very strict, hard VBF tag can greatly enhance the sensitivity to the signal process.

Chapter 8

Conclusion

This thesis has presented operations experience and troubleshooting with the Transition Radiation Tracker Data Acquisition team, and two results involving Higgs bosons decaying to at least one photon.

The operations details and projects discussed were part of a huge amount of upkeep, maintenance, and problem solving by the whole TRT DAQ team. Predictions were made about the upcoming effects of radiation damage to the radiation front-ends, and analysis was performed on the frequent resynchronization of the TRT throughout Run 2. The root of the problem has likely been identified and the biggest run-time problem of the TRT DAQ system is actively investigated and fixed.

Differential and fiducial cross section measurements of the Higgs boson decaying to two photons were presented. Results were focused on the dataset with an integrated luminosity of $36.1\,\text{fb}^{-1}$ of proton–proton collisions collected at $\sqrt{s} = 13\,\text{TeV}$ with the ATLAS detector. The inclusive diphoton cross section was measured to be $55 \pm 9\,(\text{stat.}) \pm 4\,(\text{syst.}) \pm 0.1\,(\text{theo.})\,\text{fb}$ compared with the Standard model prediction of $64 \pm 2\,\text{fb}$. In addition to inclusive cross section measurement, fiducial cross section results were presented for regions targeting the VBF, VH, and $t\bar{t}H$ production modes of the Higgs boson as well as a region targeting BSM contributions. Differential results were presented for multiple measured spectra involving kinematics of the diphoton system or variables with jets produced in association with the Higgs boson. No significant deviations from the Standard Model were observed and in their absence, limits were set on alternative hypotheses involving higher order couplings between Standard Model particles and the Higgs boson.

In addition, results were presented from a search for $h \to \tilde{\chi}_1^0\tilde{\chi}_1^0 \to \gamma\tilde{G}\gamma\tilde{G}$ and $h \to \tilde{\chi}_1^0\tilde{G} \to \gamma\tilde{G}\tilde{G}$ processes produced in association with a leptonically decaying Z boson, selecting events with two opposite-sign leptons, at least one photon, and missing transverse momentum using an integrated

luminosity of $79.8\,\text{fb}^{-1}$ of proton–proton collisions collected at $\sqrt{s} = 13\,\text{TeV}$ with the ATLAS detector. Three events are observed in the signal region, where 2.1 ± 0.5 background events are expected from SM processes. Since no significant excess was observed with respect to the Standard Model prediction, upper limits at 95% CL of less than 11% (18%) on the cross section times branching fraction of each process are observed for massless gravitinos (massive neutralinos).

Where to go next?

With the foundation of the Run 1 TRT DAQ team, the Run 2 TRT DAQ team was very successful in ensuring the continued high data-taking efficiency of the TRT. For Run 3 the radiation damage should not be a continuing problem, and hopefully with the Long Shutdown II (lasting until 2021), the resynchronization issues can be cured.

This thesis has only presented the searches and measurements with the partial Run 2 dataset. The full Run 2 dataset should decrease statistical uncertainties of the Higgs to diphoton differential and fiducial cross sections substantially. Looking toward this dataset and the Run 3 dataset, with increased statistics we may be pushed into a regime where the analysis is systematically dominated. Most importantly, the "spurious signal" technique of building a Monte Carlo background template to determine the analytic function will no longer work. The datasets are getting so gargantuan that ATLAS does not have the computing infrastructure in order to generate the requisite Monte Carlo. This technique will have to be replaced a more data-driven approach, robust against the ever growing dataset size. Some procedures such as Gaussian process or functional decomposition seem promising, though rigorous studies of the systematic uncertainties and a complete validation of the process will be necessary before a result can be published. With these bountiful datasets, just the increase in statistics or even finer binning of variables like $p_{\text{T}}^{\gamma\gamma}$ can constrain Effective Field Theories and BSM parameterizations of Higgs interactions.

In regard to the search for exotic Higgs decays involving photons and BSM particles, there is quite a bit to expand upon. This thesis laid the groundwork for a bigger, better analysis which could probe Higgs bosons branching fractions to neutralinos and gravitinos below the percent level. Dedicated single and di photon regions can isolate the kinematics and provide higher sensitives to models. The $m_T^{\gamma, E_{\text{T}}^{\text{miss}}}$ and $\Delta\phi(E_{\text{T}}^{\text{miss}}, \gamma)$ variables, which were not employed for discrimination, can be used in rectangular based cuts or even used in multi-bin "shape" fits where the background from WZ events would be further constrained. A multitude of studies into jets mis-identified as photons, involving a breakdown of quark-initiated vs gluon-initiated mis-identified photons could

be an interesting avenue to probe. This would be one of the first studies on ATLAS regarding this topic and all other analyses involving photons would greatly benefit from that. The VBF channel of this Higgs production should also be explored. A search with the same model was explored in Run 1 and with further optimization in both the ZH and VBF channel, in addition to all the ideas explored above, we estimate that a search could attain below percent level expected sensitivity of Higgs branching fractions.

Given the enormous success of the Standard Model, including the discovery of the Higgs boson in *only* 2012, physicists are inching closer to fully describing the world around us in a truly fundamental way. There are still many searches and precision measurements to perform in order to elucidate its fundamental properties. Even though no deviations or unpredicted decay mode have been observed, increased statistics and improved analysis techniques in the differential and fiducial cross sections can help investigate the Higgs coupling to Standard Model bosons and fermions. Likewise, statistics and improved analysis design can help push the boundaries of the exotic Higgs decay searches. No one knows where deviations and answers to Standard Model problems may lie and there is still an exceeding amount to learn about the Higgs boson.

Appendix A

Extra Transition Radiation Tracker Data Acquisition Material

This appendix will document the additional studies on the TRT resynchronization errors.

Figure A.1 displays the RODs with 10 or more *lock* errors during 2015–2018 **non**-stable beam data taking. For this figure, and Figures A.2 and A.3, the error shown is a binary string, where the four GOLs on the patch panels are represented as 1's (no error) or 0's (error). The left-most digit refers to the GOL 3, and then counts downward as the right-most digit refers to GOL 0. For instance the binary string `0110` translates into GOL 3 and GOL 0 having errors while GOL 1 and GOL 2 are returning data as expected. For ease of viewing, errors with only one GOL asserting an error is denoted as "GOL X" (where X is the GOL number returning the error). In the figures, the ROD's are indexed by a string of numbers (i.e `0x341401`), this is just an identifier for individual RODs. This should be treated as just an index with no deeper meaning, but further explanations of what specific ROD this refers to can be seen in Ref. [121] (This is an internal ATLAS note and may be access restricted.) Figures A.2 and A.3 show the RODs with 10 or more *buffer* errors during Run 2 for stable and non-stable beams, respectively.

Figure A.4 shows the lock and buffer errors for all RODs as a function of when they occurred during the LHC stable beam fills. This is split into lengths of less than 4 hours (blue dashed), 4-8 hours (purple), and 8 or more hours (yellow/black). Furthermore, this is studied (separately for lock and buffer errors) for each given fill duration. The RODs are now identified in Figures A.5–A.7, where now the time of the buffer error, after stable beams were declared, and the time of the error, before stable beams ended, is shown. Figures A.8–A.10 displays the same plots, but for the lock errors.

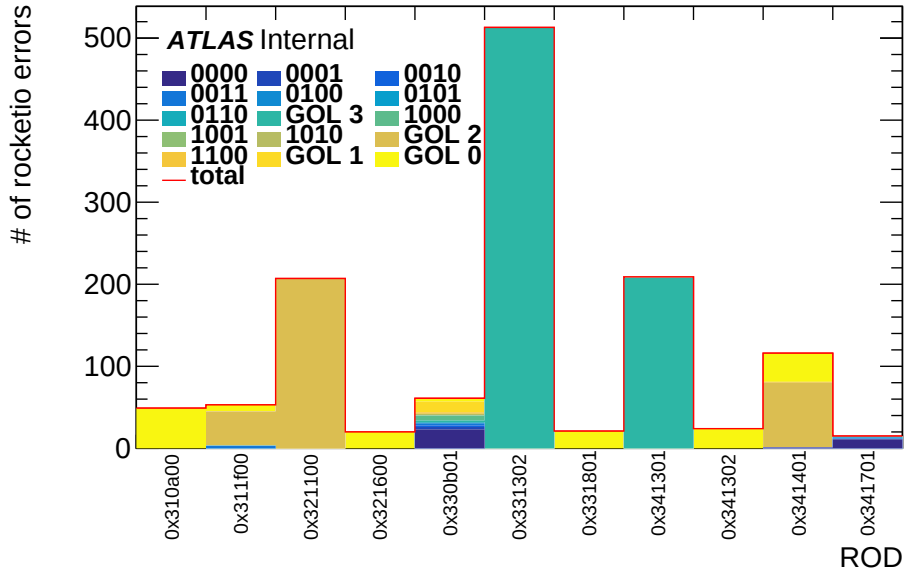

Figure A.1: RODs with more than 10 lock errors during non-stable beams and their frequencies. The error type is typically constant, as seen by the solid colors. These errors are less understood, but may come at times on the border of stable beams and non-stable beams. The lock error shown is a binary string, where the four GOLs on the patch panels are represented as 1's (no error) or 0's (error). The left-most digit refers to the GOL 3, and then counts downward as the right-most digit refers to GOL 0. For ease of viewing, errors with only one GOL asserting an error is denoted as "GOL X" (where X is the GOL number returning the error).

Figures A.11 and A.12 show visually the integrated lock errors of the other two RODs tested in Run 2 in order to determine the cause of the errors. Figure A.11 shows the errors for ROD `0x321600` for which the GOL cables were swapped, and Figure A.12 shows the errors for ROD `0x331801` where the ROD was re-seated in the VME crate. For both RODs the error rate did not diminish or change.

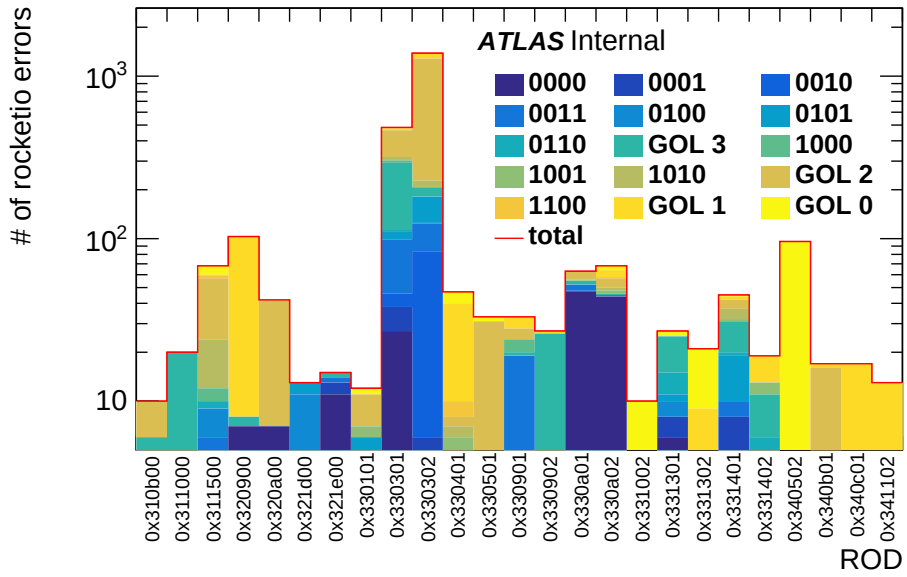

Figure A.2: RODs with more than 10 buffer errors during stable beams and their frequencies. The error type is typically distributed, as seen by the many colors for a single ROD. Generally these errors are from broken ROD patch panels. The legend is described in the text or in Figure A.1.

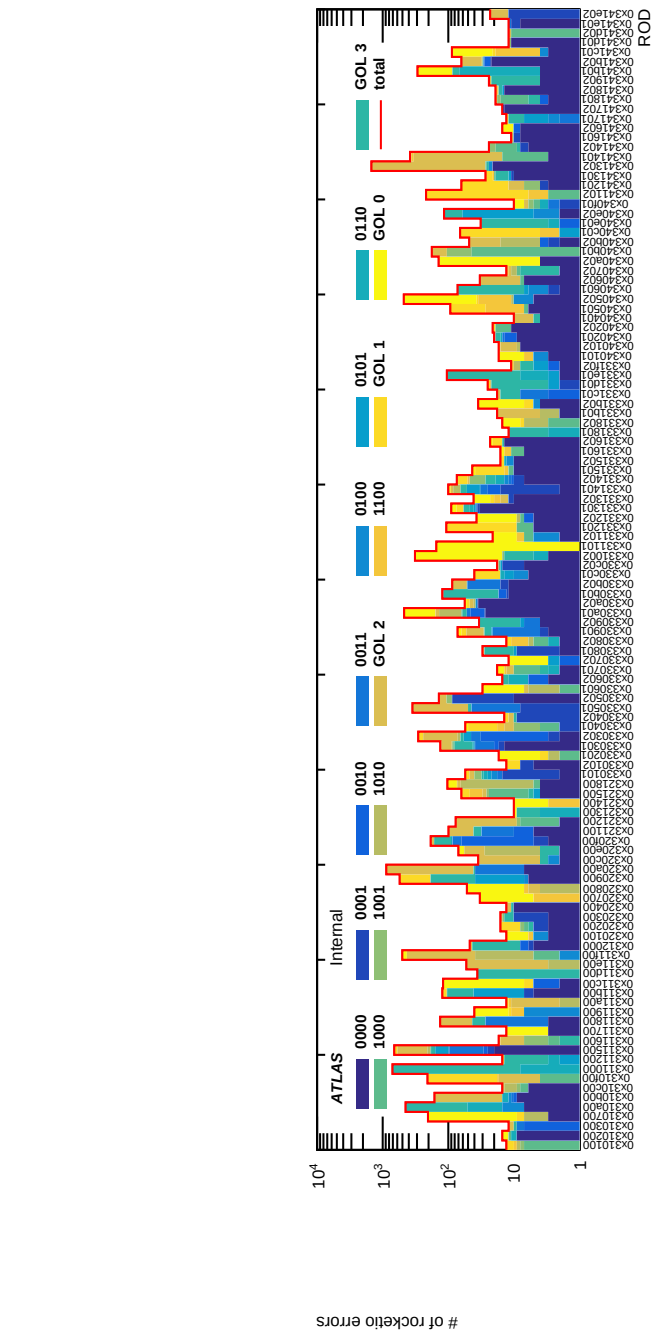

Figure A.3: RODs with more than 10 buffer errors during non-stable beams and their frequencies. The error type is typically distributed, as seen by the many colors for a single ROD, indicating the error is coming from some LHC clock jitter. The buffer error shown is a binary string, where the four GOLs on the patch panels are represented as 1's (no error) or 0's (error). The left-most digit refers to the GOL 3, and then counts downward as the right-most digit refers to GOL 0. For ease of viewing, errors with only one GOL asserting an error is denoted as "GOL X" (where X is the GOL number returning the error).

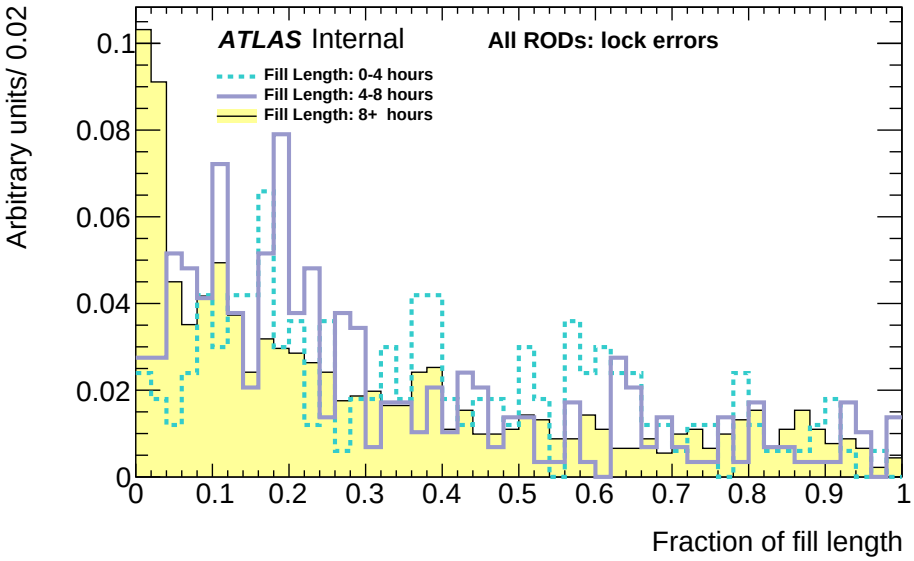

(a)

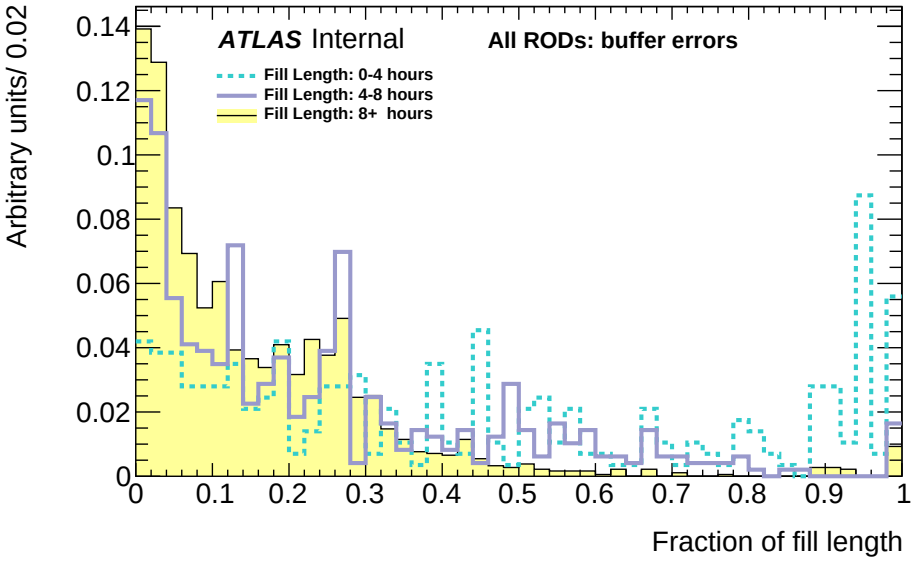

(b)

Figure A.4: All (a) lock and (b) buffer errors as a function of when they occurred during the LHC fills. This is split by fill lengths of less than 4 hours (blue dashed), 4-8 hours (purple), and 8 or more hours (yellow/black).

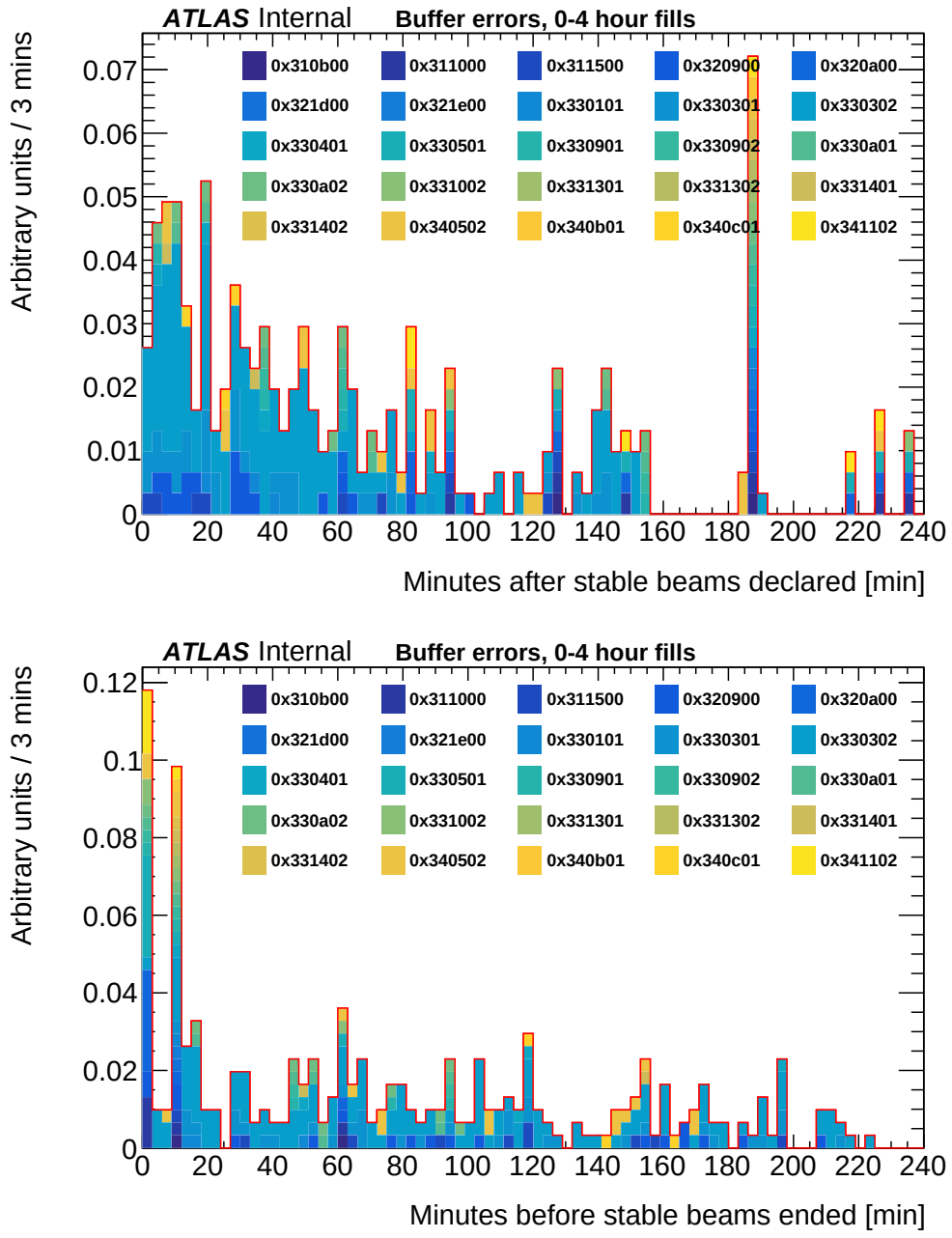

Figure A.5: Buffer errors as a function of minutes after (before) when stable beams were declared (ended), for 0-4 hour length LHC fills. The different RODs are shown as different colors.

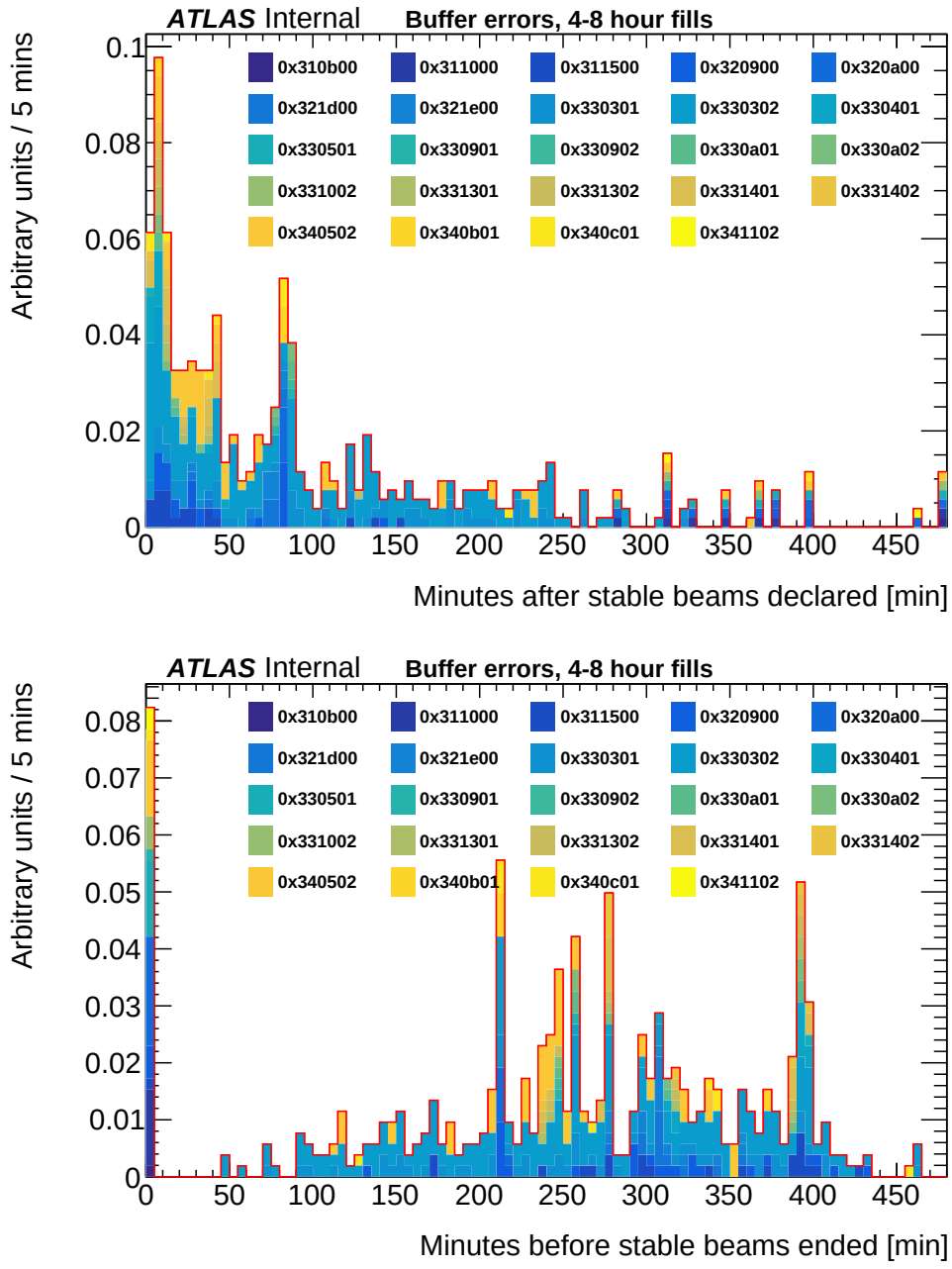

Figure A.6: Buffer errors as a function of minutes after (before) when stable beams were declared (ended), for 4-8 hour length LHC fills. The different RODs are shown as different colors.

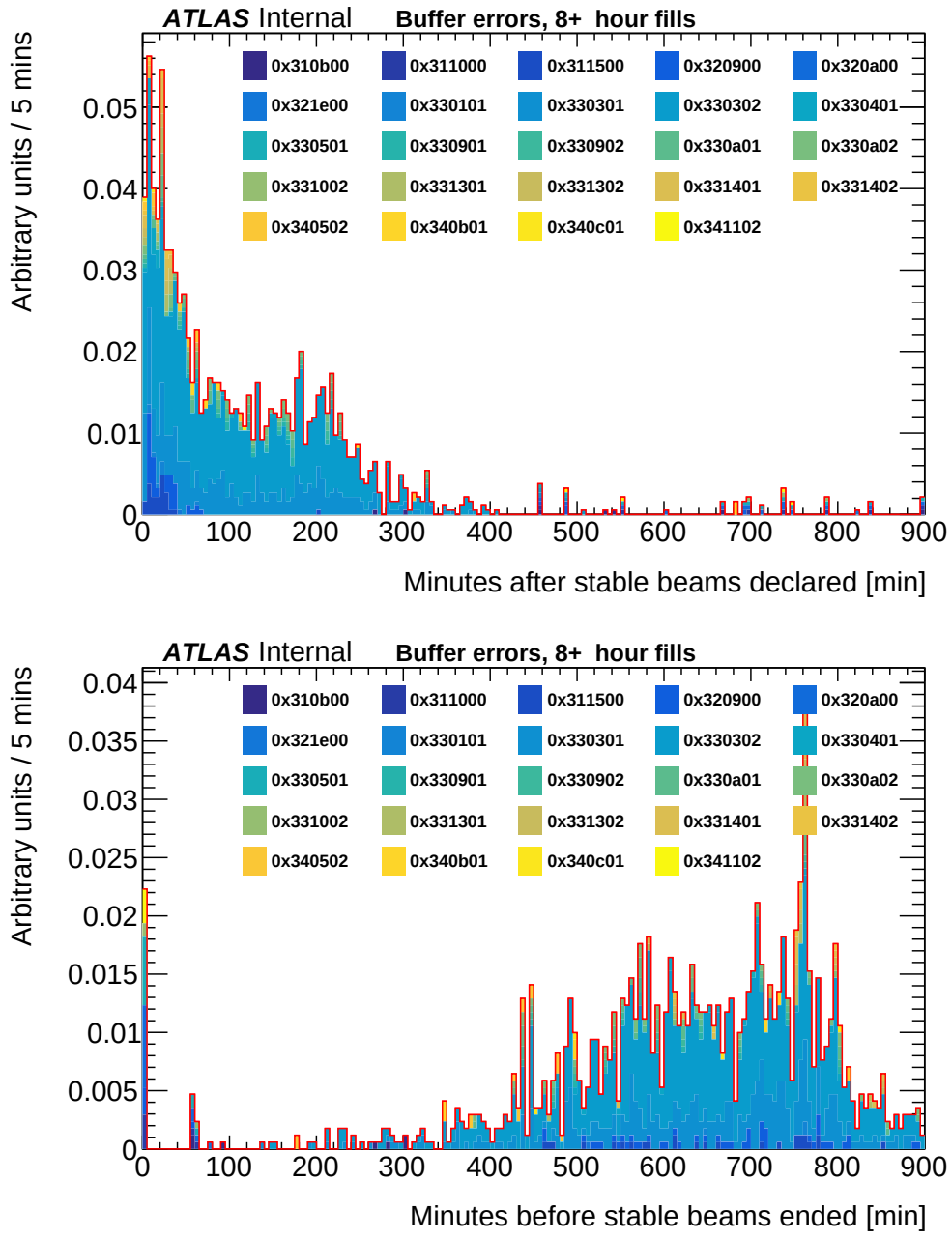

Figure A.7: Buffer errors as a function of minutes after (before) when stable beams were declared (ended), for 8+ hour length LHC fills. The different RODs are shown as different colors.

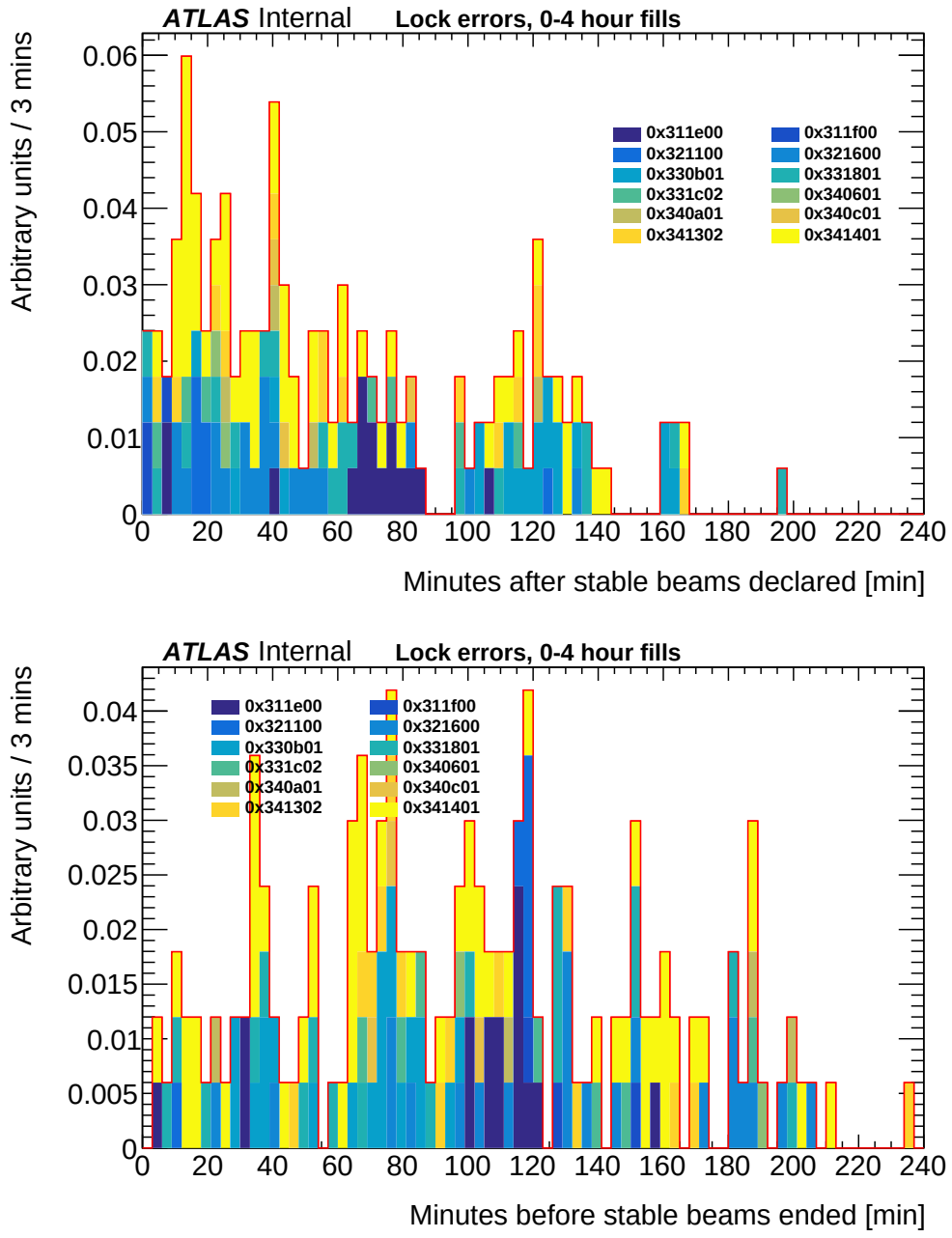

Figure A.8: Lock errors as a function of minutes after (before) when stable beams were declared (ended), for 0-4 hour length LHC fills. The different RODs are shown as different colors.

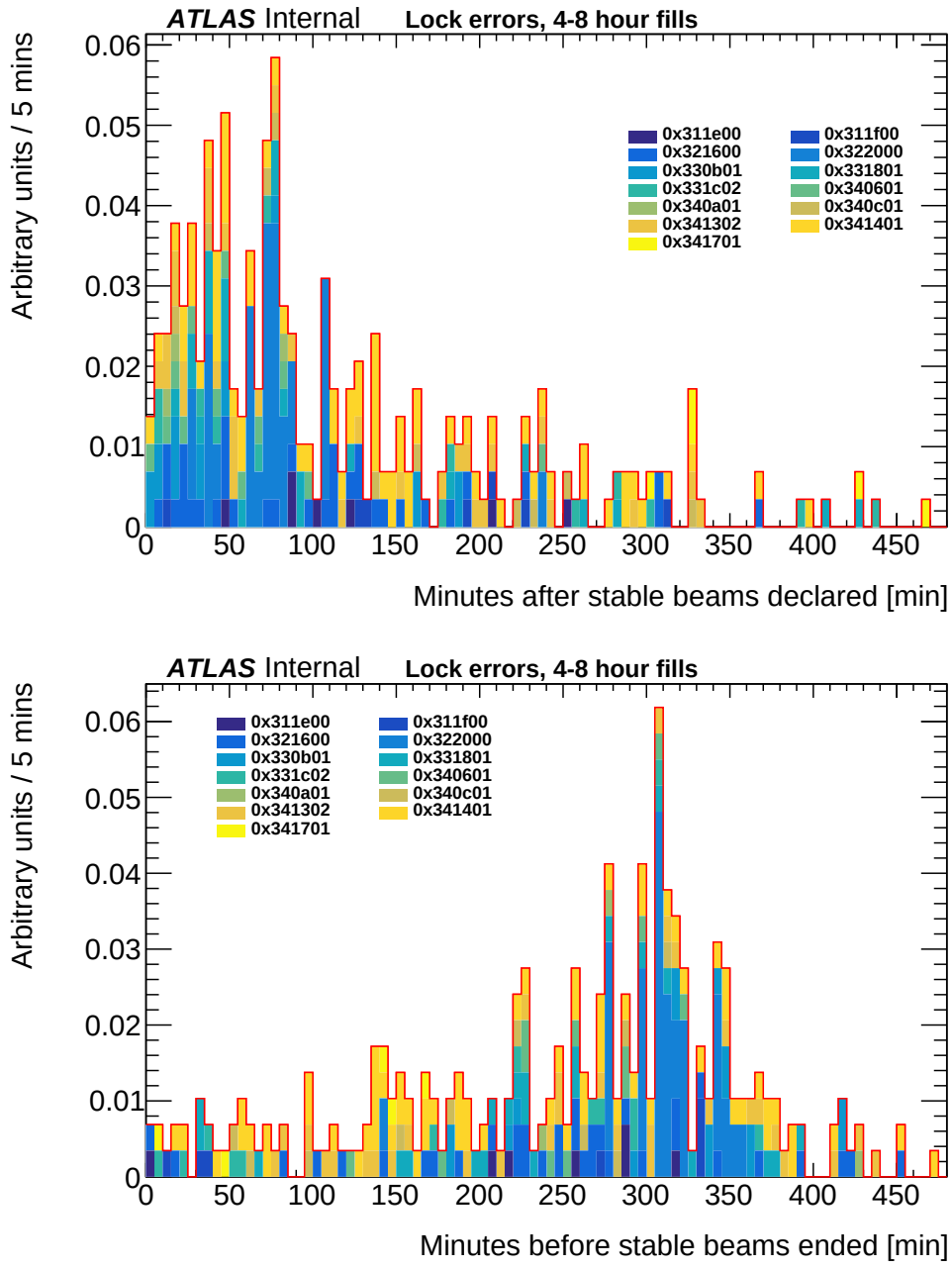

Figure A.9: Lock errors as a function of minutes after (before) when stable beams were declared (ended), for 4-8 hour length LHC fills. The different RODs are shown as different colors.

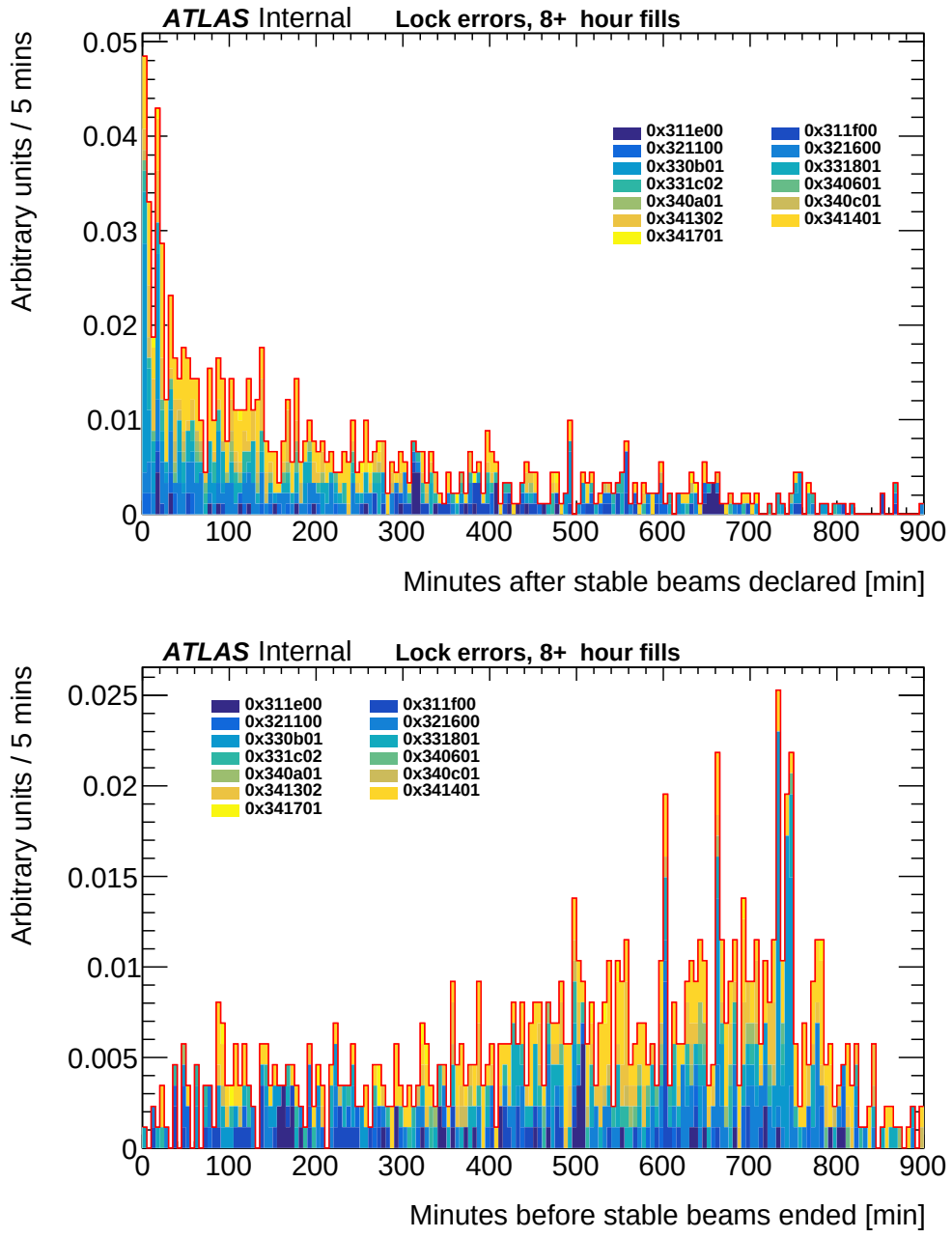

Figure A.10: Lock errors as a function of minutes after (before) when stable beams were declared (ended), for 8+ hour length LHC fills. The different RODs are shown as different colors.

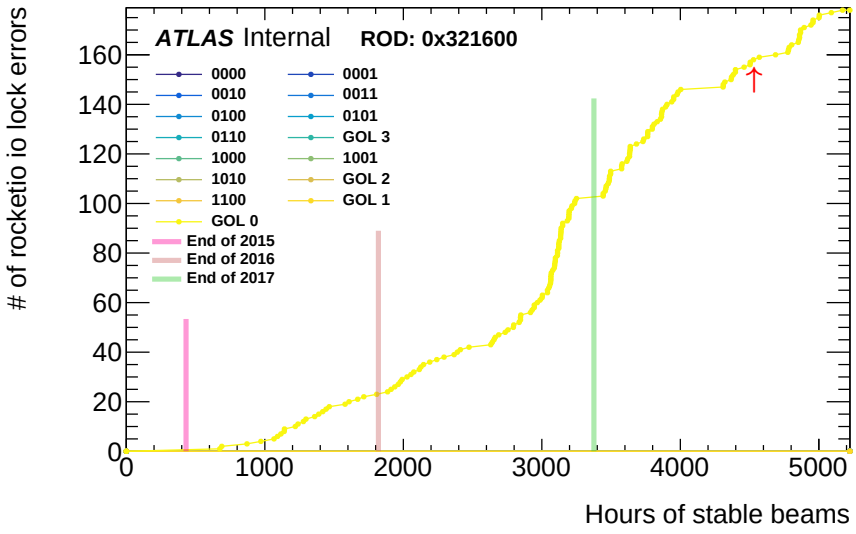

Figure A.11: Integrated stable beam lock resync errors vs. hours of stable beam time for ROD `0x321600`. GOL 0 consistently shows the same error pattern throughout Run 2, with ends of years shown in the colored lines. The red arrow denotes when the GOL cable swap occurred, and there was no change in error rate.

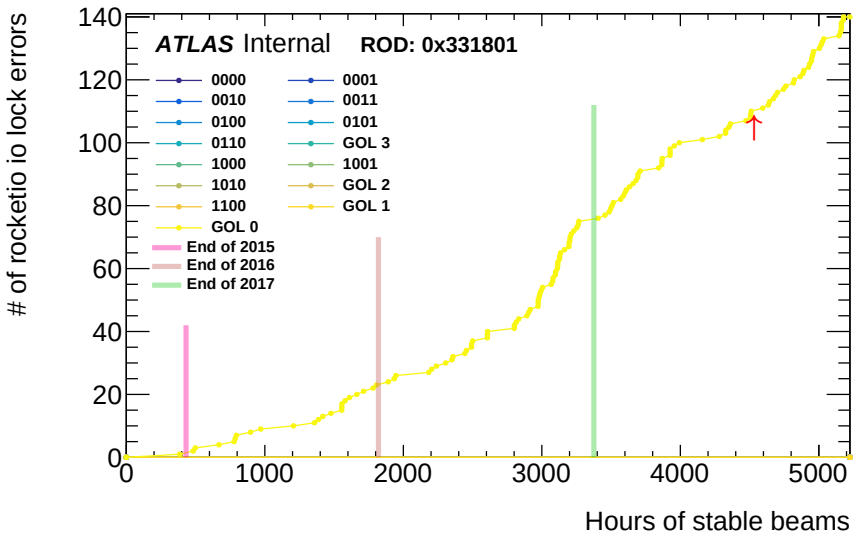

Figure A.12: Integrated stable beam lock resync errors vs. hours of stable beam time for ROD `0x331801`. GOL 0 consistently shows the same error pattern throughout Run 2, with ends of years shown in the colored lines. The red arrow denotes when the ROD re-seat occurred, and there was no change in error rate.

Appendix B

Extra Photon ID Material

B.1 Nominal Fudge Factors Values

In this appendix, the derived fudge factor values are shown with comparisons to the previous 2012 FF tune as a function of p_{T} and $|\eta|$. The systematic errors are shown as the gray band, with the colored bars showing total uncertainty (statistical + systematic). The FFs below 60 GeV were derived from radiative Z photon candidates, and above 60 GeV were derived with photon candidates from inclusive photon+jet events. This is apparent in the plots are the statistical uncertainty decreases from the 50-60 GeV bin to the 60-80 GeV bin. Nevertheless, the transition of measured FF value is smooth. The nominal FF values for converted photons are shown in Section B.1.1, while the FFs for unconverted photons are displayed in Section B.1.2. Of particular note are Figures B.8 (converted) and B.16 (unconverted), where a summary of all nominal FF values for all the fudged variables is shown in a 2D heat map.

B.1.1 Converted Photon Fudge Factors

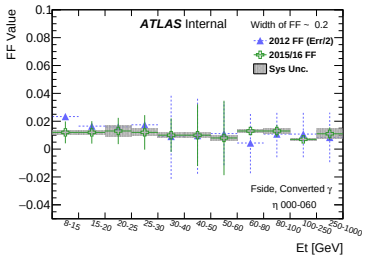

(a) $0.00 < |\eta| < 0.60$

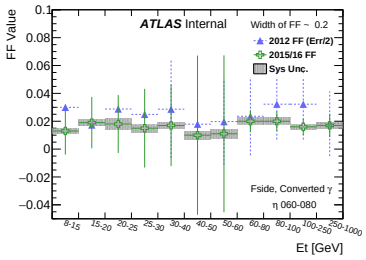

(b) $0.60 < |\eta| < 0.80$

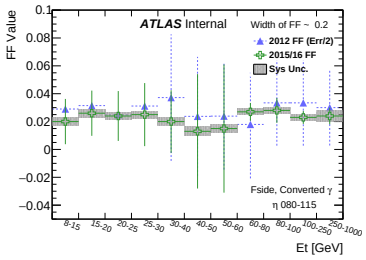

(c) $0.80 < |\eta| < 1.15$

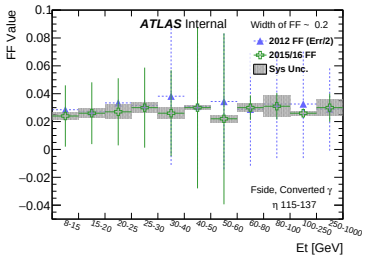

(d) $1.15 < |\eta| < 1.37$

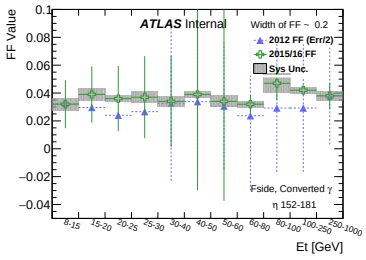

(e) $1.52 < |\eta| < 1.81$

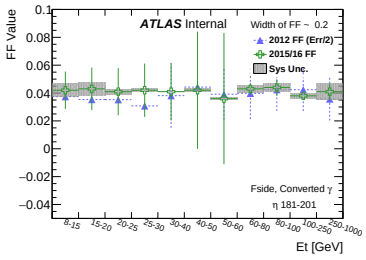

(f) $1.81 < |\eta| < 2.01$

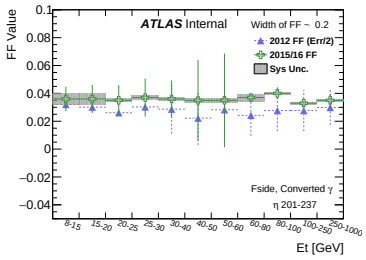

(g) $2.01 < |\eta| < 2.37$

Figure B.1: Nominal fudge factor values, for converted photons, of the F_{side} discriminating variable as a function of p_{T} and $|\eta|$. Different $|\eta|$ regions are shown in (a)-(g). The 2015–2016 FF values are compared with the 2012 Run 1 vales and the systematic errors of the FF derivation are shown as the gray band.

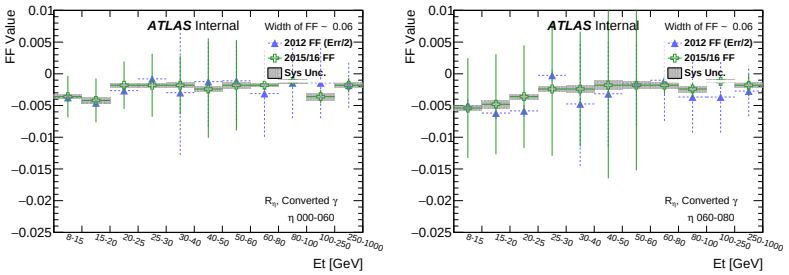

(a) $0.00 < |\eta| < 0.60$

(b) $0.60 < |\eta| < 0.80$

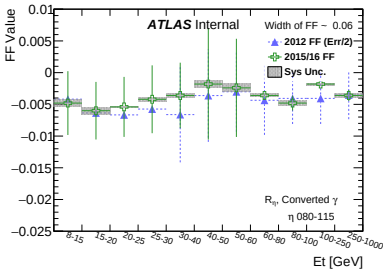

(c) $0.80 < |\eta| < 1.15$

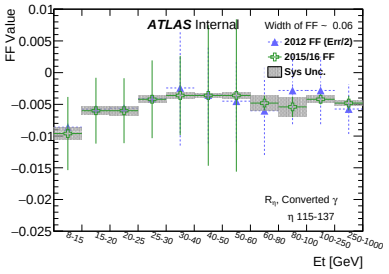

(d) $1.15 < |\eta| < 1.37$

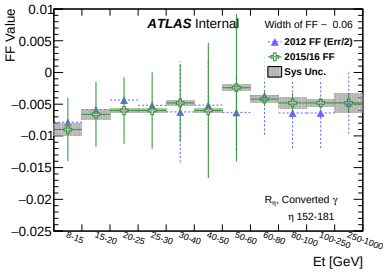

(e) $1.52 < |\eta| < 1.81$

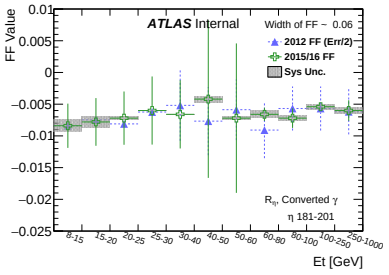

(f) $1.81 < |\eta| < 2.01$

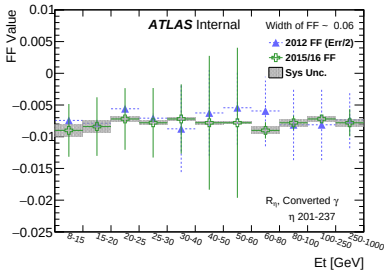

(g) $2.01 < |\eta| < 2.37$

Figure B.2: Nominal fudge factor values, for converted photons, of the R_η discriminating variable as a function of p_{T} and $|\eta|$. Different $|\eta|$ regions are shown in (a)-(g). The 2015–2016 FF values are compared with the 2012 Run 1 vales and the systematic errors of the FF derivation are shown as the gray band.

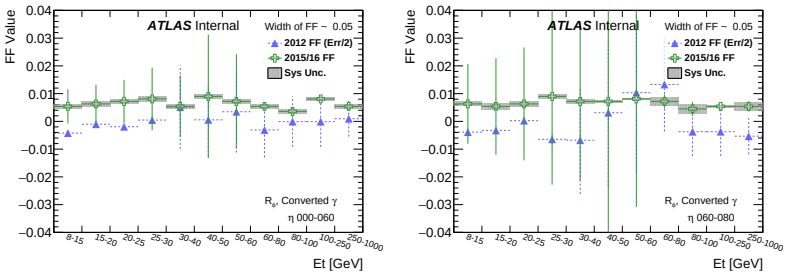

(a) $0.00 < |\eta| < 0.60$

(b) $0.60 < |\eta| < 0.80$

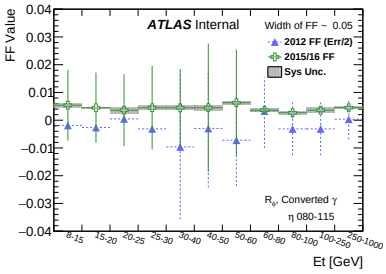

(c) $0.80 < |\eta| < 1.15$

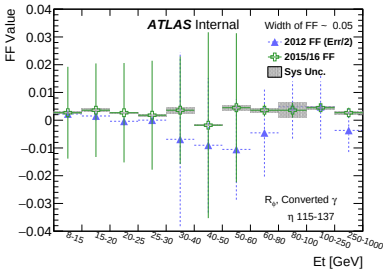

(d) $1.15 < |\eta| < 1.37$

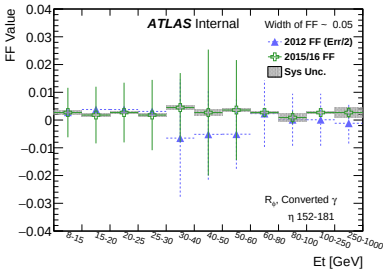

(e) $1.52 < |\eta| < 1.81$

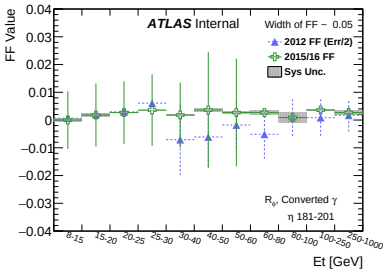

(f) $1.81 < |\eta| < 2.01$

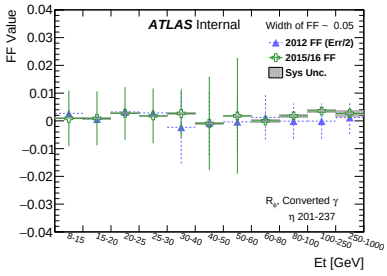

(g) $2.01 < |\eta| < 2.37$

Figure B.3: Nominal fudge factor values, for converted photons, of the R_ϕ discriminating variable as a function of p_{T} and $|\eta|$. Different $|\eta|$ regions are shown in (a)-(g). The 2015–2016 FF values are compared with the 2012 Run 1 vales and the systematic errors of the FF derivation are shown as the gray band.

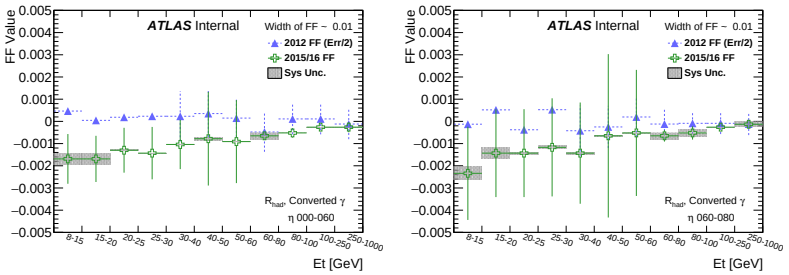

(a) $0.00 < |\eta| < 0.60$

(b) $0.60 < |\eta| < 0.80$

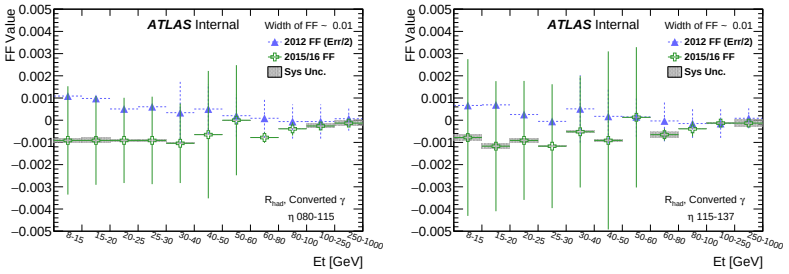

(c) $0.80 < |\eta| < 1.15$

(d) $1.15 < |\eta| < 1.37$

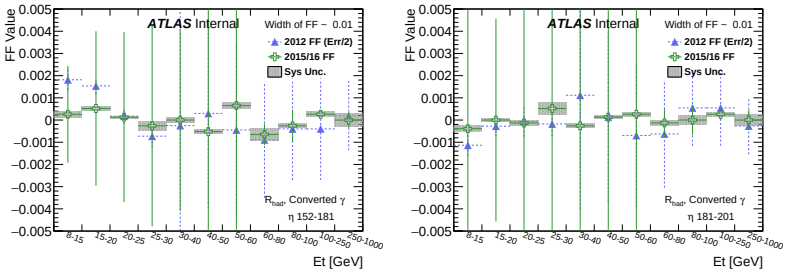

(e) $1.52 < |\eta| < 1.81$

(f) $1.81 < |\eta| < 2.01$

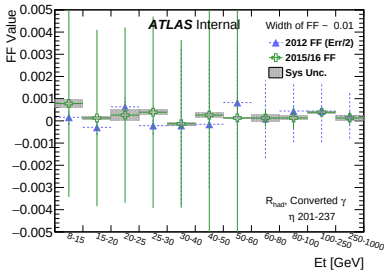

(g) $2.01 < |\eta| < 2.37$

Figure B.4: Nominal fudge factor values, for converted photons, of the R_{had} discriminating variable as a function of p_{T} and $|\eta|$. Different $|\eta|$ regions are shown in (a)-(g). The 2015–2016 FF values are compared with the 2012 Run 1 vales and the systematic errors of the FF derivation are shown as the gray band.

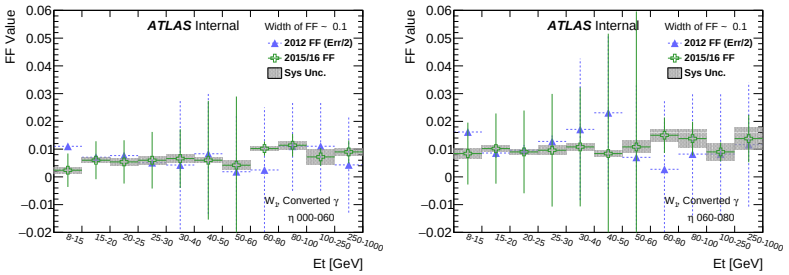

(a) $0.00 < |\eta| < 0.60$

(b) $0.60 < |\eta| < 0.80$

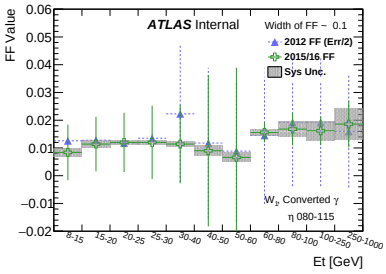

(c) $0.80 < |\eta| < 1.15$

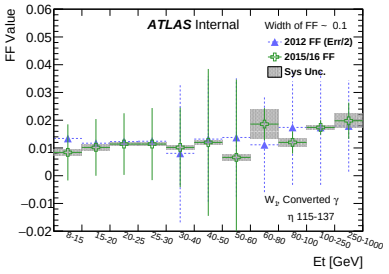

(d) $1.15 < |\eta| < 1.37$

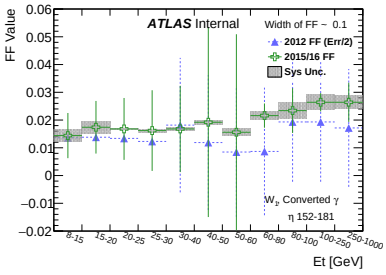

(e) $1.52 < |\eta| < 1.81$

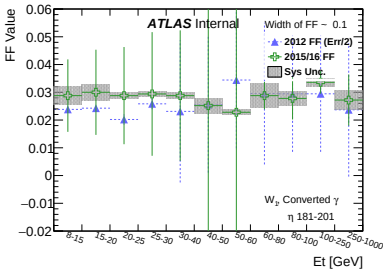

(f) $1.81 < |\eta| < 2.01$

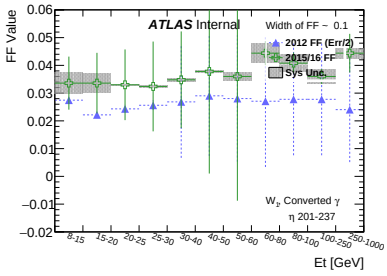

(g) $2.01 < |\eta| < 2.37$

Figure B.5: Nominal fudge factor values, for converted photons, of the $w_{s\,3}$ discriminating variable as a function of p_{T} and $|\eta|$. Different $|\eta|$ regions are shown in (a)-(g). The 2015–2016 FF values are compared with the 2012 Run 1 vales and the systematic errors of the FF derivation are shown as the gray band.

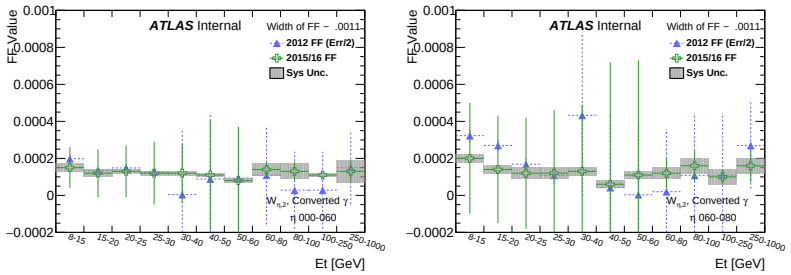

(a) $0.00 < |\eta| < 0.60$

(b) $0.60 < |\eta| < 0.80$

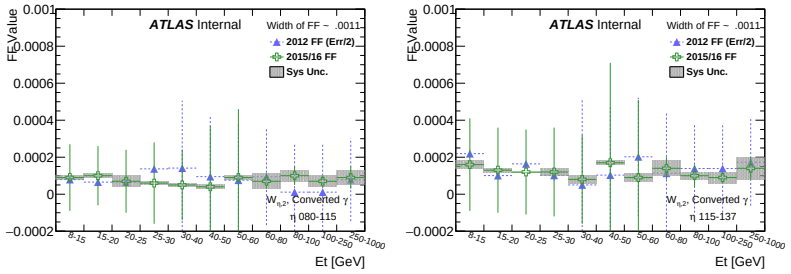

(c) $0.80 < |\eta| < 1.15$

(d) $1.15 < |\eta| < 1.37$

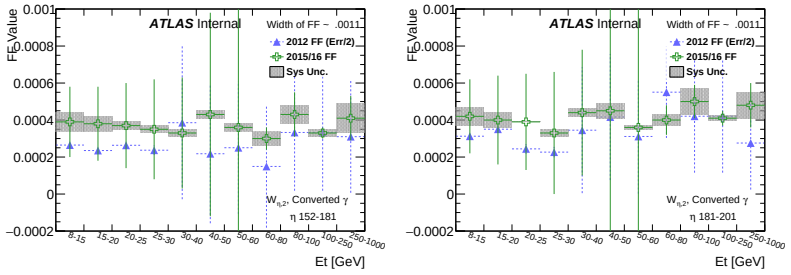

(e) $1.52 < |\eta| < 1.81$

(f) $1.81 < |\eta| < 2.01$

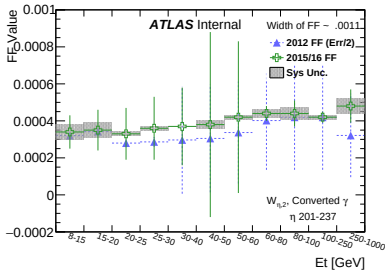

(g) $2.01 < |\eta| < 2.37$

Figure B.6: Nominal fudge factor values, for converted photons, of the w_{η_2} discriminating variable as a function of p_{T} and $|\eta|$. Different $|\eta|$ regions are shown in (a)-(g). The 2015–2016 FF values are compared with the 2012 Run 1 vales and the systematic errors of the FF derivation are shown as the gray band.

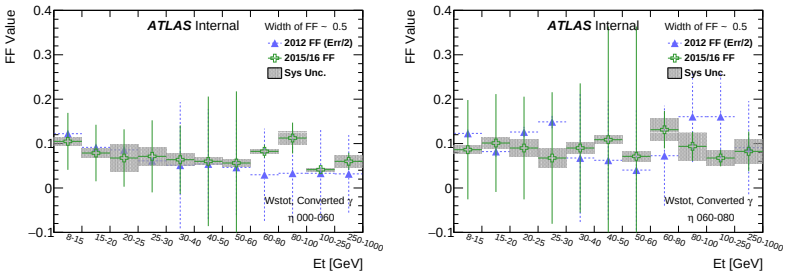

(a) $0.00 < |\eta| < 0.60$

(b) $0.60 < |\eta| < 0.80$

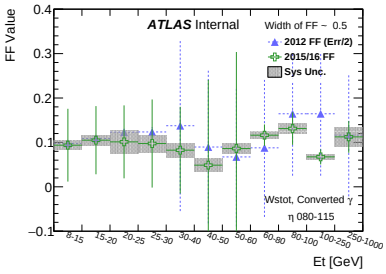

(c) $0.80 < |\eta| < 1.15$

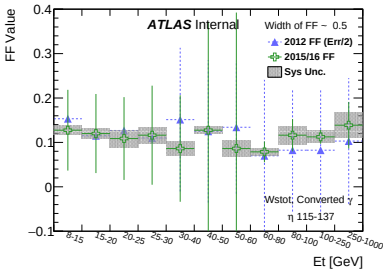

(d) $1.15 < |\eta| < 1.37$

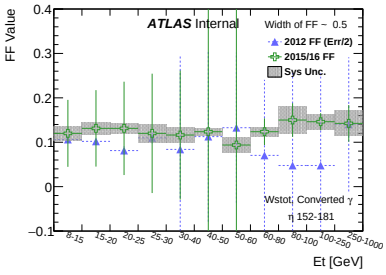

(e) $1.52 < |\eta| < 1.81$

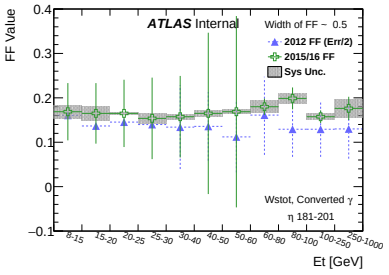

(f) $1.81 < |\eta| < 2.01$

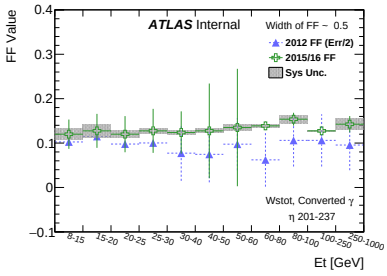

(g) $2.01 < |\eta| < 2.37$

Figure B.7: Nominal fudge factor values, for converted photons, of the $w_{s\,\mathrm{tot}}$ discriminating variable as a function of p_{T} and $|\eta|$. Different $|\eta|$ regions are shown in (a)-(g). The 2015–2016 FF values are compared with the 2012 Run 1 vales and the systematic errors of the FF derivation are shown as the gray band.

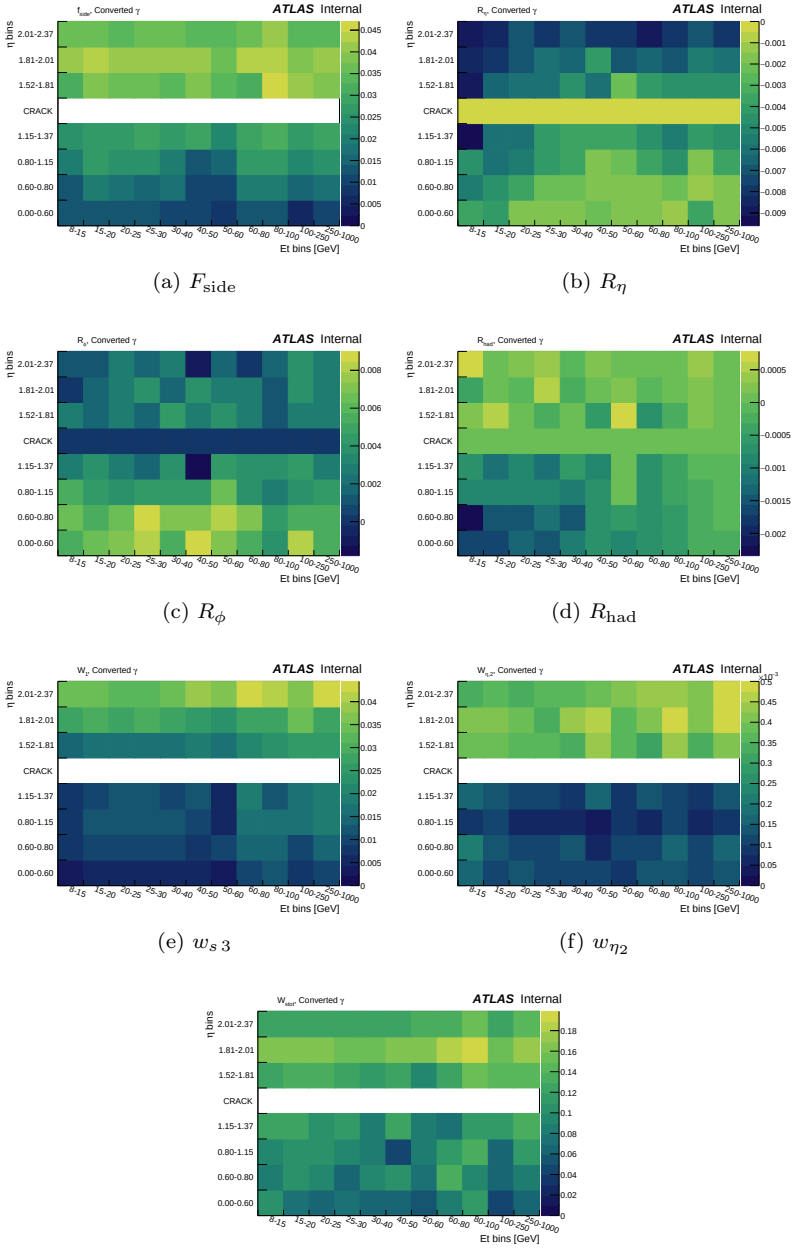

(a) F_{side} (b) R_{η}

(c) R_{ϕ} (d) R_{had}

(e) $w_{s\,3}$ (f) w_{η_2}

(g) $w_{s\,\text{tot}}$

Figure B.8: 2D plots of the nominal fudge factor values, for converted photons, of the various "fudged" discriminating variables as a function of p_{T} and $|\eta|$. The relative uniformity of the 2015–2016 fudge factors can be seen.

B.1.2 Unconverted Photon Fudge Factors

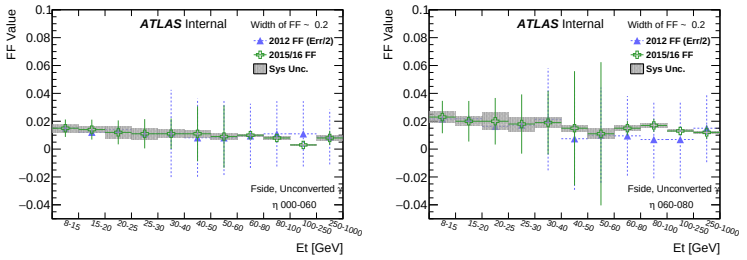

(a) $0.00 < |\eta| < 0.60$

(b) $0.60 < |\eta| < 0.80$

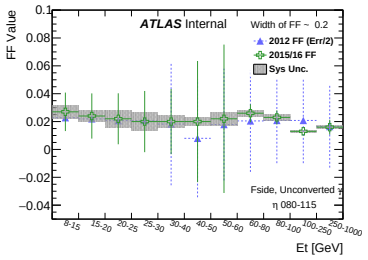

(c) $0.80 < |\eta| < 1.15$

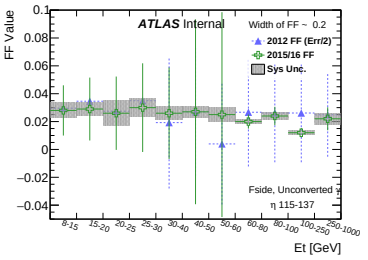

(d) $1.15 < |\eta| < 1.37$

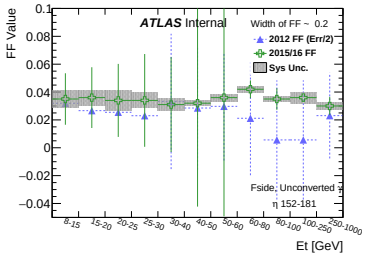

(e) $1.52 < |\eta| < 1.81$

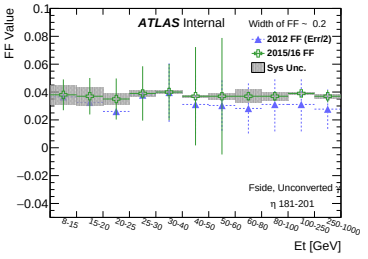

(f) $1.81 < |\eta| < 2.01$

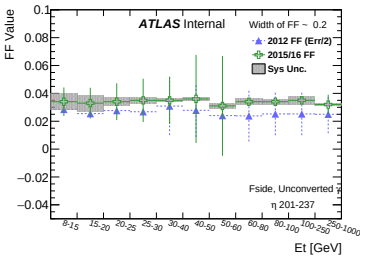

(g) $2.01 < |\eta| < 2.37$

Figure B.9: Nominal fudge factor values, for unconverted photons, of the F_{side} discriminating variable as a function of p_{T} and $|\eta|$. Different $|\eta|$ regions are shown in (a)-(g). The 2015–2016 FF values are compared with the 2012 Run 1 vales and the systematic errors of the FF derivation are shown as the gray band.

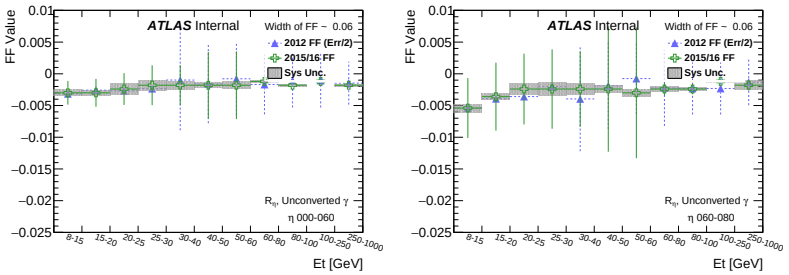

(a) $0.00 < |\eta| < 0.60$

(b) $0.60 < |\eta| < 0.80$

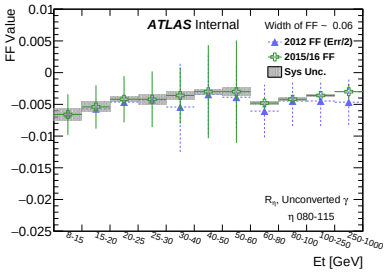

(c) $0.80 < |\eta| < 1.15$

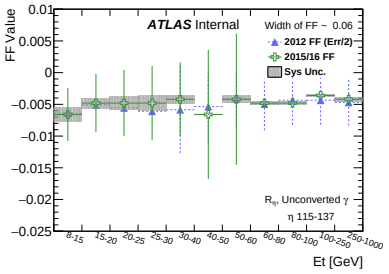

(d) $1.15 < |\eta| < 1.37$

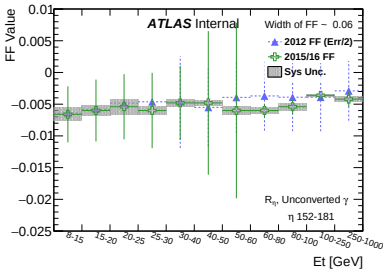

(e) $1.52 < |\eta| < 1.81$

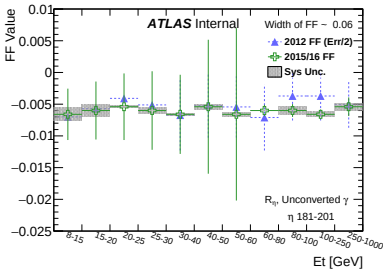

(f) $1.81 < |\eta| < 2.01$

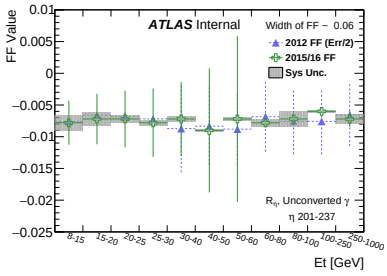

(g) $2.01 < |\eta| < 2.37$

Figure B.10: Nominal fudge factor values, for unconverted photons, of the R_η discriminating variable as a function of p_{T} and $|\eta|$. Different $|\eta|$ regions are shown in (a)-(g). The 2015–2016 FF values are compared with the 2012 Run 1 vales and the systematic errors of the FF derivation are shown as the gray band.

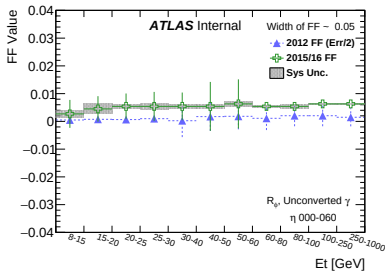

(a) $0.00 < |\eta| < 0.60$

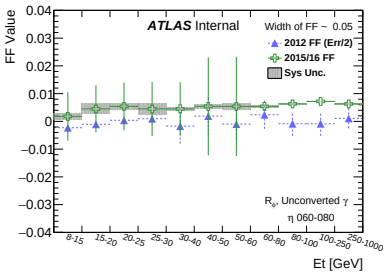

(b) $0.60 < |\eta| < 0.80$

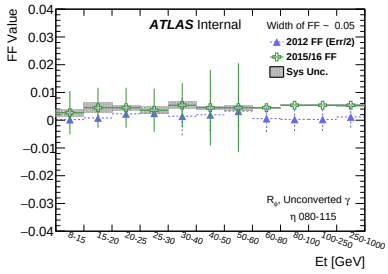

(c) $0.80 < |\eta| < 1.15$

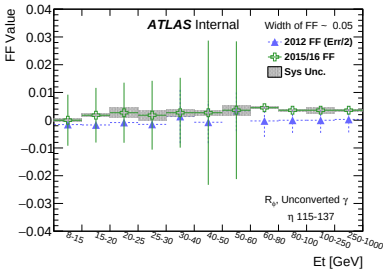

(d) $1.15 < |\eta| < 1.37$

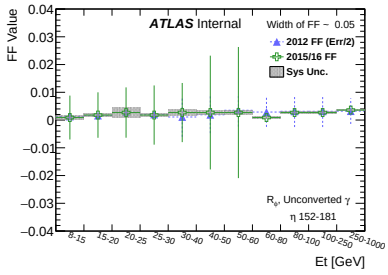

(e) $1.52 < |\eta| < 1.81$

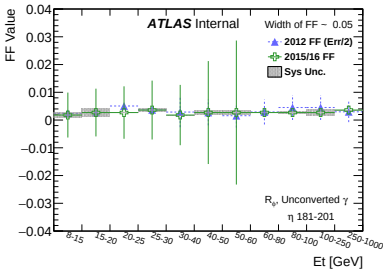

(f) $1.81 < |\eta| < 2.01$

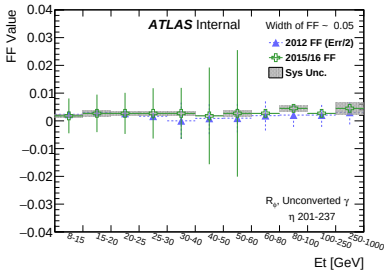

(g) $2.01 < |\eta| < 2.37$

Figure B.11: Nominal fudge factor values, for unconverted photons, of the R_ϕ discriminating variable as a function of p_{T} and $|\eta|$. Different $|\eta|$ regions are shown in (a)-(g). The 2015–2016 FF values are compared with the 2012 Run 1 vales and the systematic errors of the FF derivation are shown as the gray band.

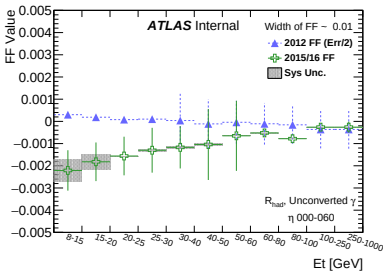

(a) $0.00 < |\eta| < 0.60$

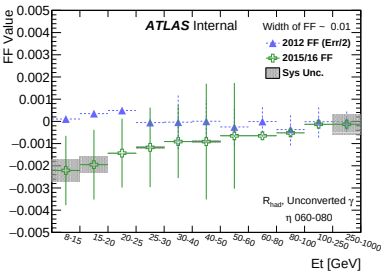

(b) $0.60 < |\eta| < 0.80$

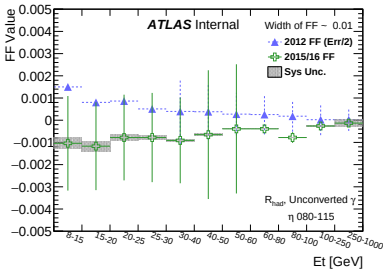

(c) $0.80 < |\eta| < 1.15$

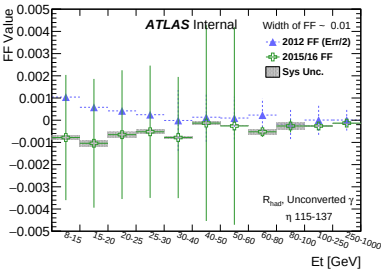

(d) $1.15 < |\eta| < 1.37$

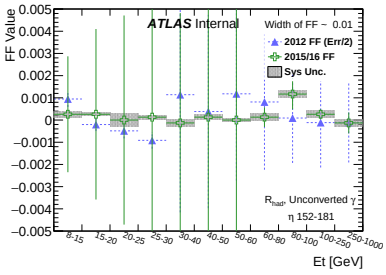

(e) $1.52 < |\eta| < 1.81$

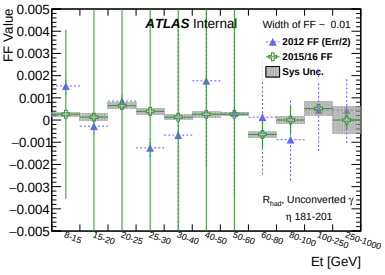

(f) $1.81 < |\eta| < 2.01$

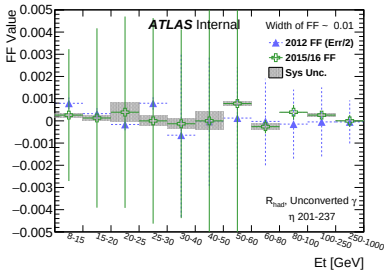

(g) $2.01 < |\eta| < 2.37$

Figure B.12: Nominal fudge factor values, for unconverted photons, of the R_{had} discriminating variable as a function of p_{T} and $|\eta|$. Different $|\eta|$ regions are shown in (a)-(g). The 2015–2016 FF values are compared with the 2012 Run 1 vales and the systematic errors of the FF derivation are shown as the gray band.

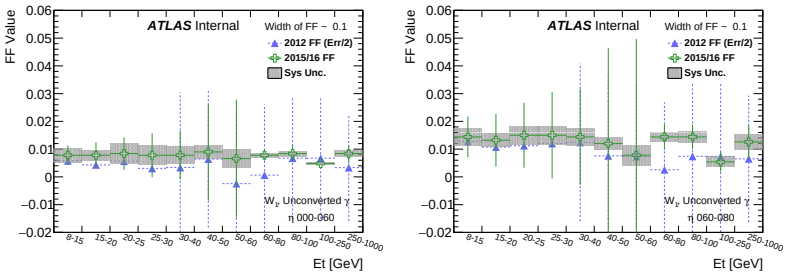

(a) $0.00 < |\eta| < 0.60$

(b) $0.60 < |\eta| < 0.80$

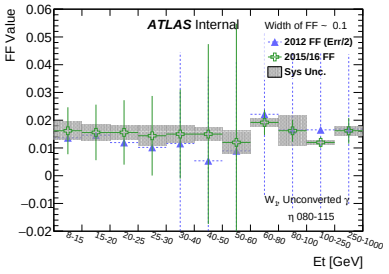

(c) $0.80 < |\eta| < 1.15$

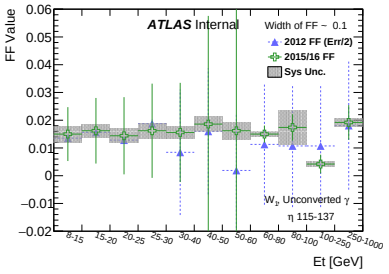

(d) $1.15 < |\eta| < 1.37$

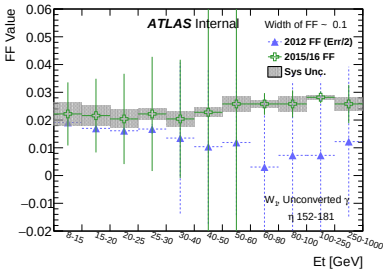

(e) $1.52 < |\eta| < 1.81$

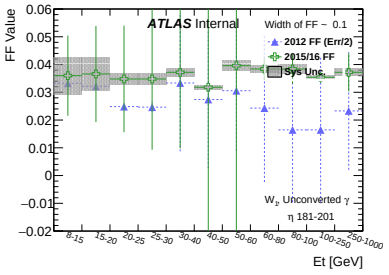

(f) $1.81 < |\eta| < 2.01$

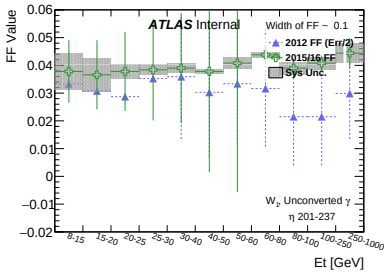

(g) $2.01 < |\eta| < 2.37$

Figure B.13: Nominal fudge factor values, for unconverted photons, of the $w_{s\,3}$ discriminating variable as a function of p_{T} and $|\eta|$. Different $|\eta|$ regions are shown in (a)-(g). The 2015–2016 FF values are compared with the 2012 Run 1 vales and the systematic errors of the FF derivation are shown as the gray band.

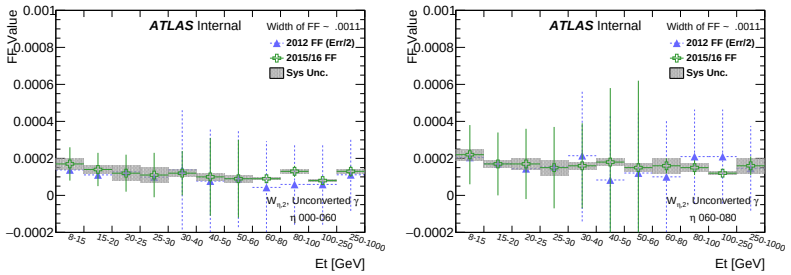

(a) $0.00 < |\eta| < 0.60$

(b) $0.60 < |\eta| < 0.80$

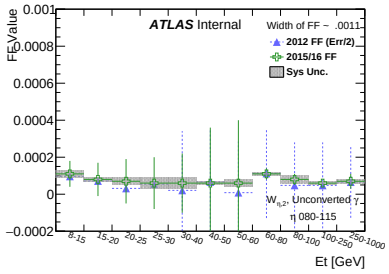

(c) $0.80 < |\eta| < 1.15$

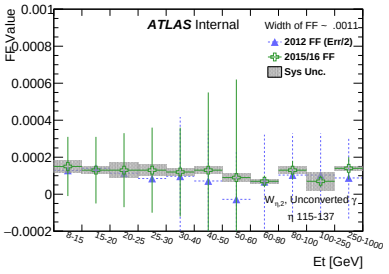

(d) $1.15 < |\eta| < 1.37$

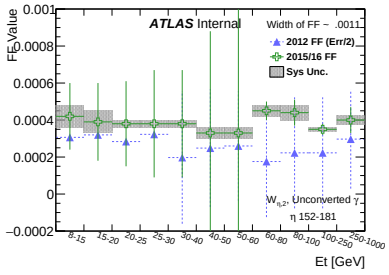

(e) $1.52 < |\eta| < 1.81$

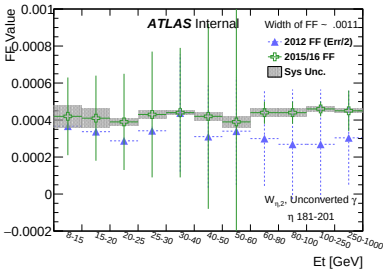

(f) $1.81 < |\eta| < 2.01$

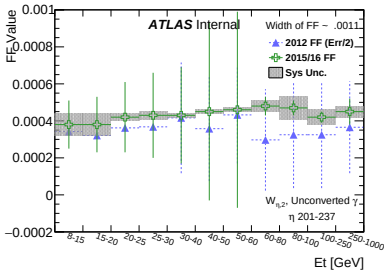

(g) $2.01 < |\eta| < 2.37$

Figure B.14: Nominal fudge factor values, for unconverted photons, of the w_{η_2} discriminating variable as a function of p_{T} and $|\eta|$. Different $|\eta|$ regions are shown in (a)-(g). The 2015–2016 FF values are compared with the 2012 Run 1 vales and the systematic errors of the FF derivation are shown as the gray band.

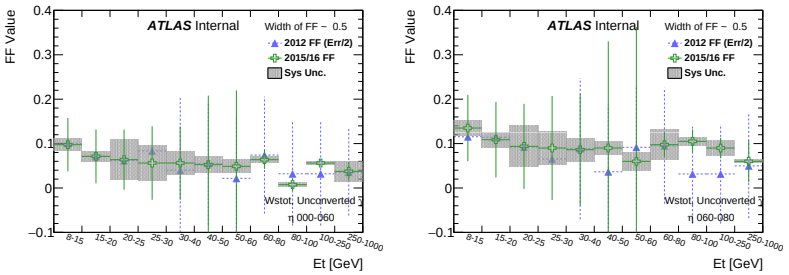

(a) $0.00 < |\eta| < 0.60$

(b) $0.60 < |\eta| < 0.80$

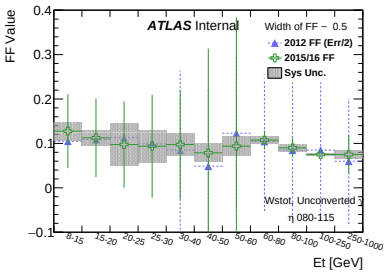

(c) $0.80 < |\eta| < 1.15$

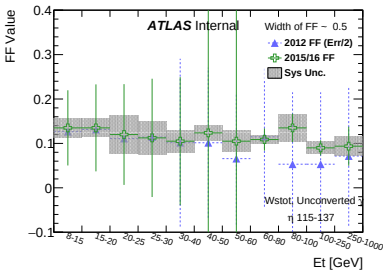

(d) $1.15 < |\eta| < 1.37$

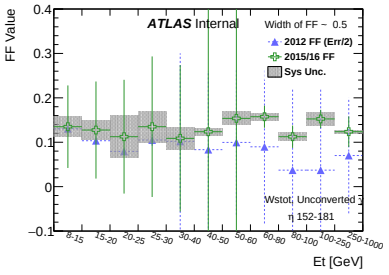

(e) $1.52 < |\eta| < 1.81$

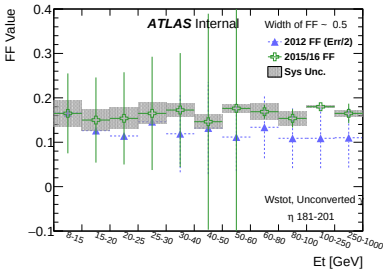

(f) $1.81 < |\eta| < 2.01$

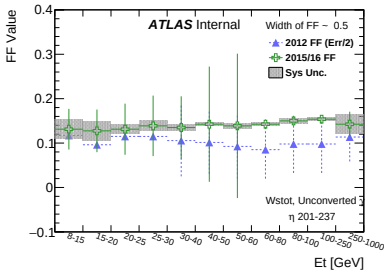

(g) $2.01 < |\eta| < 2.37$

Figure B.15: Nominal fudge factor values, for unconverted photons, of the $w_{s\,\mathrm{tot}}$ discriminating variable as a function of p_{T} and $|\eta|$. Different $|\eta|$ regions are shown in (a)-(g). The 2015–2016 FF values are compared with the 2012 Run 1 vales and the systematic errors of the FF derivation are shown as the gray band.

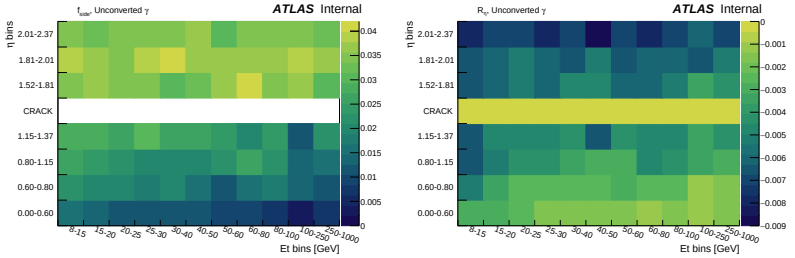

(a) F_{side} (b) R_{η}

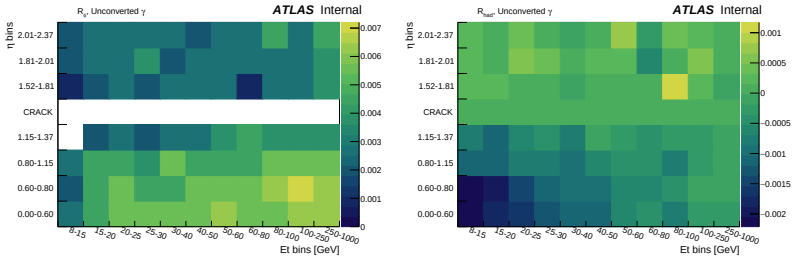

(c) R_{ϕ} (d) R_{had}

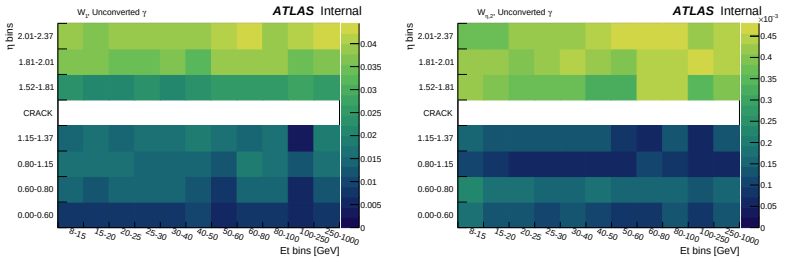

(e) $w_{s\,3}$ (f) $w_{\eta 2}$

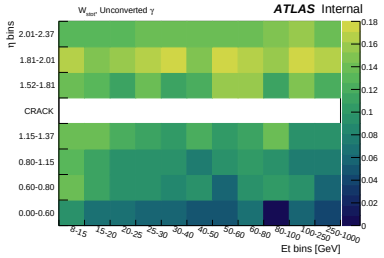

(g) $w_{s\,\text{tot}}$

Figure B.16: 2D plots of the nominal fudge factor values, for unconverted photons, of the various "fudged" discriminating variables as a function of p_{T} and $|\eta|$. The relative uniformity of the 2015–2016 fudge factors can be seen.

B.2 Discriminating Variable Distributions

This section shows the effects of the fudge factors on the Monte Carlo simulations. Each figure shows photon candidates with $p_{\mathrm{T}} \in [10, 50]$ GeV and $|\eta| < 2.37$ (excluding $1.37 \leq |\eta| < 1.52$) selected from $\ell^+\ell^-\gamma$ events. The data are compared with simulated $Z \to \ell\ell\gamma$ events where the red solid histogram corresponds to the uncorrected Monte Carlo, and the solid blue line is the corrected simulation via the Fudge Factor. The variables ΔE_s, and E_{ratio} are not corrected as there is reasonable agreement between the data and Monte Carlo. Additionally, the variable f_1 was not corrected because the rectangular cut on f_1 is on the order of the FF uncertainty and very non-uniform/physical MC efficiencies are seen if the variable is corrected. Nonetheless, the discriminating variables of ΔE_s, f_1, and E_{ratio} are shown below in Figures B.22–B.24. There are some slight differences between the data and simulation due to the χ^2 shifting method, but the R_{had} variable seems to show more of a difference than most. This is most likely due to pileup, improper material modeling before the calorimeter, as well as retunings of noise thresholds in the hadronic calorimeter from Run 1 to Run 2.

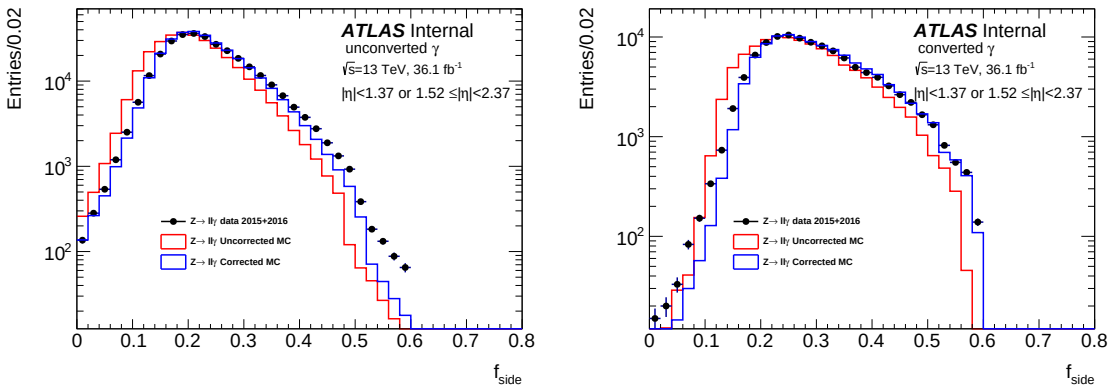

(a) Unconverted F_{side} (b) Converted F_{side}

Figure B.17: Distributions of F_{side} for (a) unconverted and (b) unconverted photon candidates with $p_{\mathrm{T}} \in [10, 50]$ GeV and $|\eta| < 2.37$ (excluding $1.37 \leq |\eta| < 1.52$) selected from $\ell^+\ell^-\gamma$ events. The data are compared with simulated $Z \to \ell\ell\gamma$ events where the red solid histogram corresponds to the uncorrected Monte Carlo, and the solid blue line is the corrected simulation via the fudge factor.

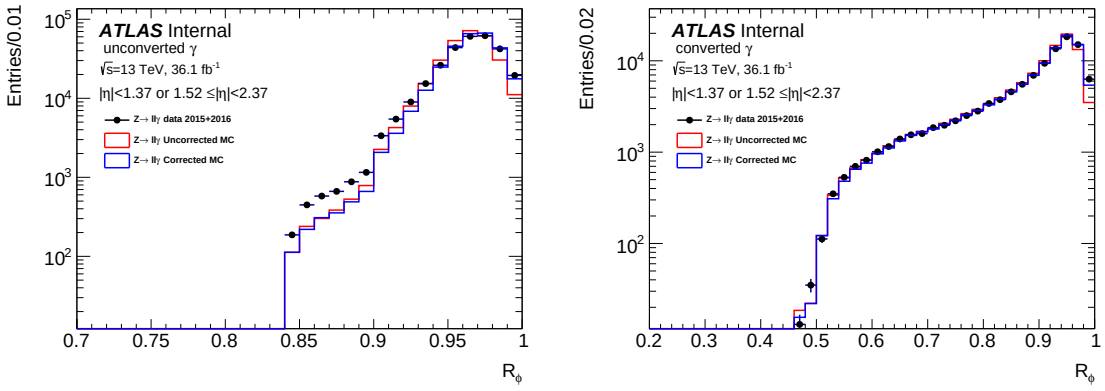

(a) Unconverted R_ϕ (b) Converted R_ϕ

Figure B.18: Distributions of R_ϕ for (a) unconverted and (b) unconverted photon candidates with $p_{\mathrm{T}} \in [10, 50]$ GeV and $|\eta| < 2.37$ (excluding $1.37 \leq |\eta| < 1.52$) selected from $\ell^+\ell^-\gamma$ events. The data are compared with simulated $Z \to \ell\ell\gamma$ events where the red solid histogram corresponds to the uncorrected Monte Carlo, and the solid blue line is the corrected simulation via the fudge factor.

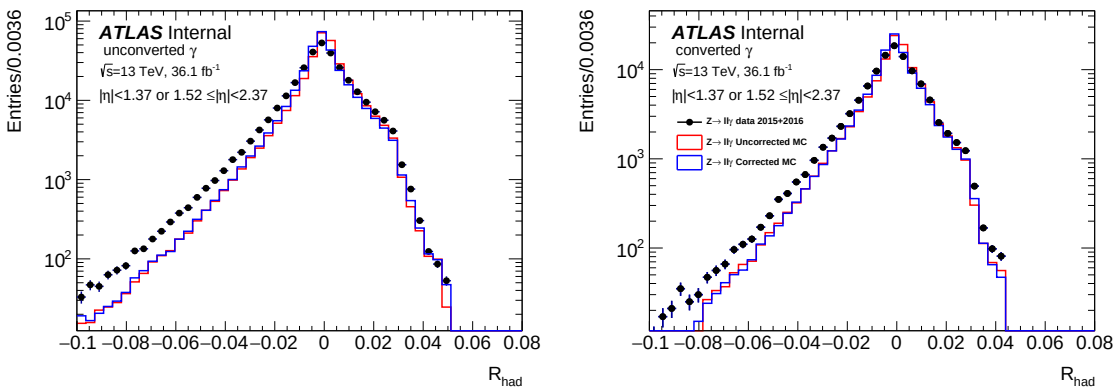

(a) Unconverted R_{had} (b) Converted R_{had}

Figure B.19: Distributions of R_{had} for (a) unconverted and (b) unconverted photon candidates with $p_{\mathrm{T}} \in [10, 50]$ GeV and $|\eta| < 2.37$ (excluding $1.37 \leq |\eta| < 1.52$) selected from $\ell^+\ell^-\gamma$ events. The data are compared with simulated $Z \to \ell\ell\gamma$ events where the red solid histogram corresponds to the uncorrected Monte Carlo, and the solid blue line is the corrected simulation via the fudge factor.

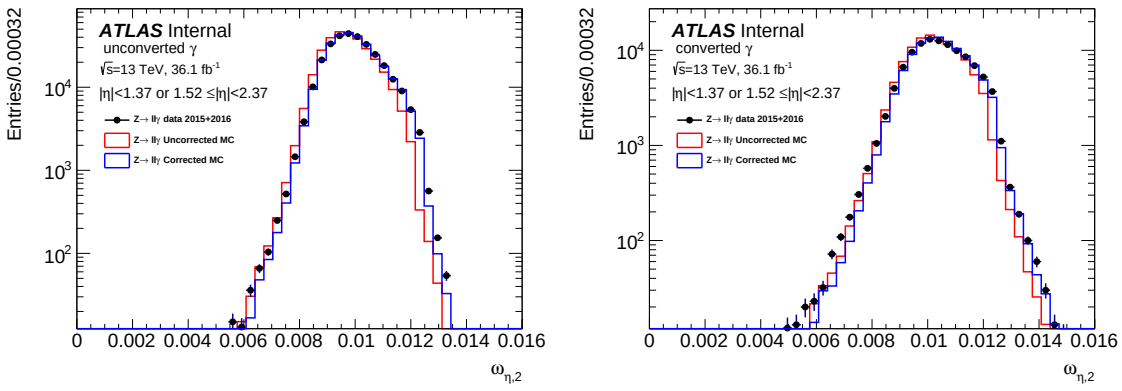

(a) Unconverted w_{η_2} (b) Converted w_{η_2}

Figure B.20: Distributions of w_{η_2} for (a) unconverted and (b) unconverted photon candidates with $p_{\mathrm{T}} \in [10, 50]$ GeV and $|\eta| < 2.37$ (excluding $1.37 \leq |\eta| < 1.52$) selected from $\ell^+\ell^-\gamma$ events. The data are compared with simulated $Z \to \ell\ell\gamma$ events where the red solid histogram corresponds to the uncorrected Monte Carlo, and the solid blue line is the corrected simulation via the fudge factor.

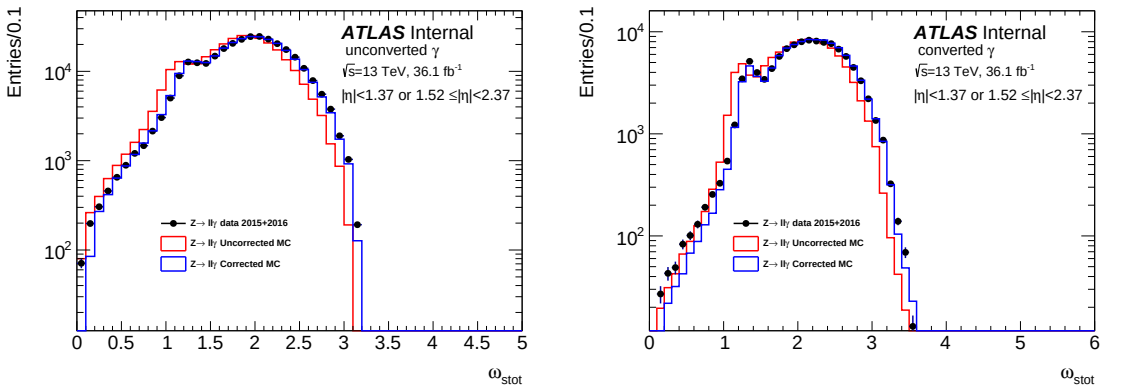

(a) Unconverted $w_{s\,\mathrm{tot}}$ (b) Converted $w_{s\,\mathrm{tot}}$

Figure B.21: Distributions of $w_{s\,\mathrm{tot}}$ for (a) unconverted and (b) unconverted photon candidates with $p_{\mathrm{T}} \in [10, 50]$ GeV and $|\eta| < 2.37$ (excluding $1.37 \leq |\eta| < 1.52$) selected from $\ell^+\ell^-\gamma$ events. The data are compared with simulated $Z \to \ell\ell\gamma$ events where the red solid histogram corresponds to the uncorrected Monte Carlo, and the solid blue line is the corrected simulation via the fudge factor.

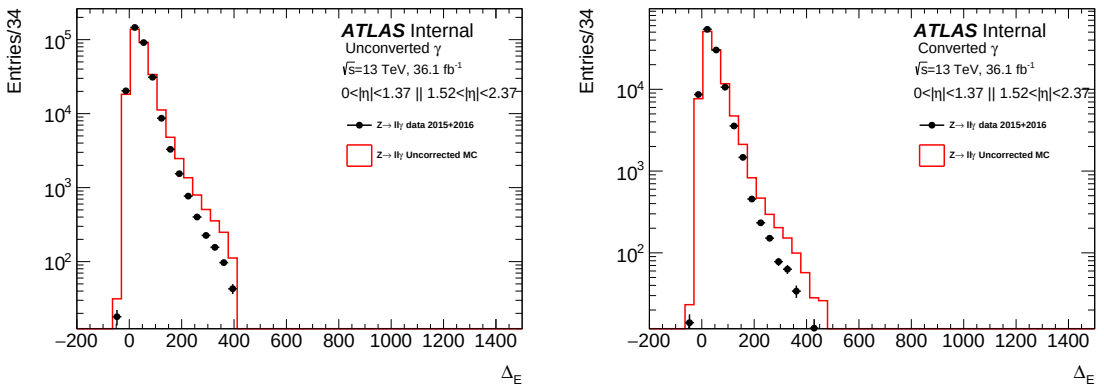

(a) Unconverted ΔE_s (b) Converted ΔE_s

Figure B.22: Distributions of ΔE_s for (a) unconverted and (b) unconverted photon candidates with $p_{\mathrm{T}} \in [10, 50]$ GeV and $|\eta| < 2.37$ (excluding $1.37 \leq |\eta| < 1.52$) selected from $\ell^+\ell^-\gamma$ events. The data are compared with simulated $Z \to \ell\ell\gamma$ events where the red solid histogram corresponds to the uncorrected Monte Carlo. This variable was not corrected due to reasons outlined in Section 5.1.3.2.

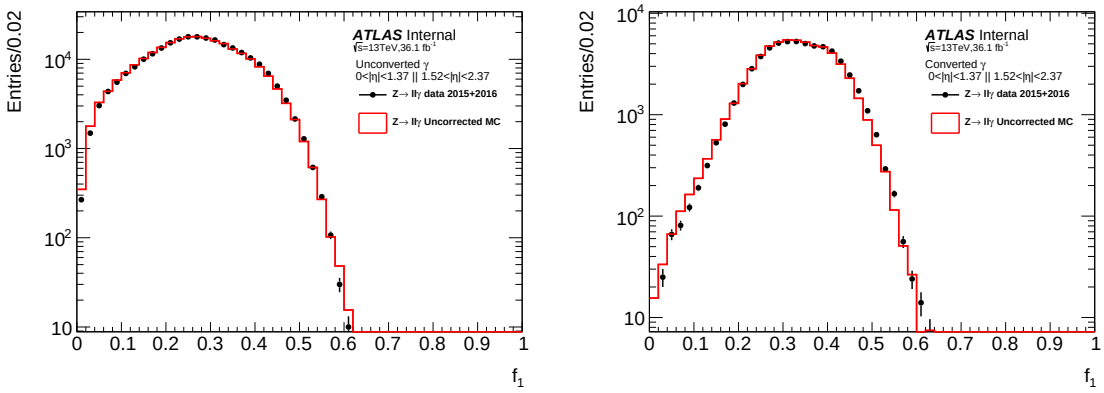

(a) Unconverted f_1 (b) Converted f_1

Figure B.23: Distributions of f_1 for (a) unconverted and (b) unconverted photon candidates with $p_{\mathrm{T}} \in [10, 50]$ GeV and $|\eta| < 2.37$ (excluding $1.37 \leq |\eta| < 1.52$) selected from $\ell^+\ell^-\gamma$ events. The data are compared with simulated $Z \to \ell\ell\gamma$ events where the red solid histogram corresponds to the uncorrected Monte Carlo. This variable was not corrected due to reasons outlined in Section 5.1.3.2.

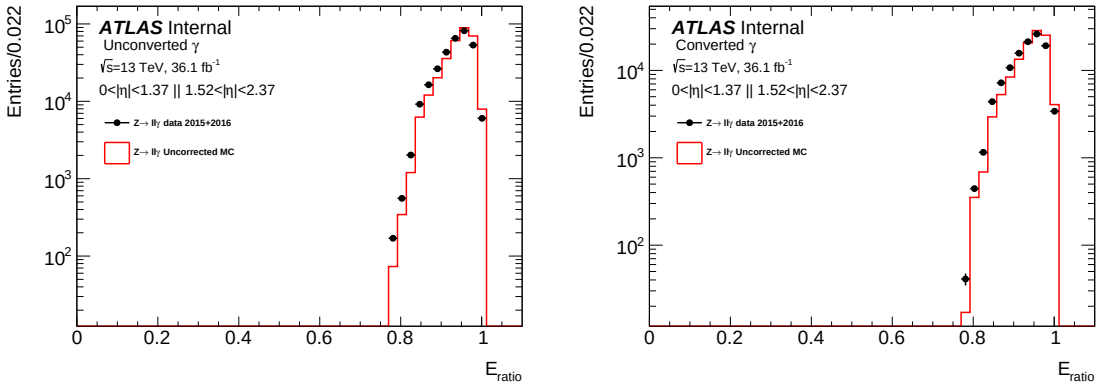

(a) Unconverted E_{ratio} (b) Converted E_{ratio}

Figure B.24: Distributions of E_{ratio} for (a) unconverted and (b) unconverted photon candidates with $p_{\text{T}} \in [10, 50]$ GeV and $|\eta| < 2.37$ (excluding $1.37 \leq |\eta| < 1.52$) selected from $\ell^+\ell^-\gamma$ events. The data are compared with simulated $Z \to \ell\ell\gamma$ events where the red solid histogram corresponds to the uncorrected Monte Carlo. This variable was not corrected due to reasons outlined in Section 5.1.3.2.

Appendix C

Extra Differential and Fiducial Cross Sections Material

This appendix will display the other differential spectra measured in the Higgs to diphoton differential and fiducial analysis.

C.1 2015–2016 Analysis

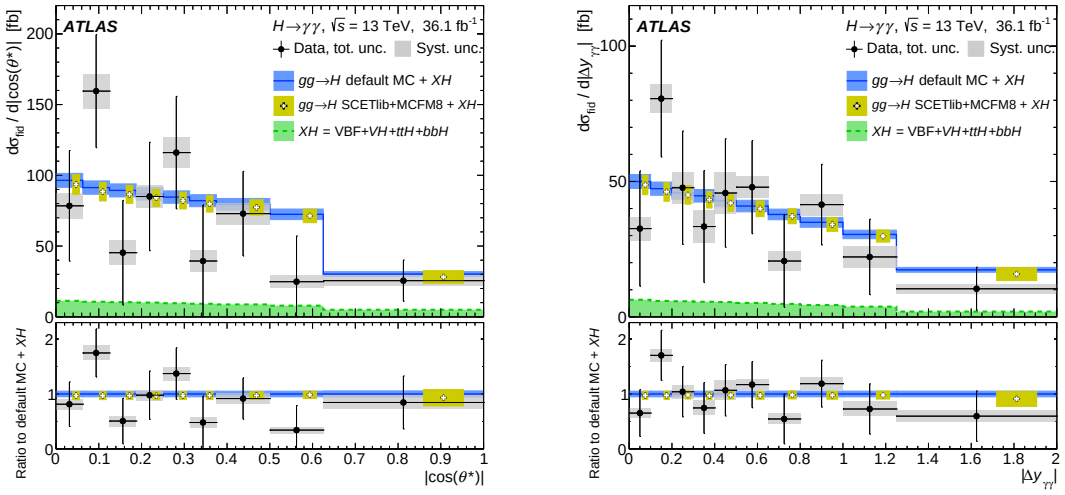

(a) $|\cos\theta^*|$ (b) $|\Delta y_{\gamma\gamma}|$

Figure C.1: Measured differential spectra for (a) $|\cos\theta^*|$ and (b) $|\Delta y_{\gamma\gamma}|$ compared with different theoretical predictions using the 36.1 fb^{-1}dataset collected in 2015–2016. The data are shown as filled black circles. The vertical error bar on each data point represents the total uncertainty in the measured cross section and the shaded gray band is the systematic component. The small contribution from VBF $+VH+t\bar{t}H+b\bar{b}H$ is also shown as a (green) histogram and denoted as XH.

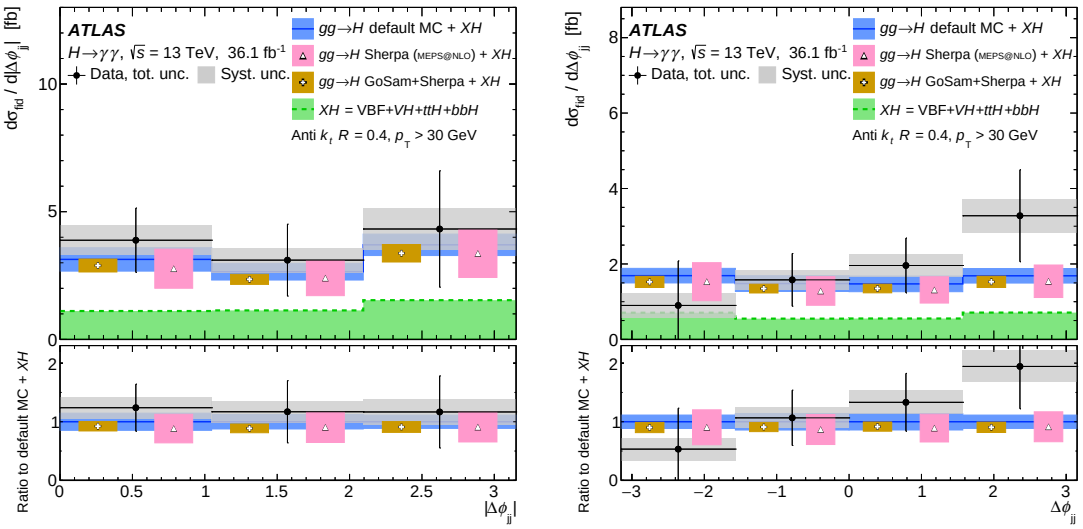

(a) $|\Delta\phi_{jj}|$ (b) $\Delta\phi_{jj,\text{signed}}$

Figure C.2: Measured differential spectra for (a) $|\Delta\phi_{jj}|$ and (b) $\Delta\phi_{jj,\text{signed}}$ compared with different theoretical predictions using the 36.1 fb^{-1}dataset collected in 2015–2016. The components of the plots are described in Figure C.1.

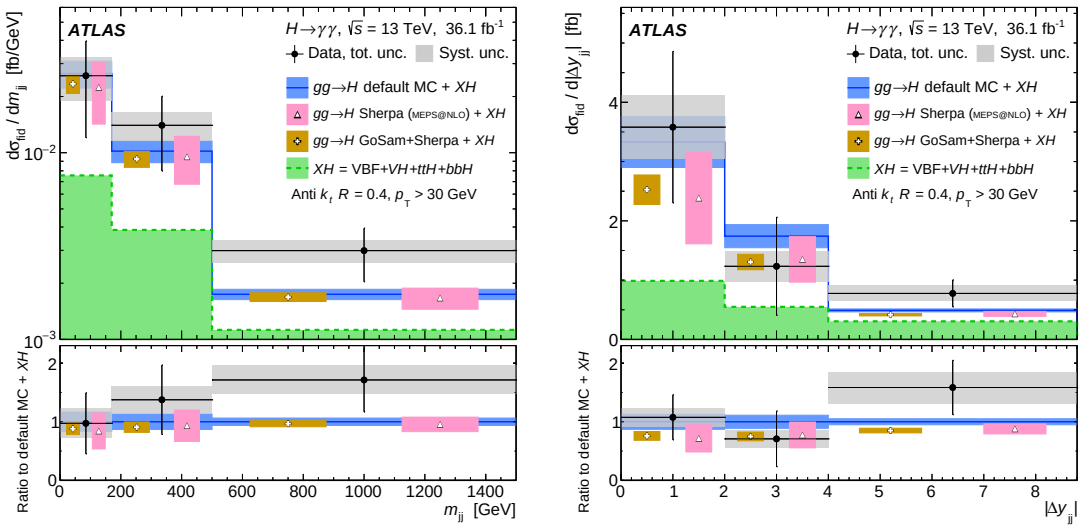

(a) m_{jj} (b) $|\Delta y_{jj}|$

Figure C.3: Measured differential spectra for (a) m_{jj} and (b) $|\Delta y_{jj}|$ compared with different theoretical predictions using the 36.1 fb^{-1}dataset collected in 2015–2016. The components of the plots are described in Figure C.1.

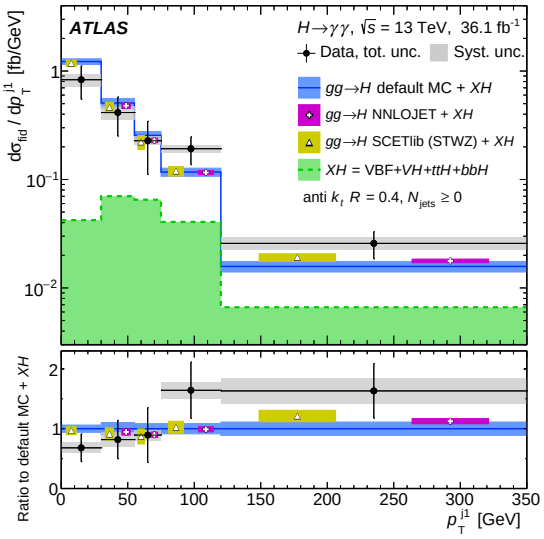

(a) $p_{\mathrm{T}}^{j_1}$

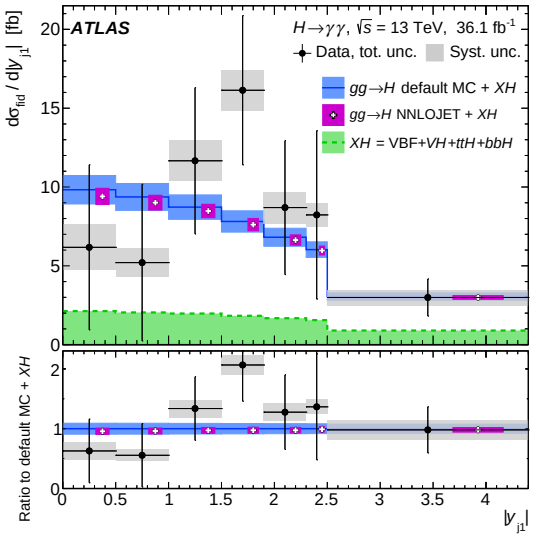

(b) $|y_{j_1}|$

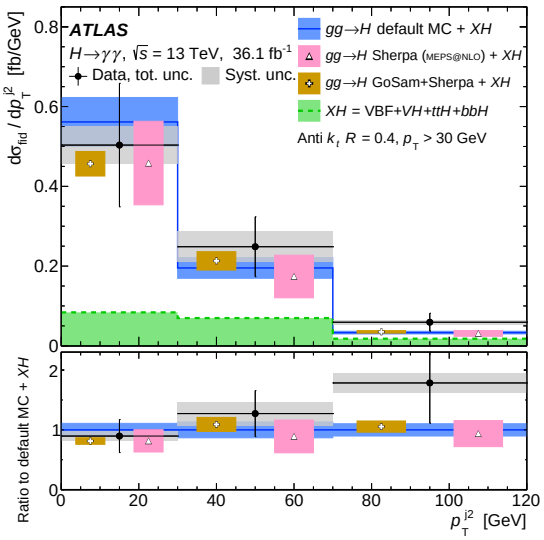

(c) $p_{\mathrm{T}}^{j_2}$

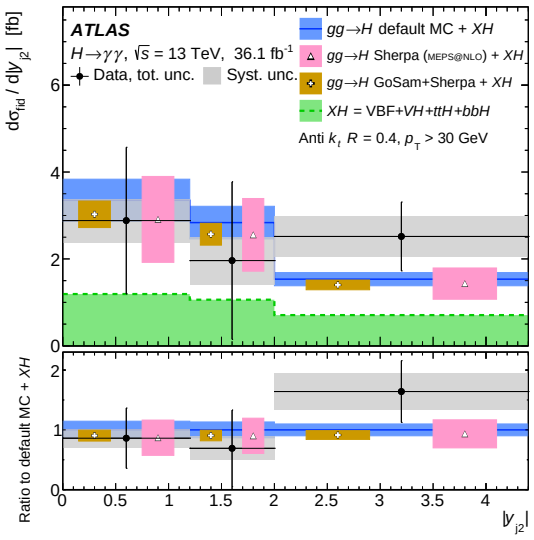

(d) $|y_{j_2}|$

Figure C.4: Measured differential spectra for (a) $p_{\mathrm{T}}^{j_1}$, (b) $|y_{j_1}|$, (c) $p_{\mathrm{T}}^{j_2}$ and (d) $|y_{j_2}|$ compared with different theoretical predictions using the 36.1 fb^{-1}dataset collected in 2015–2016. The components of the plots are described in Figure C.1.

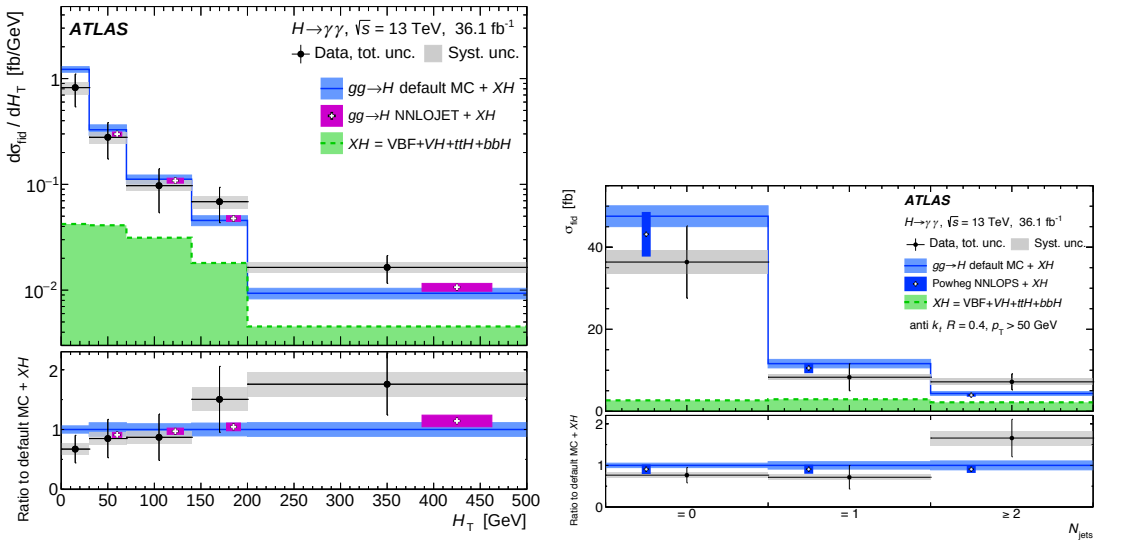

(a) H_T (b) $N_{\text{jets}}^{\geq 50\text{ GeV}}$

Figure C.5: Measured differential spectra for (a) H_T and (b) $N_{\text{jets}}^{\geq 50\text{ GeV}}$ compared with different theoretical predictions using the 36.1 fb^{-1}dataset collected in 2015–2016. The components of the plots are described in Figure C.1.

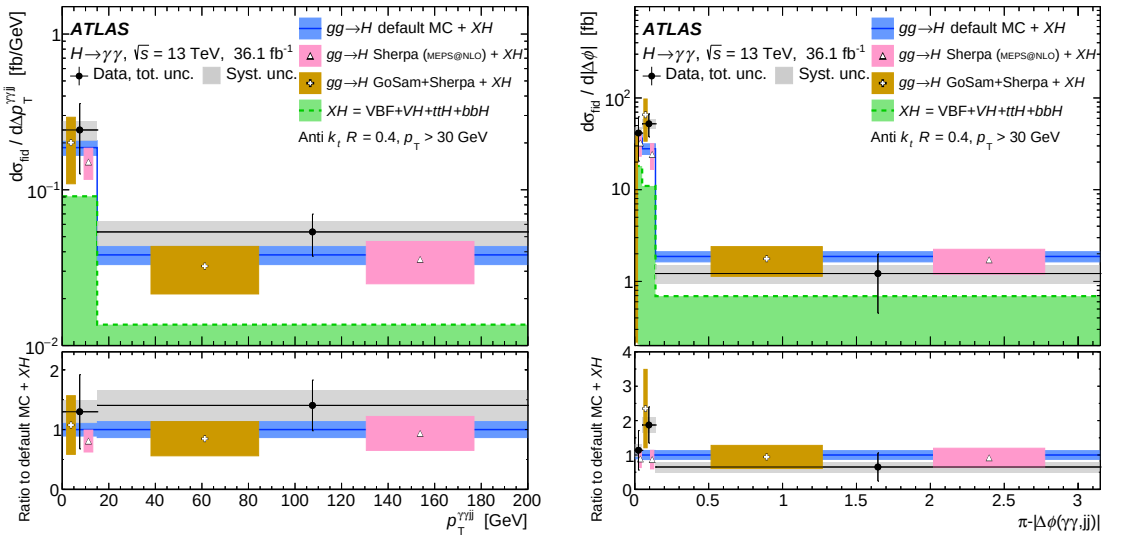

(a) $p_{\mathrm{T},\gamma\gamma jj}$ (b) $|\Delta\phi_{\gamma\gamma,jj}|$

Figure C.6: Measured differential spectra for (a) $p_{\mathrm{T},\gamma\gamma jj}$ and (b) $|\Delta\phi_{\gamma\gamma,jj}|$ compared with different theoretical predictions using the 36.1 fb^{-1}dataset collected in 2015–2016. The components of the plots are described in Figure C.1.

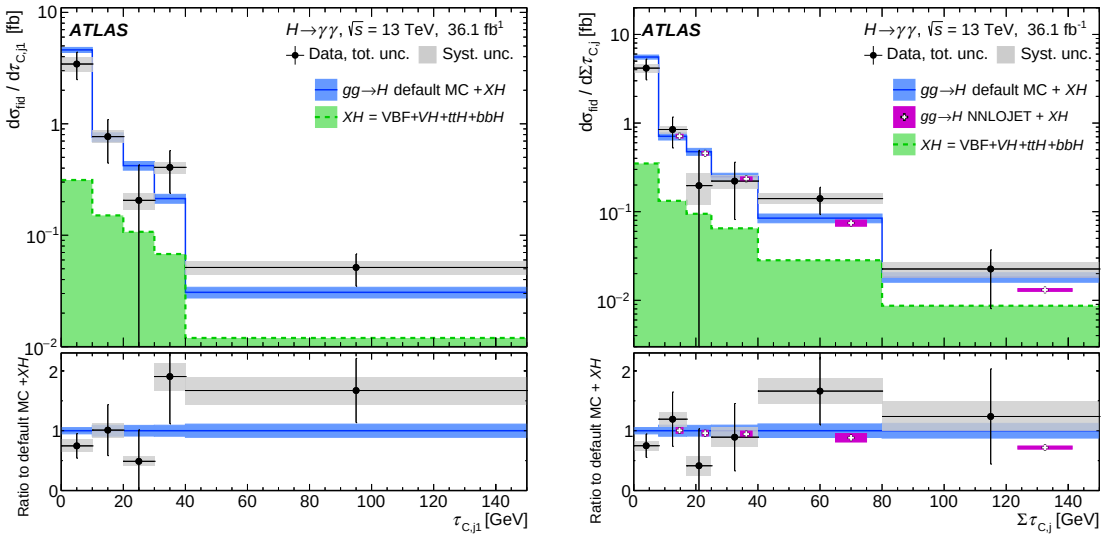

(a) $\tau_{C,j1}$ (b) $\sum\tau_{C,j}$

Figure C.7: Measured differential spectra for (a) $\tau_{C,j1}$ and (b) $\sum\tau_{C,j}$ compared with different theoretical predictions using the 36.1 fb^{-1}dataset collected in 2015–2016. The components of the plots are described in Figure C.1.

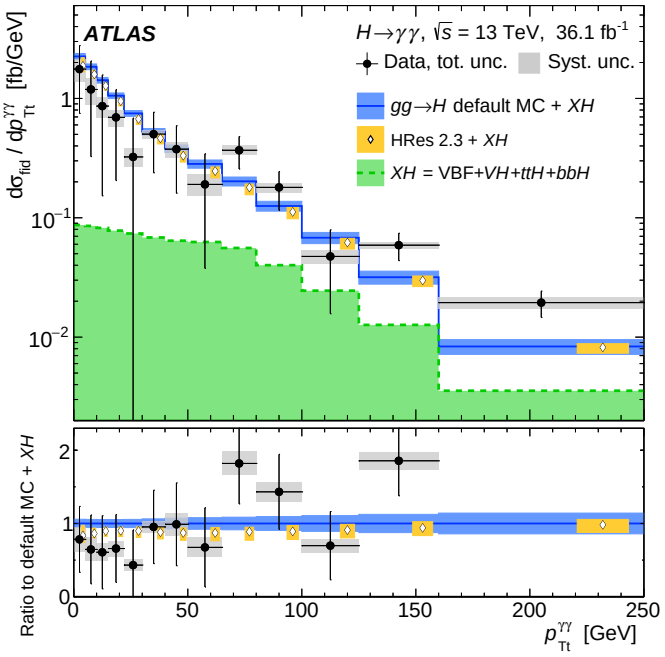

Figure C.8: Measured differential spectra for $p_{\mathrm{Tt}}^{\gamma\gamma}$ compared with different theoretical predictions using the 36.1 fb^{-1}dataset collected in 2015–2016. The components of the plot are described in Figure C.1.

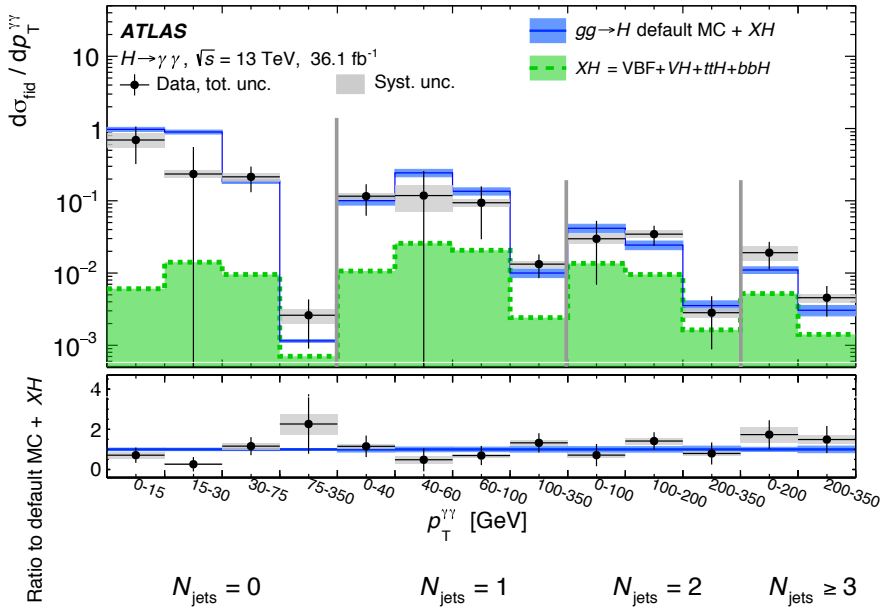

Figure C.9: The $pp \to H \to \gamma\gamma$ double-differential cross section as a function of $p_{\mathrm{T}}^{\gamma\gamma}$ and $N_{\mathrm{jets}}^{\geq 30\ \mathrm{GeV}}$ where the $p_{\mathrm{T}}^{\gamma\gamma}$ spectrum is measured for different jet multiplicities. The components of the plot are described in Figure C.1.

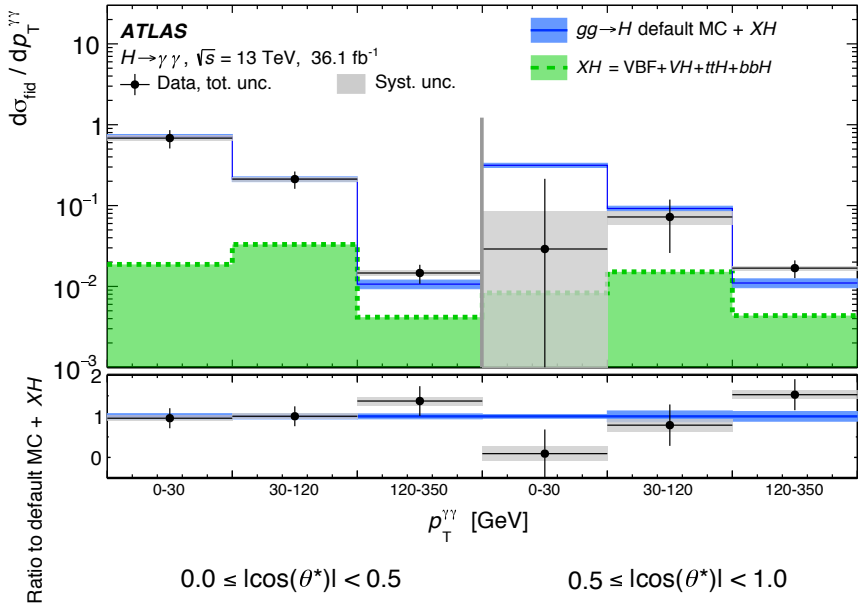

Figure C.10: The $pp \to H \to \gamma\gamma$ double-differential cross section as a function of $p_{\mathrm{T}}^{\gamma\gamma}$ and $|\cos\theta^*|$, where the $p_{\mathrm{T}}^{\gamma\gamma}$ spectrum is measured for $||\cos\theta^*|| < 0.5$ and $||\cos\theta^*|| > 0.5$. The components of the plot are described in Figure C.1.

C.2 2017 Update

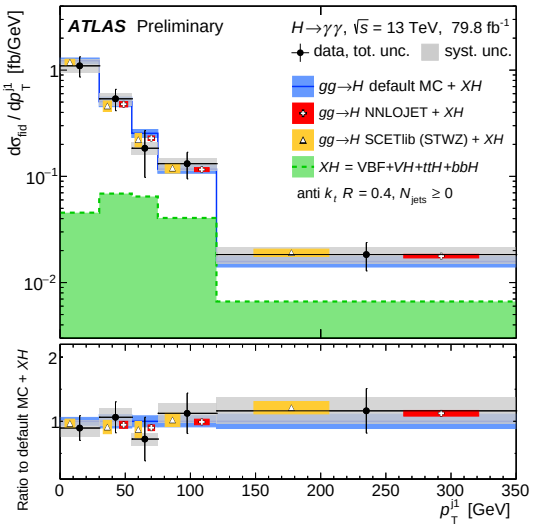

Figure C.11: Measured differential spectra for $p_{\mathrm{T}}^{j_1}$, compared with different theoretical predictions using the 79.8 fb^{-1}dataset collected in 2015–2017. The components of the plot are described in Figure C.1.

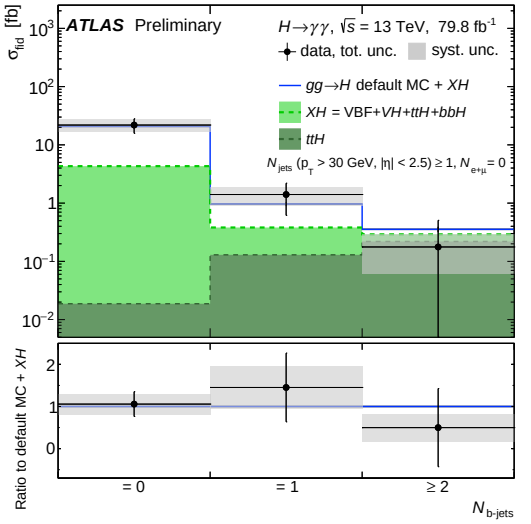

Figure C.12: Measured differential spectra for $N_{\text{b-jets}}^{\geq 30\text{ GeV}}$, compared with different theoretical predictions using the 79.8 fb^{-1}dataset collected in 2015–2017. Events are also required to have no electrons or muons. The components of the plot are described in Figure C.1, but with the $t\bar{t}H$ component added as the dark green histogram. Additionally, the theoretical uncertainty of the $N_{\text{b-jets}}^{\geq 30\text{ GeV}}$ prediction is not well understood, and is therefore omitted.

Appendix D

Extra Meta Thesis Material

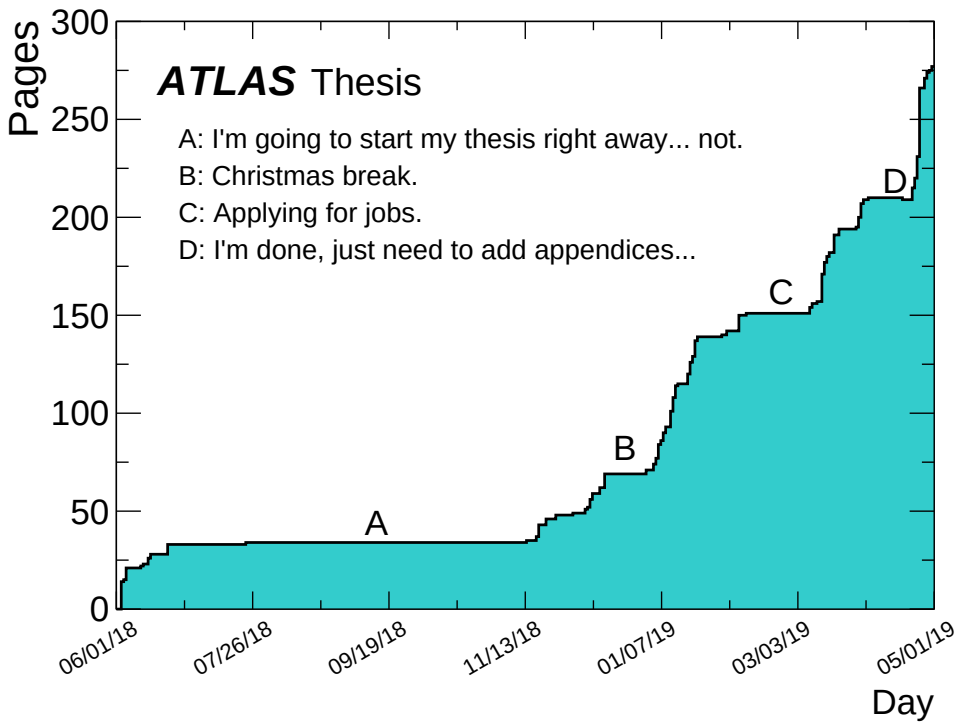

Figure D.1: "Luminosity" plot for this dissertation. This shows the number of pages in the dissertation as a function of date. Notable periods of stagnation are explained.

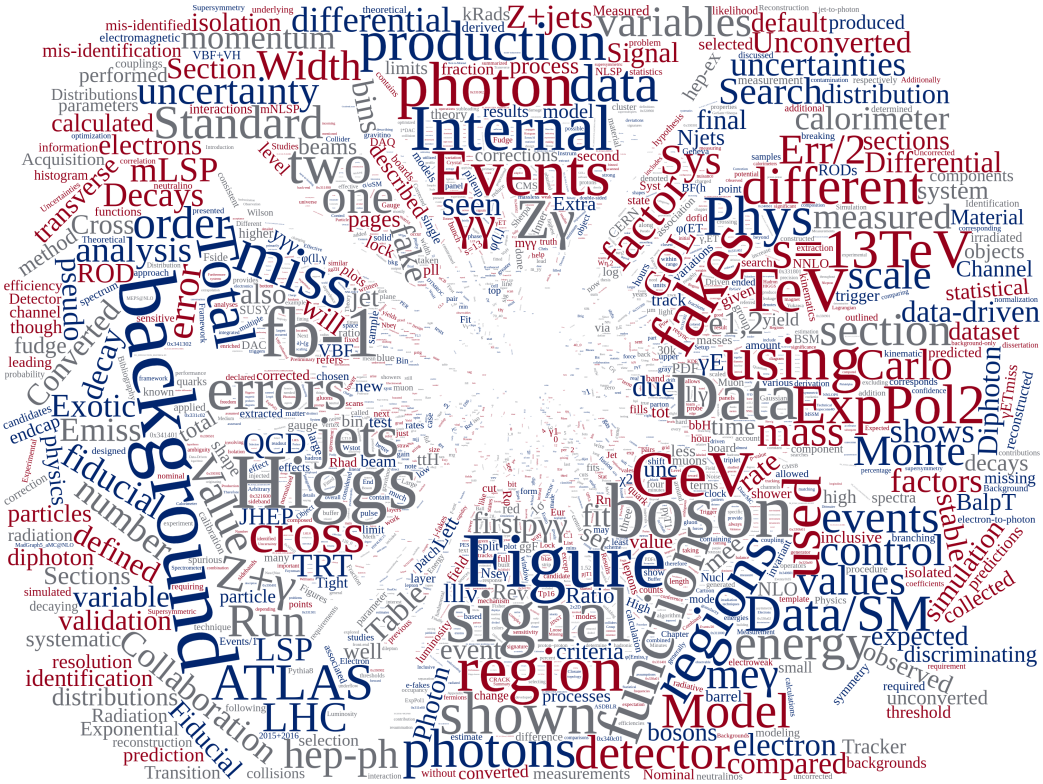

Figure D.2: Word cloud for this dissertation. The larger the word, the more frequent it was in this document. Words from figures are also included, hence the large "Internal" word. The negative space is in the shape of a simulated ATLAS collision event from Ref. [279].

Bibliography

[1] ATLAS Collaboration, *Search for new phenomena in high-mass diphoton final states using 37 fb^{-1} of proton–proton collisions collected at $\sqrt{s} = 13$ TeV with the ATLAS detector*, Phys. Lett. B **775** (2017) 105, arXiv:1707.04147 [hep-ex]. Cited on page xxvi.

[2] ATLAS Collaboration, *Photon identification in 2015 ATLAS data*, ATL-PHYS-PUB-2016-014, 2016, https://cds.cern.ch/record/2203125. Cited on pages xxvi and 52.

[3] ATLAS Collaboration, *Measurement of fiducial, differential and production cross sections in the $H \to \gamma\gamma$ decay channel with 13.3 fb^{-1} of 13 TeV proton–proton collision data with the ATLAS detector*, ATLAS-CONF-2016-067, 2016, https://cds.cern.ch/record/2206210. Cited on pages xxvi and 67.

[4] ATLAS Collaboration, *Measurements of Higgs boson properties in the diphoton decay channel with 36.1 fb^{-1} pp collision data at the center-of-mass energy of 13 TeV with the ATLAS detector*, ATLAS-CONF-2017-045, 2017, https://cds.cern.ch/record/2273852. Cited on pages xxvi and 67.

[5] ATLAS Collaboration, *Search for exotic decays of the Higgs boson to at least one photon and missing transverse momentum using 79.8 fb^{-1} of proton–proton collisions collected at $\sqrt{s} = 13$ TeV with the ATLAS detector*, ATLAS-CONF-2018-019, 2018, http://cds.cern.ch/record/2621481. Cited on pages xxvii and 114.

[6] ATLAS Collaboration, *Measurements of Higgs boson properties in the diphoton decay channel with 36 fb^{-1} of pp collision data at $\sqrt{s} = 13$ TeV with the ATLAS detector*, Phys. Rev. D**98** 87, arXiv:1802.04146 [hep-ex]. Cited on pages xxvii, 67, and 74.

[7] ATLAS Collaboration, *Measurements of Higgs boson properties in the diphoton decay channel using 80 fb^{-1} of pp collision data at $\sqrt{s} = 13$ TeV with the ATLAS detector*, ATLAS-CONF-2018-028, 2018, http://cds.cern.ch/record/2628771. Cited on pages xxvii and 67.

[8] ATLAS Collaboration, *Measurement of the photon identification efficiencies with the ATLAS detector using LHC Run 2 data collected in 2015 and 2016*, Eur. Phys. J. **C79** (2019) 205, arXiv:1810.05087 [hep-ex]. Cited on pages xxvii and 52.

[9] P. Langacker, *The Standard Model and Beyond; 2nd ed.* High energy physics, cosmology and gravitation. CRC Press, Jul, 2017. https://cds.cern.ch/record/2256595. Cited on page 3.

[10] M. E. Peskin and D. V. Schroeder, *An Introduction to quantum field theory*. Addison-Wesley, Reading, USA, 1995. http://www.slac.stanford.edu/~mpeskin/QFT.html. Cited on page 3.

[11] C.-N. Yang and R. L. Mills, *Conservation of Isotopic Spin and Isotopic Gauge Invariance*, Phys. Rev. **96** (1954) 191–195. Cited on page 3.

[12] Latham Boyle, *File:Standard Model Of Particle Physics–Most Complete Diagram.png*, 2015. https://upload.wikimedia.org/wikipedia/commons/2/2f/Standard_Model_Of_Particle_Physics--Most_Complete_Diagram.png. [Online; accessed 2-April-2019]. Cited on page 4.

[13] A. Salam, *Weak and Electromagnetic Interactions*, Conf. Proc. **C680519** (1968) 367–377. Cited on page 4.

[14] S. Weinberg, *A Model of Leptons*, Phys. Rev. Lett. **19** (1967) 1264–1266. Cited on page 4.

[15] S. L. Glashow, *Partial Symmetries of Weak Interactions*, Nucl. Phys. **22** (1961) 579–588. Cited on page 4.

[16] M. Y. Han and Y. Nambu, *Three Triplet Model with Double SU(3) Symmetry*, Phys. Rev. **139** (1965) B1006–B1010. Cited on page 5.

[17] M. Gell-Mann, *A Schematic Model of Baryons and Mesons*, Phys. Lett. **8** (1964) 214–215. Cited on page 5.

[18] G. Zweig, *An SU(3) model for strong interaction symmetry and its breaking. Version 2*, pp. , 22–101. 1964. Cited on page 5.

[19] D. J. Gross and F. Wilczek, *Asymptotically Free Gauge Theories - I*, Phys. Rev. **D8** (1973) 3633–3652. Cited on page 5.

[20] D. J. Gross and F. Wilczek, *Asymptotically Free Gauge Theories - II*, Phys. Rev. **D9** (1974) 980–993. Cited on page 5.

[21] D. J. Gross and F. Wilczek, *Ultraviolet Behavior of Nonabelian Gauge Theories*, Phys. Rev. Lett. **30** (1973) 1343–1346. Cited on page 5.

[22] P. W. Higgs, *Broken symmetries, massless particles and gauge fields*, Phys. Lett. **12** (1964) 132–133. Cited on page 5.

[23] P. W. Higgs, *Broken Symmetries and the Masses of Gauge Bosons*, Phys. Rev. Lett. **13** (1964) 508–509. Cited on page 5.

[24] F. Englert and R. Brout, *Broken Symmetry and the Mass of Gauge Vector Mesons*, Phys. Rev. Lett. **13** (1964) 321–323. Cited on page 5.

[25] R. P. Feynman, *Mathematical formulation of the quantum theory of electromagnetic interaction*, Phys. Rev. **80** (1950) 440–457. Cited on page 7.

[26] H. Yukawa, *On the Interaction of Elementary Particles I*, Proc. Phys. Math. Soc. Jap. **17** (1935) 48–57. Cited on page 7.

[27] ATLAS and CMS Collaborations, *Combined Measurement of the Higgs Boson Mass in pp Collisions at $\sqrt{s} = 7$ and 8 TeV with the ATLAS and CMS Experiments*, Phys. Rev. Lett. **114** (2015) 191803, arXiv:1503.07589 [hep-ex]. Cited on page 8.

[28] UA1 Collaboration, *Experimental Observation of Isolated Large Transverse Energy Electrons with Associated Missing Energy at s**(1/2) = 540-GeV*, Phys. Lett. **B122** (1983) 103–116. Cited on page 8.

[29] UA2 Collaboration, *Observation of Single Isolated Electrons of High Transverse Momentum in Events with Missing Transverse Energy at the CERN anti-p p Collider*, Phys. Lett. **B122** (1983) 476–485. Cited on page 8.

[30] UA1 Collaboration, *Experimental Observation of Lepton Pairs of Invariant Mass Around 95-GeV/c**2 at the CERN SPS Collider*, Phys. Lett. **B126** (1983) 398–410. Cited on page 8.

[31] UA2 Collaboration, *Evidence for Z0 —> e+ e- at the CERN anti-p p Collider*, Phys. Lett. **B129** (1983) 130–140. Cited on page 8.

[32] LHC Higgs Cross Section Working Group (D. de Florian et al.), *Handbook of LHC Higgs Cross Sections: 4. Deciphering the Nature of the Higgs Sector*, 2016, arXiv:1610.07922 [hep-ph]. Cited on pages 8, 72, 116, 160, and 169.

[33] S. e. a. Perlmutter, *Measurements of Omega and Lambda from 42 high redshift supernovae,*. Cited on page 14.

[34] A. G. e. a. Riess, *Observational evidence from supernovae for an accelerating universe and a cosmological constant,*. Cited on page 14.

[35] D. e. a. Clowe, *A direct empirical proof of the existence of dark matter*, Astrophys. J. **648** (2006) L109–L113, arXiv:astro-ph/0608407 [astro-ph]. Cited on page 14.

[36] V. C. Rubin and W. K. Ford, Jr., *Rotation of the Andromeda Nebula from a Spectroscopic Survey of Emission Regions*, Astrophys. J. **159** (1970) 379–403. Cited on page 14.

[37] J. H. Christenson, J. W. Cronin, V. L. Fitch, and R. Turlay, *Evidence for the 2π Decay of the K_2^0 Meson*, Phys. Rev. Lett. **13** (1964) 138–140. Cited on page 14.

[38] KTeV, *Observation of direct CP violation in $K_{S,L} \to \pi\pi$ decays*, Phys. Rev. Lett. **83** (1999) 22–27, arXiv:hep-ex/9905060 [hep-ex]. Cited on page 14.

[39] V. Fanti et al., *A New measurement of direct CP violation in two pion decays of the neutral kaon*, Phys. Lett. **B465** (1999) 335–348, arXiv:hep-ex/9909022 [hep-ex]. Cited on page 14.

[40] BaBar, *Measurement of CP violating asymmetries in B^0 decays to CP eigenstates*, Phys. Rev. Lett. **86** (2001) 2515–2522, arXiv:hep-ex/0102030 [hep-ex]. Cited on page 14.

[41] Belle, *Observation of large CP violation in the neutral B meson system*, Phys. Rev. Lett. **87** (2001) 091802, arXiv:hep-ex/0107061 [hep-ex]. Cited on page 14.

[42] LHCb, *Measurement of CP asymmetry in $D^0 \to K^-K^+$ and $D^0 \to \pi^-\pi^+$ decays*, JHEP **07** (2014) 041, arXiv:1405.2797 [hep-ex]. Cited on page 14.

[43] LHCb, *Observation of CP violation in charm decays*, arXiv:1903.08726 [hep-ex]. Cited on page 14.

[44] Yu. A. Golfand and E. P. Likhtman, *Extension of the Algebra of Poincare Group Generators and Violation of p Invariance*, JETP Lett. **13** (1971) 323–326. Cited on page 14.

[45] D. V. Volkov and V. P. Akulov, *Is the Neutrino a Goldstone Particle?*, Phys. Lett. **46B** (1973) 109–110. Cited on page 14.

[46] J. Wess and B. Zumino, *Supergauge Transformations in Four-Dimensions*, Nucl. Phys. **B70** (1974) 39–50. Cited on page 14.

[47] J. Wess and B. Zumino, *Supergauge Invariant Extension of Quantum Electrodynamics*, Nucl. Phys. **B78** (1974) 1. Cited on page 14.

[48] S. Ferrara and B. Zumino, *Supergauge Invariant Yang-Mills Theories*, Nucl. Phys. **B79** (1974) 413. Cited on page 14.

[49] A. Salam and J. A. Strathdee, *Supersymmetry and Nonabelian Gauges*, Phys. Lett. **51B** (1974) 353–355. Cited on page 14.

[50] P. D. Group, *Review of Particle Physics*, Chin. Phys. **C40** (2016) 100001. Cited on pages 15 and 160.

[51] S. P. Martin, *A Supersymmetry primer*, arXiv:hep-ph/9709356 [hep-ph]. Cited on page 15.

[52] M. Drees, *An Introduction to supersymmetry*, in *Current topics in physics. Proceedings, Inauguration Conference of the Asia-Pacific Center for Theoretical Physics (APCTP), Seoul, Korea, June 4-10, 1996. Vol. 1, 2.* 1996. arXiv:hep-ph/9611409 [hep-ph]. Cited on page 15.

[53] A. Bilal, *Introduction to supersymmetry*, arXiv:hep-th/0101055 [hep-th]. Cited on page 15.

[54] D. e. a. Curtin, *Exotic decays of the 125 GeV Higgs boson*, Phys. Rev. **D90** (2014) 075004, arXiv:1312.4992 [hep-ph]. Cited on pages 16 and 113.

[55] M. Dine and W. Fischler, *A Phenomenological Model of Particle Physics Based on Supersymmetry*, Phys. Lett. **110B** (1982) 227–231. Cited on pages 16 and 113.

[56] L. Alvarez-Gaume, M. Claudson, and M. B. Wise, *Low-Energy Supersymmetry*, Nucl. Phys. **B207** (1982) 96. Cited on pages 16 and 113.

[57] C. R. Nappi and B. A. Ovrut, *Supersymmetric Extension of the SU(3) x SU(2) x U(1) Model*, Phys. Lett. **113B** (1982) 175–179. Cited on pages 16 and 113.

[58] M. Dine and A. E. Nelson, *Dynamical supersymmetry breaking at low-energies*, Phys. Rev. **D48** (1993) 1277–1287, arXiv:hep-ph/9303230 [hep-ph]. Cited on pages 16 and 113.

[59] M. Dine, A. E. Nelson, Y. Nir, and Y. Shirman, *New tools for low-energy dynamical supersymmetry breaking*, Phys. Rev. **D53** (1996) 2658–2669, arXiv:hep-ph/9507378 [hep-ph]. Cited on pages 16 and 113.

[60] M. Dine, A. E. Nelson, and Y. Shirman, *Low-energy dynamical supersymmetry breaking simplified*, Phys. Rev. **D51** (1995) 1362–1370, arXiv:hep-ph/9408384 [hep-ph]. Cited on page 16.

[61] G. F. Giudice and R. Rattazzi, *Theories with gauge mediated supersymmetry breaking*, Phys. Rept. **322** (1999) 419–499, arXiv:hep-ph/9801271 [hep-ph]. Cited on page 16.

[62] C. F. Kolda, *Gauge mediated supersymmetry breaking: Introduction, review and update*, Nucl. Phys. Proc. Suppl. **62** (1998) 266–275, arXiv:hep-ph/9707450 [hep-ph]. Cited on page 16.

[63] N. Craig, D. Green, and A. Katz, *(De)Constructing a Natural and Flavorful Supersymmetric Standard Model*, JHEP **07** (2011) 045, arXiv:1103.3708 [hep-ph]. Cited on pages 16 and 113.

[64] R. Auzzi, A. Giveon, and S. B. Gudnason, *Flavor of quiver-like realizations of effective supersymmetry*, JHEP **02** (2012) 069, arXiv:1112.6261 [hep-ph]. Cited on pages 16 and 113.

[65] C. Csaki, L. Randall, and J. Terning, *Light Stops from Seiberg Duality*, Phys. Rev. **D86** (2012) 075009, arXiv:1201.1293 [hep-ph]. Cited on pages 16 and 113.

[66] N. Craig, S. Dimopoulos, and T. Gherghetta, *Split families unified*, JHEP **04** (2012) 116, arXiv:1203.0572 [hep-ph]. Cited on pages 16 and 113.

[67] G. Larsen, Y. Nomura, and H. L. L. Roberts, *Supersymmetry with Light Stops*, JHEP **06** (2012) 032, arXiv:1202.6339 [hep-ph]. Cited on pages 16 and 113.

[68] R. Casalbuoni, S. De Curtis, D. Dominici, F. Feruglio, and R. Gatto, *A Gravitino - Goldstino High-energy Equivalence Theorem*, Phys. Lett. **B215** (1988) 313–316. Cited on page 16.

[69] P. Fayet, *Mixing Between Gravitational and Weak Interactions Through the Massive Gravitino*, Phys. Lett. **70B** (1977) 461. Cited on page 16.

[70] OPAL Collaboration, *Search for chargino and neutralino production at $\sqrt{s}$ = 192-GeV to 209 GeV at LEP*, Eur. Phys. J. **C35** (2004) 1–20, arXiv:hep-ex/0401026 [hep-ex]. Cited on page 17.

[71] DELPHI Collaboration, *Searches for supersymmetric particles in e+ e- collisions up to 208-GeV and interpretation of the results within the MSSM*, Eur. Phys. J. **C31** (2003) 421–479, arXiv:hep-ex/0311019 [hep-ex]. Cited on page 17.

[72] DELPHI Collaboration, *Photon events with missing energy in e+ e- collisions at s**(1/2) = 130-GeV to 209-GeV*, Eur. Phys. J. **C38** (2005) 395–411, arXiv:hep-ex/0406019 [hep-ex]. Cited on page 17.

[73] OPAL Collaboration, *A Measurement of photon radiation in lepton pair events from Z0 decays*, Phys. Lett. **B273** (1991) 338–354. Cited on page 17.

[74] J. F. Gunion and H. E. Haber, *Higgs Bosons in Supersymmetric Models. 1.*, Nucl. Phys. **B272** (1986) 1. Cited on page 17.

[75] H. E. Haber and G. L. Kane, *The Search for Supersymmetry: Probing Physics Beyond the Standard Model*, Phys. Rept. **117** (1985) 75–263. Cited on page 17.

[76] C. Petersson, A. Romagnoni, and R. Torre, *Higgs Decay with Monophoton + MET Signature from Low Scale Supersymmetry Breaking*, JHEP **10** (2012) 016, arXiv:1203.4563 [hep-ph]. Cited on pages 18 and 113.

[77] A. Djouadi and M. Drees, *Higgs boson decays into light gravitinos*, Phys. Lett. **B407** (1997) 243–249, arXiv:hep-ph/9703452 [hep-ph]. Cited on page 18.

[78] J. D. Mason, D. E. Morrissey, and D. Poland, *Higgs Boson Decays to Neutralinos in Low-Scale Gauge Mediation*, Phys. Rev. D **80** (2009) 115015, arXiv:0909.3523 [hep-ph]. Cited on pages 18 and 114.

[79] U. Ellwanger, C. Hugonie, and A. M. Teixeira, *The Next-to-Minimal Supersymmetric Standard Model*, Phys. Rept. **496** (2010) 1–77, arXiv:0910.1785 [hep-ph]. Cited on page 18.

[80] P. Draper, T. Liu, C. E. M. Wagner, L.-T. Wang, and H. Zhang, *Dark Light Higgs*, Phys. Rev. Lett. **106** (2011) 121805, arXiv:1009.3963 [hep-ph]. Cited on page 18.

[81] J. Kozaczuk and S. Profumo, *Light NMSSM neutralino dark matter in the wake of CDMS II and a 126 GeV Higgs boson*, Phys. Rev. **D89** (2014) 095012, arXiv:1308.5705 [hep-ph]. Cited on page 18.

[82] J.-J. Cao, K.-i. Hikasa, W. Wang, J. M. Yang, K.-i. Hikasa, W.-Y. Wang, and J. M. Yang, *Light dark matter in NMSSM and implication on Higgs phenomenology*, Phys. Lett. **B703** (2011) 292–297, arXiv:1104.1754 [hep-ph]. Cited on page 18.

[83] J. Huang, T. Liu, L.-T. Wang, and F. Yu, *Supersymmetric Exotic Decays of the 125 GeV Higgs Boson*, Phys. Rev. Lett. **112** (2014) 221803, arXiv:1309.6633 [hep-ph]. Cited on pages 18 and 113.

[84] L. R. Evans and P. Bryant, *LHC Machine*, JINST **3** (2008) S08001, https://cds.cern.ch/record/1129806. Cited on page 20.

[85] J. Haffner, *The CERN accelerator complex*, https://cds.cern.ch/record/1621894. Cited on page 21.

[86] ATLAS Collaboration, *The ATLAS experiment at the CERN Large Hadron Collider*, JINST **3** (2008) S08003. Cited on page 20.

[87] CMS Collaboration, *The CMS experiment at the CERN LHC*, JINST **3** (2008) S08004. Cited on page 21.

[88] LHCb Collaboration, *The LHCb Detector at the LHC*, JINST **3** (2008) S08005. Cited on page 21.

[89] ALICE Collaboration, K. Aamodt et al., *The ALICE experiment at the CERN LHC*, JINST **3** (2008) S08002. Cited on page 21.

[90] P. Grafstrom and W. Kozanecki, *Luminosity determination at proton colliders*, Prog. Part. Nucl. Phys. **81** (2015) 97–148. Cited on page 22.

[91] ATLAS Collaboration, *The ATLAS Experiment at the CERN Large Hadron Collider*, JINST **3** (2008) S08003. Cited on page 24.

[92] ATLAS Collaboration,, *ATLAS inner detector: Technical Design Report, Vol. 2*. CERN, Geneva, 1997. https://cds.cern.ch/record/331064. Cited on page 25.

[93] ATLAS Collaboration,, *ATLAS inner detector: Technical Design Report, Vol. 1*. CERN, Geneva, 1997. https://cds.cern.ch/record/331063. Cited on page 25.

[94] ATLAS Collaboration, *The ATLAS Inner Detector commissioning and calibration*, Eur. Phys. J. C **70** (2010) 787, arXiv:1004.5293 [hep-ex]. Cited on page 25.

[95] ATLAS Collaboration, M. e. a. Capeans, *ATLAS Insertable B-Layer Technical Design Report*. CERN, Geneva, 2010. https://cds.cern.ch/record/1291633. Cited on page 25.

[96] G. Aad et al., *ATLAS pixel detector electronics and sensors*, JINST **3** (2008) P07007. Cited on page 25.

[97] ATLAS Collaboration, M. e. a. Alam, *ATLAS pixel detector: Technical design report*. CERN, Geneva, 1998. http://cds.cern.ch/record/381263. Cited on page 25.

[98] A. Ahmad et al., *The Silicon microstrip sensors of the ATLAS semiconductor tracker*, Nucl. Instrum. Meth. **A578** (2007) 98–118. Cited on page 26.

[99] A. e. a. Abdesselam, *The barrel modules of the ATLAS semiconductor tracker*, Nucl. Instrum. Meth. **A568** (2006) 642–671. Cited on page 26.

[100] ATLAS Collaboration, A. e. a. Abdesselam, *The ATLAS semiconductor tracker end-cap module*, Nucl. Instrum. Meth. **A575** (2007) 353–389. Cited on page 26.

[101] E. Abat et al., *The ATLAS Transition Radiation Tracker (TRT) proportional drift tube: Design and performance*, JINST **3** (2008) P02013. Cited on page 27.

[102] E. Abat et al., *The ATLAS TRT Barrel Detector*, JINST **3** (2008) P02014. Cited on page 27.

[103] E. Abat et al., *The ATLAS TRT end-cap detectors*, JINST **3** (2008) P10003. Cited on page 27.

[104] S. Fratina and E. Klinkby, *The Geometry of the ATLAS Transition Radiation Tracker*, ATL-COM-INDET-2010-002, 2010. Cited on page 27.

[105] ATLAS Collaboration, *Particle Identification Performance of the ATLAS Transition Radiation Tracker*, ATLAS-CONF-2011-128, 2011, https://cds.cern.ch/record/1383793. Cited on page 27.

[106] ATLAS Collaboration,, *ATLAS liquid-argon calorimeter: Technical Design Report*. CERN, Geneva, 1996. https://cds.cern.ch/record/331061. Cited on page 28.

[107] ATLAS Collaboration,, *ATLAS tile calorimeter: Technical Design Report*. CERN, Geneva, 1996. https://cds.cern.ch/record/331062. Cited on page 29.

[108] ATLAS Collaboration,, *ATLAS muon spectrometer: Technical Design Report*. CERN, Geneva, 1997. https://cds.cern.ch/record/331068. Cited on page 30.

[109] F. Bauer et al., *Construction and Test of MDT Chambers for the ATLAS Muon Spectrometer*, Nucl. Instrum. Meth. **A461** (2001) 17–20, arXiv:1604.02000 [physics.ins-det]. Cited on page 30.

[110] G. Aielli et al., *The RPC first level muon trigger in the barrel of the ATLAS experiment*, Nucl. Phys. Proc. Suppl. **158** (2006) 11–15. Cited on page 30.

[111] T. Argyropoulos et al., *Cathode strip chambers in ATLAS: Installation, commissioning and in situ performance*, IEEE Trans. Nucl. Sci. **56** (2009) 1568–1574. Cited on page 30.

[112] S. Majewski, G. Charpak, A. Breskin, and G. Mikenberg, *A Thin Multiwire Chamber Operating In The High Multiplication Mode*, Nucl. Instrum. Meth. **217** (1983) 265–271. Cited on page 30.

[113] A. Yamamoto et al., *The ATLAS central solenoid*, Nucl. Instrum. Meth. **A584** (2008) 53–74. Cited on page 31.

[114] ATLAS Collaboration,, *ATLAS barrel toroid: Technical design report*. CERN, Geneva, 1997. http://cdsweb.cern.ch/record/331065. Cited on page 31.

[115] ATLAS Collaboration,, *ATLAS endcap toroids: Technical design report*. CERN, Geneva, 1997. http://cdsweb.cern.ch/record/331066. Cited on page 31.

[116] ATLAS Collaboration, W. Panduro Vazquez, *The ATLAS Data Acquisition system in LHC Run 2*, J. Phys. Conf. Ser. **898** (2017) 032017. Cited on page 32.

[117] ATLAS Collaboration, *Trigger Menu in 2016*, ATL-DAQ-PUB-2017-001, 2017, https://cds.cern.ch/record/2242069. Cited on page 32.

[118] *Delay25 Manual*, Geneva, http://proj-delay25.web.cern.ch/proj-delay25/manuals/manual.pdf. Cited on page 45.

[119] M. Hance, *Readout of the ATLAS Transition Radiation Tracker: Timing Parameters and Constraints*, ATL-INDET-PUB-2008-008, Geneva, Sep, 2007, https://cds.cern.ch/record/1092926. Cited on page 45.

[120] P. Moreira and A. Marchioro, *QPLL. a quartz crystal based pll for jitter filtering application in LHC*, Amsterdam, 2003. Cited on page 45.

[121] Hance, M and Olivito, D and Saxon, J and Wagner, P, *Readout of the ATLAS Transition Radiation Tracker: Data Structure and Detector Granularity*, ATL-COM-INDET-2009-016, Geneva, May, 2009, https://cds.cern.ch/record/1179456. Cited on pages 46 and 188.

[122] W. Lampl et al., *Calorimeter Clustering Algorithms: Description and Performance*, ATL-LARG-PUB-2008-002, 2008, https://cds.cern.ch/record/1099735. Cited on page 52.

[123] ATLAS Collaboration, *Electron and photon energy calibration with the ATLAS detector using LHC Run 1 data*, Eur. Phys. J. C **74** (2014) 3071, arXiv:1407.5063 [hep-ex]. Cited on page 52.

[124] ATLAS Collaboration, *Topological cell clustering in the ATLAS calorimeters and its performance in LHC Run 1*, Eur. Phys. J. C **77** (2017) 490, arXiv:1603.02934 [hep-ex]. Cited on page 53.

[125] H. Abreu et al., *Performance of the electronic readout of the ATLAS liquid argon calorimeters*, JINST **5** (2010) P09003. Cited on page 54.

[126] W. E. Cleland and E. G. Stern, *Signal processing considerations for liquid ionization calorimeters in a high rate environment*, Nucl. Instrum. Meth. **A338** (1994) 467–497. Cited on page 54.

[127] M. e. a. Aharrouche, *Response Uniformity of the ATLAS Liquid Argon Electromagnetic Calorimeter*, Nucl. Instrum. Meth. **582** (2007). Cited on page 54.

[128] ATLAS Collaboration, *Electron and photon energy calibration with the ATLAS detector using 2015-2016 LHC proton-proton collision data*, Submitted to: JINST (2018), arXiv:1812.03848 [hep-ex]. Cited on pages 54 and 165.

[129] LEP Electroweak Working Group, *Precision electroweak measurements on the Z resonance*, Phys. Rept. **427** (2006) 257–454, arXiv:hep-ex/0509008 [hep-ex]. Cited on page 55.

[130] J. Saxon, *Discovery of the Higgs Boson, Measurements of its Production, and a Search for Higgs Boson Pair Production*, Jul, 2014. https://cds.cern.ch/record/1746004. Cited on page 57.

[131] CDF Collaboration, *First measurements of inclusive W and Z cross sections from Run II of the Tevatron collider*, Phys. Rev. Lett. **94** (2005) 091803, arXiv:hep-ex/0406078 [hep-ex]. Cited on pages 64 and 135.

[132] D0 Collaboration, *Measurement of the shape of the boson rapidity distribution for $p\bar{p} \to Z/gamma^* \to e^+e^- + X$ events produced at $\sqrt{s}$ of 1.96-TeV*, Phys. Rev. **D76** (2007) 012003, arXiv:hep-ex/0702025 [HEP-EX]. Cited on pages 64 and 135.

[133] ATLAS Collaboration, *Muon reconstruction performance of the ATLAS detector in proton–proton collision data at $\sqrt{s} = 13$ TeV*, Eur. Phys. J. C **76** (2016) 292, arXiv:1603.05598 [hep-ex]. Cited on pages 65 and 166.

[134] M. Cacciari, G. P. Salam, and G. Soyez, *The anti-k_t jet clustering algorithm*, JHEP **04** (2008) 063, arXiv:0802.1189 [hep-ph]. Cited on page 65.

[135] ATLAS Collaboration, *Pile-up subtraction and suppression for jets in ATLAS*, ATLAS-CONF-2013-083, 2013, https://cds.cern.ch/record/1570994. Cited on page 65.

[136] ATLAS Collaboration, *Tagging and suppression of pileup jets with the ATLAS detector*, ATLAS-CONF-2014-018, 2014, https://cds.cern.ch/record/1700870. Cited on page 65.

[137] ATLAS Collaboration, *Jet energy scale measurements and their systematic uncertainties in proton–proton collisions at $\sqrt{s} = 13$ TeV with the ATLAS detector*, Phys. Rev. D **96** (2017) 072002, arXiv:1703.09665 [hep-ex]. Cited on pages 65 and 167.

[138] ATLAS Collaboration, *Optimisation of the ATLAS b-tagging performance for the 2016 LHC Run*, ATL-PHYS-PUB-2016-012, 2016, https://cds.cern.ch/record/2160731. Cited on page 65.

[139] ATLAS Collaboration, *Observation of a new particle in the search for the Standard Model Higgs boson with the ATLAS detector at the LHC*, Phys. Lett. B **716** (2012) 1, arXiv:1207.7214 [hep-ex]. Cited on page 67.

[140] CMS Collaboration, *Observation of a new boson at a mass of 125 GeV with the CMS experiment at the LHC*, Phys. Lett. B **716** (2012) 30, arXiv:1207.7235 [hep-ex]. Cited on page 67.

[141] ATLAS Collaboration, *Measurements of fiducial and differential cross sections for Higgs boson production in the diphoton decay channel at* $\sqrt{s} = 8$ *TeV with ATLAS*, JHEP **09** (2014) 112, arXiv:1407.4222 [hep-ex]. Cited on page 67.

[142] CMS Collaboration, *Measurement of differential cross sections for Higgs boson production in the diphoton decay channel in pp collisions at* $\sqrt{s} = 8$ *TeV*, Eur. Phys. J. C **76** (2016) 13, arXiv:1508.07819 [hep-ex]. Cited on page 67.

[143] ATLAS Collaboration, *Constraints on non-Standard Model Higgs boson interactions in an effective Lagrangian using differential cross sections measured in the* $H \to \gamma\gamma$ *decay channel at* $\sqrt{s} = 8$ *TeV with the ATLAS detector*, Phys. Lett. B **753** (2016) 69, arXiv:1508.02507 [hep-ex]. Cited on pages 67 and 112.

[144] ATLAS Collaboration, *Measurement of Higgs boson production in the diphoton decay channel in pp collisions at center-of-mass energies of* 7 *and* 8 *TeV with the ATLAS detector*, Phys. Rev. D **90** (2014) 112015, arXiv:1408.7084 [hep-ex]. Cited on page 69.

[145] J. C. Collins, D. E. Soper, and G. F. Sterman, *Transverse Momentum Distribution in Drell-Yan Pair and W and Z Boson Production*, Nucl. Phys. **B250** (1985) 199. Cited on page 71.

[146] LHC Higgs Cross Section Working Group (S. Heinemeyer et al.), *Handbook of LHC Higgs Cross Sections: 3. Higgs Properties*, 2013, arXiv:1307.1347 [hep-ph]. Cited on page 72.

[147] A. Djouadi, J. Kalinowski, and M. Spira, *HDECAY: a program for Higgs boson decays in the Standard Model and its supersymmetric extension*, Comput. Phys. Commun. **108** (1998) 56, arXiv:hep-ph/9704448. Cited on page 72.

[148] A. Djouadi, M. M. Mühlleitner, and M. Spira, *Decays of supersymmetric particles: The Program SUSY-HIT (SUspect-SdecaY-Hdecay-InTerface)*, Acta Phys. Polon. **B38** (2007) 635, arXiv:hep-ph/0609292. Cited on page 72.

[149] A. Bredenstein, A. Denner, S. Dittmaier, and M. M. Weber, *Radiative corrections to the semileptonic and hadronic Higgs-boson decays* $H \to WW/ZZ \to 4$ *fermions*, JHEP **02** (2007) 80, arXiv:hep-ph/0611234. Cited on page 72.

[150] A. Bredenstein, A. Denner, S. Dittmaier, and M. M. Weber, *Precise predictions for the Higgs-boson decay* $H \to WW/ZZ \to 4$ *leptons*, Phys. Rev. D **74** (2006) 013004, arXiv:hep-ph/0604011. Cited on page 72.

[151] A. Bredenstein, A. Denner, S. Dittmaier, and M. M. Weber, *Precision calculations for the Higgs decays* $H \to ZZ/WW \to 4$ *leptons*, Nucl. Phys. Proc. Suppl. **160** (2006) 131, arXiv:hep-ph/0607060. Cited on page 72.

[152] K. Hamilton, P. Nason, E. Re, and G. Zanderighi, *NNLOPS simulation of Higgs boson production*, JHEP **10** (2013) 222, arXiv:1309.0017 [hep-ph]. Cited on page 72.

[153] J. Butterworth et al., *PDF4LHC recommendations for LHC Run II*, J. Phys. G **43** (2016) 023001, arXiv:1510.03865 [hep-ph]. Cited on page 72.

[154] K. Hamilton, P. Nason, C. Oleari, and G. Zanderighi, *Merging H/W/Z + 0 and 1 jet at NLO with no merging scale: a path to parton shower + NNLO matching*, JHEP **05** (2013) 82, arXiv:1212.4504 [hep-ph]. Cited on page 72.

[155] S. Catani and M. Grazzini, *An NNLO subtraction formalism in hadron collisions and its application to Higgs boson production at the LHC*, Phys. Rev. Lett. **98** (2007) 222002, arXiv:hep-ph/0703012. Cited on page 72.

[156] T. Sjöstrand, S. Mrenna, and P. Z. Skands, *A brief introduction to PYTHIA 8.1*, Comput. Phys. Commun. **178** (2008) 852, arXiv:0710.3820 [hep-ph]. Cited on pages 72 and 116.

[157] T. Sjöstrand, S. Ask, J. R. Christiansen, R. Corke, N. Desai, P. Ilten, S. Mrenna, S. Prestel, C. O. Rasmussen, and P. Z. Skands, *An Introduction to PYTHIA 8.2*, Comput. Phys. Commun. **191** (2015) 159, arXiv:1410.3012 [hep-ph]. Cited on pages 72 and 116.

[158] T. Sjostrand, S. Mrenna, and P. Z. Skands, *PYTHIA 6.4 Physics and Manual*, JHEP **05** (2006) 026, arXiv:hep-ph/0603175 [hep-ph]. Cited on pages 72 and 116.

[159] ATLAS Collaboration, *Measurement of the Z/γ^* boson transverse momentum distribution in pp collisions at $\sqrt{s} = 7$ TeV with the ATLAS detector*, JHEP **09** (2014) 145, arXiv:1406.3660 [hep-ex]. Cited on page 72.

[160] C. Anastasiou, C. Duhr, F. Dulat, F. Herzog, and B. Mistlberger, *Higgs Boson Gluon-Fusion Production in QCD at Three Loops*, Phys. Rev. Lett. **114** (2015) 212001, arXiv:1503.06056 [hep-ph]. Cited on page 73.

[161] C. Anastasiou, C. Duhr, F. Dulat, E. Furlan, T. Gehrmann, F. Herzog, A. Lazopoulos, and B. Mistlberger, *High precision determination of the gluon fusion Higgs boson cross-section at the LHC*, JHEP **05** (2016) 58, arXiv:1602.00695 [hep-ph]. Cited on page 73.

[162] S. Actis, G. Passarino, C. Sturm, and S. Uccirati, *NLO electroweak corrections to Higgs boson production at hadron colliders*, Phys. Lett. B **670** (2008) 12, arXiv:0809.1301 [hep-ph]. Cited on page 73.

[163] C. Anastasiou, R. Boughezal, and F. Petriello, *Mixed QCD-electroweak corrections to Higgs boson production in gluon fusion*, JHEP **04** (2009) 3, arXiv:0811.3458 [hep-ph]. Cited on page 73.

[164] P. Nason, *A New method for combining NLO QCD with shower Monte Carlo algorithms*, JHEP **11** (2004) 40, arXiv:hep-ph/0409146. Cited on pages 73 and 117.

[165] S. Frixione, P. Nason, and C. Oleari, *Matching NLO QCD computations with parton shower simulations: the POWHEG method*, JHEP **11** (2007) 70, arXiv:0709.2092 [hep-ph]. Cited on pages 73 and 117.

[166] S. Alioli, P. Nason, C. Oleari, and E. Re, *A general framework for implementing NLO calculations in shower Monte Carlo programs: the POWHEG BOX*, JHEP **06** (2010) 43, arXiv:1002.2581 [hep-ph]. Cited on pages 73 and 117.

[167] P. Nason and C. Oleari, *NLO Higgs boson production via vector-boson fusion matched with shower in POWHEG*, JHEP **02** (2010) 37, arXiv:0911.5299 [hep-ph]. Cited on page 73.

[168] M. Ciccolini, A. Denner, and S. Dittmaier, *Strong and electroweak corrections to the production of Higgs + 2 jets via weak interactions at the LHC*, Phys. Rev. Lett. **99** (2007) 161803, arXiv:0707.0381 [hep-ph]. Cited on page 73.

[169] M. Ciccolini, A. Denner, and S. Dittmaier, *Electroweak and QCD corrections to Higgs production via vector-boson fusion at the LHC*, Phys. Rev. D **77** (2008) 013002, arXiv:0710.4749 [hep-ph]. Cited on page 73.

[170] P. Bolzoni, F. Maltoni, S.-O. Moch, and M. Zaro, *Higgs production via vector-boson fusion at NNLO in QCD*, Phys. Rev. Lett. **105** (2010) 011801, arXiv:1003.4451 [hep-ph]. Cited on page 73.

[171] K. Mimasu, V. Sanz, and C. Williams, *Higher order QCD predictions for associated Higgs production with anomalous couplings to gauge bosons*, JHEP **08** (2016) 39, arXiv:1512.02572 [hep-ph]. Cited on page 73.

[172] O. Brein, A. Djouadi, and R. Harlander, *NNLO QCD corrections to the Higgs-strahlung processes at hadron colliders*, Phys. Lett. B **579** (2004) 149, arXiv:hep-ph/0307206. Cited on page 73.

[173] L. Altenkamp, S. Dittmaier, R. V. Harlander, H. Rzehak, and T. J. E. Zirke, *Gluon-induced Higgs-strahlung at next-to-leading order QCD*, JHEP **02** (2013) 78, arXiv:1211.5015 [hep-ph]. Cited on page 73.

[174] A. Denner, S. Dittmaier, S. Kallweit, and A. Mück, *Electroweak corrections to Higgs-strahlung off W/Z bosons at the Tevatron and the LHC with HAWK*, JHEP **03** (2012) 75, arXiv:1112.5142 [hep-ph]. Cited on page 73.

[175] J. Alwall, R. Frederix, S. Frixione, V. Hirschi, F. Maltoni, O. Mattelaer, H. S. Shao, T. Stelzer, P. Torrielli, and M. Zaro, *The automated computation of tree-level and next-to-leading order differential cross sections, and their matching to parton shower simulations*, JHEP **07** (2014) 79, arXiv:1405.0301 [hep-ph]. Cited on pages 73, 105, and 116.

[176] NNPDF Collaboration, *Parton distributions for the LHC Run II*, JHEP **04** (2015) 040, arXiv:1410.8849 [hep-ph]. Cited on pages 73 and 116.

[177] ATLAS Collaboration, *ATLAS Pythia 8 tunes to 7 TeV data*, ATL-PHYS-PUB-2014-021, 2014, https://cds.cern.ch/record/1966419. Cited on pages 73 and 116.

[178] W. Beenakker et al., *NLO QCD corrections to $t\bar{t}H$ production in hadron collisions*, Nucl. Phys. B **653** (2003) 151, arXiv:hep-ph/0211352. Cited on page 73.

[179] S. Dawson, C. Jackson, L. Orr, L. Reina, and D. Wackeroth, *Associated Higgs production with top quarks at the large hadron collider: NLO QCD corrections*, Phys. Rev. D **68** (2003) 034022, arXiv:hep-ph/0305087. Cited on page 73.

[180] Y. Zhang, W.-G. Ma, R.-Y. Zhang, C. Chen, and L. Guo, *QCD NLO and EW NLO corrections to $t\bar{t}H$ production with top quark decays at hadron collider*, Phys. Lett. B **738** (2014) 1, arXiv:1407.1110 [hep-ph]. Cited on page 73.

[181] S. Frixione, V. Hirschi, D. Pagani, H.-S. Shao, and M. Zaro, *Electroweak and QCD corrections to top-pair hadroproduction in association with heavy bosons*, JHEP **06** (2015) 184, arXiv:1504.03446 [hep-ph]. Cited on page 73.

[182] H.-L. Lai et al., *New parton distributions for collider physics*, Phys. Rev. D **82** (2010) 074024, arXiv:1007.2241 [hep-ph]. Cited on page 73.

[183] S. Dawson, C. Jackson, L. Reina, and D. Wackeroth, *Exclusive Higgs boson production with bottom quarks at hadron colliders*, Phys. Rev. D **69** (2004) 074027, arXiv:hep-ph/0311067. Cited on page 73.

[184] S. Dittmaier, M. Krämer, and M. Spira, *Higgs radiation off bottom quarks at the Tevatron and the CERN LHC*, Phys. Rev. D **70** (2004) 074010, arXiv:hep-ph/0309204. Cited on page 73.

[185] R. Harlander, M. Kramer, and M. Schumacher, *Bottom-quark associated Higgs-boson production: reconciling the four- and five-flavour scheme approach*, 2011, arXiv:1112.3478 [hep-ph]. Cited on page 73.

[186] S. Gieseke, A. Ribon, M. H. Seymour, P. Stephens, and B. Webber, *Herwig++ 1.0: an event generator for e^+ e^- annihilation*, JHEP **02** (2004) 005, arXiv:hep-ph/0311208. Cited on page 73.

[187] J. Bellm et al., *Herwig++ 2.7 release note*, 2013, arXiv:1310.6877 [hep-ph]. Cited on page 73.

[188] M. Bahr et al., *Herwig++ physics and manual*, 2008, arXiv:0803.0883 [hep-ph]. Cited on page 73.

[189] F. Demartin, F. Maltoni, K. Mawatari, and M. Zaro, *Higgs production in association with a single top quark at the LHC*, Eur. Phys. J. C **75** (2015) 267, arXiv:1504.00611 [hep-ph]. Cited on page 74.

[190] S. Agostinelli et al., *GEANT4 - a simulation toolkit*, Nucl. Instrum. Meth. **A506** (2003) 250–303. Cited on pages 74 and 117.

[191] ATLAS Collaboration, *The ATLAS Simulation Infrastructure*, Eur. Phys. J. C **70** (2010) 823, arXiv:1005.4568 [physics.ins-det]. Cited on pages 74 and 117.

[192] T. Gleisberg et al., *Event generation with SHERPA 1.1*, JHEP **02** (2009) 007, arXiv:0811.4622 [hep-ph]. Cited on pages 74, 103, and 116.

[193] S. Schumann and F. Krauss, *A Parton shower algorithm based on Catani-Seymour dipole factorisation*, JHEP **03** (2008) 38, arXiv:0709.1027 [hep-ph]. Cited on pages 74, 103, and 116.

[194] S. Höche, F. Krauss, S. Schumann, and F. Siegert, *QCD matrix elements and truncated showers*, JHEP **05** (2009) 53, arXiv:0903.1219 [hep-ph]. Cited on page 74.

[195] ATLAS Collaboration, *The simulation principle and performance of the ATLAS fast calorimeter simulation FastCaloSim*, ATL-PHYS-PUB-2010-013, 2010, https://cds.cern.ch/record/1300517. Cited on pages 74 and 116.

[196] A. D. Martin, W. J. Stirling, R. S. Thorne, and G. Watt, *Parton distributions for the LHC*, Eur. Phys. J. C **63** (2009) 189, arXiv:0901.0002 [hep-ph]. Cited on page 74.

[197] ATLAS Collaboration, *Summary of ATLAS Pythia 8 tunes*, ATL-PHYS-PUB-2012-003, 2012, https://cds.cern.ch/record/1474107. Cited on pages 74 and 117.

[198] M. Oreglia, *A Study of the Reactions $\psi' \to \gamma\gamma\psi$*, http://slac.stanford.edu/pubs/slacreports/reports13/slac-r-236.pdf. Cited on page 75.

[199] ATLAS Collaboration, *Measurement of the isolated diphoton cross section in pp collisions at $\sqrt{s} = 7$ TeV with the ATLAS detector*, Phys. Rev. D **85** (2012) 012003, arXiv:1107.0581 [hep-ex]. Cited on pages 76 and 78.

[200] ATLAS Collaboration, *Measurement of isolated-photon pair production in pp collisions at $\sqrt{s} = 7$ TeV with the ATLAS detector*, JHEP **01** (2013) 086, arXiv:1211.1913 [hep-ex]. Cited on pages 76 and 78.

[201] R. Brun and F. Rademakers, *ROOT: An object oriented data analysis framework*, Nucl. Instrum. Meth. **A389** (1997) 81. Cited on page 85.

[202] G. Cowan, K. Cranmer, E. Gross, and O. Vitells, *Asymptotic formulae for likelihood-based tests of new physics*, Eur. Phys. J. **C71** (2011) 1554, arXiv:1007.1727 [physics.data-an]. Cited on pages 85 and 89.

[203] S. S. Wilks, *The Large-Sample Distribution of the Likelihood Ratiofor Testing Composite Hypotheses*, Annals Math. Statist. **9** (1938) 60. Cited on page 89.

[204] G. Cowan, *A survey of unfolding methods for particle physics*, Conf. Proc. **C0203181** (2002) 248. Cited on page 98.

[205] A. Hocker and V. Kartvelishvili, *SVD approach to data unfolding*, Nucl. Instrum. Meth. **A372** (1996) 469, arXiv:hep-ph/9509307 [hep-ph]. Cited on page 98.

[206] G. D'Agostini, *A Multidimensional unfolding method based on Bayes'theorem*, Nucl. Instrum. Meth. **A362** (1995) 487. Cited on page 98.

[207] B. Malaescu, *An Iterative, dynamically stabilized method of data unfolding*, arXiv:0907.3791 [physics.data-an]. Cited on page 98.

[208] ATLAS Collaboration, *Performance of the Electron and Photon Trigger in pp Collisions at $\sqrt{s} = 7$ TeV with the ATLAS Detector at the LHC*, ATLAS-CONF-2011-114, 2011, https://cds.cern.ch/record/1375551. Cited on page 101.

[209] ATLAS Collaboration, *Measurement of the Inelastic Proton–Proton Cross Section at $\sqrt{s} = 13$ TeV with the ATLAS Detector at the LHC*, Phys. Rev. Lett. **117** (2016) 182002, arXiv:1606.02625 [hep-ex]. Cited on page 101.

[210] ATLAS Collaboration, *Improved luminosity determination in pp collisions at $\sqrt{s} = 7$ TeV using the ATLAS detector at the LHC*, Eur. Phys. J. C **73** (2013) 2518, arXiv:1302.4393 [hep-ex]. Cited on page 101.

[211] S. van der Meer ISR-PO/68-31, KEK 68-64. Cited on page 101.

[212] N. Greiner, S. H<9a>che, G. Luisoni, M. Sch<9a>nherr, J.-C. Winter, and V. Yundin, *Phenomenological analysis of Higgs boson production through gluon fusion in association with jets*, JHEP **01** (2016) 169, arXiv:1506.01016 [hep-ph]. Cited on page 103.

[213] S. Höche, F. Krauss, M. Schonherr, and F. Siegert, *A critical appraisal of NLO+PS matching methods*, JHEP **09** (2012) 49, arXiv:1111.1220 [hep-ph]. Cited on page 103.

[214] S. Höche, F. Krauss, M. Schonherr, and F. Siegert, *QCD matrix elements + parton showers: The NLO case*, JHEP **04** (2013) 27, arXiv:1207.5030 [hep-ph]. Cited on pages 103 and 116.

[215] M. Buschmann, D. Goncalves, S. Kuttimalai, M. Schonherr, F. Krauss, and T. Plehn, *Mass effects in the Higgs-gluon coupling: boosted vs off-shell production*, JHEP **02** (2015) 038, arXiv:1410.5806 [hep-ph]. Cited on page 103.

[216] E. Bothmann, M. Schonherr, and S. Schumann, *Reweighting QCD matrix-element and parton-shower calculations*, Eur. Phys. J. C **76** (2016) 590, arXiv:1606.08753 [hep-ph]. Cited on page 103.

[217] T. Gleisberg and S. Höche, *Comix, a new matrix element generator*, JHEP **12** (2008) 39, arXiv:0808.3674 [hep-ph]. Cited on page 103.

[218] F. Krauss, R. Kuhn, and G. Soff, *AMEGIC++ 1.0: A matrix element generator in C++*, JHEP **02** (2002) 044, arXiv:hep-ph/0109036. Cited on page 103.

[219] G. Cullen et al. Cited on pages 103 and 105.

[220] S. Höche and M. Schonherr, *Uncertainties in next-to-leading order plus parton shower matched simulations of inclusive jet and dijet production*, Phys. Rev. D **86** (2012) 094042, arXiv:1208.2815 [hep-ph]. Cited on page 103.

[221] S. Höche, F. Krauss, and M. Schonherr, *Uncertainties in MEPS@NLO calculations of h+jets*, Phys. Rev. D **90** (2014) 014012, arXiv:1401.7971 [hep-ph]. Cited on page 103.

[222] D. de Florian, G. Ferrera, M. Grazzini, and D. Tommasini, *Higgs boson production at the LHC: transverse momentum resummation effects in the $H \to \gamma\gamma$, $H \to WW \to \ell\nu\ell\nu$ and $H \to ZZ \to 4\ell$ decay modes*, JHEP **06** (2012) 132, arXiv:1203.6321 [hep-ph]. Cited on page 104.

[223] M. Grazzini and H. Sargsyan, *Heavy-quark mass effects in Higgs boson production at the LHC*, JHEP **09** (2013) 129, arXiv:1306.4581 [hep-ph]. Cited on page 104.

[224] P. F. Monni, E. Re, and P. Torrielli, *Higgs Transverse-Momentum Resummation in Direct Space*, Phys. Rev. Lett. **116** (2016) 242001, arXiv:1604.02191 [hep-ph]. Cited on page 104.

[225] X. Chen, T. Gehrmann, E. W. N. Glover, and M. Jaquier, *Precise QCD predictions for the production of Higgs + jet final states*, Phys. Lett. B **740** (2015) 147, arXiv:1408.5325 [hep-ph]. Cited on page 104.

[226] X. Chen, J. Cruz-Martinez, T. Gehrmann, E. W. N. Glover, and M. Jaquier, *NNLO QCD corrections to Higgs boson production at large transverse momentum*, JHEP **10** (2016) 066, arXiv:1607.08817 [hep-ph]. Cited on page 104.

[227] M. A. Ebert, J. K. L. Michel, and F. J. Tackmann, *Resummation improved rapidity spectrum for gluon fusion Higgs production*, JHEP **05** (2017) 088, arXiv:1702.00794 [hep-ph]. Cited on page 105.

[228] M. A. Ebert et al., *SCETlib: A C++ Package for Numerical Calculations in QCD and Soft-Collinear Effective Theory*, http://scetlib.desy.de. Cited on page 105.

[229] R. Boughezal, J. M. Campbell, R. K. Ellis, C. Focke, W. Giele, X. Liu, F. Petriello, and C. Williams, *Color singlet production at NNLO in MCFM*, Eur. Phys. J. C **77** (2017) 7, arXiv:1605.08011 [hep-ph]. Cited on page 105.

[230] J. Gaunt, M. Stahlhofen, F. J. Tackmann, and J. R. Walsh, *N-jettiness Subtractions for NNLO QCD calculations*, JHEP **09** (2015) 058, arXiv:1505.04794 [hep-ph]. Cited on page 105.

[231] A. Banfi, F. Caola, F. A. Dreyer, P. F. Monni, G. P. Salam, G. Zanderighi, and F. Dulat, *Jet-vetoed Higgs cross section in gluon fusion at N^3LO+NNLL with small-R resummation*, JHEP **04** (2016) 049, arXiv:1511.02886 [hep-ph]. Cited on page 105.

[232] I. W. Stewart, F. J. Tackmann, J. R. Walsh, and S. Zuberi, *Jet p_T Resummation in Higgs Production at $NNLL' + NNLO$*, Phys. Rev. D **89** (2014) 054001, arXiv:1307.1808 [hep-ph]. Cited on page 105.

[233] R. Boughezal, X. Liu, F. Petriello, F. J. Tackmann, and J. R. Walsh, *Combining resummed Higgs predictions across jet bins*, Phys. Rev. D **89** (2014) 074044, arXiv:1312.4535 [hep-ph]. Cited on page 105.

[234] G. Cullen, N. Greiner, G. Heinrich, G. Luisoni, P. Mastrolia, G. Ossola, T. Reiter, and F. Tramontano, *Automated one-loop calculations with GoSam*, Eur. Phys. J. C **72** (2012) 1889, arXiv:1111.2034 [hep-ph]. Cited on page 105.

[235] R. Frederix, S. Frixione, E. Vryonidou, and M. Wiesemann, *Heavy-quark mass effects in Higgs plus jets production*, JHEP **08** (2016) 006, arXiv:1604.03017 [hep-ph]. Cited on page 105.

[236] R. Frederix and S. Frixione, *Merging meets matching in MC@NLO*, JHEP **12** (2012) 061, arXiv:1209.6215 [hep-ph]. Cited on page 105.

[237] X. Chen, T. Gehrmann, E. W. N. Glover, A. Huss, Y. Li, D. Neill, M. Schulze, I. W. Stewart, and H. X. Zhu, *Precise QCD Description of the Higgs Boson Transverse Momentum Spectrum*, Phys. Lett. **B788** (2019) 425, arXiv:1805.00736 [hep-ph]. Cited on page 105.

[238] F. L. Wilson, *Fermi's Theory of Beta Decay*, Am. J. Phys. **36** (1968) 1150–1160, https://doi.org/10.1119/1.1974382. Cited on page 107.

[239] G. F. Giudice, C. Grojean, A. Pomarol, and R. Rattazzi, *The Strongly-Interacting Light Higgs*, JHEP **06** (2007) 045, arXiv:hep-ph/0703164 [hep-ph]. Cited on page 108.

[240] B. Grzadkowski, M. Iskrzynski, M. Misiak, and J. Rosiek, *Dimension-Six Terms in the Standard Model Lagrangian*, JHEP **10** (2010) 085, arXiv:1008.4884 [hep-ph]. Cited on page 108.

[241] R. Contino, M. Ghezzi, C. Grojean, M. Muhlleitner, and M. Spira, *Effective Lagrangian for a light Higgs-like scalar*, JHEP **07** (2013) 035, arXiv:1303.3876 [hep-ph]. Cited on pages 108 and 109.

[242] J. Elias-Miro, J. R. Espinosa, E. Masso, and A. Pomarol, *Higgs windows to new physics through d=6 operators: constraints and one-loop anomalous dimensions*, JHEP **11** (2013) 066, arXiv:1308.1879 [hep-ph]. Cited on page 108.

[243] A. Alloul, B. Fuks, and V. Sanz, *Phenomenology of the Higgs Effective Lagrangian via FEYNRULES*, JHEP **04** (2014) 110, arXiv:1310.5150 [hep-ph]. Cited on page 109.

[244] A. Pomarol and F. Riva, *Towards the Ultimate SM Fit to Close in on Higgs Physics*, JHEP **01** (2014) 151, arXiv:1308.2803 [hep-ph]. Cited on page 109.

[245] J. Ellis, V. Sanz, and T. You, *The Effective Standard Model after LHC Run I*, JHEP **03** (2015) 157, arXiv:1410.7703 [hep-ph]. Cited on page 109.

[246] A. Buckley, H. Hoeth, H. Lacker, H. Schulz, and J. E. von Seggern, *Systematic event generator tuning for the LHC*, Eur. Phys. J. **C65** (2010) 331–357, arXiv:0907.2973 [hep-ph]. Cited on page 109.

[247] ATLAS and CMS Collaborations, *Measurements of the Higgs boson production and decay rates and constraints on its couplings from a combined ATLAS and CMS analysis of the LHC pp collision data at $\sqrt{s} = 7$ and 8 TeV*, JHEP **08** (2016) 045, arXiv:1606.02266 [hep-ex]. Cited on page 113.

[248] CMS Collaboration, *Combined measurements of the Higgs boson's couplings at $\sqrt{s} = 13$ TeV*, Cms-pas-hig-17-031, 2018, https://cds.cern.ch/record/2308127. Cited on page 113.

[249] J. R. Ellis, J. F. Gunion, H. E. Haber, L. Roszkowski, and F. Zwirner, *Higgs Bosons in a Nonminimal Supersymmetric Model*, Phys. Rev. **D39** (1989) 844. Cited on page 113.

[250] ATLAS Collaboration, *Search for exotic Higgs-boson decays in events with at least one photon, missing transverse momentum, and two forward jets produced in $\sqrt{s} = 8$ TeV pp collisions with the ATLAS detector*, ATLAS-CONF-2015-001, 2015, https://cds.cern.ch/record/1988425. Cited on pages 115 and 184.

[251] CMS Collaboration, *Search for exotic decays of a Higgs boson into undetectable particles and one or more photons*, Phys. Lett. B **753** (2016) 363, arXiv:1507.00359 [hep-ex]. Cited on page 115.

[252] ATLAS Collaboration, *Search for supersymmetry in a final state containing two photons and missing transverse momentum in $\sqrt{s} = 13$ TeV pp collisions at the LHC using the ATLAS detector*, Eur. Phys. J. C **76** (2016) 517, arXiv:1606.09150 [hep-ex]. Cited on page 115.

[253] ATLAS Collaboration, *Search for photonic signatures of gauge-mediated supersymmetry in 13 TeV pp collisions with the ATLAS detector*, Phys. Rev. **D97** (2018) 092006, arXiv:1802.03158 [hep-ex]. Cited on page 115.

[254] ATLAS Collaboration, *Search for dark matter in association with a Higgs boson decaying to two photons at $\sqrt{s} = 13$ TeV with the ATLAS detector*, Phys. Rev. D **96** (2017) 112004, arXiv:1706.03948 [hep-ex]. Cited on page 115.

[255] ATLAS Collaboration, *Search for dark matter at $\sqrt{s} = 13$ TeV in final states containing an energetic photon and large missing transverse momentum with the ATLAS detector*, Eur. Phys. J. C **77** (2017) 393, arXiv:1704.03848 [hep-ex]. Cited on page 115.

[256] CMS Collaboration, *Search for gauge-mediated supersymmetry in events with at least one photon and missing transverse momentum in pp collisions at $\sqrt{s} = 13$ TeV*, Phys. Lett. B **780** (2018) 118, arXiv:1711.08008 [hep-ex]. Cited on page 115.

[257] CMS Collaboration, *Search for new physics in final states with a single photon and missing transverse momentum in proton-proton collisions at $\sqrt{s} = 13$ TeV*, Submitted to: JHEP (2018), arXiv:1810.00196 [hep-ex]. Cited on page 115.

[258] J. Alwall, P. Schuster, and N. Toro, *Simplified Models for a First Characterization of New Physics at the LHC*, Phys. Rev. **D79** (2009) 075020, arXiv:0810.3921 [hep-ph]. Cited on page 116.

[259] L. N. P. W. Group, *Simplified Models for LHC New Physics Searches*, J. Phys. **G39** (2012) 105005, arXiv:1105.2838 [hep-ph]. Cited on page 116.

[260] R. B. et al., *Parton distributions with LHC data*, Nucl. Phys. **B867** (2013) 244–289, arXiv:1207.1303 [hep-ph]. Cited on page 116.

[261] M. Grazzini, S. Kallweit, D. Rathlev, and M. Wiesemann, *$W^{\pm}Z$ production at hadron colliders in NNLO QCD*, Phys. Lett. **B761** (2016) 179–183, arXiv:1604.08576 [hep-ph]. Cited on page 119.

[262] C. Anastasiou, L. J. Dixon, K. Melnikov, and F. Petriello, *High precision QCD at hadron colliders: Electroweak gauge boson rapidity distributions at NNLO*, Phys. Rev. D **69** (2004) 094008, arXiv:hep-ph/0312266 [hep-ph]. Cited on page 120.

[263] R. D. Cousins, K. E. Hymes, and J. Tucker, *Frequentist evaluation of intervals estimated for a binomial parameter and for the ratio of Poisson means*, Nucl. Instrum. Meth. **A612** (2010) 388–398, arXiv:0905.3831 [physics.data-an]. Cited on page 120.

[264] K. Cranmer, *Statistical challenges for searches for new physics at the LHC*, in *Statistical Problems in Particle Physics, Astrophysics and Cosmology (PHYSTAT 05): Proceedings, Oxford, UK,September 12-15, 2005*. Cited on page 120.

[265] ATLAS Collaboration, *Searches for the $Z\gamma$ decay mode of the Higgs boson and for new high-mass resonances in pp collisions at $\sqrt{s} = 13$ TeV with the ATLAS detector*, JHEP **10** (2017) 112, arXiv:1708.00212 [hep-ex]. Cited on page 160.

[266] ATLAS Collaboration, *Luminosity determination in pp collisions at $\sqrt{s} = 8$ TeV using the ATLAS detector at the LHC*, Eur. Phys. J. C **76** (2016) 653, arXiv:1608.03953 [hep-ex]. Cited on page 165.

[267] ATLAS Collaboration, *Electron and photon energy calibration with the ATLAS detector using data collected in 2015 at $\sqrt{s} = 13$ TeV*, ATL-PHYS-PUB-2016-015, 2016, https://cds.cern.ch/record/2203514. Cited on page 165.

[268] ATLAS Collaboration, *Electron efficiency measurements with the ATLAS detector using the 2012 LHC proton–proton collision data*, ATLAS-CONF-2014-032, 2014, https://cds.cern.ch/record/1706245. Cited on page 165.

[269] ATLAS Collaboration, *Muon reconstruction performance in early $\sqrt{s} = 13$ TeV data*, ATL-PHYS-PUB-2015-037, 2015, https://cds.cern.ch/record/2047831. Cited on page 166.

[270] ATLAS Collaboration, *Jet energy measurement and its systematic uncertainty in proton–proton collisions at $\sqrt{s} = 7$ TeV with the ATLAS detector*, Eur. Phys. J. C **75** (2015) 17, arXiv:1406.0076 [hep-ex]. Cited on page 167.

[271] ATLAS Collaboration, *Forward Jet Vertex Tagging: A new technique for the identification and rejection of forward pileup jets*, ATL-PHYS-PUB-2015-034, 2015, https://cds.cern.ch/record/2042098. Cited on page 167.

[272] ATLAS Collaboration, *Expected performance of missing transverse momentum reconstruction for the ATLAS detector at $\sqrt{s} = 13$ TeV*, ATL-PHYS-PUB-2015-023, 2015, https://cds.cern.ch/record/2037700. Cited on page 167.

[273] ATLAS Collaboration, *Performance of missing transverse momentum reconstruction with the ATLAS detector using proton–proton collisions at $\sqrt{s} = 13$ TeV*, arXiv:1802.08168 [hep-ex]. Cited on page 167.

[274] M. Grazzini, S. Kallweit, and D. Rathlev, *$W\gamma$ and $Z\gamma$ production at the LHC in NNLO QCD*, JHEP **07** (2015) 085, arXiv:1504.01330 [hep-ph]. Cited on page 169.

[275] K. Melnikov, M. Schulze, and A. Scharf, *QCD corrections to top quark pair production in association with a photon at hadron colliders*, Phys. Rev. **D83** (2011) 074013, arXiv:1102.1967 [hep-ph]. Cited on page 169.

[276] M. Baak, G. J. Besjes, D. CÃťte, A. Koutsman, J. Lorenz, and D. Short, *HistFitter software framework for statistical data analysis*, Eur. Phys. J. **C75** (2015) 153, arXiv:1410.1280 [hep-ex]. Cited on pages 170 and 172.

[277] A. L. Read, *Presentation of search results: The CL(s) technique*, J. Phys. **G28** (2002) 2693–2704. Cited on page 171.

[278] G. Zech, *Upper Limits in Experiments with Background Or Measurement Errors*, Nucl. Instrum. Meth. **A277** (1989) 608. Cited on page 171.

[279] ATLAS Collaboration, *ATLAS Collision Events*, 2012. http://atlasexperiment.org/atlas_photos/fulldetector/events_jpg.html. [Online; accessed 1-May-2019]. Cited on page 230.